Measurement of the chemical composition of ultra high energy cosmic rays with the HEAT telescopes of the Pierre Auger Observatory

Von der Fakultät für Mathematik, Informatik und Naturwissenschaften der RWTH Aachen University zur Erlangung des akademischen Grades eines Doktors der Naturwissenschaften genehmigte Dissertation

vorgelegt von

Diplom-Physiker

Matthias Plum

aus Aachen

Berichter: Universitätsprofessor Dr.rer.nat. Thomas Hebbeker
Universitätsprofessor Dr.rer.nat. Christopher Wiebusch

Tag der mündlichen Prüfung: 7.11.2016

Abstract

The Pierre Auger Observatory is currently the largest detector for measurements of cosmic rays with energies beyond 10^{18} eV. It uses a hybrid detection method with fluorescence telescopes and surface detector stations. Cosmic rays with energies above 10^{15} eV cannot be studied directly but they interact with the atmosphere and produce secondary particle cascades, called extensive air shower. These air showers carry information about the energy, the arrival direction and the chemical composition of the primary cosmic ray particle. The fluorescence telescopes measure the longitudinal air shower profile, whereas the surface detector stations study the lateral profile on the ground. The combination of both detectors provides measurements of cosmic rays with high accuracy.

This thesis is focused on the study of the chemical composition of cosmic rays with the virtual fluorescence telescope HECO, which is the combination of the low energy enhancement HEAT (High Elevation Auger Telescopes) and the Coihueco telescope station. HEAT consists of 3 additional fluorescence telescopes, extending the energy range down to below $10^{17.0}$ eV. The cosmic rays with energies between 10^{17} eV to $10^{18.4}$ eV are studied, which is the expected transition region from galactic to extra galactic cosmic rays. For the analysis of the chemical composition the atmospheric depth of the air shower maximum X_{max} is used. The distribution of X_{max} is depending on the atomic mass of the primary cosmic ray particle.

An improved profile reconstruction using air shower universality is introduced in the reconstruction and several cross checks on the acquired data and simulations are performed. A complete Monte Carlo based composition analysis is performed to validate the analysis method. The systematic uncertainties of the analysis are studied in detail.

The resulting first moments $\langle X_{max} \rangle$ and $\sigma_{X_{max}}$ of the measured X_{max}-distribution per energy bin are compared to theoretical predictions from current cosmic ray interaction models. Additionally, a new fit method is introduced to fit chemical composition fractions based on prediction from interaction models. A parametrization based on Gumbel statistics and air shower simulation is used to describe the X_{max}-distribution as a function of energy and primary atomic mass. A superposition model of these parametrization is fitted on a simulated scenario to find the optimal fit routine. The method is applied on the measured X_{max} data including all know systematic uncertainties. The findings of this thesis are compared to published results of other experiments. The results of all interaction models suggest a heavy composition at $10^{17.0}$ eV that becomes lighter up to $10^{18.4}$ eV, where it is composed of a mixture of nuclei with light atomic masses.

Zusammenfassung

Das Pierre Auger Observatorium ist zur Zeit der weltweit größte Detektor für kosmische Strahlung mit Energien über 10^{18} eV. Es nutzt eine Hybriddetektions-Methode mit Fluoreszenz-Teleskopen und Oberflächen-Detektoren. Kosmische Strahlung mit Energien über 10^{15} eV kann nicht direkt gemessen werden, aber sie wechselwirken mit der Atmosphäre und produzieren Kaskaden von Sekundärteilchen, die ausgedehnte Luftschauer. Die Entwicklung dieser Luftschauer enthält Information über die Energie, die Ankunftsrichtung und die chemische Zusammensetzung des Primärteilchen. Die Fluoreszenz-Teleskope vermessen das longitudinale, die Oberflächen-Detektoren das laterale Luftschauerprofil. Die Kombination von beiden Detektormethoden ermöglicht die Messung von kosmischer Strahlung mit sehr großer Genauigkeit.
Diese Doktorarbeit beschäftigt sich mit der Messung der chemischen Zusammensetzung der kosmischen Strahlung mit Hilfe des virtuellen Fluoreszenz-Teleskop HECO, einer Kombination aus der Niederenergie-Erweiterung HEAT (High Elevation Auger Telescopes) und der Coihueco Teleskopstation. HEAT besteht aus 3 zusätzlichen Fluoreszenz-Teleskopen, mit denen die Energieschwelle der Luftschauer-Detektion auf unter $10^{17.0}$ eV gesenkt wird. Die kosmische Strahlung mit Energien von 10^{17} eV bis $10^{18.4}$ eV werden untersucht, da in diesem Bereich der Übergang von galaktischer zu extra-galaktischer kosmischer Strahlung erwartet wird. Für die Analyse der chemischen Zusammensetzung wird die Position des Luftschauermaximums X_{max} in der Atmosphäre verwendet. Die statistische Verteilung von X_{max} ist abhängig von der atomaren Masse der Primärteilchen. Es werden eine verbesserte Luftschauer-Profilrekonstruktion und verschiedene Kontrolltest der Daten und der Simulationen präsentiert. Eine Monte Carlo basierte Kompositionsanalyse ist durchgeführt worden, um die Analysemethode zu validieren. Zusätzlich werden die systematischen Unsicherheiten der Analyse untersucht. Der Mittelwert $\langle X_{max} \rangle$ und die Streuung $\sigma_{X_{max}}$ der X_{max}-Verteilungen als Funktion der Energie wird mit theoretische Vorhersagen von aktuellen Wechselwirkungsmodellen verglichen. Eine Parametrisierung der X_{max}-Verteilungen mit Hilfe von Gumbel-Statistik und Simulationen ermöglicht das Beschreiben dieser als Funktion der Energie und der atomaren Masse. Dies ermöglicht eine Analyse der chemischen Zusammensetzung der kosmischen Strahlung. Ein Superposition-Model dieser Parametrisierungen bestehend aus unterschiedlichen Elementgruppen wurde an einen Monte Carlo-Szenario zur Optimierung getestet und auf die gemessenen X_{max} Daten angewendet. Dabei wurden alle systematischen Unsicherheiten berücksichtigt.
Die Resultate dieser Doktorarbeit werden mit aktuellen Veröffentlichungen unterschiedlicher Experimente verglichen. Die Ergebnisse von allen Wechselwirkungsmodellen sehen tendenziell eine chemische Komposition von schweren Elementen um $10^{17.0}$ eV. Mit steigender Energie wird die Komposition leichter bis diese bei $10^{18.4}$ eV aus einem Mix leichter Elemente zu bestehen scheint.

Contents

Chapter 1

Introduction

Cosmic rays have been observed on earth for over 100 years. They are measured over a wide energy range from below 10^6 eV to beyond 10^{20} eV, the highest energies measured in particle physics. These ultra high energies are currently unreachable by man made accelerators. As these events are extremely rare, very large detector areas are needed to observe them. If high energetic cosmic rays hit the earth's atmosphere, they interact and form cascades of secondary particles, which can reach the surface. These secondary cascades are called extensive air showers as the dimension of their footprints can reach several km^2. The secondary particle showers are currently the only way to study the cosmic rays at the highest energies.
Today it is still unknown where the highest cosmic rays come from, as their acceleration processes and their source regions are still unknown. At the highest energies the cosmic rays consist mostly of charged particles, which are deflected by the extra galactic and galactic magnetic fields. Therefore, the chemical composition is one of the keys to understand the origin of these particles.

The Pierre Auger Observatory is the largest detector for cosmic rays, designed for cosmic ray energies above 10^{18}eV. It is located near the city of Malargüe in the province Mendoza, Argentina. The detection area covers 3000 km^2. This observatory studies cosmic rays at the highest energies in two ways.
The surface detector, which consists of autonomous water Cherenkov stations, measures the lateral profile of the secondary shower and reconstructs the properties of the extensive air shower by simultaneous measurements in many of these stations. The characteristics, like energy and arrival direction, of the primary cosmic rays are derived by these measurements.
The fluorescence detector studies the longitudinal air shower profile by measuring fluorescence light caused by secondary shower particles during their flight through the atmosphere. These air shower profiles provide very accurate measurements of the energy of the primary cosmic ray. Additionally, these shower profiles carry information about the chemical composition of the primary particle by measuring the position of the air shower maximum, X_{max}. The fluorescence telescopes are located at the border of the surface detector array overseeing the atmosphere above them. In that way extensive air showers are studied simultaneously by two different detection principles.

The High Elevation Auger Telescopes (HEAT) installation is one of the low energy enhancements of the Pierre Auger Observatory, and is designed to extensively study very close and low energetic air showers, with the same accuracy as the regular telescopes, but for energies down to 10^{17}eV. As HEAT is located nearby a regular FD station called Coihueco, both telescope stations can be combined to form the virtual HECO telescope, which has a very large field of view and is sensitive to extensive air showers in a wide energy range.

In this work, a brief introduction into cosmic ray and air shower physics is given, followed by a short description of the Pierre Auger Observatory. The purpose of this thesis is the analysis of the HECO telescope data for the chemical composition of the UHECRs in the energy range from 10^{17} eV to $10^{18.4}$ eV by studying the distribution of the air shower maximum X_{max}. This is done by performing a high quality selection of the reconstructed HECO showers to get an almost unbiased data set. By extensive detector studies performed with time dependent Monte Carlo simulations, the possible biases and uncertainties of the HECO reconstruction are described and if necessary corrected. These selected and corrected data are then compared to predictions derived from Monte Carlo simulations with different interaction models. The data are analyzed by various procedures. The methods used in this thesis are the comparisons of the first two moments of the X_{max}-distributions as a function of energy to theoretical predictions. Additionally, these X_{max}-distributions are analyzed with Monte Carlo parametrizations for different primary distributions to study the evolution of the chemical composition over the whole energy range in more detail. Therefore, a new analysis method is applied, which uses probability models based on Gumbel distributions. In this way, the cosmic ray's X_{max}-distribution of a given energy bin is transferred into fractions of various chemical element groups. Finally, the results will be compared to the experimental data from other studies and other experiments.

Chapter 2

High Energy Cosmic Rays

The Earth is constantly exposed to a flux of particles from outer space with observed energies up to $\sim 10^{20}$ eV. These *Cosmic rays* carry information about the fundamental structure of the universe.

They were discovered indirectly by Victor Hess in 1912 by measuring an unknown ionizing radiation originating from outside the atmosphere [1]. In 1939, Pierre Auger and his colleagues proved the existence of cascades of secondary particles in the atmosphere, so called extensive air showers, induced by primary cosmic rays with energies of 10^{15} eV [2]. In 1963, John Linsley found the first cosmic rays around 10^{20} eV using a large surface detector array [3]. In the early years, the analysis of the cosmic rays and their secondary particles also led to the discovery of new particles like the positron, muon and pion, which were groundbreaking discoveries in particle physics. Therefore, astrophysics and particle physics are strongly connected.

Modern experiments and observatories have measured the flux of cosmic rays up to at least 10^{20} eV, which is still inaccessible by modern accelerators like the Large Hadron Collider (LHC) [4]. Today the origin, the acceleration mechanisms and the chemical composition of cosmic rays are still unknown and of big interest for the physical understanding of the universe and the search for new physics beyond the standard model.

2.1 The Origin of Cosmic Rays

Cosmic rays consist to a large fraction of ionized atomic nuclei and are observed with kinetic energies from 10^6 eV to at least 10^{20} eV [5]. Apart from particles associated with solar flares, the cosmic radiation above a few GeV originates from outside the solar system.

To compare the cosmic ray flux measured by different experiments, it is given as a differential flux

$$\Phi(E) = \frac{d^4N}{dE\, dA\, d\Omega\, dt}, \tag{2.1}$$

where N is the number of detected particles, A is the sensitive area, Ω the solid angle and t the exposure time of the detectors. The differential energy spectrum of many experiments is shown in figure 2.1. Below energies of 10 GeV the cosmic ray flux is modulated by solar activity [6], whereas above 10 GeV the flux is decreasing as a function of energy which follows a power law distribution, which is approximately given by

$$\Phi(E) \propto E^{-\gamma}, \tag{2.2}$$

where γ is the so called 'spectral index'. The power law behavior indicates a non-thermal acceleration process of the nuclei. The spectrum is nearly featureless besides a few exceptions.

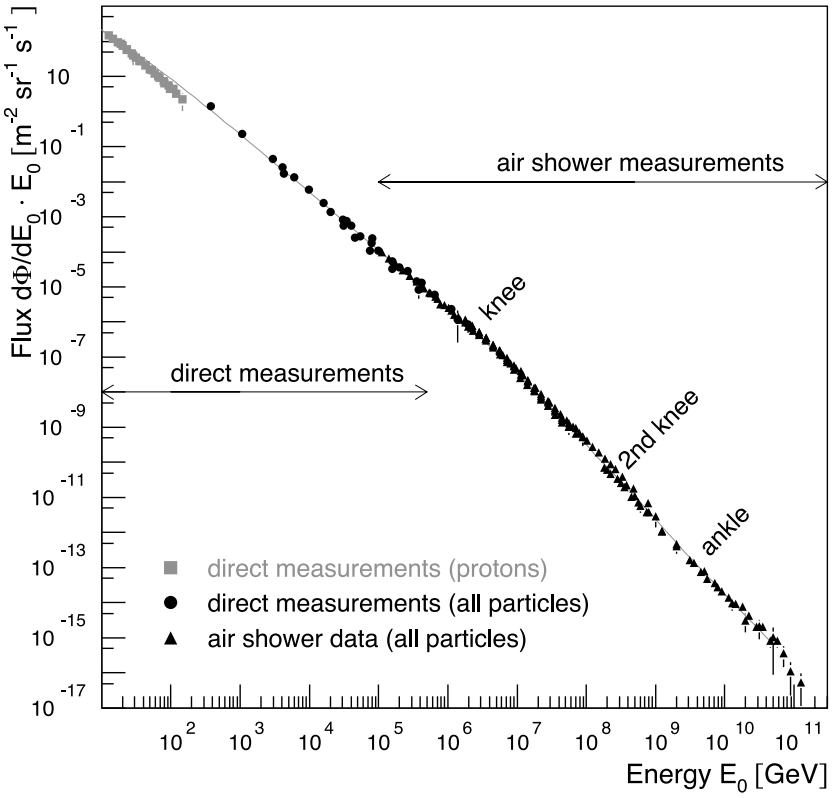

Figure 2.1: All-particle energy spectrum of cosmic rays [5] as measured directly with detectors above the atmosphere and with air shower detectors at the ground. At low energies, only the flux of primary protons is shown.

These features are the so called 'knee', the 'second knee', the 'ankle' and the strong suppression at the highest energies, where the spectral index changes significantly. To enhance these small features, an energy scaled spectrum is shown in figure 2.2. Up to an energy of 10^{14} eV the energy, the mass and the charge of the cosmic rays can be measured directly with balloon and satellite experiments, which is shown in figure 2.1. The chemical composition of cosmic rays consists of all elements of the periodic table, however the element abundance of cosmic rays compared to the element abundance in the solar system is slightly different, which is shown in figure 2.3. From these differences, information on the acceleration, propagation of cosmic rays and the galactic magnetic fields can be derived [5].

Due to the low flux at higher energies, only indirect measurements with large ground detectors can be made. These experiments use the atmosphere as a calorimeter and the primary cosmic rays are reconstructed by their secondary particle cascades inside the atmosphere and/or on the ground. As cosmic rays are composed of charged particles, their arrival direction at Earth is influenced by geomagnetic, galactic and extra-galactic magnetic fields. Therefore, they do not point back to their source regions and the flux of cosmic rays is smeared isotropically over the whole sky. At the highest energies at $\approx 10^{19}$ eV, the deflection effects are less dominant and the particles still may carry information about their source region. To explain the features of the

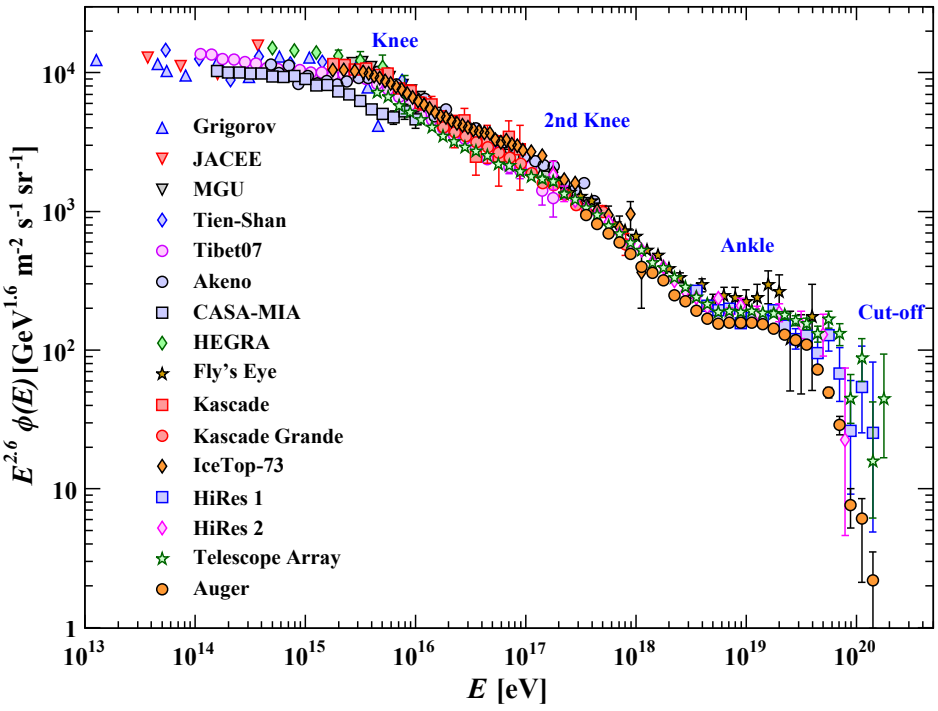

Figure 2.2: All particle cosmic ray spectrum as a function of E(energy-per-nucleus) measured by several air shower experiments, scaled by $E^{2.6}$ [6].

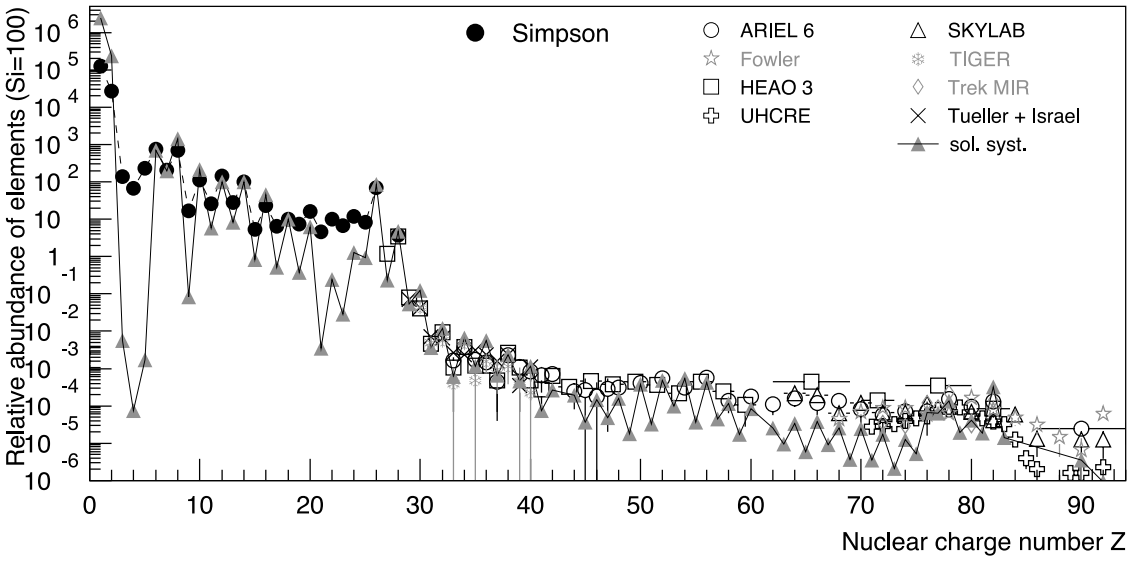

Figure 2.3: Abundance of elements in cosmic rays as a function of their nuclear charge number Z at energies of around 1 GeV per nucleon, normalized to Si(Z = 14) = 100 [5]. The abundance of the elements in the solar system is shown for comparison.

energy spectrum it is necessary to consider galactic and extra-galactic source and acceleration models.

2.1.1 Galactic Cosmic Rays

The currently preferred model by Baade and Zwicky [7] of galactic cosmic rays assumes, that to sustain a constant cosmic ray density in our galaxy a fraction ($\approx 10\%$ [5]) of the kinetic energy release of supernovae is used. A possible acceleration model was invented by Fermi [8] by deriving an acceleration process of cosmic rays that involve the interaction of the particles with large-scale magnetic fields. This leads to the standard model of galactic cosmic rays [9], which is based on the assumption that supernova remnants (SNR) are the main source of the galactic cosmic rays. The acceleration of these cosmic rays takes place due to multiple diffuse shock acceleration at the SNR according to first-order Fermi acceleration [10, 11]. Cosmic rays could be accelerated up to energies of $10^{17}\,\mathrm{eV}$ with this mechanism [5, 12, 13].

The spectral features 'knee' and the second 'knee' of the spectrum, shown in the figures 2.1 and 2.2, can be explained by a rigidity dependent acceleration process [12, 14, 15]. In this acceleration model, the maximal energy of cosmic rays E_{max} is limited by the source region energy and is proportional to the charge number Z of the nuclei. The 'knee' is caused by reaching E_{max} of the source regions by light elements like protons or helium. The second 'knee' consequently corresponds to the cut-off acceleration at SNR of the heavy elements, like iron. This prediction is in good agreement with the observed nuclei spectrum measured by the Kascade Grande experiment [16].

Another theory describing these features is called galactic leakage [5, 17]. In this model, the cosmic rays are accelerated to high energies and above a certain energy the magnetic field of our galaxy is not able to contain them inside our galaxy disc anymore. This effect is also dependent on charge number Z of the nuclei. The Larmor radius of cosmic ray is exceeding the size of the galactic disc and the high energy particles are escaping into the intergalactic space. The Larmor radius is given by

$$r_L = 1.08\,\mathrm{pc}\,\frac{E/\mathrm{PeV}}{Z \cdot B/\mu\mathrm{G}}, \tag{2.3}$$

where E is the energy of the cosmic ray particle and B the strength of the galactic magnetic field ($B \approx 3\,\mu\mathrm{G}$ [18]). This loss of particle leads to a subsequent cut-off for all elements of the spectrum. If the knee and the second knee of the all-particle spectrum are caused by the end of acceleration at their sources and/or the leakage of particles from our galaxy, they mark regions, where the chemical composition of the cosmic rays is changing.

2.1.2 Extra-galactic Cosmic Rays

As cosmic rays with energies above $10^{18}\,\mathrm{eV}$ are no longer confined to our galaxy by the galactic magnetic field, it is plausible to explain the measured particles up to $10^{20}\,\mathrm{eV}$ with an extra-galactic cosmic ray component. Similar to the galactic cosmic ray component, diffuse shock accelerations by numerous encounters with regions of changing magnetic fields are considered to explain the acceleration of particles to these high energies, which was derived by Hillas

[19]. The maximal acceleration energy of the ultra high energy cosmic rays (UHECRs) is proportional to the magnetic field with the strength B and the size of the source region R following

$$E_{max} = 10^{18}\text{eV} \cdot Z \cdot \beta_s \left(\frac{R}{\text{kpc}}\right)\left(\frac{B}{\mu\text{G}}\right), \tag{2.4}$$

where β_s is the shock velocity in units of c and Z the charge of the nuclei. In figure 2.4, several possible source candidates, the required magnetic field strength and the source region size for proton and iron cosmic rays with 10^{20} eV are shown. As shown in this plot, only a few astro-

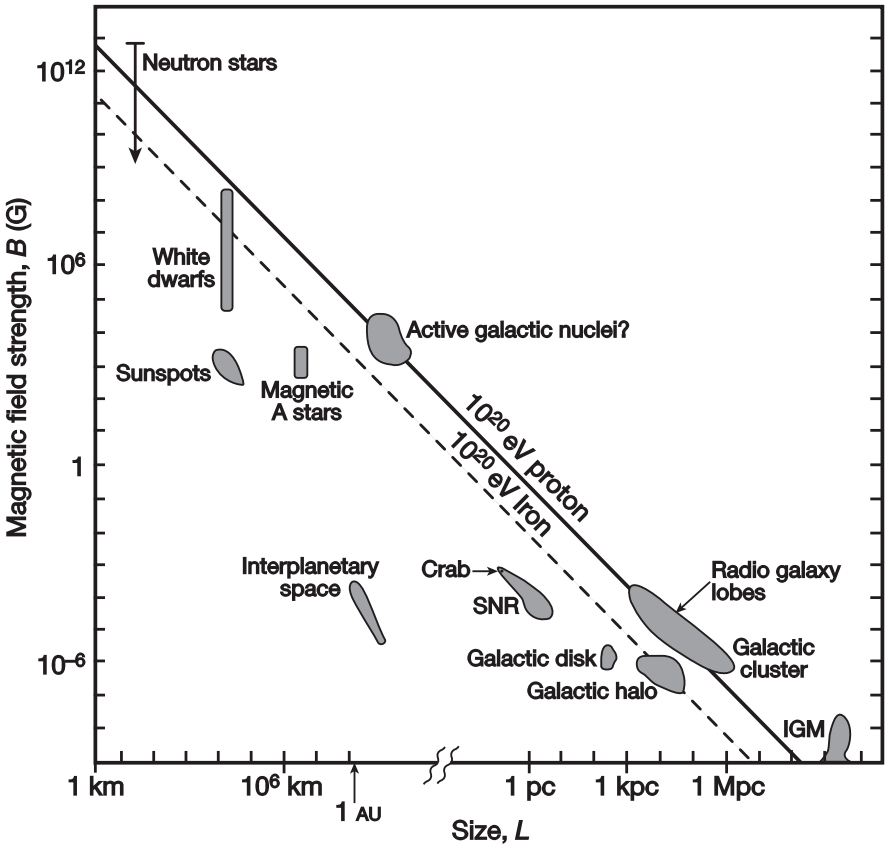

Figure 2.4: Hillas plot [19] of possible source regions of UHECRs. Expected magnetic fields and sizes of source candidates are shown [20].

physical objects are known possible accelerator candidates of UHECRs. At these high energies the trajectories of the particles are expected to carry information of their origin source region. However, due to the expected deflection by the extra-galactic and galactic magnetic fields, this is strongly dependent on the chemical composition of the cosmic rays. The Pierre Auger (Auger) collaboration has found a correlation of the UHECRs with known active galactic nuclei (AGN). The hypothesis of isotropic arrival directions of cosmic rays with an energy above 57 EeV was rejected in [21, 22]. However, the correlation signal with the AGN became weaker in the later measurement period [23], but is still above the expectation value of isotropic arrival directions of UHECRs. The cosmic ray data taken by the High Resolution Fly's Eye (HiRes)

collaboration [24] and by the Telescope Array (TA) collaboration [25] are compatible with an isotropic scenario of the arrival direction, but they cannot rule out the correlation scenario with AGN seen by Auger. The TA collaboration recently published a possible hot-spot of UHECRs in the northern hemisphere [26]. Joined analysis [27, 28] by different cosmic ray experiments of the arrival direction of UHECRs did not find any significant correlation of UHECRs and nearby source candidates.
The end of the energy spectrum is marked by a cut-off, which is observed by the HiRes [29], TA [30] and Auger [31] experiments. The nature of this cut-off is still unknown and has several possible causes.
In the case of UHECRs consisting of protons propagating through the cosmic microwave background (CMB), the spectrum will steeply decline at the highest energies due to the Greisen-Zatsepin-Kuz'min (GZK) cut-off [32, 33]. The GZK cut-off is caused by photopion production of UHECRs protons with CMB photons following

$$p + \gamma_{CMB} \rightarrow \pi + N \text{ with } N = n, p. \tag{2.5}$$

In the other case of the UHECRs consisting of heavier nuclei up to iron, a similar effect in the same energy range could cause an abrupt cut-off the spectrum. A nucleus with atomic mass A could break up and lose one or more (x) nucleons (N) due to interaction with the CMB or extragalactic background light (EBL) by photo-disintegration [34, 14] following

$$A + \gamma_{CMB,EBL} \rightarrow (A - xN) + xN. \tag{2.6}$$

Both effects lead to a short energy loss length of the UHECRs and indicate that sources of 10^{20} eV cosmic rays should be in a sphere of ~ 100 Mpc radius and galactic sources are unlikely [5]. The cut-off could also be related to the maximum cosmic ray acceleration energy by the source region [35]. To find an answer to this open question a study of the chemical composition up to the highest energies is necessary to constraint the different source scenarios of UHECRs. If the composition is heavy at the highest energies, the observed suppression of the flux would then be caused by the exhaustion of the source spectrum.

The change of the spectral index at the 'ankle' of the energy spectrum is considered to mark the transition region from galactic to extra-galactic components between $10^{17} - 10^{19}$ eV. There are several possible transition models to explain this feature, which are called 'ankle', 'dip' and 'mixed composition' model [14].

The 'ankle'-model [36] assumes that the galactic component is dominated by iron cosmic rays after the iron 'knee' and that the extra-galactic component consists of a pure proton spectrum. The 'ankle' in the energy spectrum emerges because of the much harder spectrum of the extra-galactic component. The 'ankle'-model is illustrated in figure 2.5a. The extra-galactic proton spectrum has a flat generation spectrum $\propto E^{-2}$, which is valid for non-relativistic shock acceleration and is nearly unmodified by energy losses for energies below $\leq 4 \cdot 10^{19}$ eV until the GZK cut-off occurs. However, in this model the galactic component needs another mechanism that accelerates cosmic rays up to 30-40 times higher than the expected maximum iron

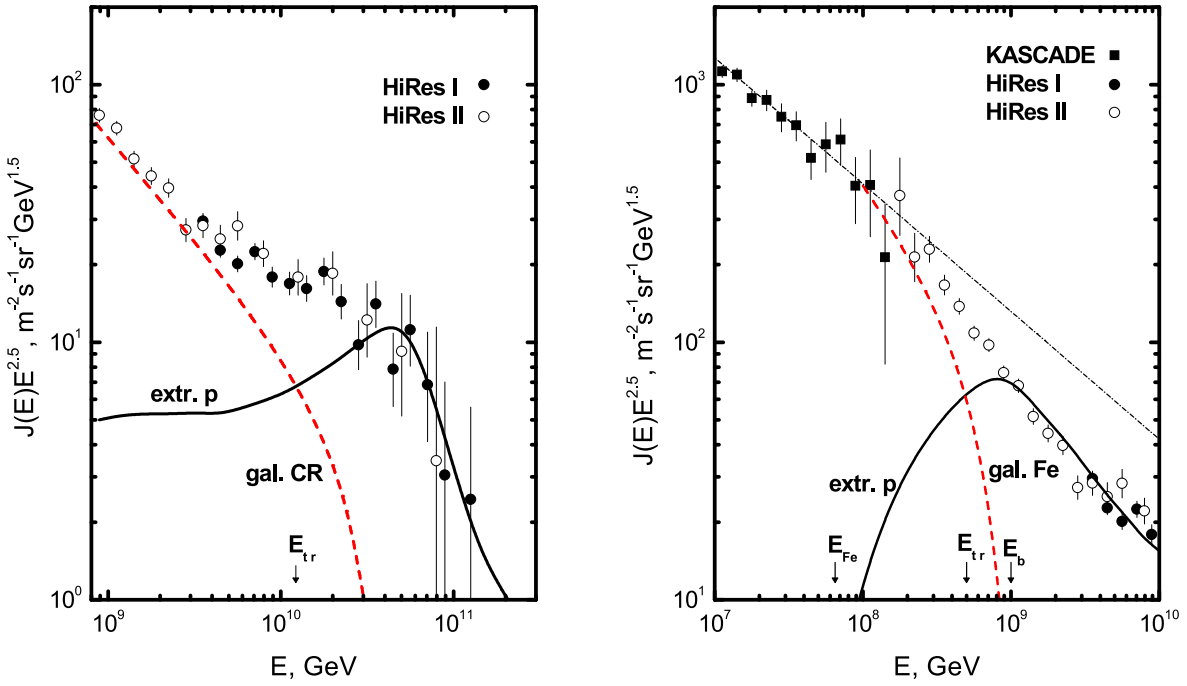

(a) Ankle model [14].

(b) Dip model [14].

Figure 2.5: The dashed line describes the calculated galactic spectrum, the solid line gives the extragalactic proton flux. E_{Fe} is the position of the iron 'knee'. E_{tr} marks the transition from galactic to extra-galactic cosmic ray components. The transition is completed at E_b, where the end of galactic spectrum component is reached.

cosmic ray energy [14]. This new cosmic ray component could consists of a heavy composition accelerated by rare galactic magnetars [37]. The 'ankle'-model also contradicts the measured anisotropy of UHECRs and chemical composition of UHECRs by the HiRes and the Pierre Auger experiment and is therefore disfavored.

The 'dip'-model [38] also assumes that the extra-galactic component consists mostly of extra-galactic protons. The 'ankle' and the suppression of the energy spectrum are explained by a pair-production dip of the ultra high energy protons with photons from the CMB or the EBL, following

$$p + \gamma_{CMB,EBL} \rightarrow p + e^+ e^-, \tag{2.7}$$

and the GZK cut-off mechanism with photopion production. To illustrate the spectral shape due to the different energy losses the modification factor is defined as

$$\eta(E) = \frac{J_p(E)}{J_p^{unm}(E)}, \tag{2.8}$$

where $J_p(E)$ is the energy spectrum with energy losses taken into account and $J_p^{unm}(E)$ is the unmodified spectrum which includes only adiabatic energy losses due to the expanding universe. The modification factor for a proton dominated energy spectrum is shown in figure 2.6.

The measured energy spectrum data and the model are shown in figure 2.5b. This figure shows

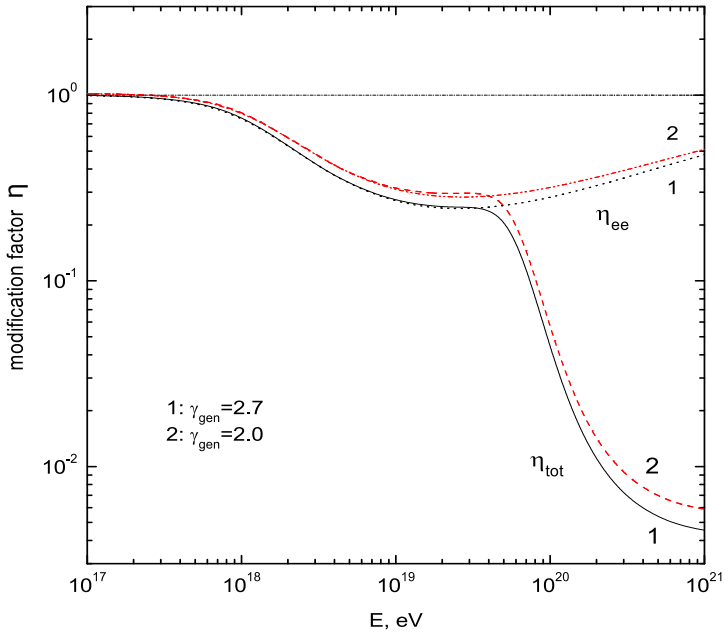

Figure 2.6: Modification factor for the power-law generation spectra with γ_{gen} in the range of 2.0 - 2.7. $\eta = 1$ corresponds to only adiabatic energy losses, curves η_{ee} to adiabatic and pair production energy losses and curves η_{tot} to all energy losses [38].

the starting of the extra-galactic proton flux after the iron 'knee' (E_{Fe}) and the beginning of the shallow dip (E_b), where the extra-galactic protons become the dominant component. The shape of the dip allows an added mixture of light elements, but not more than 15% [14]. The chemical composition of this cosmic ray model predicts a heavy composition between the iron 'knee' and the transition region (E_{tr}). After the transition the composition is expected to be light up to the highest energies. The 'dip' model and the proton dominated extra-galactic flux are still under discussion, as it is supported by HiRes [39] and TA [40] measurements, but contradicted by Auger measurements [41, 42] of the chemical composition. These differences are currently studied by a joint working group of the Auger and the TA collaborations [43].

The 'mixed composition'-model [15, 35, 44, 45] assumes that the extra-galactic component consists of various nuclei from light to heavy and can be used to explain the Auger measurements shown in figure 2.7. The maximal acceleration energy of the UHECRs is depending on the charge of the nuclei Z following

$$E_i^{max} = Z_i \cdot E_p^{max}. \tag{2.9}$$

In this model, the 'ankle' occurs in the energy region between 'ankle'- and 'dip'-model and the strong suppression can be explained by the end of the source acceleration and photo-disintegration. In figure 2.8, the Auger energy spectrum is shown with a fitted chemical composition of different element groups to describe the 'ankle' and the suppression region.

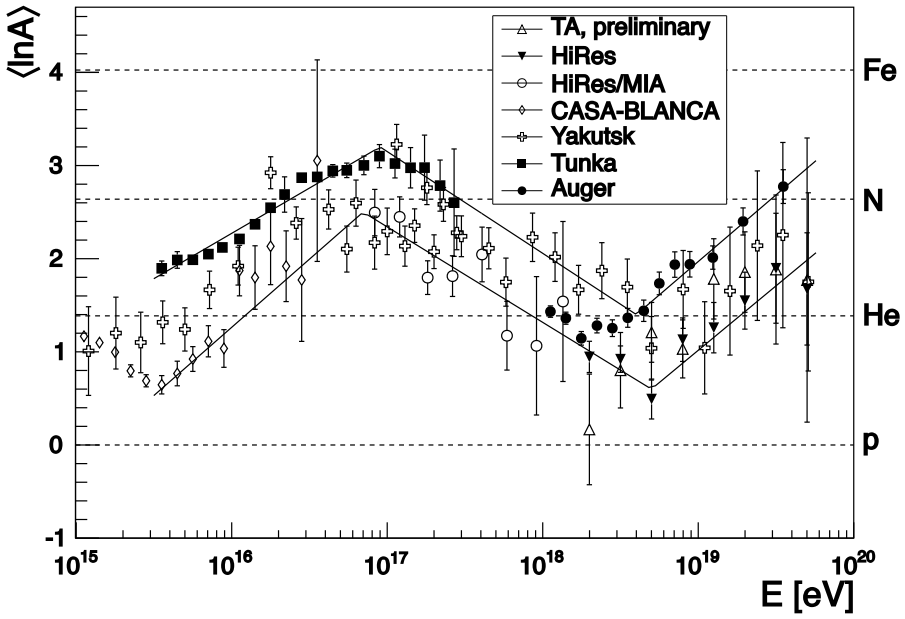

Figure 2.7: Measured average logarithmic mass of cosmic rays as a function of energy from optical detectors with the EPOS 1.99 interaction model [35]. The solid lines represent the upper and lower systematic boundaries.

To explain the features, an enhanced galactic component and a hard injection spectrum are needed in this model [46].

Besides these models, there are also non-accelerating models, so called top-down models. In these models cosmic rays are produced by decaying super-heavy objects. These objects could be decaying super-heavy dark matter [48], Z-bursts [49] or topological defects [50]. However, these models predict a strong high energy photon flux and recent studies of the photon flux have put stringent limits on top-down models [51].

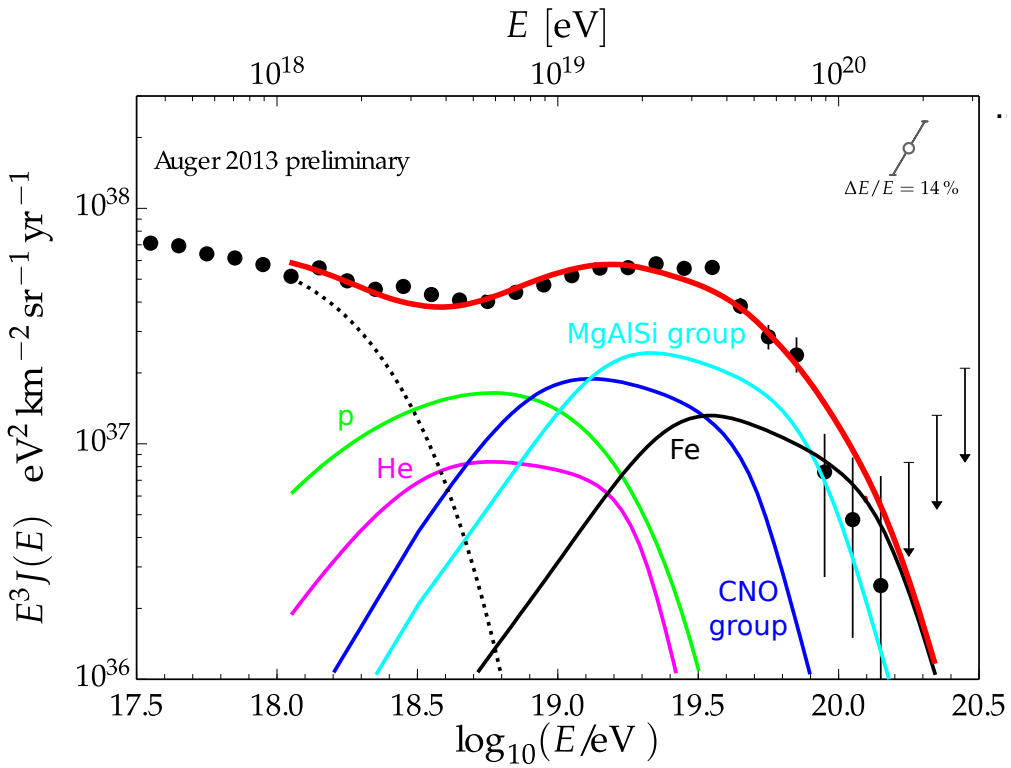

Figure 2.8: Pierre Auger energy spectrum compared to a mixed composition model [47]. The dashed line represents the galactic component and the solid lines stand for the different extragalactic elements and element group contributions to the all particle spectrum (red solid line) [35].

2.2 Extensive Air Showers

As UHECRs mainly consist of hadronic nuclei, they interact with the atmospheric components (mainly nitrogen, oxygen and argon nuclei) once reaching Earth. Typically, this interaction happens at a height of 15 to 35 km and produces a shower of secondary particles. The hadronic part of these secondaries consists mostly of neutral and charged pions. The neutral pions decay almost instantaneously into two photons. These photons are the main source of electromagnetic cascades. The charged pions have a longer lifetime, which allows them to interact again, before decaying into muons:

$$\pi^{\pm} \quad = \quad \mu^{\pm} + \nu_{\mu}/\bar{\nu}_{\mu}. \tag{2.10}$$

Almost 90% of the muons of the shower are produced from the decay of charged pions and kaons. The muons lose only a small amount of energy while traveling through the atmosphere, and reach the ground nearly unattenuated. The lateral particle density and the longitudinal shower profile from CORSIKA [52] simulations are shown in figures 2.9a and 2.9b.

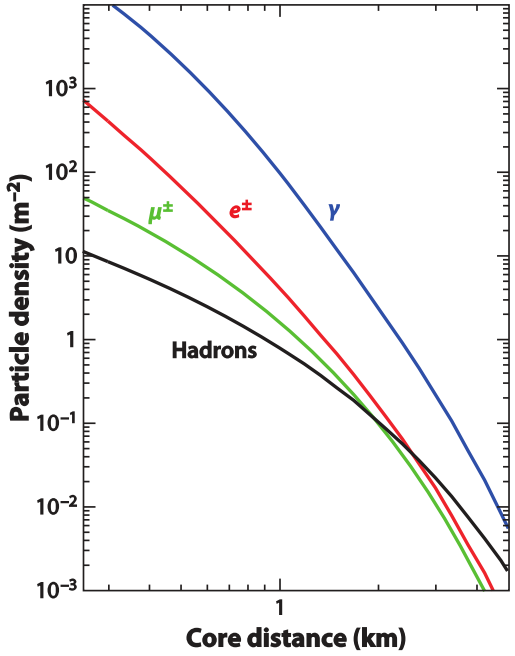

(a) Simulated average lateral shower profile at 870g/cm^2 (vertical depth of the Pierre Auger Observatory) [53].

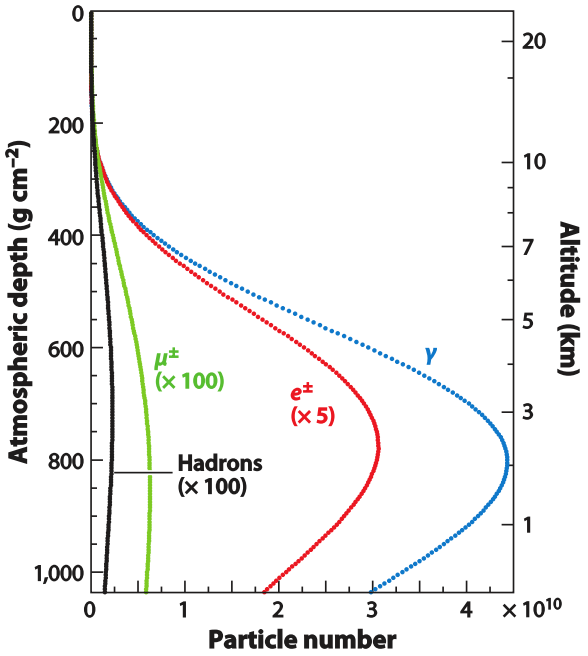

(b) Simulated average longitudinal shower profile in the atmosphere [53].

Figure 2.9: Average shower profiles for vertical 10^{19} eV proton induced air showers simulated with CORSIKA [52]. The simulation energy threshold is 0.25 MeV for γ and $e^{\pm}$ and 0.1 GeV for $\mu^{\pm}$ and hadrons.

2.2.1 Electromagnetic Cascades

The electromagnetic component of an extensive air shower is formed by high energy photons and $e^{\pm}$. A cascade of secondary particles is produced due to $e^{\pm}$ pair production by photons and bremsstrahlung by $e^{\pm}$. This cascade can be described by the Heitler model [54]. In principle it can be described as a binary tree, where all particles interact and produce two secondaries of equal energy. This is shown in figure 2.10. The Heitler model assumes that every electron or positron split their energy in half by bremsstrahlung emission of a single photon and every photon produces an $e^{\pm}$ pair of equal energy [55]. In this model, the cross sections of both processes are taken as independent of energy, and other energy loss processes are ignored. The slant depth at the n shower generation is given by $X = n \cdot d + X_0$, where d is the step size between the generation and X_0 the position of the first interaction. d is given by $d = \lambda_r \ln(2)$ with the radiation length $\lambda_r \approx 37\,\mathrm{g/cm^2}$ in air. The number of particles after n steps is therefore given by $N_n = 2^n$ and their energy is given by E_0/N_n. The particle production continues n_c steps until the individual energy of the $e^{\pm}$ is below the critical energy E_c. The energy loss due to ionization is equal to the energy loss due to bremsstrahlung. This critical energy of the electromagnetic component is about 86 MeV in air [53]. The shower therefore reaches its maximum if $E = E_c$, which leads to the following relations:

$$N_{max} = 2^{n_c} = \frac{E_0}{E_c} \tag{2.11}$$

and

$$X_{max}^{EM} = X_0 + n_c \lambda_r ln(2) = X_0 + \lambda_r \ln\left(\frac{E_0}{E_c}\right). \tag{2.12}$$

The position of the shower maximum X_{max}^{EM} in the electromagnetic shower is therefore logarithmically dependent on the energy of the primary particle.

2.2.2 Hadronic Cascades

The hadronic cascade of the shower are modeled similar to an electromagnetic shower, which is shown in figure 2.11. This model assumes an atmosphere with layers of fixed thickness $d = \lambda_I \ln(2)$, where λ_I is the interaction length [56]. This interaction length of pions in air is $\lambda_I \approx 120\,\mathrm{g/cm^2}$. Hadrons interact after one layer and produce N_{ch} charged pions and $\frac{1}{2}N_{ch}$ neutral pions, due to the assumed multiplicity in pion-nucleon collisions. The energy is distributed uniformly among the secondaries. The neutral pions decay almost instantaneously into two photons and form an electromagnetic cascade, so they do not participate to the hadronic shower anymore. After n generations the number of charged pions is given by

$$N_\pi = (N_{ch})^n \tag{2.13}$$

and the energies of the hadronic E_{had} and electromagnetic E_{EM} component are given by

$$E_{had} = \left(\frac{2}{3}\right)^n E_0 \qquad \text{and} \qquad E_{EM} = \left(1 - \left(\frac{2}{3}\right)^n\right) E_0. \tag{2.14}$$

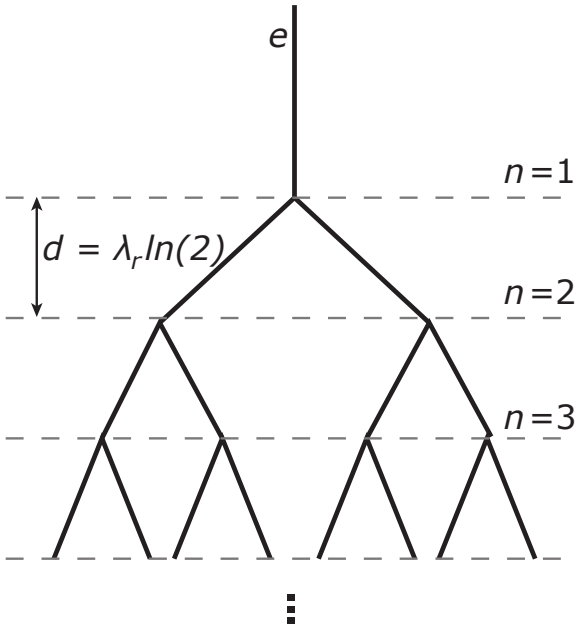

Figure 2.10: Schematic of an electromagnetic cascade of the Heitler model [54] adapted from [53].

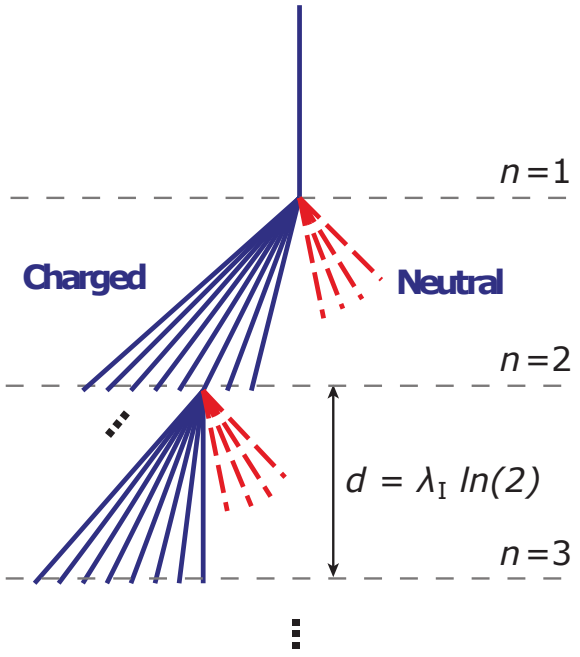

Figure 2.11: Schematic of a hadronic shower cascade [53].

After $n \approx 6$ generations around 90% of the primary energy is carried by the electromagnetic component of the shower [53]. Assuming an equal energy distribution during the particle

production, the energy of the charged pions after n steps is given by

$$E_\pi = \frac{E_0}{\left(\frac{3}{2}N_{ch}\right)^n}. \tag{2.15}$$

The cascade stops if the energy of the pions is below the critical energy E_c^π, which means that the decay length of the pions is bigger than the distance to the next interaction. All remaining charged pions decay then into muons and neutrinos. In air E_c^π is around 20 GeV [56].

The number of interaction needed to reach $E_\pi = E_c^\pi$ is given by

$$n_c = \frac{\ln\left(E_0/E_c^\pi\right)}{\ln\left(\frac{3}{2}N_{ch}\right)}. \tag{2.16}$$

The number of muons N_μ in an extensive air shower is proportional to the energy E_0 of the primary particle and the multiplicity N_{ch} is given by

$$N_\mu = N_\pi = (N_{ch})^{n_c} = \left(\frac{E_0}{E_c^\pi}\right)^\beta \qquad \text{with} \qquad \beta = \frac{\ln(N_{ch})}{\ln(3/2\,N_{ch})} \approx 0.82 \ldots 0.94. \tag{2.17}$$

A primary nucleus with atomic number A and total energy E_0 is modeled as a superposition of A individual nuclei with energy E_0/A. For a larger nucleus the number of muons is given by

$$N_\mu = A\left(\frac{E_0/A}{E_c^\pi}\right)^\beta = A^{1-\beta}\left(\frac{E_0}{E_c^\pi}\right)^\beta. \tag{2.18}$$

The total energy of the primary particle is therefore divided into the hadronic and electromagnetic shower parts $E_0 = E_{had} + E_{EM}$. Due to conservation of energy, the hadronic energy is given by the muons from the pion decay as $E_{had} = N_\mu E_c^\pi$. With equation 2.18 the electromagnetic energy fraction is given as

$$\frac{E_{EM}}{E_0} = 1 - \left(\frac{E_0}{E_c^\pi}\right)^{\beta-1} A^{1-\beta}. \tag{2.19}$$

For a proton shower($A = 1$) with $E_0 = 10^{14}$ eV this fraction is 72% and it is rising with increasing energy up to 90% for proton shower with $E_0 = 10^{17}$ eV [56].

As a simplification, only the first generation photon showers are used to estimate the atmospheric depth of the extensive air shower maximum X_{max} [56]. As 1/3 of the primary energy E_0 transfers into the electromagnetic channel by the π_0-decays after the first interaction, the number of photons N_γ is given by the number of produced neutral pions N_{π_0} as

$$N_\gamma = 2N_{\pi_0} = 2\frac{1}{2}N_{ch}, \tag{2.20}$$

and each photon initiates an electromagnetic shower with the energy

$$E_\gamma = \frac{E_0}{3N_{ch}}. \tag{2.21}$$

Following equation 2.12, the air shower maximum X_{max} for a proton induced air shower is given by

$$X^p_{max} = X_0 + X^{EM}_{max} = X_0 + \lambda_r \ln \frac{E_0}{3N_{ch}E_c}, \tag{2.22}$$

where X_0 is the position of the first hadronic interaction. It is given by $X_0 = \lambda^p_I \ln 2$, where λ^p_I is the interaction length of a primary proton based on the p-air cross section. For a heavier nuclei, the value of X_{max} is given by

$$X^A_{max} = X^p_{max} - \lambda_r \ln A. \tag{2.23}$$

This model only qualitatively describes the development of extensive air showers, due to the simplified assumptions in the hadronic interactions and due to the not included sub-shower components respectively to their points of origin and their attenuation near and after their maxima [56]. In hadronic interactions, only one component of the hadron interacts, which also only carries a fraction κ of the hadron energy. κ is known as 'inelasticity' and describes the amount of energy which is transferred into the pion production. It depends on the energy and mass of the particles and in this simple model $\kappa = 1$. These effects are taken into account in more precise particle simulations and deliver good approximations about the slant depth of hadronic showers.

The evolution of the average mean $\langle X_{max} \rangle$ per energy can be used to compare cosmic ray data to cosmic ray simulations. For pure cosmic ray compositions, it is expected to have a nearly constant slope in the energy development of $\langle X_{max} \rangle$, which is called elongation rate [57]. The elongation rate is defined as

$$D_{10} = \frac{d\langle X_{max} \rangle}{d \log(E/\mathrm{eV})}, \tag{2.24}$$

and predicts, for pure compositions depending on the interaction model, a value in the range of 54 to 64g/cm^2/decade [41]. A change of the elongation rate from this range could indicate a change in the chemical composition of UHECRs. With the elongation rate, the chemical composition of cosmic rays can be constrained by hadronic interaction models as shown in figure 2.12. In this figure, the first two moments of the measured X_{max} distribution by the Pierre Auger observatory are shown in comparison to the expected moments derived from air shower simulations. The elongation rate seems to change as a function of energy, from a mixed to a heavier composition.

2.2.3 Hadronic Interaction Models

There are several hadronic interaction models, which are currently used to study the chemical composition at the Pierre Auger observatory. The used models are SIBYLL 2.1 [58], QGSJETII-04 [59, 60] and EPOS-LHC [61, 62]. EPOS-LHC and QGSJETII-04 use extrapolated LHC measurements for the p-air cross-section to improve hadronic interaction simulations at the highest energies. However, current data of extensive air showers cannot describe all aspects of the measured data and cannot rule out any of these models. A detailed comparison of these models can be found in [63].

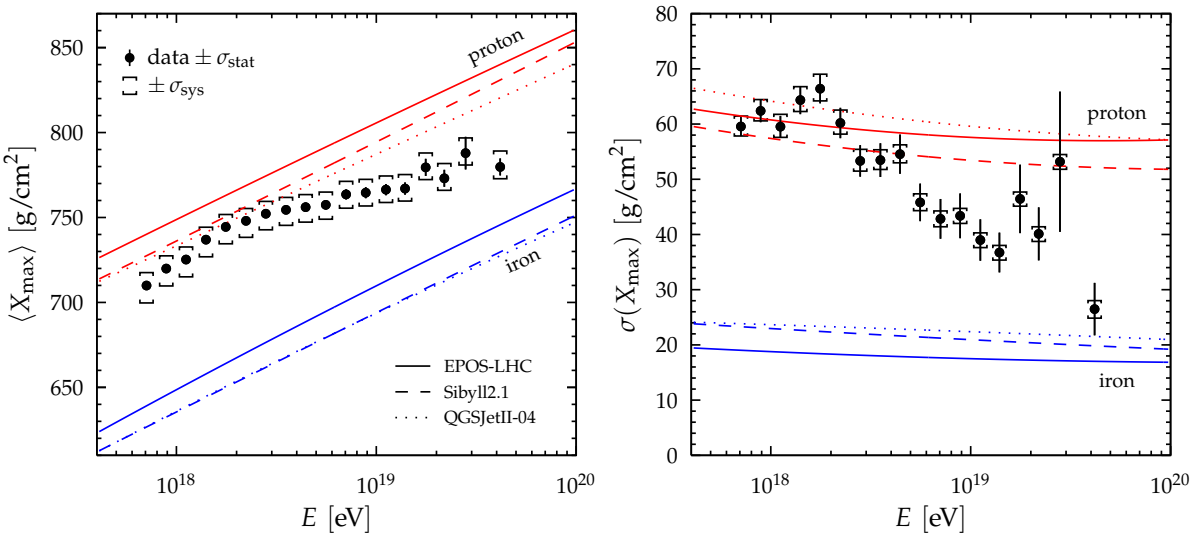

Figure 2.12: Energy evolution of the X_{max} moments measured by the Pierre Auger observatory [41] compared to the simulations of pure proton and pure iron cosmic rays.

Chapter 3

The Pierre Auger Observatory

The Pierre Auger Observatory is the world largest detector for cosmic rays with energies from 10^{17} eV to above 10^{20} eV. It is located in the Pampa Amerilla in Argentina as shown in figure 3.1. It was originally designed to measure the energy spectrum, the arrival directions and the chemical composition of UHECRs. The Pierre Auger Observatory uses a hybrid detector principle, which means that the cosmic ray induced air showers are measured by different detector types at the same time. The Surface Detector (SD) array instruments an effective area of 3000 km^2 with 1660 water-Cherenkov detectors to measure the lateral shower profile of the air showers on the ground. The SD array is overlooked by 27 fluorescence telescopes which are located at 5 Fluorescence Detector (FD) stations at the border of the SD array. The FD telescopes measure the longitudinal air shower profile in the atmosphere. The combined measurement of the extensive air shower allows the reconstruction of their properties with a high accuracy. SD and FD are cross-calibrated detectors to combine the advantages of both detector types.

3.1 Surface Detector

The Surface Detector (SD) array consists of 1660 water-Cherenkov detector stations, shown in figure 3.2a, arranged in a hexagonal grid with a 1500 m spacing for the regular grid. Each detector station is a 3.6 m diameter water tank with a reflective inner surface liner made of Tyvek [65], which is filled with 12 t of pure water. Three nine-inch-diameter photomultiplier tubes (PMTs) collect the Cherenkov-light of charged particles passing through the water. The PMTs are positioned symmetrical 1.2 m from the center of the tank and look downwards through transparent windows in the liner. A schematic view of a SD station is shown in figure 3.2b. Each SD station is equipped with a 10 W solar panel and batteries to operate autonomously and to allow for a nearly 100% duty cycle. The electronics consist of a signal processor, GPS receiver, radio transceiver and a power control. The readout of the data is performed via a wireless network with communication radio towers at the FD telescope buildings. From there the data are sent to the Central Data Acquisition System (CDAS) at the Malargüe Campus. The monitoring information are also sent automatically to CDAS every 10 minutes. This includes water temperature, PMT-, battery- and CPU board-voltage. Each station is also equipped with an on-board LED flasher, which can be used to study the PMTs linearity [67]. A detailed SD description is given in [65, 67, 68].

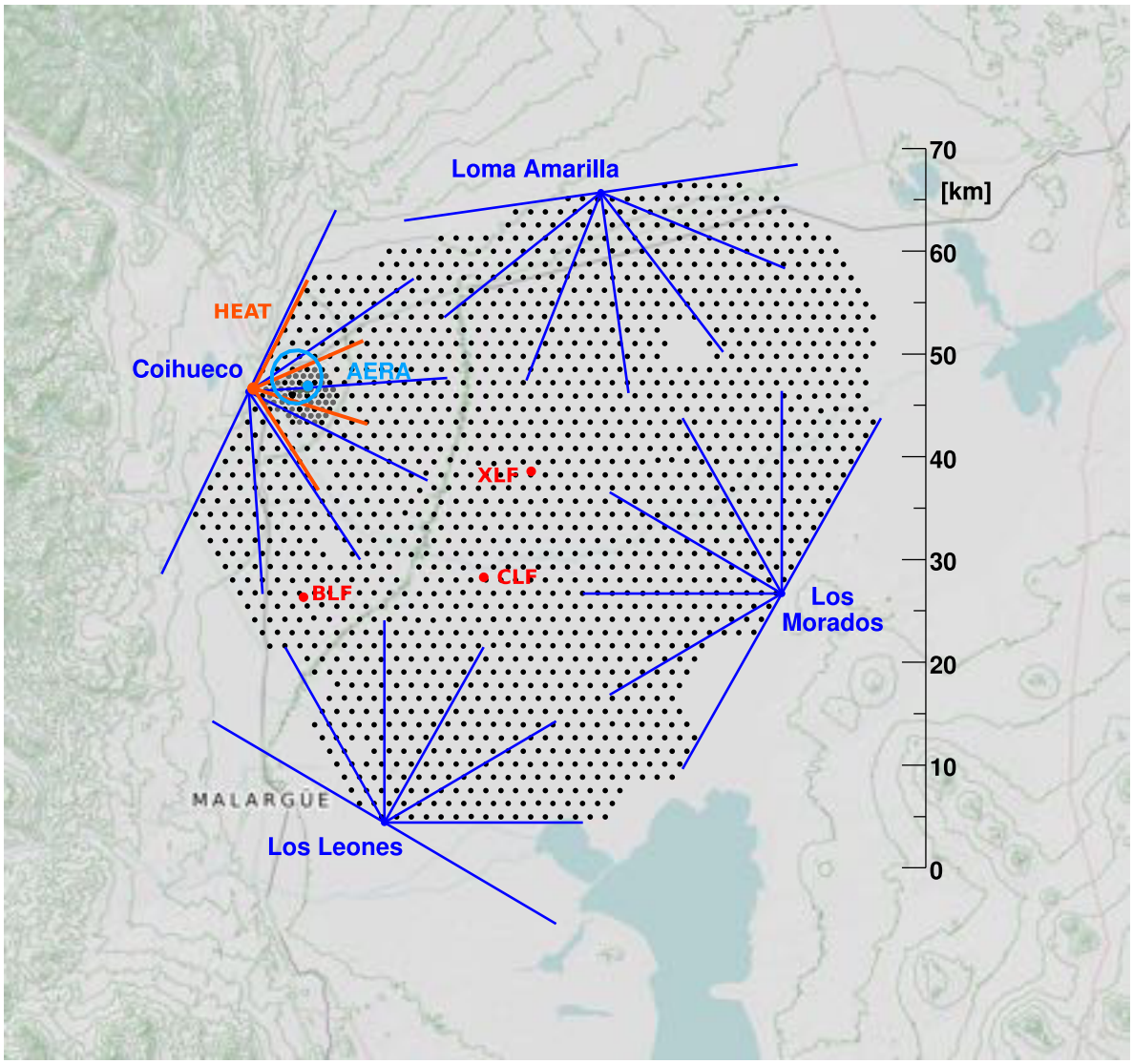

Figure 3.1: The Pierre Auger Observatory near Malargüe, Argentina [64]. Black dots represent the SD stations. Blue and orange lines indicate the field of view of the FD telescopes. The red dots represent the atmospheric monitoring sites 'eXtreme Laser Facility' (XLF), 'Central Laser Facility' (CLF) and balloon launch sites (BLF).

3.1.1 SD Reconstruction

For the simplest reconstruction of the shower geometry of an extensive air shower, the starting times t_i in each SD station are fitted to an incoming plane wave front. For events with enough SD stations, an inflating spherical shower front is used to fit the starting times following

$$c(t_i - t_0) = |\vec{x}_{sh} - \vec{x}_i|, \tag{3.1}$$

where $\vec{x}_i$ are the station position on the ground and $\vec{x}_{sh}$ and t_0 are the virtual origin and the start time of the shower development shown in figure 3.3a. An event display of a reconstructed

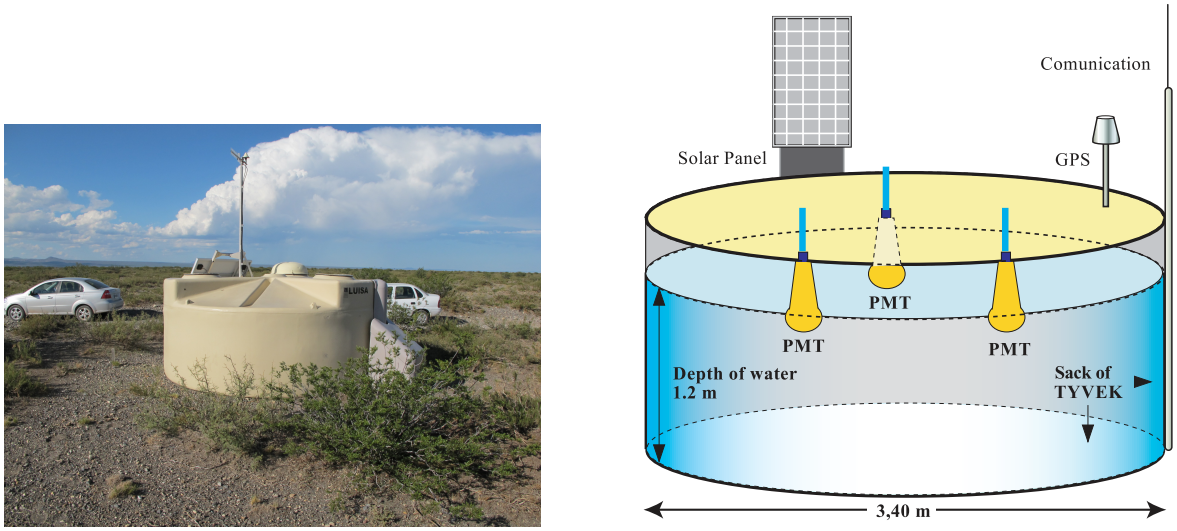

(a) Photo of a SD station.

(b) Schematic of a SD station adapted from [66].

Figure 3.2: Surface detector station of the Pierre Auger Observatory.

SD event is shown in figure 3.3b, with the timing information color coded from early (yellow) to late (red). The signal strength is indicated by the size of the station markers. The signal

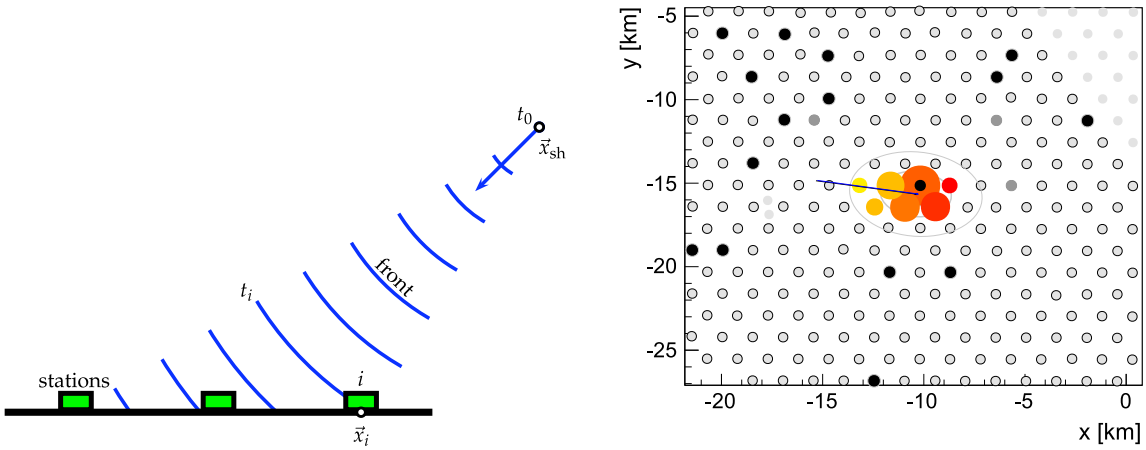

(a) Determination of the extensive air shower geometry with SD stations. Adapted from [67].

(b) Event display of a reconstructed SD event. The starting times are color coded from early (yellow) to late (red). The signal strength of each SD station is shown as the marker size. Black line indicates the reconstructed shower axis. The stations marked as a black dot are flagged as bad stations in the monitoring.

Figure 3.3: Illustration of the lateral air shower profile reconstruction measured with the surface detector array (SD).

strength of the SD stations is used to reconstruct the energy of the primary particle. During

the shower reconstruction, the amount of Cherenkov-light in the tank measured by the SD PMTs is recorded in units of the signal a muon produces by flying vertically through the SD station, which is called Vertical Equivalent Muon (VEM). The total shower energy and the arrival direction are fitted using a Lateral Distribution Function (LDF) to describe the the signal on the ground, which is a modified Nishimura-Kamata-Greisen function [69, 70] given by

$$S(r) = S(r_{opt}) \left(\frac{r}{r_{opt}} \right)^{\beta} \left(\frac{r + r_1}{r_{opt} + r_1} \right)^{\beta+\gamma}, \tag{3.2}$$

where r_{opt} is the optimal distance, $r_1 = 700\,\mathrm{m}$ and $S(r_{opt})$ is an estimator of the shower size used in the energy reconstruction. Therefore, it necessary to define the optimum core distance r_{opt}, which depends solely on the array geometry. At this point the variation of the shower to shower fluctuations in the predicted signals is minimal. For the regular SD the signal variation is minimal at a core distance of around 1000 m and therefore the energy estimator is named $S(1000)$ [71]. The parameter β is depending on the shower size and the zenith angle. An example of the LDF fit for a single event is shown in figure 3.4 and an example for the timing fit is shown in figure 3.5. The SD energy conversion is based on cross-calibration with hybrid

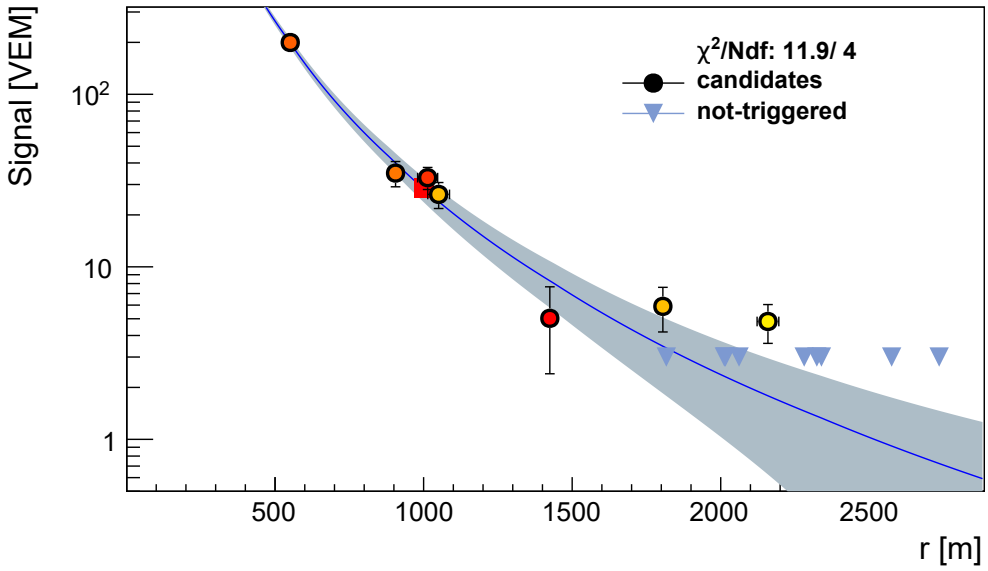

Figure 3.4: Lateral distribution function fit on the SD station signal of an extensive air shower against the shower core distance r.

events recorded by SD and FD simultaneously, which will be described in chapter 3.3.

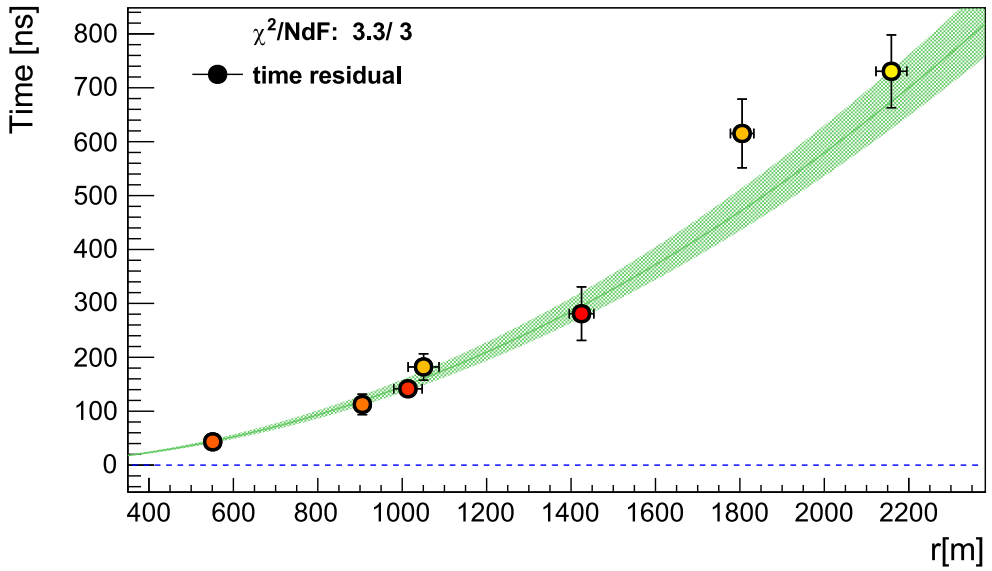

Figure 3.5: SD station timing function fit of the air shower geometry reconstruction.

3.2 Fluorescence Detector

The Fluorescence Detector (FD) of the Pierre Auger Observatory consists of 27 telescopes. The 'standard' telescopes are grouped in 4 FD buildings with 6 separate telescope bays, which are called Los Leones (LL), Los Morados (LM), Loma Amerilla (LA) and Coihueco (CO)[72]. At Coihueco, a low energy extension named High Elevation Auger Telescopes (HEAT) is located. It consists of 3 additional telescopes, shown in figure 3.1. The telescope design is a modified Schmidt optic, which is shown in figure 3.6a, with a segmented 13 m^2 telescope mirror consisting of anodized aluminum for Los Leones and Los Morados and aluminum coated glass for Loma Amerilla, Coihueco and HEAT. Each FD camera is composed of 440 PMTs with a hexagonal

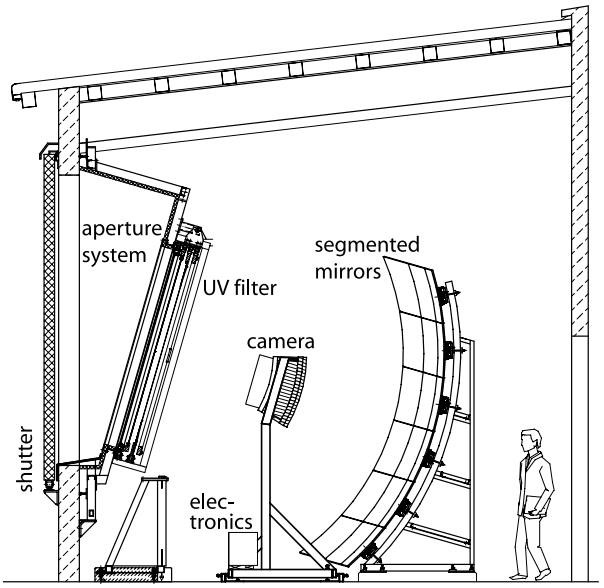

(a) Schematic view of a fluorescence telescope bay of the Pierre Auger Observatory [72].

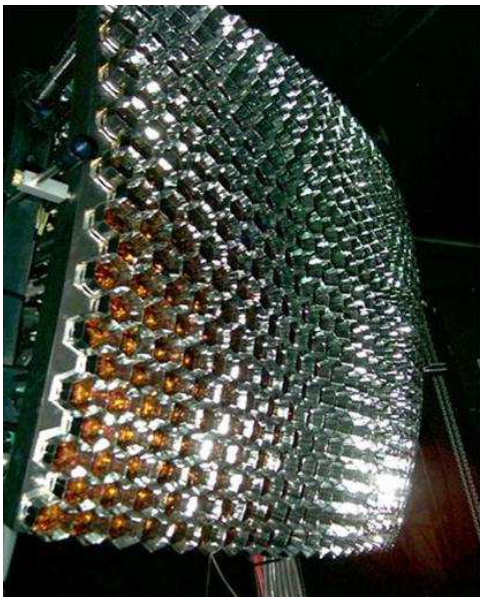

(b) Photo of a camera installed in FD telescopes, which consists of 440 hexagonal PMTs [72].

Figure 3.6: FD telescope of the Pierre Auger Observatory.

window and a field of view of $1.5° \times 1.5°$ arranged in a matrix of 22 rows by 20 columns, which are shown in figure 3.6b. The total field of view of each telescope is $30° \times 30°$. The aperture of each telescope is 2.2 m. To correct for spherical aberrations at the edge of the aperture a corrector ring is implemented. To reduce the visible ambient background light, the aperture window is an optical filter, which is mostly transparent for the UV light of de-excited nitrogen. To protect the telescopes and camera from damage through weather and too much light, shutter doors were installed at each bay. The steering of the FD is done remotely by a slow control from the Campus at Malargüe and/or from a Remote-Control room at one of the participating institutes. The slow control steers the shutter, the high voltage of the PMTs and the calibration of the camera. As a last fail safe, a curtain is mounted at the aperture to protect the camera from too much light exposure. In combination with the SD, the 'standard'

FD stations are fully efficient above an energy threshold of 10^{18} eV. The FD stations can only take data during good atmospheric conditions and moonless nights, which lead to a duty cycle of roughly 15%. There are efforts ongoing to increase the duty cycle by lowering the gain of the PMTs during the twilight and high-moon nights to increase the sensitivity of FD for the very rare high energy events beyond 10^{19} eV [73].

3.2.1 Low Energy Enhancement HEAT and Infill

To discriminate between different astrophysical models, the spectrum and the chemical composition in the expected transition region from galactic to extra-galactic cosmic rays need to be measured. Therefore, several detector enhancement for FD and SD were installed to lower the energy threshold down to 10^{17} eV. The High Elevation Auger Telescopes (HEAT) are located 180 m north-east of the Coihueco FD station. A picture of the telescopes is shown in figure 3.7. The main purpose of HEAT is to measure the energy spectrum and to determine the

Figure 3.7: Photo of the 3 tilted HEAT bays [74].

chemical composition by measuring the depth of the shower maximum of extensive air showers. As the fluorescence signal is proportional to the energy of the primary particle, the low energy showers can only be detected close to the detector. In addition to that they develop their shower maximum higher in the atmosphere. The HEAT telescopes are similar to the standard FD telescopes but can be tilted by 29° upward to see those close and high showers. HEAT can measure air showers in two modes, 'downward' and 'upward', as an independent FD station, which is shown in figure 3.8. If it is in the 'downward' mode, the events can be compared directly with the Coihueco events for systematic studies. If the telescopes are tilted in 'upward' mode, then they can study the shower profile of air showers with a lower energy than the standard FD telescopes as shown in figure 3.9. In this mode, HEAT and Coihueco can be combined to one virtual FD eye HECO and measure shower profiles with high accuracy as shown in figure 3.10. In this figure the timing information of the extensive air shower is

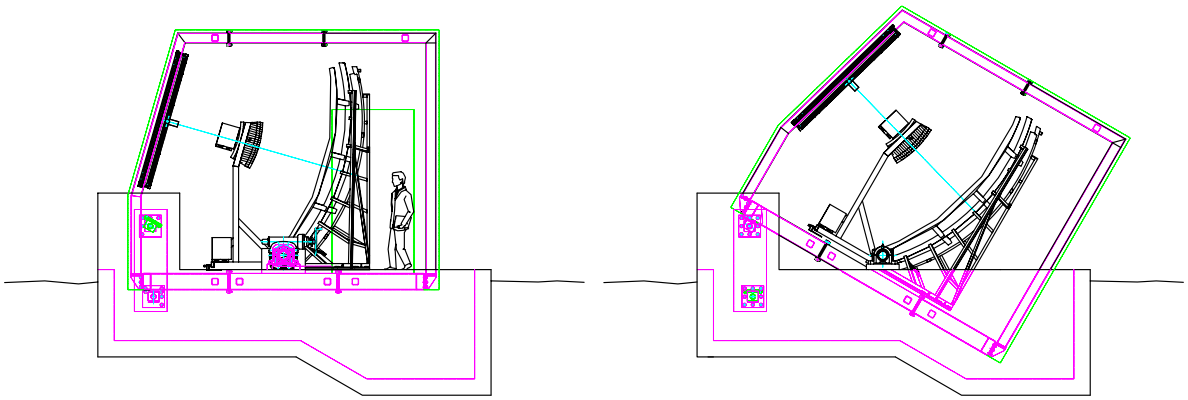

Figure 3.8: HEAT detector scheme for the 'downward' (left) and 'upward' (right) measurement mode [74].

color coded in the PMT pixels from early (purple) to late (red). The thin red line corresponds to the fitted shower axis and the red dot represent the position of the air shower maximum X_{max}.

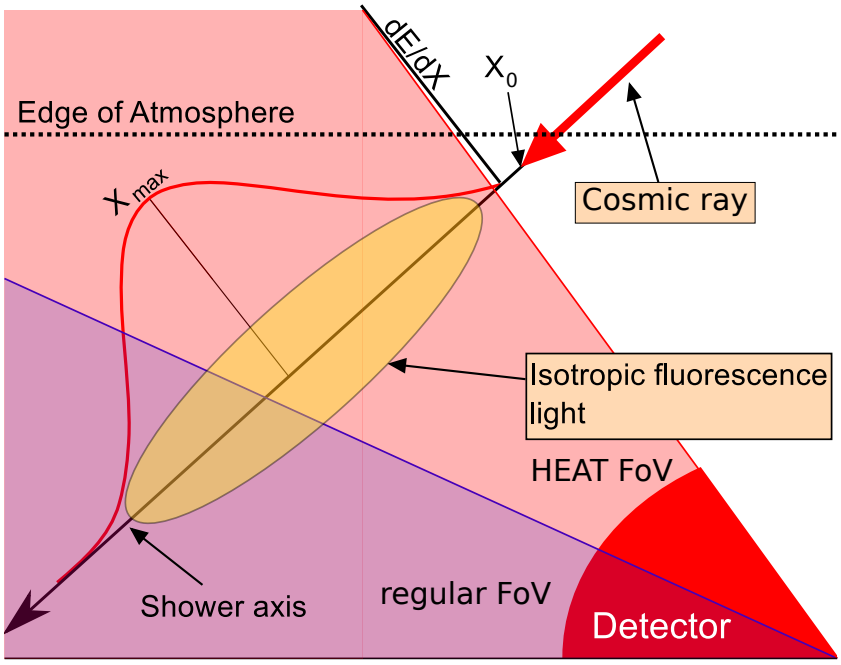

Figure 3.9: Schematic view of the energy deposit measurement of extensive air shower profiles with HEAT [75].

Since September 2009, HEAT has been taken first data [74], and since June 2010 the data taking is stable. Together with the low energy extension Infill, which consists of 42 additional SD stations on an hexagonal grid with 750 m spacing and HEATLET, which consists of 5 additional SD station near HEAT, a good hybrid detection efficiency of low energy showers is

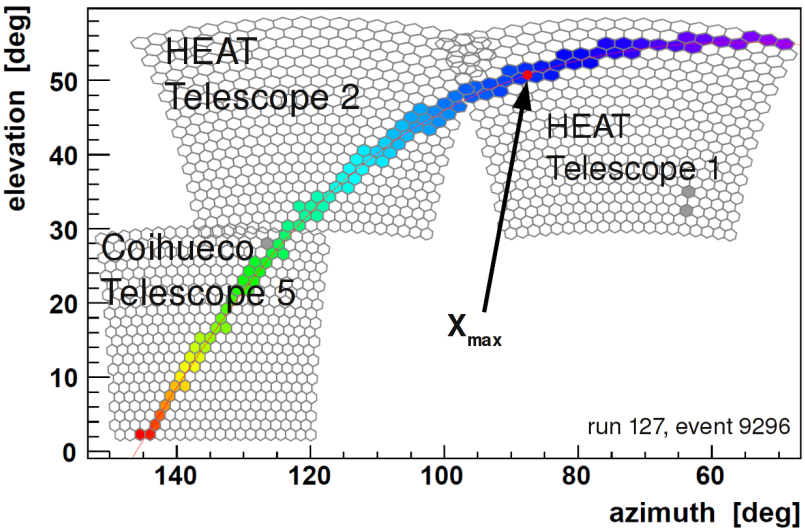

Figure 3.10: Event display of a reconstructed low energy HECO event seen by two HEAT telescopes and one Coihueco telescope [76]. The timing information of the extensive air shower is color coded in the PMT pixels from early (purple) to late (red). The thin red line shows the fitted shower axis and the red dot shows the position of the air shower maximum X_{max}. The bending of the shower track is due to the projection of the event view.

assured. The positions of the additional SD stations are shown in figure 3.11 as red dots for the Infill and blue dots for the HEATLET. First calculations of the energy spectrum measured by the enhancements are given for HEAT in [77] and for Infill in [78].

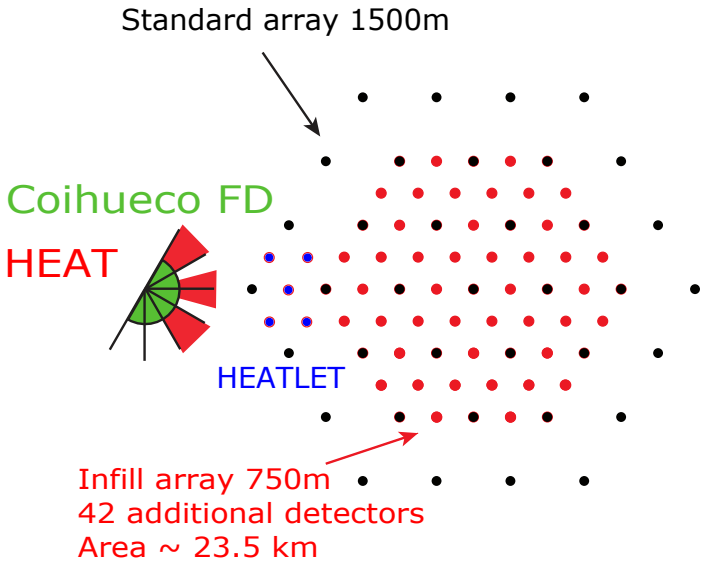

Figure 3.11: Positions of the additional SD station from the Infill (red dots) and HEATLET (blue dots) [74].

3.2.1.1 Tilt Monitoring of HEAT

Due to the ability to tilt the HEAT telescopes, it is necessary to monitor the mechanical stability of the whole telescope system. For this purpose, a dedicated tilt monitoring system was developed, calibrated, tested and installed by the RWTH Aachen Auger group after the construction of HEAT. The tilt monitoring system consists of 4 inclination and 4 distance sensors for each HEAT telescope. The schematics of the sensor positions of the tilt monitoring are shown in the figures 3.12a and 3.12b. The inclination sensors are small bi-axial inclination

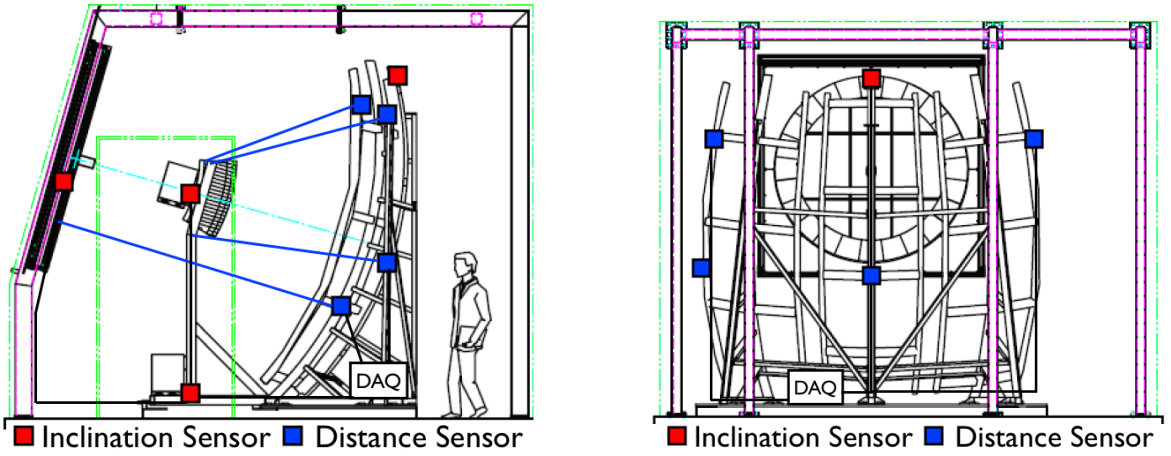

(a) HEAT tilt monitoring position side view.

(b) HEAT tilt monitoring position back view.

Figure 3.12: HEAT tilt monitoring scheme adapted from [79].

MEMS (Micro Electro-Mechanical System) sensors shown in figure 3.13a. They are using a silicon capacitive transductor, consisting of two fixed capacitor plates and a seismic mass located in between, to measure the angular orientation of the sensor. The angular resolution of these sensors is about 0.01°. The schematic is shown in figure 3.13b. The location of the

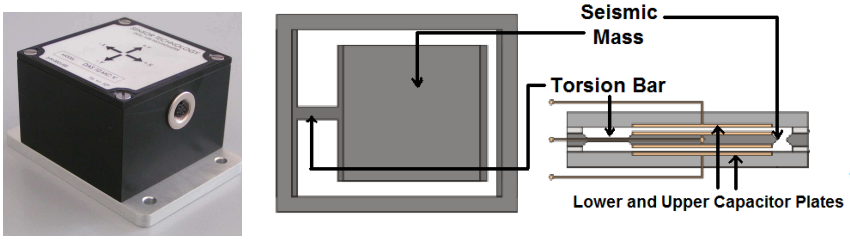

(a) Photo of an inclination sensor.

(b) Schematic of the inclination sensor.

Figure 3.13: Bi-axial capacitive inclination sensor of the HEAT tilt monitoring system [79].

inclination sensors in the HEAT bays are at

- base of the camera
- top of the camera

- top middle of the mirror
- left side of the shutter.

The distance sensors consist of roll potentiometers with temperature stable cables. This sensor provides a voltage signal proportional to the linear movement of the attached cable. It is possible to determine the distance variations with a high accuracy from the sensor by measuring the resulting voltage variation. The resolution of these sensors is about 0.1 mm. An example of these sensors is shown in figure 3.14. The monitored distances in the HEAT bays are

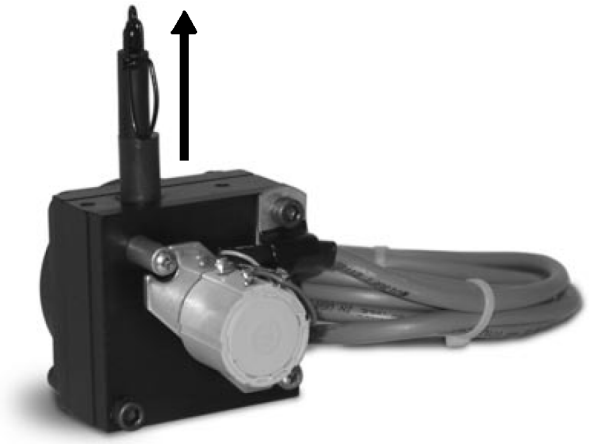

Figure 3.14: Photo of a roll potentiometer distance sensor. The arrow indicates the direction of the attached temperature stable cable [79].

- top left of mirror to top left of the camera
- top right of mirror to top right of the camera
- bottom left of the mirror to the left side of the shutter
- center of the mirror to a point beneath the camera.

Both sensor types are read out via an embedded PC located in a box beneath the telescope mirror. The output of the inclination sensors is already digitized and they are connected via a RS232-to-USB hub to the PC. The distance sensors are connected to a μ-box, which digitizes the analog sensor output. The μ-box is then connected to the PC via USB. A schematic of the data acquisition of the tilt monitoring system (DAQ) is shown in figure 3.15. For the maintenance of the system and controlling of the measured values, a Labview DAQ software is used, which is accessible via a remote desktop connection. In this program the calibration values of the sensors are used to calculate the monitoring results. These values are written into the Auger monitoring MYSQL database with a frequency of $\sim$1 Hz.

For a complete and detailed overview of the tilt monitoring system, the used sensors and the calibration process see the diploma thesis of J. Calvo de No [79] as well as the PHD theses of S. Schulte [80] and N. Scharf [77].

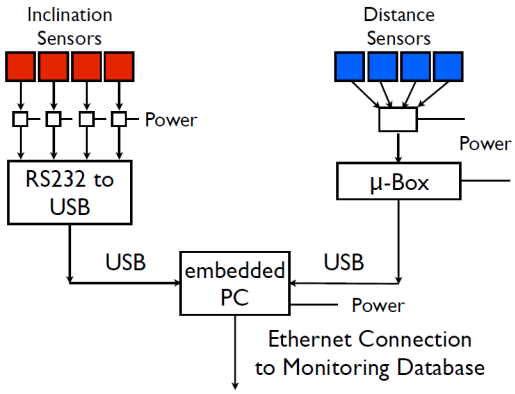

Figure 3.15: DAQ schematic of the HEAT tilt monitoring system [79].

3.2.1.2 Tilt Monitoring Analysis

The mechanical stability of HEAT is analyzed in the measured time period from June 2010 to August 2012 with the tilt monitoring system. In this thesis, the analysis of the tilt monitoring data is a crosscheck of the long time stability of the HEAT telescope structure as the alignment of the telescopes is studied with SD events and the star tracking method as described in chapter 4.5.2.4.1. In this paragraph, the stability of HEAT bay 2 is described as an example. The corresponding analyses for bay 1 and bay 3 are shown in appendix chapter B.1 and B.2.

3.2.1.2.1 Inclination Stability

For the analysis of mechanical long time stability of the telescope in bay 2 the monitoring data are selected for periods when HEAT is in the upward position as this is the normal measuring position. As the data are taken with a rate of around 1 Hz, a daily average of each sensor data is calculated. By this calculation the daily temperature variation is averaged out. As HEAT only measures at night the daily temperature can be neglected. The daily average of the inclination data in the upward telescope state is checked for deviation over time, which is shown in figure 3.18 for the x-axis and in figure 3.19 for the y-axis together with the inside and outside daily mean temperature. The shown inclination sensors are located in HEAT bay 2 at the position described in table 3.1. The plots show that the yearly variation of the temperature

Designation	located at
Inc Sensor 1	top middle of the mirror
Inc Sensor 2	top of the camera
Inc Sensor 3	left side of the shutter
Inc Sensor 4	base of the camera

Table 3.1: HEAT bay 2 inclination sensors points.

causes minor variations of the inclination sensor data, which is not necessarily a change of the optical alignment but could happen due to the temperature dependency of the used sensors. The average sensor data variation is in the same scale as the temperature dependency of the

inclination sensor [79]. The only effect visible is some construction work, which took place in November 2011 in the bay, where additional struts were attached to the camera. This explains the small incontinuities in the data of sensor 2 and 4. Overall, no large time dependent changes in the structural stability are observed. In the appendix chapter B.1 and B.2 the results are shown also for HEAT bay 1 and bay 3. No strong deviation is found in the measuring period except for the construction work.

The effect of the inclination change on the measured X_{max} value is estimated with an approximation approach. This ansatz uses an isothermal atmosphere, which is valid for vertically incident particles [81]. Here atmospheric slant depth is given by

$$X = \int_h^\infty \rho(h')dh' \sim X_0 e^{-h/h_0} \tag{3.3}$$

where $X_0 = 1030\,\mathrm{g/cm^2}$ is the atmospheric depth at sea level and $h_0 = 8.4\,\mathrm{km}$ is the scale height in the atmosphere. In figure 3.16, a scheme of the X_{max} detection with a FD telescope (1400 m above see level) is shown. The viewing angle α is depending on the X_{max} position and the horizontal distance R. In this example the air shower has a shower maximum of $X_{max} = 720\,\mathrm{g/cm^2}$ and a distance of $R = 10\,\mathrm{km}$. When the telescope pointing is really shifted,

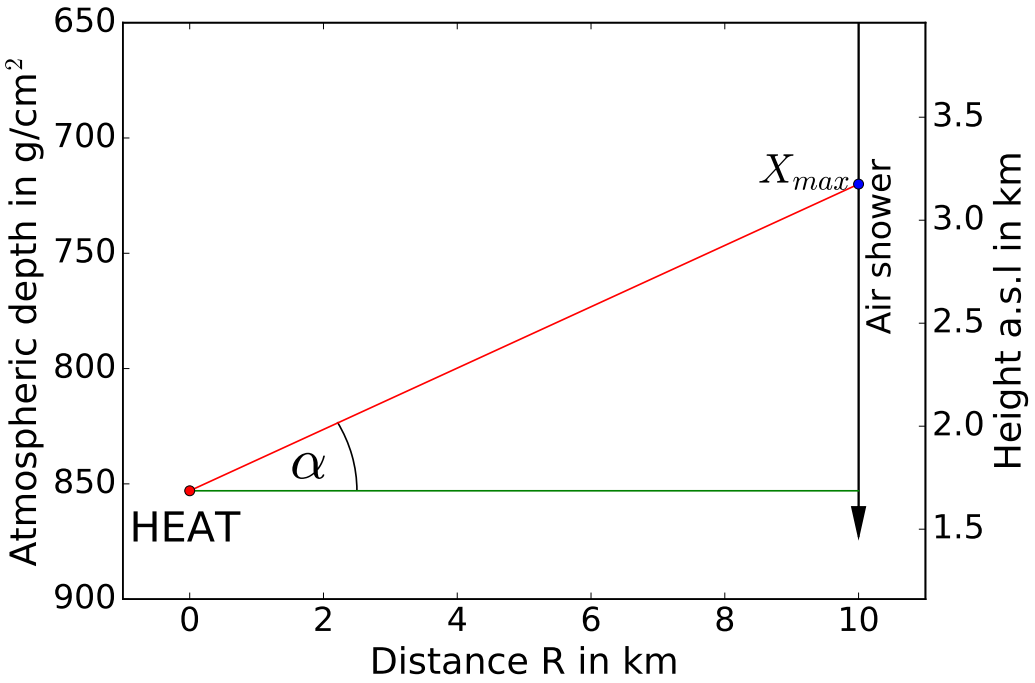

Figure 3.16: Determination of X_{max} of a vertical air shower with a maximum at $720\,\mathrm{g/cm^2}$ in a distance of 10 km. The angle α represents the viewing angle of X_{max} by the FD telescope.

by e.g. thermal effects, about $\pm 0.1°$, the reconstructed position of the shower maximum X_{max} is slightly shifted. As the viewing angle, this shift is depending on the horizontal distance R and the X_{max} position. This is shown in figure 3.17. The geometrical uncertainty of the

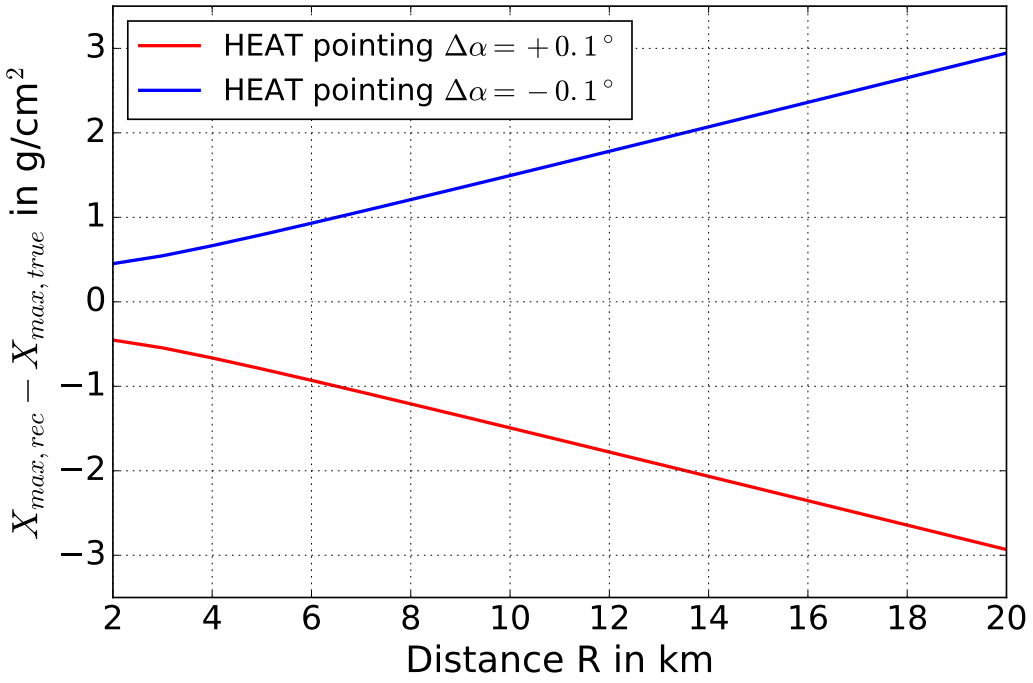

Figure 3.17: Differences of the measured X_{max} as a function of the shower distance R of a vertical air shower with a shower maximum at $720\,\mathrm{g/cm^2}$ after shifting the telescope pointing $\Delta\alpha = \pm 0.1°$.

X_{max} reconstruction due to pointing uncertainty in the inclination of HEAT seen by the tilt monitoring system is for almost all air showers well below $\pm 3\,\mathrm{g/cm^2}$.

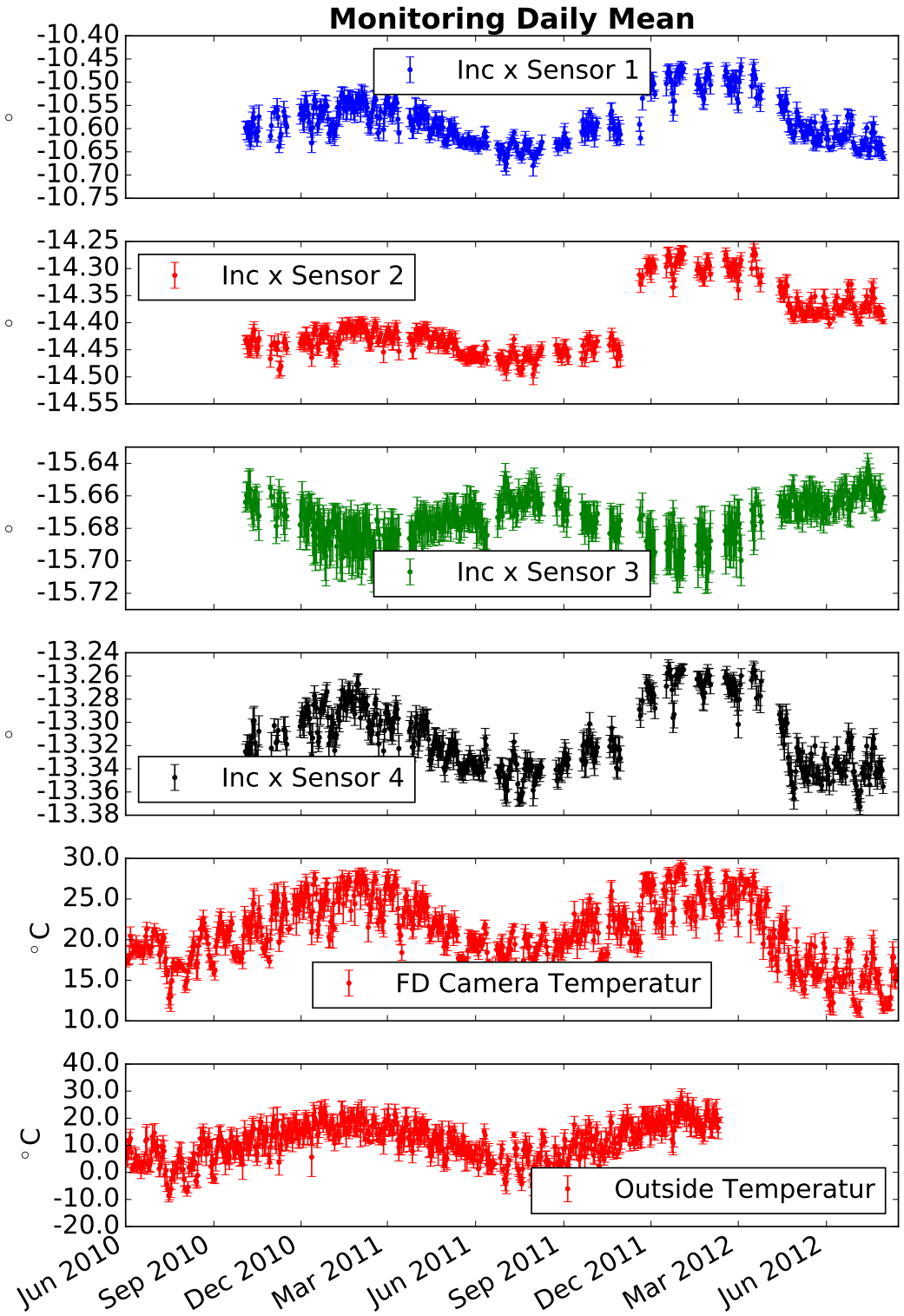

Figure 3.18: Daily mean values of the inclination sensors of the x-axis in HEAT bay 2, the outside temperature at the Coihueco weather station and the inside temperature measured at the PMT camera.

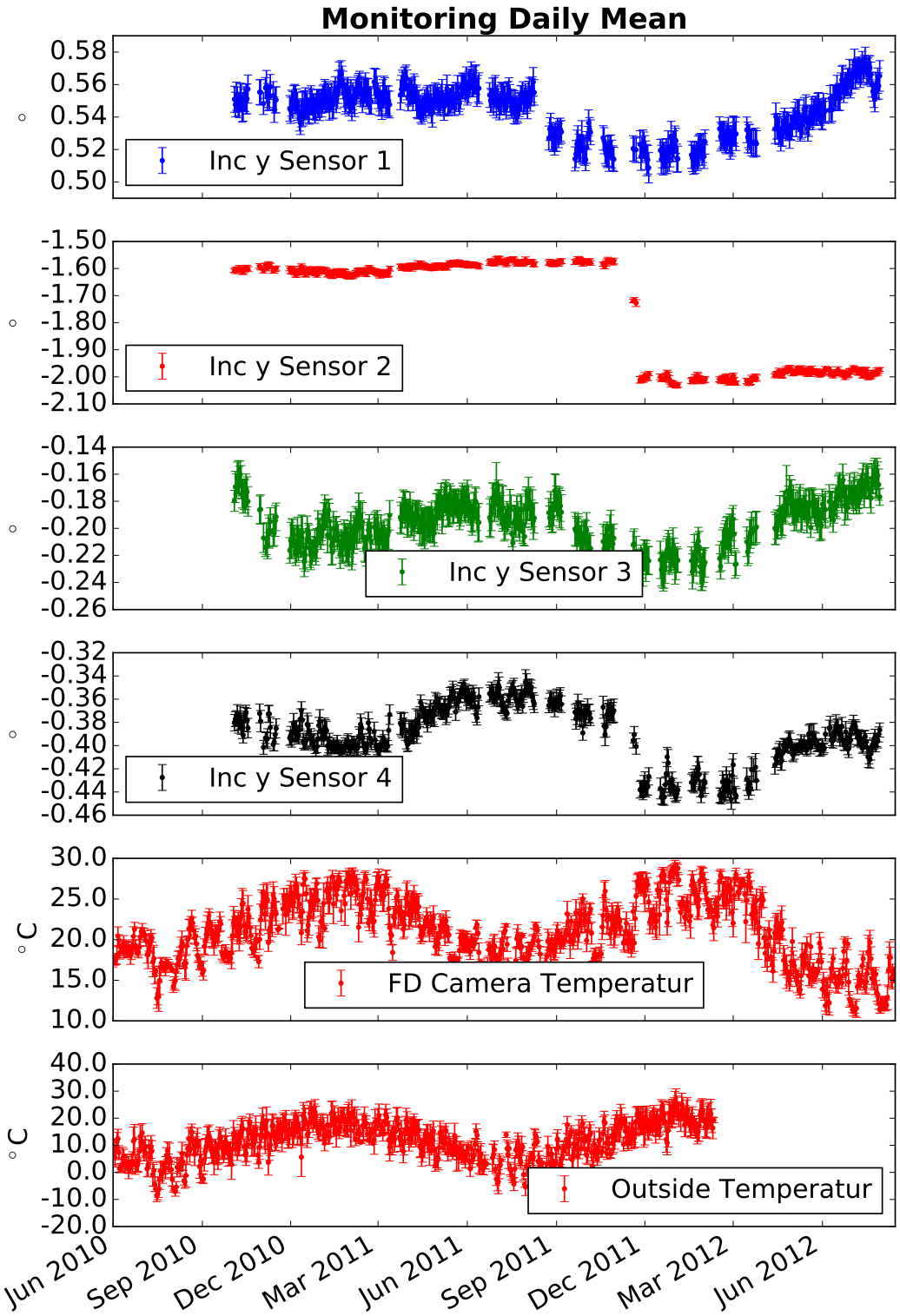

Figure 3.19: Daily mean values of the inclination sensors of the y-axis in HEAT bay 2, the outside temperature at the Coihueco weather station and the inside temperature measured at the PMT camera.

3.2.1.2.2 Distance Stability

Like the analysis of the inclination data, the signal of the distance sensors in the upward telescope state is checked for deviations over time. Again, the daily average of the sensor data is used to filter daily variation and vibrations due to strong wind or even earthquakes. The sampling rate of the sensors is not high enough to provide sensor telescope data for the variation of the geometry reconstruction. The distance sensors in HEAT bay 2 measure distances as described in table 3.2. The daily average of the sensor data together with the

Designation	Measures distance between
Dist Sensor 1	bottom left of the mirror to the left side of the shutter
Dist Sensor 2	top right of mirror to top right of the camera
Dist Sensor 3	center of the mirror to a point beneath the camera
Dist Sensor 4	top left of mirror to top left of the camera

Table 3.2: HEAT bay 2 distance sensor points.

mean temperature inside and outside of the telescope building is shown in figure 3.20. Like the inclination sensors no strong deviation over time is visible besides the construction work with the additional camera struts in November 2011. This leads to the incontinuity of the distance data set in sensor 2 to 4. Sensor 1 is constant over the whole time, but this could also be the case if the roll-in mechanism of the sensor is most likely completely relaxed and therefore no distance is measured at all. As the cable used for the distance measurement is temperature stable, only small temperature effects are visible. Overall, no strong variations of the distance happen during the used measuring period. According to [79] the variations of the sensor data are below the required camera-distance tolerance of 0.5 mm, which ensure a good geometry reconstruction of the air showers with HEAT. In the appendix chapter B.1 and B.2 the results are shown also for HEAT bay 1 and bay 3. No strong deviation is found in bay 3 in the measuring period except the construction work. In HEAT bay 1 a much strong deviation is present, but this is most likely also constructional work at the telescope. Due to a long dead time of these sensors the exact date of the change cannot be reconstructed.

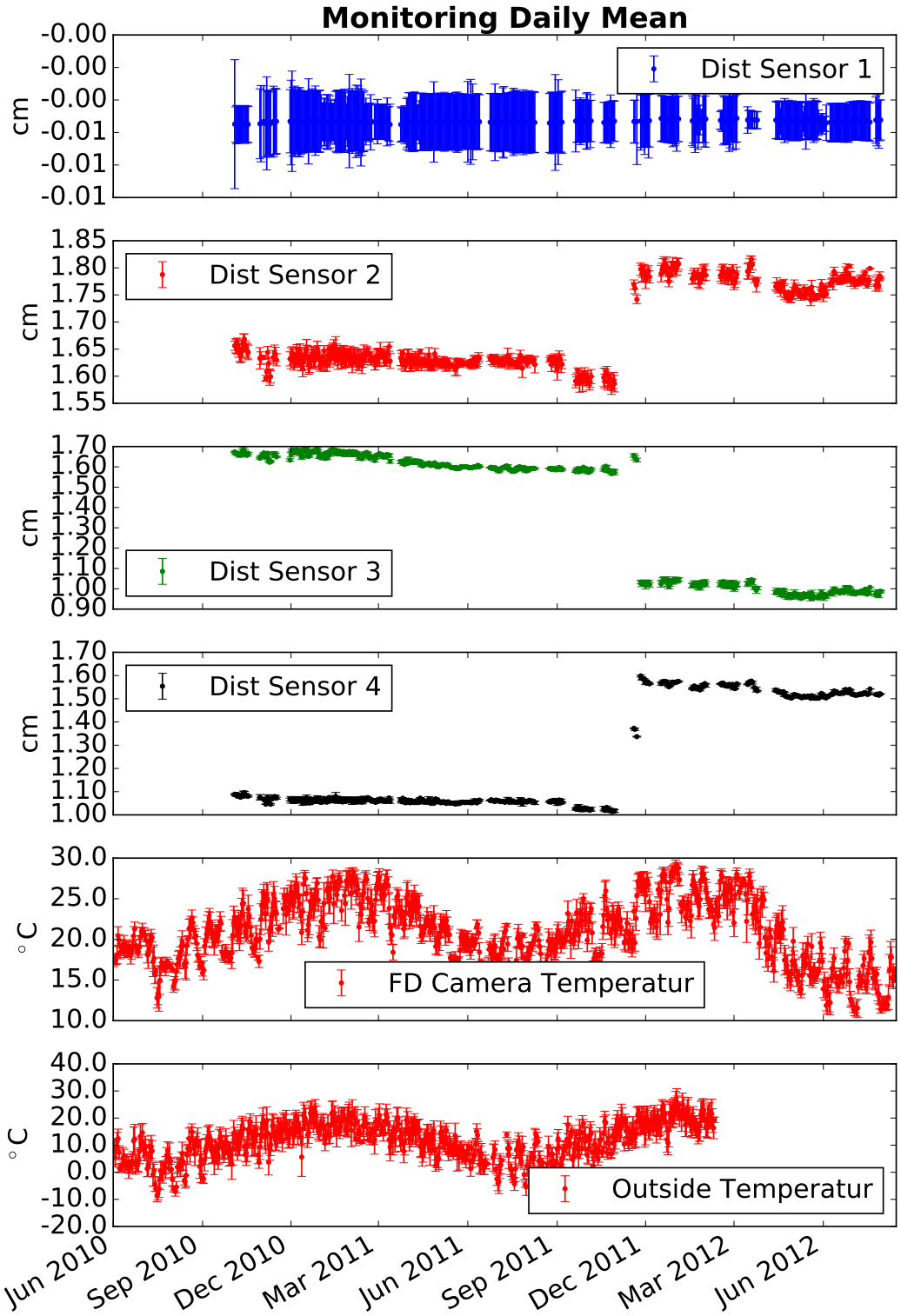

Figure 3.20: Daily mean values of the distance sensors in HEAT bay 2, the outside temperature at the Coihueco weather station and the inside temperature measured at the PMT camera.

3.2.2 Data Acquisition System and Trigger of the FD Telescopes

The Data Acquisition System (DAQ) of a FD camera contains 20 Analog Boards [72]. Each board receives the data from one column of 22 PMTs. It digitizes the data with a sampling rate of 100 ns (10 MHz) for the 'standard' FD and 50 ns (20 MHz) for HEAT.
The First Level Trigger (FLT) is a single pixel trigger. If one PMT signal is above a certain threshold, it is marked as triggered. To compensate the changing background conditions during the night, the threshold for each PMT is permanently adjusted to not exceed a trigger rate of more than 100 Hz.
The Second Level Trigger (SLT) board receives the pixel triggers of the FLT. The SLT searches for patterns of at least 5 pixels (see example patterns in figure 3.21) and compares it with the implemented 108 different pattern classes. To take into account that a track not always passes trough the pixel center and therefore does not collect enough light to trigger the pixel, the algorithm requires only 4 out of 5 pixels in a track to send a trigger to the next DAQ step. The trigger rate of the SLT is between 0.1 - 10 Hz per telescope.

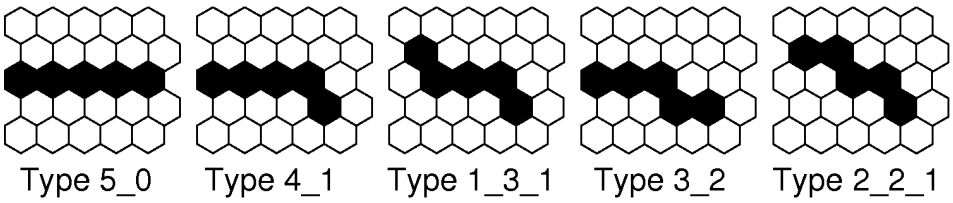

Figure 3.21: Fundamental pattern types regarded as straight track segments.[72]

The Third Level Trigger (TLT) is a software algorithm to clear the tracks from unwanted noise events like lightning, muons hitting the camera or randomly triggered pixels. Approximately 94% of all background events and only 0.7% of true showers are rejected.

If an events passes the TLT in a telescope it is sent to the EyePC of the telescope station. There an event builder merges the coincident events from different telescopes and sends an hybrid trigger (T3) to the Central Data Acquisition System (CDAS). The T3 is an external trigger for the surface array, and hybrid events with energies below 3×10^{18} eV can thereby be recorded, where the SD array is not fully efficient and often unable to generate an independent trigger. Low energy events usually trigger only one or two SD stations. The T3 algorithm is used to calculate a preliminary shower direction and impact time on the ground. With the preliminary data, CDAS requests a readout of the SD station close to the calculated impact point on the ground. The FD and SD data are merged offline for further analysis.

3.2.3 Calibration of the FD Telescopes

To determine the total energy of the reconstructed air shower the ADC counts from the PMTs have to be converted into a light flux at the telescope. Therefore, the telescopes are calibrated including the effects of aperture projection, optical filter transmittance, reflection at optical surfaces, mirror reflectivity, pixel light collection efficiency and area, cathode quantum efficiency, PMT gain, pre-amp and amplifier gains, and digital conversion [72]. There are 2

calibration methods, which are performed at the Pierre Auger Observatory. For the longtime performance of the telescopes an absolute calibration is performed once a year. Relative calibrations are performed to take local effects like PMT temperature and atmospheric conditions during each data taking into account.

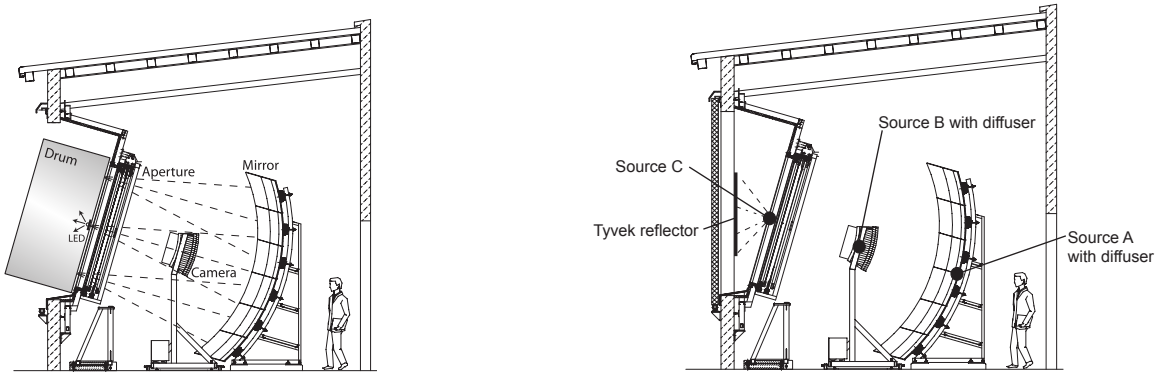

(a) Absolute calibration of the telescopes using the 'drum' at the aperture.

(b) Schematic showing positions of light sources for three different relative calibrations.

Figure 3.22: Calibration methods of the Pierre Auger Observatory [72].

For the absolute calibration, a calibrated light source known as the 'drum' is placed at the aperture and used for an absolute calibration of each telescope(see figure 3.22a). As a cross-check of the 'drum'-calibration, a dedicated roving laser system in a distance of 4 km shoots with a nitrogen laser vertical beams with a known intensity in the field of view of the telescopes [72].
The relative calibration of every telescope is performed every night before and after the data taking with three light sources built in the mirror, the camera housing and outside the UV filter window (see figure 3.22b). The pulsed 'Cal A' LED with a diffuser in the mirror is pointed directly to the camera. 'Cal B' and 'Cal C' are xenon flash lamps. 'Cal B' emits light from the side of the camera housing to the mirror. 'Cal C' uses an adjustable interference filter to emit light with different wavelengths onto a reflecting Tyvek surface inside the closed shutter doors.

3.2.4 Atmospheric Monitoring

The emitted fluorescence photons arriving at the telescope aperture have propagated through the atmosphere and therefore underwent scattering and absorption processes. To estimate the correct shower energy, the atmospheric properties have to be monitored. The Pierre Auger Observatory uses various methods to measure these effects.
The important properties of the atmosphere are molecular and aerosol scattering and cloud coverage. The influence of the light transmission in the near UV due to aerosol particles is constantly monitored by the 'Central Laser Facility' (CLF) and the 'eXtreme Laser Facility' (XLF) [82]. The cloud coverage is constantly monitored by LIDAR (LIght Detection And

Ranging) measurements [83] and dedicated night sky background cameras [84] at each FD station. The LIDAR system shoots periodical laser beams into the sky above the array and studies the back scattered light to measure aerosol densities and clouds in the FD field of view. The BGcams measure the cloud coverage above the FD stations by measuring infrared light. As an additional cloud monitoring system for the Pierre Auger Observatory, the 'Geostationary Operational Environmental Satellites' (GOES) infrared images are used [85]. Additionally, temperature, pressure and humidity of the atmosphere are monitored by five weather stations, weather balloons and the 'Global Data Assimilation System' (GDAS). GDAS provides every three hours measurements and forecasts from numerical weather predictions for the Pierre Auger Observatory area [86]. The light attenuation in the atmosphere depends on the molecular and aerosol scattering.

The molecular transmission factor $T_{mol}(\lambda, s)$ [82, 87, 88] is given by the wavelength λ dependent Rayleigh scattering cross section $\sigma_{mol}(\lambda)$ and by the atmospheric density profile $N_{mol}(s)$ along the line of sight s as

$$T_{mol}(\lambda, s) = e^{-\int \sigma_{mol}(\lambda) N_{mol}(s) ds}. \tag{3.4}$$

The wavelength-dependent Rayleigh scattering cross section is given by

$$\sigma_{mol}(\lambda) = \frac{24\pi^3}{N_{mol}^2 \lambda^4} \cdot \left(\frac{n_{air}^2(\lambda) - 1}{n_{air}^2(\lambda) + 2} \right)^2 \cdot F_{air}(\lambda), \tag{3.5}$$

where $N_{mol}(s)$ is the molecular number density along the line of sight s in molecules per m^{-3} and calculated by

$$N_{mol}(s) = \frac{N_A}{R} \cdot \frac{p(h)}{T(h)}, \tag{3.6}$$

where N_A is Avogadro's number, R is the universal gas constant, $p(h)$ is the atmospheric pressure and $T(h)$ is the temperature at vertical height h. $n_{air}(\lambda)$ is the refractive index of the air for the wavelength λ and F_{air} is the King factor accounting for anisotropies in the scattering due to non-spherical N_2, O_2 molecules. $n_{air}(\lambda)$ depends on several atmospheric state variables, like pressure, humidity and temperature [89]. Therefore, this factor can be calculated analytically with the knowledge of temperature, pressure and humidity of the atmosphere.

The aerosol scattering component T_{aer} [82, 88] is based on the Mie scattering theory. It is based on the assumption of spherical scatterers, but this condition is not always fulfilled. Moreover, the scattering depends on the nature of the particles. The knowledge of the aerosol transmission factor therefore depends on the field measurements of 'Vertical Aerosol Optical Depth' ($VAOD(h)$), which is a function of the vertical height h. Assuming a horizontally uniform aerosol distribution, the aerosol transmission factor is given by

$$T_{aer}(h, \theta) = e^{-\frac{VAOD(h)}{sin(\theta)}}, \tag{3.7}$$

where θ is the angle between the telescope and the point where the scattering took place. The measurements are performed during data taking once every hour by recording CLF and

XLF induced FD events with each FD station and normalized the results to 'reference clear nights' or 'Rayleigh nights', where the aerosol contribution is assumed to be minimal and dominated by the molecular attenuation. When the measured VAOD values are not available, a parametric Mie model is used, which is a parametrization of the average aerosol content of the atmosphere.
A comparison of the optical depth of molecular and aerosol effects is shown in figure 3.23 as a function of height.

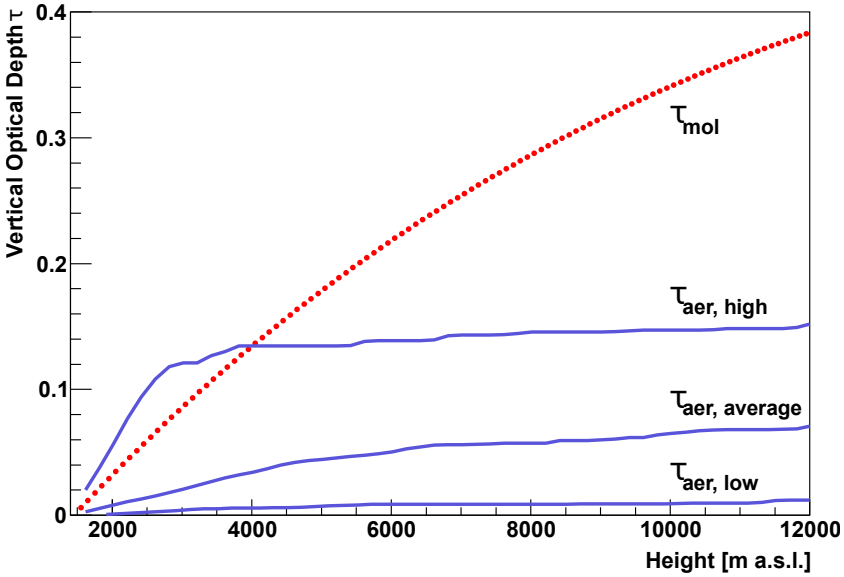

Figure 3.23: Calculated molecular optical depth profile τ_{mol} at 355 nm (red dots) as a function of height, shown together with the measured vertical aerosol optical depth profiles τ_{aer} with high, average, and low concentration of aerosols [88].

The used aerosol database used for this thesis is described in [90]. The amount of light at the aperture must be corrected for T_{mol} and T_{aer}. The uncertainties of this atmospheric description on the measurements of cosmic rays and the detector resolution will be discussed in chapter 4.5.2.3.
After that the photon flux can be converted into the deposited energy in the atmosphere by the fluorescence yield Y_{air}, which also depends on the atmospheric conditions. The Pierre Auger Observatory uses the most recent results of the fluorescence yield of the AIRFLY collaboration [91, 92].

3.3 Hybrid Reconstruction

As a hybrid detector, the Pierre Auger Observatory can measure the same extensive air shower with multiple independent detector components to achieve accurate and independent reconstructions of the energy, the arrival direction and the shower profile, as seen in figure 3.24. There are two types of hybrid events in the Auger data sets. A merged triggered FD event with the complete SD reconstruction is called 'golden hybrid' and is used for the cross-calibration

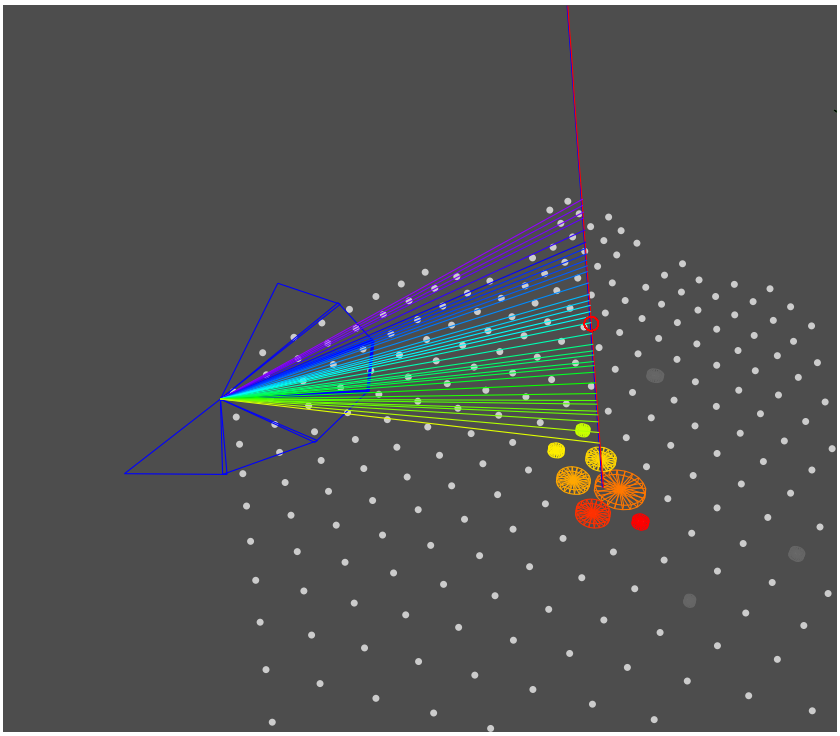

Figure 3.24: Event view of a reconstructed air shower. For FD the timing information of the triggered pixels are color coded from early (blue) to late (red). The reconstructed shower maximum X_{max} is marked as a red circle. For SD the timing information of the triggered pixels are color-coded from early (yellow) to late (red). The SD signal strength is marked as the size of the station.

of FD and SD. However, a full SD reconstruction needs at least 3 triggered stations as shown in chapter 3.1. At low energies, where SD is not 100 % efficient, the SD station are mostly read out due to the external FD trigger request. These hybrid events without complete SD reconstruction are called 'brass hybrid'. The events use the timing information of SD for the better geometry determination of the shower track. In this work both golden and brass events are used for the analysis.

3.3.1 Geometrical Reconstruction

The best geometrical accuracy is achieved by the combination of the timing information of FD pixels and SD stations. The timing information of the pixels is used for reconstructing the shower axis within the 'shower detector plane' (SDP), which is shown in figure 3.25. The reconstruction uncertainties on the SDP are validated using events with known geometries as scattered light from laser beams of the CLF [67]. The light arrives at the i^{th} pixel at the time

$$t_i = T_0 + \frac{R_p}{c} \tan\left(\frac{\chi_0 - \chi_i}{2}\right), \tag{3.8}$$

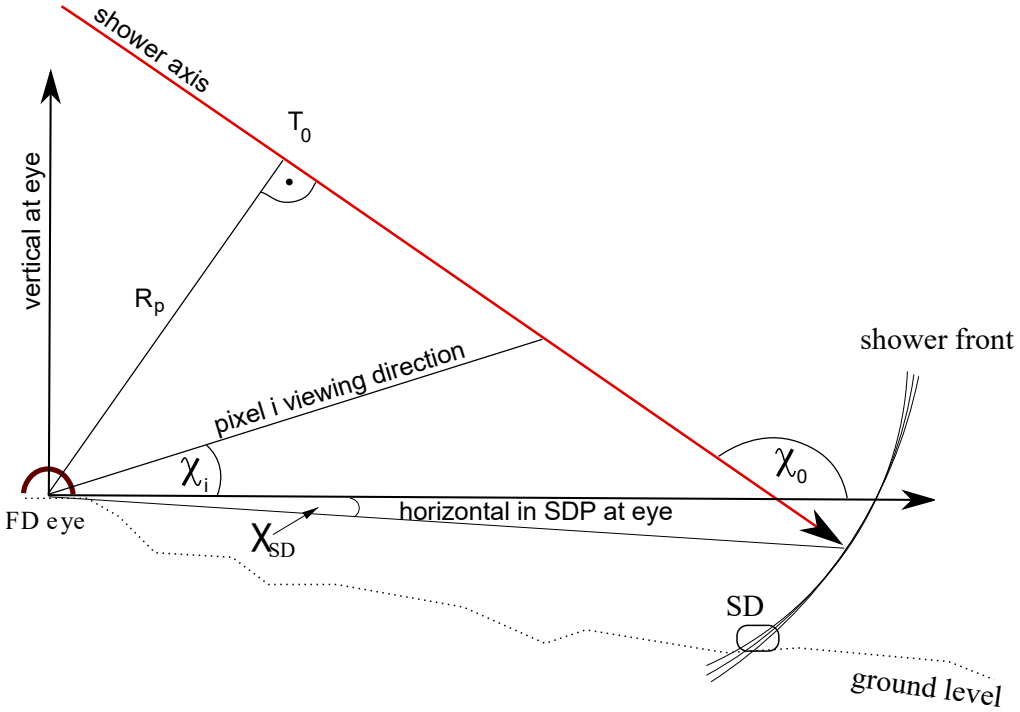

Figure 3.25: Illustration of the geometrical shower reconstruction of hybrid events within the shower detector plane (SDP) [67].

where R_p is the perpendicular distance from the shower axis to the telescope and the shower axis at the time T_0 with an angle of the shower track χ_0 with respect to the horizontal axis at the telescope. The free parameters R_p, T_0 and χ_0 are determined by the minimization of the function

$$\chi^2 = \sum_i \frac{(t_i - t(\chi_i))^2}{\sigma(t_i)^2} + \frac{(t_{SD} - t(\chi_{SD}))^2}{\sigma(t_{SD})^2}, \tag{3.9}$$

which also includes the timing information of the SD station closest to the reconstructed shower core. Example of the camera event view and the geometry fit are shown in the figures 3.26a and 3.26b .

3.3.2 Energy and Shower Profile Reconstruction

After the geometry determination, the number of collected photons at the aperture as a function of time is converted into an energy deposit profile as a function of slant depth. This is shown in the figures 3.27a and 3.27b. The light attenuation from the emission point in the air shower to the detector needs to be known and all contributing light sources need to be disentangled. As most of the charged shower particles travel faster than the speed of light in air, Cherenkov light is emitted. The optical signal of an extensive air shower measured at the FD stations consists of fluorescence and Cherenkov light. The Cherenkov light contribution is composed of direct and scattered (Mie and Rayleigh) light [93, 94]. Additionally photons from all light components can be scattered multiple times in the atmosphere and are contributing to the

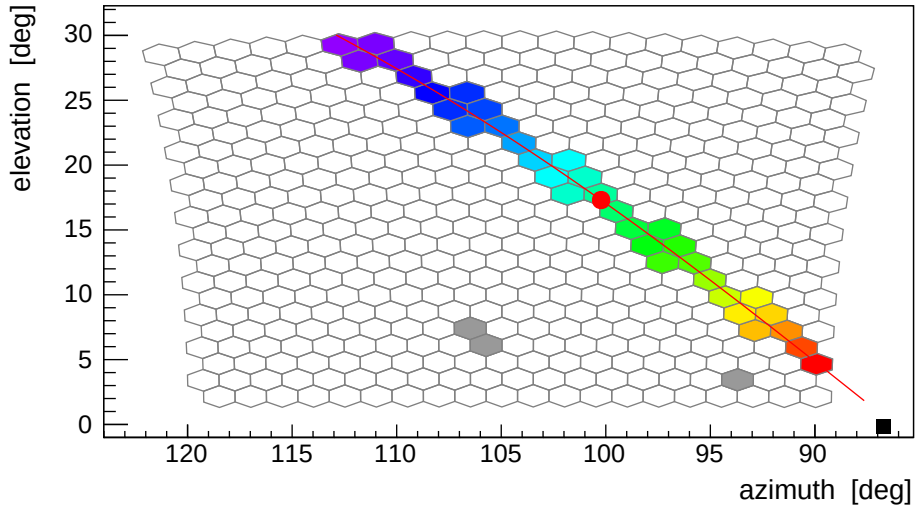

(a) Event view of a reconstructed shower track in a FD camera. Reconstructed air shower maximum X_{max} is marked as a red dot on the shower axis.

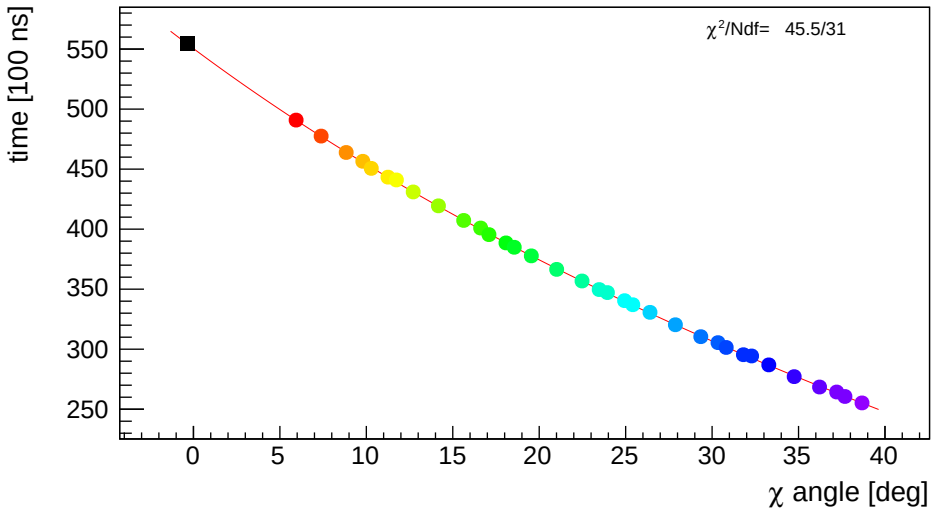

(b) Shower track in the $\chi-$time plane.

Figure 3.26: Event display of a single FD event (run 3259, event 444) at Los Leones. Color coded is the timing information from early (blue) to late (red). The black point represents the used SD station.

total light signal [95]. The detected light at the telescope aperture can be dominated by the Cherenkov light due to the forward peaked nature of Cherenkov light production for air shower pointing towards the telescopes.

As stated in chapter 3.2.4, the proportionality between fluorescence light and energy deposit is given by the fluorescence yield Y_{air}, which depends on the atmospheric condition. Also due to the lateral extend of the shower, not all light is collected in the reconstructed shower track,

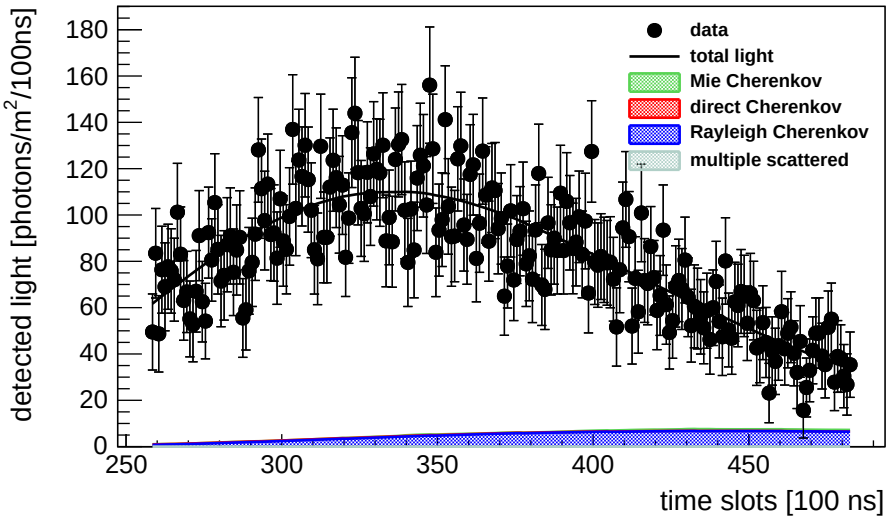

(a) Collected UV photons at telescope aperture per 100 ns time bin including calculated Cherenkov and multiple scattering photons contributions. Fitted light curve is marked as black line. Night sky background light is subtracted. Due to the shower geometry of the event, the contributions from Mie and direct Cherenkov light are very small.

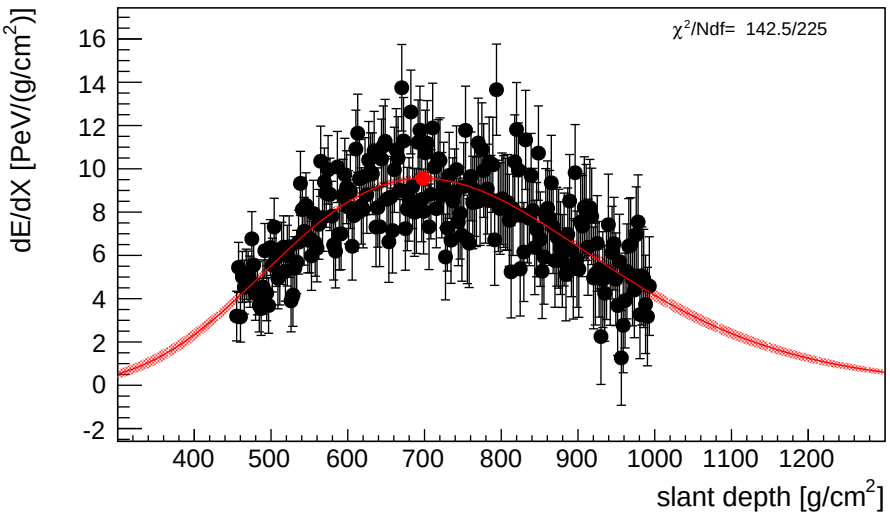

(b) Energy deposit profile as a function of the atmospheric slant depth with Gaisser-Hillas fit in red. Position of the shower maximum X_{max} is marked as a red dot and fit uncertainties are marked as a red shaded area.

Figure 3.27: Profile measurements as a function of light and deposited energy dE/dX of a single FD event (run 3259, event 444) at Los Leones.

therefore a correction for the universal lateral fluorescence distribution [96] and Cherenkov light distribution [97] must be taken into account. The conversion is performed by solving a linear set of equations. Once the light flux is converted into an energy deposit profile, the shower profile is obtained analytically by linear least square minimization of a 4-parameter

Gaisser-Hillas function f_{GH} [98], which is given by

$$f_{GH}(X) = \left.\frac{dE}{dX}\right|_{max} \left(\frac{X - X_0}{X_{max} - X_0}\right)^{\frac{X_{max}-X_0}{\lambda}} e^{\frac{X_{max}-X}{\lambda}}, \tag{3.10}$$

where X_{max} is the position when the shower reaches the maximal energy deposit $\frac{dE}{dX}|_{max}$. The two shape parameters X_0 and λ have no direct physical meaning. The minimization of equation 3.10 works for all 4 free parameters, when a large fraction of the shower is measured above and below the shower maximum X_{max}. If the shower track is too small or the shower maximum X_{max} is outside the field of view of the telescopes, the problem is underdetermined and therefore not sufficient enough to reconstruct all four Gaisser-Hillas parameters. To overcome this complication, the shape parameters X_0 and λ are constraint in the fit to their average values [99]. The total deposited energy in the atmosphere, the so-called calorimetric energy E_{cal}, is the integral of the f_{GH}, which is given by

$$E_{cal} = \int_0^\infty f_{GH}(X)dX. \tag{3.11}$$

Due to missing energy, which is carried away by high energy muons and neutrinos, the total energy of the primary particle is given by

$$E_{tot} = E_{cal} \cdot f_{invis}, \tag{3.12}$$

where f_{invis} is a correctional factor for 'invisible energy' [100, 101, 102]. This correction factor is $f_{invis} = 1.21$ at $\log(E/\text{eV}) = 17.0$ and $f_{invis} = 1.15$ at $\log(E/\text{eV}) = 18.4$).
The statistical uncertainties are given by the error propagation from the fit parameters, the geometrical uncertainties and the atmospheric uncertainties. The systematic uncertainties on the energy scale [103] depend on the FD calibration (9.9%), fluorescence yield (3.6%), atmosphere (3.4-6.2%), FD profile reconstruction (6.5-5.6%), invisible energy (3.0-1.5%), stat. error of the SD calibration fit (0.7-1.8%) and stability of the energy scale(5%). The contributions sum up to a total systematic uncertainty of ≈14%.

3.4 Additional Enhancements

To study the muonic component of an extensive air shower in more detail, the 'Auger Muons and Infill for the Ground Array' (AMIGA) [104, 105] was developed and constructed. It consists of two parts: The Infill SD array which was already presented in chapter 3.2.1. The second component consists of buried scintillator muon detectors close to the SD stations. The muon detectors are 2.3 m below the ground to shield the electromagnetic component of the air shower; they cover an area of 30 m^2. As the electromagnetic shower component is shielded by the ground, a detailed measurement of the muonic shower component can be made in combination with SD detector, like the description of the muonic shower development and the measurement of the muonic shower maximum X^{μ}_{max}.
The Pierre Auger Observatory also uses the radio detection principle to study cosmic ray showers. The 'Auger Engineering Radio Array' (AERA) [106, 107] has been constructed and is taking data since 2010. It uses the electromagnetic emissions of the electromagnetic shower component to reconstruct the direction, energy and shower profile of an extensive air shower.
To study the chemical composition of the UHECRs on a shower-by-shower basis, it was decided in 2015 to build an upgrade to the SD station. This upgrade is the 'Scintillator Surface Detector' (SSD) [108]. Each SD station will get an update of the electronics and a scintillator detector on top of the water tank. With the simultaneous measurements in both detectors the muonic shower development of the air shower can be improved. This new detector type and several improvements of the old detector will form the 'Auger prime' detector [64] to improve the understanding of the highest UHECRs.

3.5 Data Processing and Offline-Framework

The raw data of the detector components and the monitoring database are sent and stored at CDAS, where a first reconstruction is performed. These data are mirrored to a data center in Europe. As SD and FD data are kept in separate data streams, they need to be merged for hybrid analysis. These merged hybrid data are then used for the final reconstruction.
The Offline software of the Pierre Auger Observatory provides the framework for simulation and reconstruction of air showers for all detector components. It is a C++ based object oriented design including common open source tools. The framework is capable to handle user code, the user-contributed configuration files and to provide access to event and time-dependent detector information from various data sources. It is also adjustable and has grown over the last years to handle besides SD and FD also the current (AMIGA, HEAT and AERA) and future (SSD) detector enhancements. A detailed description of the software structure and performance is given in [109].

Chapter 4
Study of the Chemical Composition of UHECRs

The chemical composition of UHECRs is one of the key observables to understand the origin and the acceleration mechanism of these cosmic ray particles. As shown in in chapter 2.2, the composition can be studied by using the atmospheric depth of the shower maximum X_{max} and comparing it to simulations based on different interaction models. The comparison to Monte Carlo data is done by comparing the first two momenta of the X_{max}-distributions, namely $\langle X_{max} \rangle$ and $\sigma_{X_{max}}$, of a given energy bin to simulation values. Additionally, a superposition model of X_{max} parametrizations for different element groups is fitted to the X_{max}-distributions to compute possible chemical composition fractions of the UHECRs based on the interaction models. To focus on HEAT, the energy range of this analysis extends from $10^{17.0} - 10^{18.4}$ eV. To make a quantitative statement about the composition in this energy range, several quality checks of the data are done and the best detector knowledge is used to get an almost unbiased data set of hybrid air showers.

4.1 FD Data Set

In this thesis only the FD hybrid data containing the SD information of the virtual telescope combining HEAT and Coihueco (HECO) are studied. This data set includes the events of HEAT, Coihueco, and HECO. To study the chemical composition of the UHECRs, only high quality data are taken into account. Therefore, several quality cuts are made on the reconstructed air showers. Furthermore, some studies are made to ensure that the data set is unbiased concerning the limited field of view of the telescopes.
A similar study of the hybrid data including HECO was performed in a recent PhD thesis of A. Porcelli [110] and a study of the first two momenta of the X_{max}-distributions was recently published at the ICRC15 [111]. This thesis uses a sub-sample of this data set for comparison. A universality constraint based on air shower simulations is introduced into the reconstruction process, which will be described in chapter 4.3.1. This constraint is dependent on the primary particle and the interaction model. To reduce the primary particle dependency of the constraint, a 50% H:50% Fe composition is used for the determination of the constraint. Concerning the dependency on the interaction model, the EPOS LHC and QgsjetII-04 have similar constraint properties and are combined as the LHC constraint. Sibyll2.1 has different constraint values and is used separately. Therefore the raw data are reconstructed with a constraint based on the Sibyll2.1 and the LHC models.
In the following chapters the selection criteria on the HECO sample is explained in detail. The number of events before and after the selection cuts are given in table 4.1.

HECO Data Set from June 2010 to August 2012		
Constraint Model	Sibyll2.1	LHC
Before Selection	651549	651549
After Selection for energy range of $10^{17.0} - 10^{18.4}$eV	6545	6570

Table 4.1: Summary of numbers of event selection from the HECO data set.

4.1.1 HECO Time Range

As HEAT is taking stable data since June 2010, this is the starting date of the HECO data set, which ranges to 15th of August 2012. As hybrid events are merged offline between SD and FD, a study was conducted to ensure the merging process is stable, which is described in [110]. A short summary of this study is that events triggered in both Coihueco and HEAT are selected and the differences of their time stamps of the shower cores are compared. If this difference is less than 200 μs, then the FD event is correctly merged with the corresponding SD event. The result of this study for the period 2012-2013 is shown in figure 4.1. This study

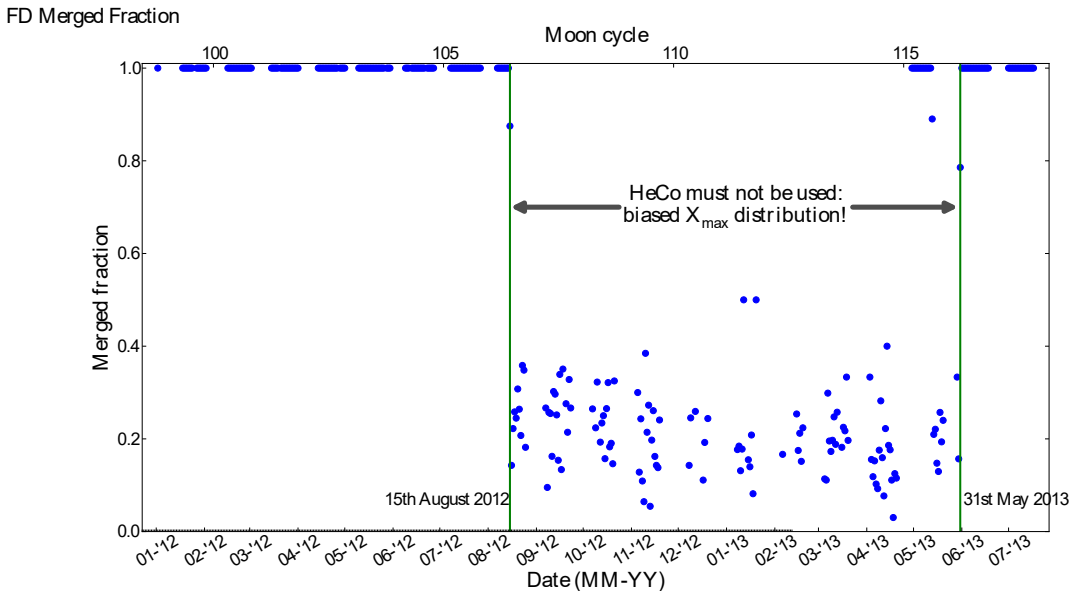

Figure 4.1: Fraction of merged SD and FD-HECO events as a function of time [110]. After the 15th of August 2012 a bug in the CDAS software caused false merging of HECO and SD. This bug was fixed on 31st of May 2013.

found a bug in the merging since 15th of August 2012, due to wrong settings of the coordinates of HEAT in the CDAS. Due to this bug, the T3 events sent by HEAT were merged with the wrong SD events and only events also seen by other FD stations were merged correctly. This bug was fixed on 31st of May 2013. However, several significant changes to the CDAS software were made and the HEAT data after this time needs further investigation and crosschecks.

Therefore, only HECO events until 15th of August 2012 were used in this thesis to ensure a stable detector performance.

4.1.2 CO-HEAT Energy Cross-Calibration

Additionally to the drum calibration campaign in 2010 [112, 113], a crosscheck of events seen by different FD stations are made to study the energy reconstruction of each station, which is described in detail in [110]. As HEAT can also operate in downward mode, this cross-calibration based on

$$\Delta E_{1-2} = \frac{E_1 - E_2}{(E_1 + E_2)/2} \tag{4.1}$$

are made with all FD stations. High quality FD stereo events are used in this study and the result is shown in figure 4.2. It shows that there is a systematic difference in the energy reconstruction of HEAT and Coihueco of $5.3 \pm 0.6\%$. As HEAT and Coihueco are combined to the virtual eye HECO, this systematic shift influences the X_{max} determination by the Gaisser-Hillas fit. This is due to events crossing HEAT and Coihueco mirrors with different calibrated dE/dX-tracks. This effect needs to be compensated before a further analysis. There are two

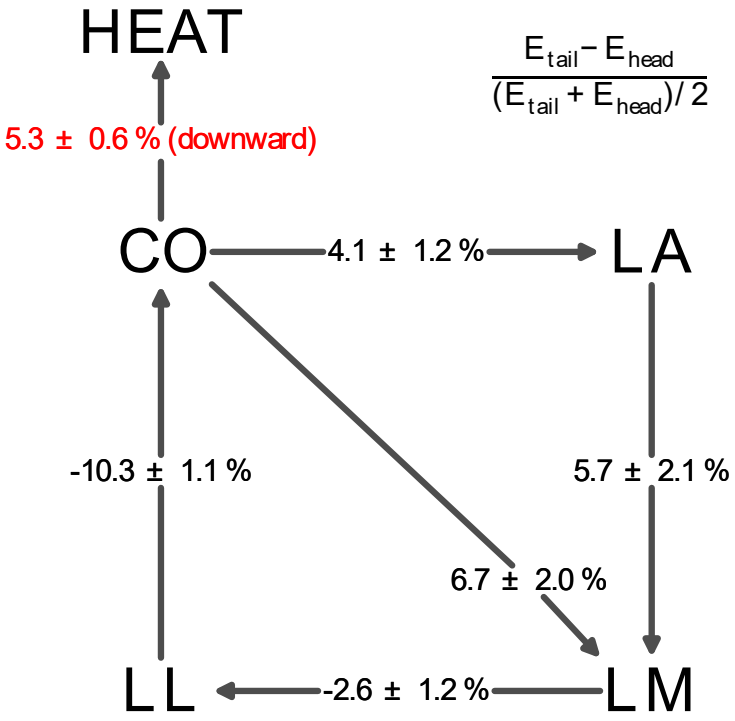

Figure 4.2: Comparison of reconstructed stereo events from the FD telescopes from [110]. Relative differences of the average reconstructed energy is shown. The arrows (head and tail) indicate the direction of the differences by $\Delta E = \frac{E_{tail} - E_{head}}{(E_{tail} + E_{head})/2}$.

ways to do this. Changing the calibration of HEAT up or lowering the calibration of Coihueco. A study on the influence on X_{max} was performed in [110] and the results are shown in figure 4.3. The results of the two options on HECO events are comparable and as it seems in figure 4.2, that Coihueco has also large differences to the other FD stations, the Coihueco shift option is preferable. During the reconstruction of the data for this thesis, the energy calibration of

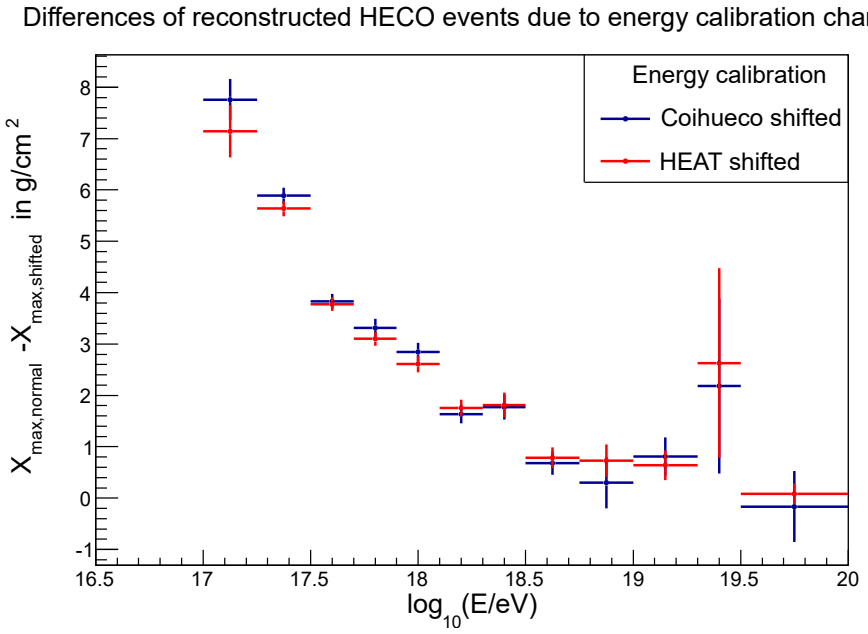

Figure 4.3: Effect of the changing of Coihueco/HEAT energy calibration on reconstructed HECO events from [110]. Average differences of the reconstructed HECO X_{max} are shown.

Coihueco is corrected down for this systematic effect. This correction was also applied in [110] and [111].

4.1.3 Event Data Selection

In the following section the quality criteria applied on the data in this thesis are explained. A summary of the selection cuts is shown in table 4.2. The specific cut list for Offline is given in the appendix F.

	Condition	Efficiency
Eye		
HEAT upwards	-	98.6%
Data Acquisition		
Remove Bad FD Period events	-	94.0%
Skip saturated PMT	-	98.7%
No Bad pixels in track	-	100.0%
Shutter	-	100.0%
Good 10 MHz correction	-	99.0%
Hybrid		
Hybrid geometry & Tot SD station	-	18.2%
Maximum zenith angle	85°	86.9%
Energy reconstructed	-	93.7%
Maximum Shower Core-SD station distance	1500 m	99.9%
Atmosphere		
Measured Mie model available	-	86.7%
Maximum vertical aerosol optical depth (VAOD) at 3 km	0.1	94.1%
Cloud cut	-	64.6%
HECO		
Minimum brass hybrid probability	90%	85.2%
Maximum brass hybrid probability difference H-Fe	5%	93.6%
No T3 Veto	-	73.2%
Reconstruction		
Successful X_{max}-error estimation	-	96.6%
Maximal gap in track	30%	96.6%
Profile χ^2-cut	5	97.7%
Field of View		
Expected FOV cut	-	48.5%
Fiducial FOV cut	-	51.0%

Table 4.2: Summary of FD selection cuts. The implementation of the cut in the Offline framework is given in appendix F.

4.1.3.1 Data Acquisition Cuts

Bad FD periods are removed from the data set, which means time ranges when the telescopes were in no good condition for taking high quality data, e.g. missing calibration, glitches from GPS, unstable baseline or wrong alignment. Also issues with the PMTs are considered. So no bad pixels (missing calibration, unstable ADC variances or other reasons) or saturated PMTs are allowed in the shower tracks. The shutter state of the FD telescopes is also taken into account. During the closure of the shutter doors, events can still be measured. However, the mean signal of the camera will be much smaller compared to normal operation periods with a smaller RMS, which leads to an unstable energy reconstruction. To check if these rare events are still usable for the analysis, the cut uses the RMS value of the camera. To be accepted, the RMS of the camera must be higher than a threshold of $17\gamma/100\,\mathrm{ns}$. This cut was introduced for all telescopes in [110], where the whole FD data set from 2004-2012 was analyzed. As shown in table 4.2, this shutter cut does not reject any HECO event in the analyzed time range of this thesis. The timing of the events is based on GPS measurements with a precise 1 pulse per second reference signal. The used oscillator has a frequency of 10 MHz and defines the time bins of 100 ns. This oscillator is a commercial product and laboratory tests have shown that such 100 ns-units are not a precise subunit of the second. It is possible to have a slightly larger or shorter time than 1 s, after accumulating a certain amount of counts. This imprecision is stored as data information and can be corrected [114]. The **Good 10 MHz Correction cut** rejects showers without this correction.

4.1.3.2 Hybrid Cuts

The **Hybrid geometry cut** selects only shower geometries constrained with at least one SD station, the hybrid events. Additionally, the **Tot(Time over Threshold) SD station cut** is used to remove SD stations, which do not have a valid Tot trigger. This cut removes hybrid events with SD stations triggered by coincidental atmospheric muons. The **Maximum zenith angle cut** is used to remove up going and horizontal events and to remove events caused by the Laser facilities of the Pierre Auger Observatory (CLF, XLF, Lidar). The **Energy reconstructed cut** selects only events with a successful reconstruction of the primary energy. The **Maximum Shower Core-SD station distance cut** rejects events, whose reconstructed shower cores are too far away ($\geq 1.5\,\mathrm{km}$) from the used SD station.

4.1.3.3 Atmospheric Cuts

The **Measured Mie model available cut** selects only events, where the aerosol content of the atmosphere is estimated by the CLF/XLF measurements (see chapter 3.2.4). The **Maximum VAOD cut** reject showers with a large Vertical Aerosol Optical Depth (VAOD) value at the reference height of 3 km above the ground. A large VAOD leads to larger systematic uncertainties on the reconstructed energy and therefore only showers with a VAOD < 0.1 are selected for the further analysis. The value is a trade-off between reducing the systematic uncertainties and keeping the event statistics high. The distribution of the VAOD before the cut is shown in figure 4.4. The **Cloud cut** uses the information of the cloud camera, the

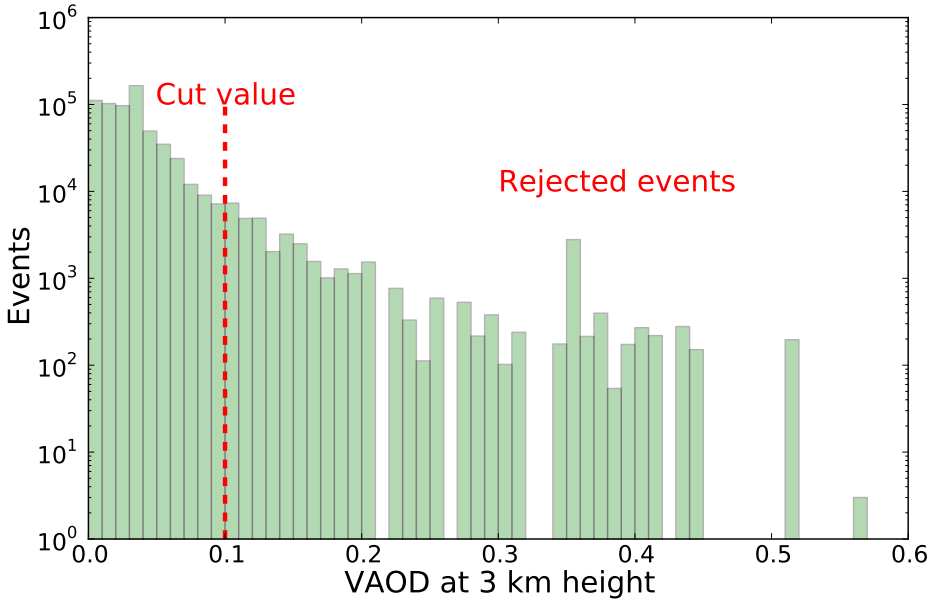

Figure 4.4: Measured vertical aerosol optical depth (VAOD) at the reference height of 3 km above the ground with the CLF/XLF(see chapter 3.2.4).

LIDAR stations and the GOES database to remove events with a too large cloud coverage in the field of view of the telescopes [41]. This is done because in clouds the fluorescence light of the shower is scattered and absorbed, which leads to wrong energy reconstruction of the events.

4.1.3.4 HECO Cuts

For the HECO reconstruction some special cuts need to be applied to study the chemical composition of air showers in an unbiased way. To have a valid hybrid geometry, at least one SD station has to have a Tot-trigger. At energies below 1 EeV, the single station Tot-trigger probability of simulated showers of the regular SD is dropping fast from 100% trigger efficiency and is dependent on the primary particle [115]. With the Infill array the trigger probability is much higher at lower energies, which is shown in figure 4.5. With this parametrization for the regular and the Infill array, it is possible to calculate the probability of a shower to trigger at least one SD station. The **Minimum brass probability cut** is introduced to have an unbiased data sample. For each event, the probability to trigger at least one surface detector station is calculated for the real set of active stations at the time of the event. This calculation is performed separately assuming proton and iron primaries. Only showers with a trigger probability above 90% are selected in this thesis. The trigger probabilities for the different primaries induce a selection bias on the measurement of the chemical composition. Therefore, the **Maximum brass probability difference H-Fe cut** is used to make sure that the difference between H and Fe trigger probability is lower than 5% to keep this bias small [116]. Due to the limited bandwidth of the SD readout communication, a veto logic was

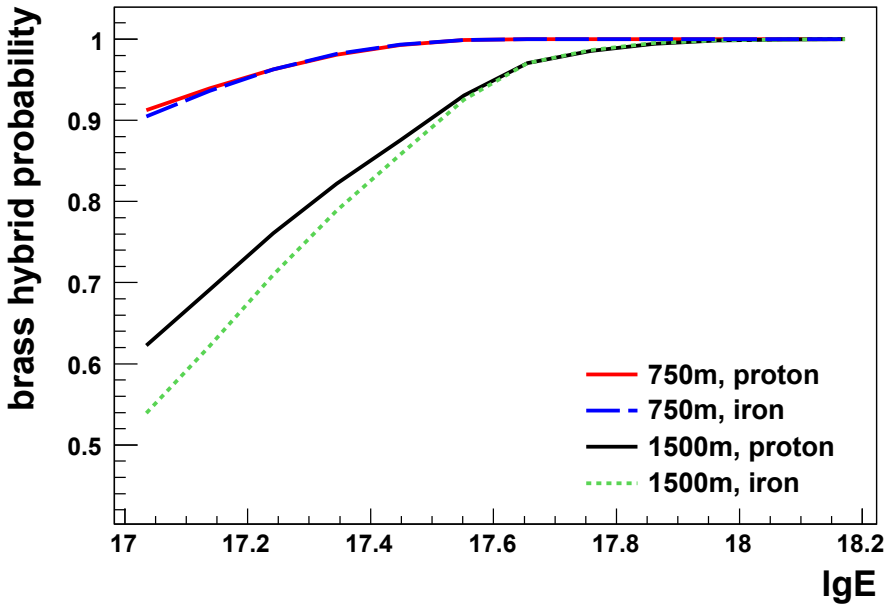

Figure 4.5: 1-Tot SD station trigger probability for the infill (750 m spacing) and the standard SD(1500 m spacing) array [116]. Zenith angles range from 0° to 60°.

Veto Co	Veto HEAT	HECO is blind to
Y	Y	No HECO hybrid
Y	N	Deep showers
N	Y	Shallow showers
N	N	Unbiased

Table 4.3: HECO T3-veto cases including possible selection biases [110].

installed at the FD telescopes to make sure that not too many T3 requests are send to the SD array. If a telescope is in veto state it would not send a request to SD and so the event will not be a hybrid event. In case of the virtual HECO telescope, there could be some cases, where the events can still be recorded. This cases are shown in table 4.3. However, these events are biased for deep or shallow showers, so in this thesis a **No T3 Veto cut** is applied to make sure only events are accepted when neither HEAT nor Coihueco is in the veto state.

4.1.3.5 Reconstruction Cuts

As HECO consists of separate telescope bays, showers can cross the field of view of several telescopes. The field of view is not overlapping for all shower geometries, which leads to gaps in the shower track. To select high quality data, a **Maximal gap in track cut** is applied and only showers where this gap is smaller than 30% of the complete shower track are used for the analysis. During the fit of the Gaisser-Hillas function in the Offline reconstruction, the error estimation of X_{max} fails sometimes and sets per default the error value equal to the

value of X_{max}. To reject these events, a cut on the **Successful X_{max}-error estimation** is used. Another cut on the reconstruction is the **Profile χ^2 cut**, which deals with the quality estimator χ^2 of the fit result. This cut rejects the outliers of the χ^2 distribution and with this low quality fit results. To identify these outliers the normalized χ^2 is used, which is given by

$$z = \frac{\chi^2 - Ndf}{\sqrt{2 \cdot Ndf}}, \tag{4.2}$$

where Ndf is the number of degree of freedom. According to the central limit theorem, the distribution of z is approximately a normal distribution. As the Gaisser-Hillas fit of the shower profiles is done using the maximum likelihood method, it is not centered at 0. Therefore an additional constant a_{shift} is added to equation 4.2 to shift the distribution to zero and to determine the final cut value. The constant shift on z used in this thesis is given as $a_{shift} = 1.454$ and only events with $z < 5$ are selected for the analysis. The normalized χ^2 distribution before the cut is shown in figure 4.6a, and in figure 4.6b after the cut. The shape of the χ^2 distribution after the cut is approximately a normal distribution.

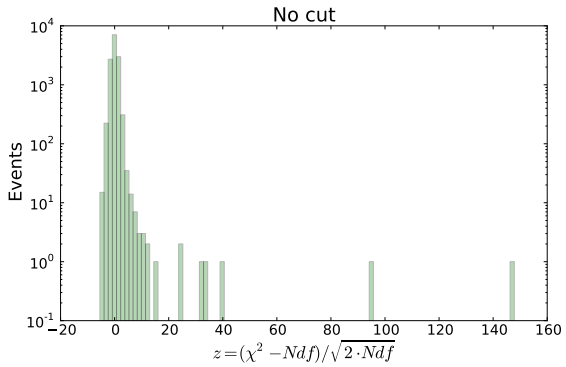

(a) Normalized χ^2 distribution before cut.

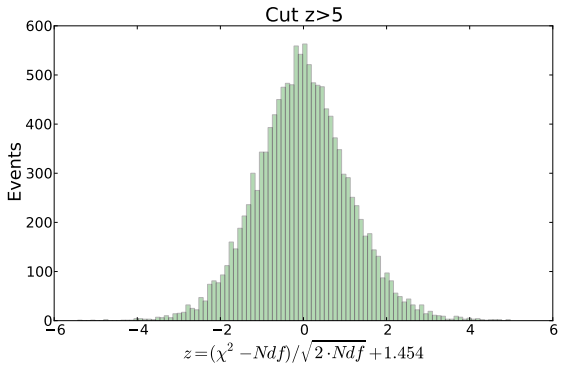

(b) Normalized χ^2 distribution after cut. The distribution is shifted by to peak at 0.

Figure 4.6: Reduced χ^2 distributions of the Gaisser-Hillas profile fit before and after the quality cut are shown.

4.1.3.6 Field of View Cuts

The field of view (FOV) is very important for the study of the slant depth of air showers. As this thesis is focused on X_{max} studies, it is important to have an unbiased measurement of this observable.

The geometrical FOV (FOV^{geo}) boundaries are given by the intersection of the projected shower detector plane with the borders of the telescope cameras [117]. For measuring X_{max}, not the FOV^{geo} but the expected FOV (FOV^{exp}) is more relevant, because even if X_{max} is in FOV^{geo}, it can not always be measured, e.g due to too large distance between shower and telescope. FOV^{exp} is the area/volume in which the shower track including X_{max} can be reconstructed with a good resolution. The expected FOV is calculated for every measured air shower during the reconstruction process. For this calculation, the observed shower profile is replaced by a Gaisser-Hillas profile using the geometry and the total energy of the reconstructed event [117]. With this parametrized profile the expected signal at the FD station is estimated by using the fluorescence yield and the knowledge of the light transmission through the atmosphere. This also predicts the number of triggered pixels. By using error propagation an expected uncertainty $\xi(X_{max})$ is calculated. By varying the X_{max} position of the artificial Gaisser-Hillas profile and propagating the uncertainties for these hypothetical showers, a depth range is determined in which X_{max} can be reconstructed with an uncertainty smaller than a certain value [117]. The longitudinal shower profile including the fitted Gaisser-Hillas profile and the calculated expected uncertainty ξ of X_{max} for a single FD event are shown in the figures 4.7a and 4.7b. In figure 4.8a the estimated uncertainty $\xi(X_{max})$ is shown against

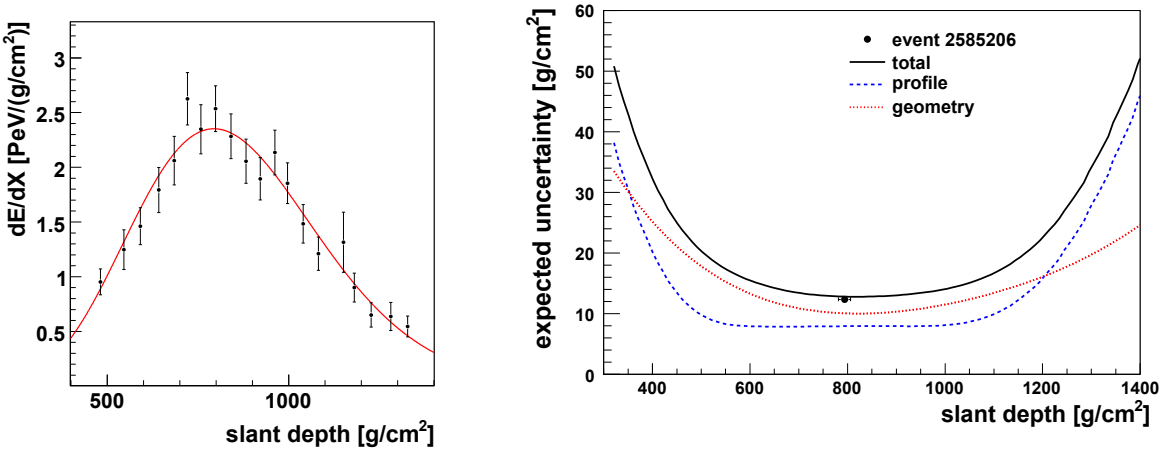

(a) Longitudinal energy deposit air shower profile including fitted Gaisser-Hillas profile in red.

(b) Calculated expected uncertainty $\xi(X_{max})$ derived from comparison with artificial Gaisser-Hillas shower profiles by using error propagation from geometry and profile reconstruction.

Figure 4.7: Measured FD event ($\log(E/\mathrm{eV}) = 18.2$) measured with Los Morados telescopes (id 2585206) [117].

the uncertainty $\sigma(X_{max})$ from the profile reconstruction. At low uncertainties there is a good correlation between expected and measured uncertainty on X_{max}, but around $40\,\mathrm{g/cm^2}$ the

ξ becomes systematically lower than the measured one. Therefore, in this thesis only events with a $\xi(X_{max}) \leq 40\,\mathrm{g/cm^2}$ are taken into account. Another important quality estimator is

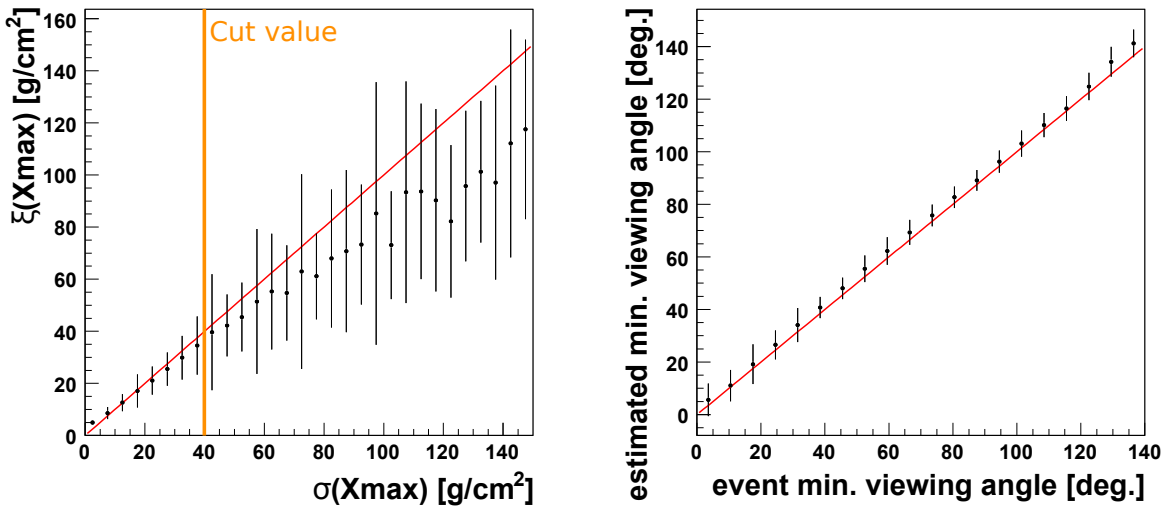

(a) Estimated uncertainty $\xi(X_{max})$ against profile reconstruction uncertainty $\sigma(X_{max})$. Yellow line represents the cut value used in this thesis.

(b) Estimated mva from Gaisser-Hillas profile shower prediction against the observed mva.

Figure 4.8: Correlation studies of estimated uncertainty $\xi(X_{max})$ and of the estimated minimum viewing angle mva. Error bar represents the RMS spread around the mean. Red lines illustrate the expectation for perfect correlation of the values [117].

the viewing angle between each pixel FOV direction and the shower axis. A schematic of the minimum viewing angle (mva) is showing in figure 4.9. For showers, where mva is small, the uncertainties of the geometric reconstruction become larger. Due to the synchronization time between FD/SD in the order of 100 ns, the geometry for short signal traces (less than 500 ns) is getting biased, which is shown in figure 4.10. As showers with a $mva \leq 20°$ point directly into the FD telescopes, these events are detected in a very short time frame and are therefore disregarded. Additionally, this also suppresses events with large Cherenkov fractions, which could also hamper the geometry reconstruction [117]. In figure 4.8b the good correlation between the estimated and the observed mva is shown.
This leads to the **Expected FOV cut**, which rejects events if X_{max} is not inside the FOV^{exp}. This FOV^{exp} is calculated for every shower by estimating $\xi(X_{max})$ and the mva. An example is shown in figure 4.11. Here the values of ξ and mva are shown together with the shower profile. The used cut values determine the accepted range for X_{max}, which is the slant depth from X_{low} to X_{up}. As shown in table 4.2, this is one of the strongest quality cut with an efficiency of 48.5%.
Another biasing effect is due to the different X_{max} distributions of different primaries, as light particles on average penetrate the atmosphere deeper than heavy particles and with a wider spread, which is shown in chapter 2.2. In figure 4.12 three examples of X_{max} distributions

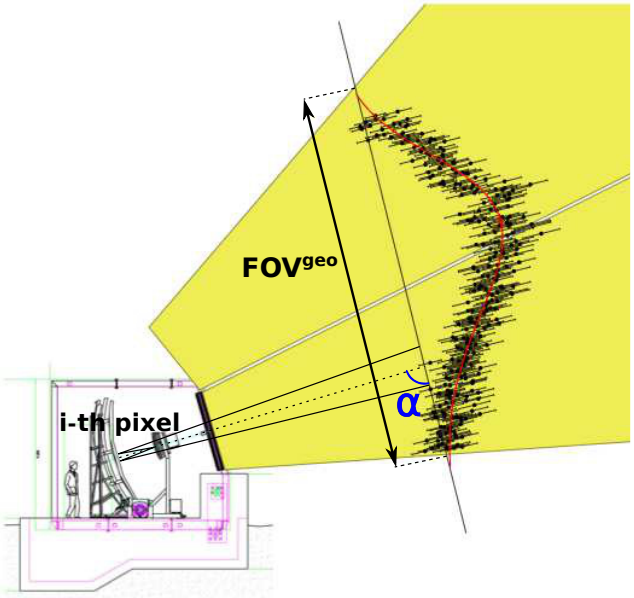

Figure 4.9: Example for the geometrical FOV (FOV^{geo}) boundaries of a HECO event. The minimum viewing angle (mva) for a single pixel FOV direction and the shower axis is shown as a blue α [110].

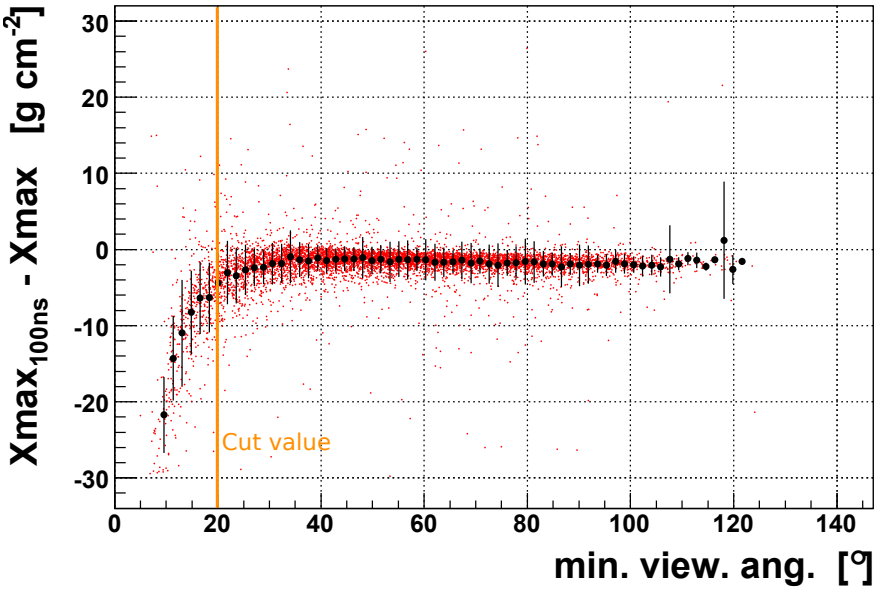

Figure 4.10: Average effect of the 100 ns SD/FD timing offset on the reconstruction of X_{max} as a function of the minimum viewing angle mva [117]. Yellow line represents the cut value used in this thesis. Events with a $mva \leq 20°$ are rejected.

are shown according to their shower tracks orientation. The distributions are distorted due to

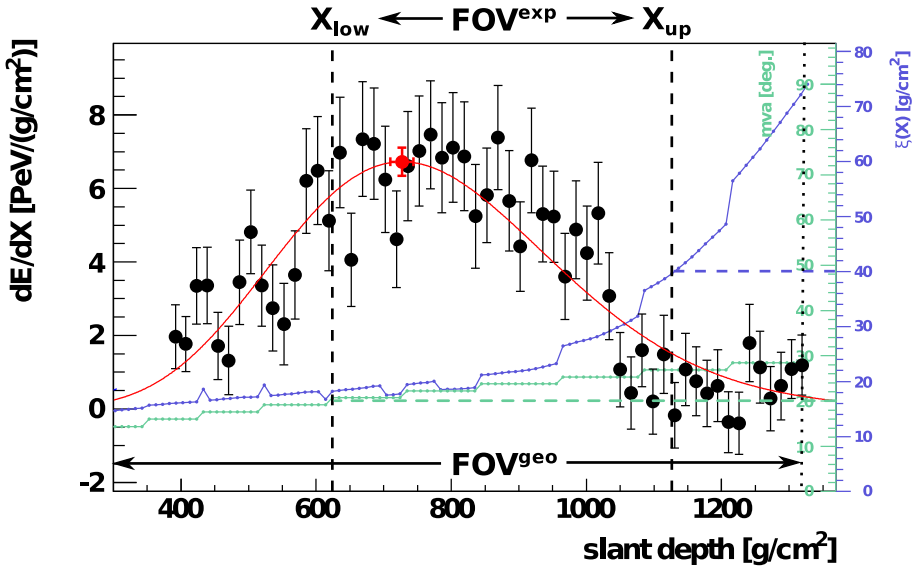

Figure 4.11: Energy deposit shower profile with geometricial (FOV^{geo}) and expected (FOV^{exp}) field of view [110]. $\xi(X)$ is represented in blue and mva is represented in green.

the truncation of the distribution on the rising flank and the tail. This could lead to wrong conclusions on the composition of the primary particles. Therefore, the **Fiducial FOV cut** is applied to the data to select only events with a field of view which is capable of detecting the whole distribution, without this truncation. As the true distribution is unknown, a data

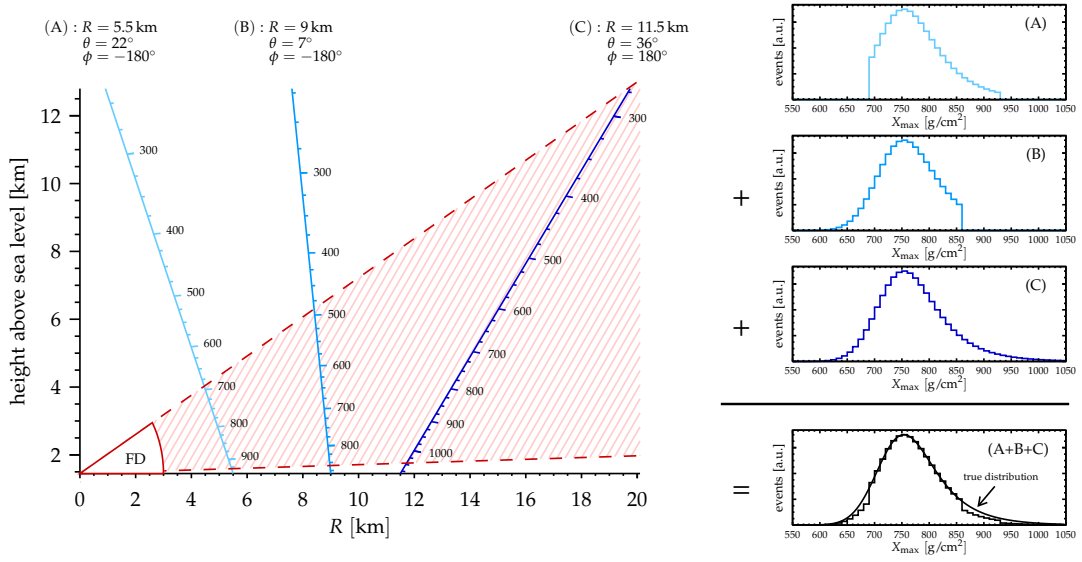

Figure 4.12: Illustration of the influence of the field of view (FOV) on the measurement of the X_{max} distributions for different shower geometries [41]. Distributions in the cases (A) and (B) are truncated by the FOV. (C) is the desirable distribution as the whole distribution inside the FOV. The stacked distribution of all three cases is also shown. The truncation due to the cases (A) and (B) is visible at the rising/falling flank of the distribution.

driven method is used to get the fiducial volume range X_{low}^{fid} and X_{up}^{fid} on the slant depth, where the deep and shallow showers are detected with equal probability. Therefore, the mean $\langle X_{max} \rangle$ of the X_{max} distribution is used. The method studies the changes of $\langle X_{max} \rangle$ as a function of the FOV boundaries. This is shown in figure 4.13 for air showers with energies $\log(E/\mathrm{eV}) = 17.6 - 17.7$. The results for the other energy bins are in the appendix A.1. Once the FOV starts to truncate the X_{max} distribution the $\langle X_{max} \rangle$ deviates from the asymptotically unbiased value.

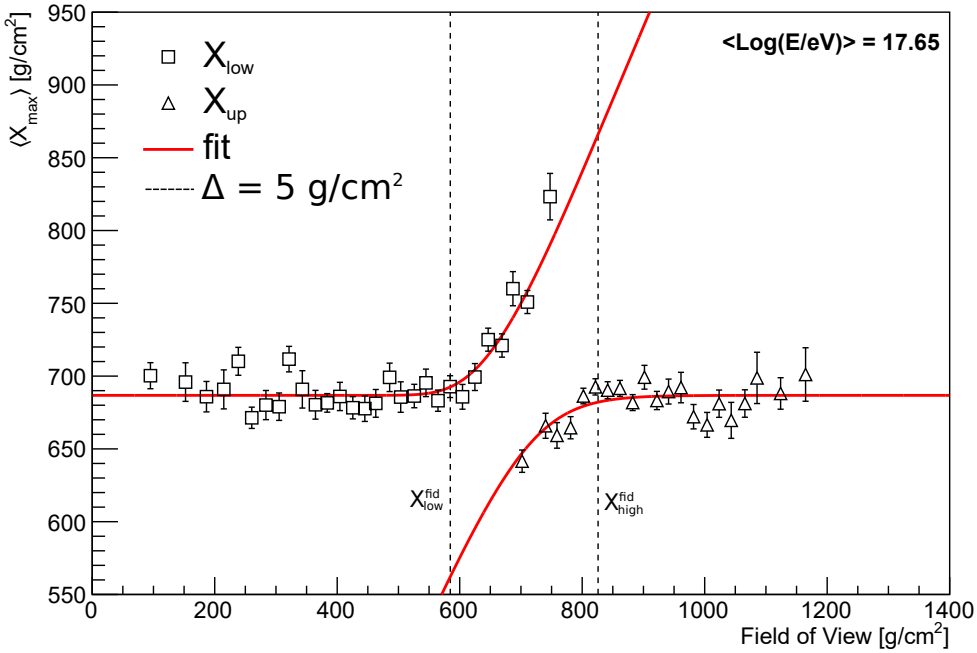

Figure 4.13: Iterative field of view analysis for HECO air shower data with reconstructed energies $\log(E/\mathrm{eV}) = 17.6 - 17.7$. The mean of the X_{max} distribution is shown as a function of the FOV boundaries. Solid red lines represent two simultaneous fits for the upper and lower boundary with the truncated mean formula in equation 4.4. The dashed line represent the fiducial FOV boundary X_{low}^{fid} and X_{up}^{fid} where the fitted function starts to deviate by more than $\Delta = 5\,\mathrm{g/cm^2}$ from the asymptotic values. $\langle X_{max} \rangle$ points shown here are calculated for X_{low} with X_{up}^{fid} and for X_{up} with X_{low}^{fid} as integration boundary.

To first order, the measured X_{max} distribution can be parametrized as a convolution of a Gaussian with an exponential distribution. For an infinite FOV the mean of the unbiased X_{max} distribution is given by

$$\langle X_{max}^{\infty} \rangle = \frac{\int_0^{\infty} x\, G \otimes E(x)\, dx}{\int_0^{\infty} G \otimes E(x)\, dx}. \tag{4.3}$$

By shrinking the integration limits to X_{low}, X_{up}, which are given by the FOV^{exp}, the truncated distribution mean is given by

$$\langle X_{max}^{trunc} \rangle = \mu_{trunc}(X_{low}, X_{up}) = \frac{\int_{X_{low}}^{X_{up}} x\, G \otimes E(x)\, dx}{\int_{X_{low}}^{X_{up}} G \otimes E(x)\, dx}. \tag{4.4}$$

When the FOV boundaries are far away from the edges of the X_{max} distributions, the $\langle X_{max}^{trunc} \rangle$ can be seen as asymptotically unbiased and therefore be used to estimate $\langle X_{max}^{trunc} \rangle \approx \langle X_{max}^{\infty} \rangle$. The fiducial FOV boundaries X_{low}^{fid} and X_{up}^{fid} are set to values, which fulfill the condition given by

$$|\langle X_{max}^{trunc} \rangle - \langle X_{max}^{\infty} \rangle| < \Delta, \tag{4.5}$$

where Δ is the maximal acceptable deviation and set to $5\,\mathrm{g/cm^2}$. This value is chosen to minimize systematic effects and to maximize the number of surviving events [117]. After this cut an event is only accepted if the expected FOV boundaries of the event fulfill the conditions $X_{low} < X_{low}^{fid}$ and $X_{up} > X_{up}^{fid}$. The fiducial FOV limits are fitted for the whole energy range of the HECO data set with a bin width of 0.1 in $\log(E/\mathrm{eV})$, which are shown in figure 4.14. The fitted values of $X_{low}^{fid}/X_{up}^{fid}$ are used to parametrize the boundaries of the fiducial FOV as

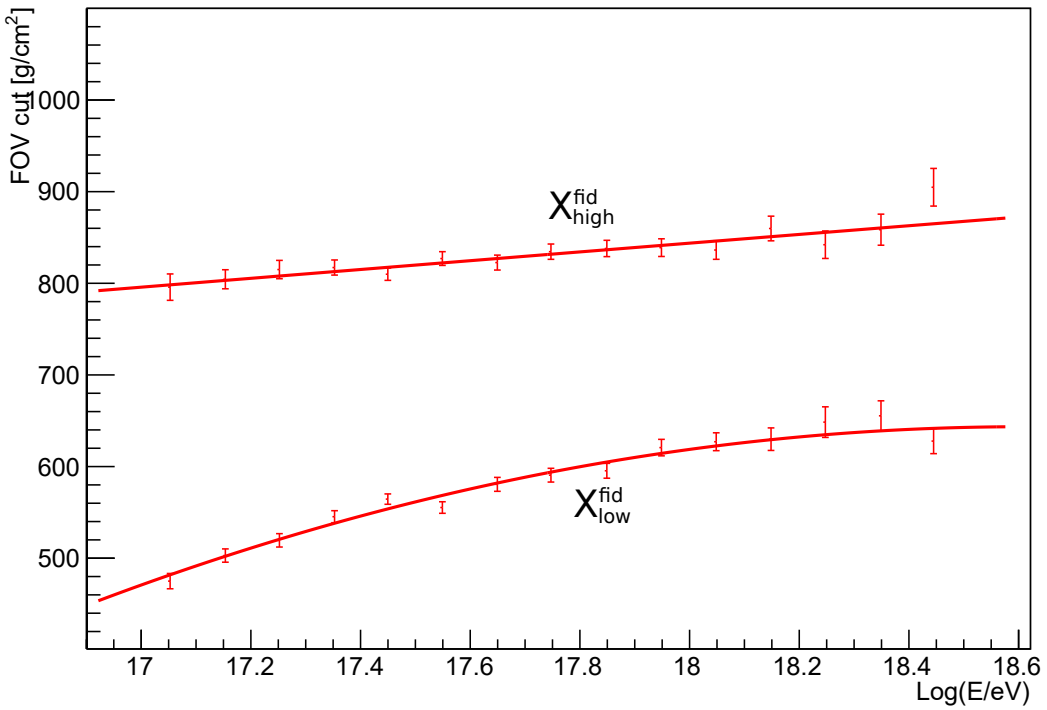

Figure 4.14: Fiducial field of view parametrization of X_{low}^{fid} and X_{up}^{fid} cut values as a function of energy.

a function of energy by

$$FOV_{up}^{fid}(\log E) = \begin{cases} (876.1 - 32.12 \cdot (\log(E/\mathrm{eV}) - 18.57)^2)\,\mathrm{g/cm^2} & \log(E/\mathrm{eV}) \leq 18.57 \\ 876.1\,\mathrm{g/cm^2} & \text{else} \end{cases} \tag{4.6}$$

and

$$FOV_{low}^{fid}(\log E) = \begin{cases} (627.7 - 99.67 \cdot (\log(E/\mathrm{eV}) - 18.31)^2)\,\mathrm{g/cm^2} & \log(E/\mathrm{eV}) \leq 18.31 \\ 627.7\,\mathrm{g/cm^2} & \text{else} \end{cases} . \tag{4.7}$$

The effect on the $\langle X_{max} \rangle$ of reconstructed air shower data as a function of energy is shown in figure 4.15. There the average shower depth $\langle X_{max} \rangle$ of the reconstructed HECO data set is shown before and after the fiducial FOV cut. Especially at low energies the truncation of the distribution through the FOV is visible. This quality cut was also used in the similar analysis

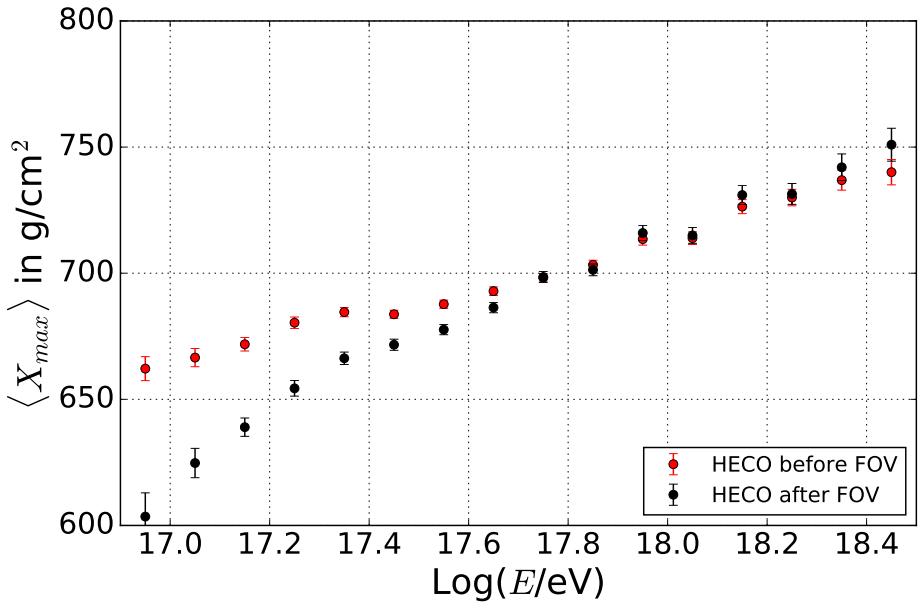

Figure 4.15: Average air shower maximum $\langle X_{max} \rangle$ before and after the application of the fiducial FOV cut. The effect of X_{max} distribution truncation is clearly visible.

of the maximum shower depth from the Pierre Auger Collaboration [41, 118, 119].

4.2 Extensive Air Shower Simulation

In this thesis mainly simulated air showers with the Monte-Carlo-tool Conex [120, 121] are used. Conex is a one-dimensional hybrid simulation scheme for UHECRs air showers. It is a combination of high-energy particle interaction, propagation and decay simulation with the numerical solution of cascade equations for the low-energy part of the air shower.
For the comparison of the data and to investigate the detector response extensive Monte Carlo (MC) studies of the virtual combined telescope HEAT and Coihueco (HECO) are performed. At the Pierre Auger Observatory, the information about the telescope calibration, atmospheric conditions and up-time fraction are daily stored in databases at the Malargüe Campus. These conditions are also taken into account in the MC production and are used to simulate an accurate detector state. This ansatz of a time dependent MC is called RealMC. The MC shower generation is divided into two different production samples:

To study the detector response and acceptance of HECO a uniform (flat) distributed X_{max}-RealMC was used. This was performed with Conex and $\overline{\text{Off}}\underline{\text{line}}$. The used parameters are given in table 4.4a.

Interaction model	Sibyll2.1
Primary	H,Fe
Energy $\log(E/\text{eV})$	16.9 - 18.6
Spectral index γ	2.5
Zenith (isotropic)	0 - 80°
Azimuth (flat)	0 - 360°
Uniform distributed X_{max}	300 - 1300 g/cm^2

(a) MC production parameters for detector acceptance determination.

Interaction model	Sibyll2.1
Primary	H,He,N,Fe
Energy $\log(E/\text{eV})$	16.9 - 18.6
Spectral index γ	2.5
Zenith (isotropic)	0 - 80 °
Azimuth (flat)	0 - 360°

(b) MC production parameters for reconstruction bias determination and End-to-End study.

Table 4.4: Summary of the extensive Conex simulations in the $\overline{\text{Off}}\underline{\text{line}}$ framework.

For reconstruction bias determination, detector validation and systematic studies, another RealMC was generated with Conex and $\overline{\text{Off}}\underline{\text{line}}$. The used parameters are shown in table 4.4b. Due to the fact that FD measures mainly the electromagnetic component of the air showers only the Sibyll2.1 interaction model is used, because Sibyll2.1 computes much faster than EPOS LHC or QgsjetII-04 showers and the simulation of the electromagnetic component is almost equally implemented in all used interaction models. For comparison purpose also a small set of Conex showers in the thesis energy range are simulated with EPOS LHC and QgsjetII-04.

4.3 Reconstruction of Simulated Air Showers

The selection procedure mentioned in chapter 4.1.3 ensures high quality minimal bias air shower data. To reduce, respectively correct, potential biases, a complete time dependent detector and environment simulation of the HECO telescopes is performed as described in chapter 4.2. The main studied effects are the reconstruction of the energy and the position of the shower maximum X_{max} for different energies and primaries. As the true composition of cosmic rays is unknown, exemplary primaries are used, namely hydrogen, helium, nitrogen and iron with the RealMC parameters shown in table 4.4b.

4.3.1 Shower Universality Profile Constraint

The analysis of the first momenta of previous HECO data sets in [110] and [111] has shown that the relative energy bias of reconstructed Monte Carlo showers is up to 20% for energies below 10^{18} eV. To reduce this large reconstruction bias, the profile reconstruction algorithm is changed in this thesis. At lower energies, the number of photons arriving at the telescopes aperture is low and therefore the measured track lengths of HECO events are shorter below 10^{18}eV. This is shown in figure 4.16. Short shower profiles have large reconstruction uncertainties. To improve the reconstruction, the hypothesis of air shower universality is used. To illustrate the

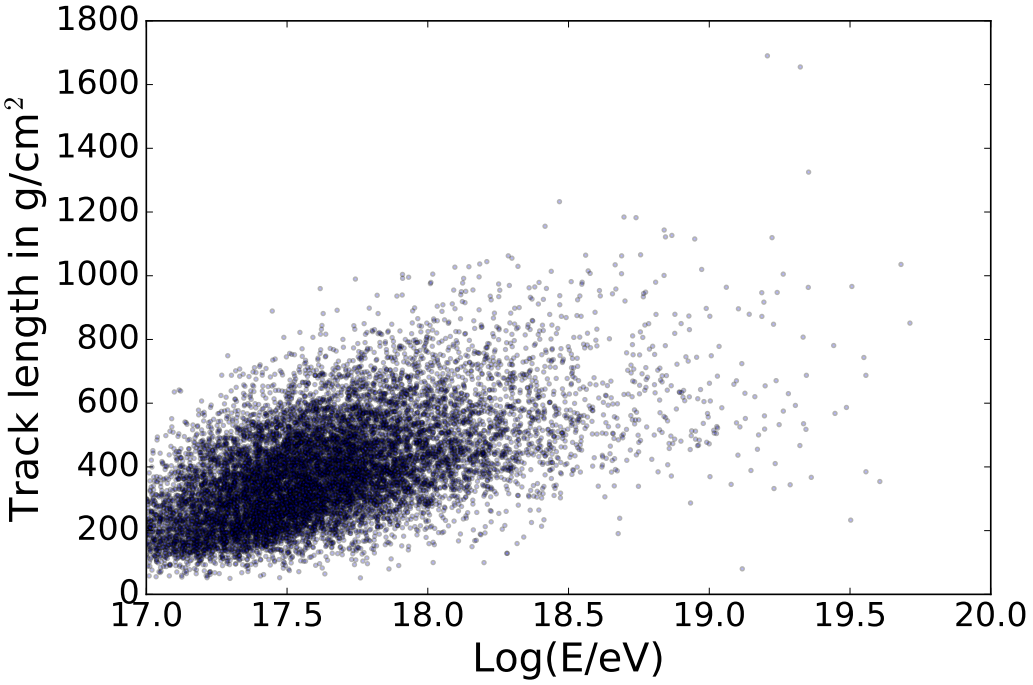

Figure 4.16: Measured track length of reconstructed air shower profiles of the HECO data set as a function of energy.

shower universality, the simulated energy deposit shower profiles for 100 H and 100 Fe showers in the same energy range of $\log(E/\text{eV}) = 16.9 - 17.0$ are produced. The energy deposit profiles

of the showers are shown in figure 4.17. These profiles show the expected shower to shower fluctuations. To show the universality, the profiles are shifted to have the maximum at 0 and the peak values are normalized to 1, which is shown in figure 4.18. This shows that all profiles

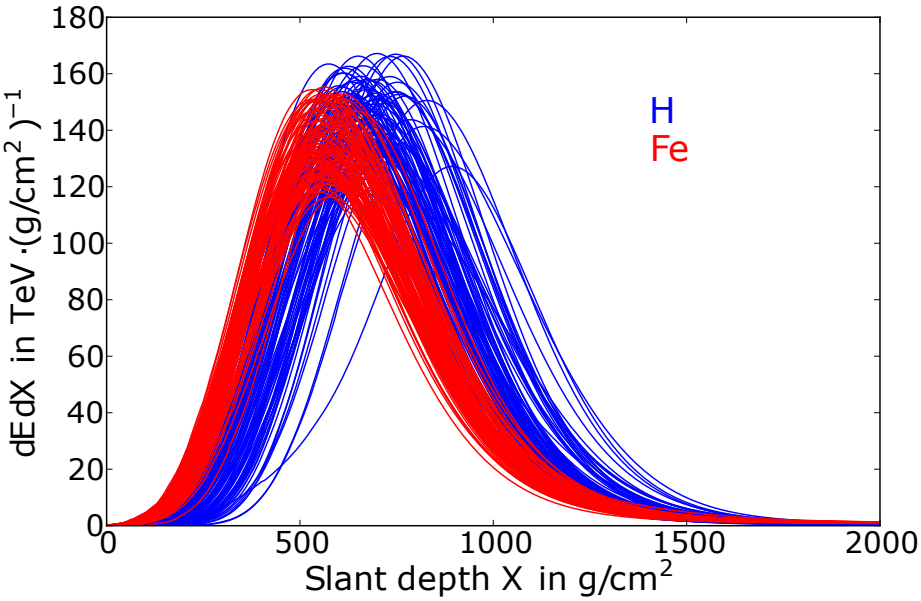

Figure 4.17: Energy deposit shower profiles from Conex simulations with Sibyll2.1 for $\log(E/\text{eV}) = 16.9 - 17.0$. H showers are shown in blue, Fe showers are shown in red.

have nearly the same shape and width. Considering the air shower universality [122, 123, 124] in the reconstruction process, the calorimetric energy given by equation 3.11 can written as

$$E_{cal} = \left.\frac{dE}{dX}\right|_{max} \lambda \left(\frac{e}{\xi}\right)^{\xi} \Gamma(\xi + 1), \tag{4.8}$$

with $\xi = \frac{X_{max} - X_0}{\lambda}$. Therefore, it can be concluded that there is a universality factor k defined by

$$k = E_{cal} \cdot \left(\left.\frac{dE}{dX}\right|_{max}\right)^{-1} \approx const. \tag{4.9}$$

The calculated k values vs. X_{max} from the ICRC15 HECO data set [111] of low energy showers are shown in figure 4.19 for all track lengths in blue and for very long track lengths ($\geq 600\text{g/cm}^2$) in red. The plot shows that only for the long track lengths, k is nearly constant and that there is a constant slope for all selected events.
Therefore, an additional constraint of the Gaisser-Hillas fit is introduced in the profile reconstruction. With this constraint of k, the shower profiles are kept in a physical reasonable range for all showers, including short track length profiles. In figure 4.20 the calculated universality k values of the different interaction models are shown as a function of the calorimetric energy derived for H and Fe Conex simulations. The post-LHC interaction models EPOS LHC and QgsjetII-04 have very similar k values for the H and Fe showers, but Sibyl2.1 has very different

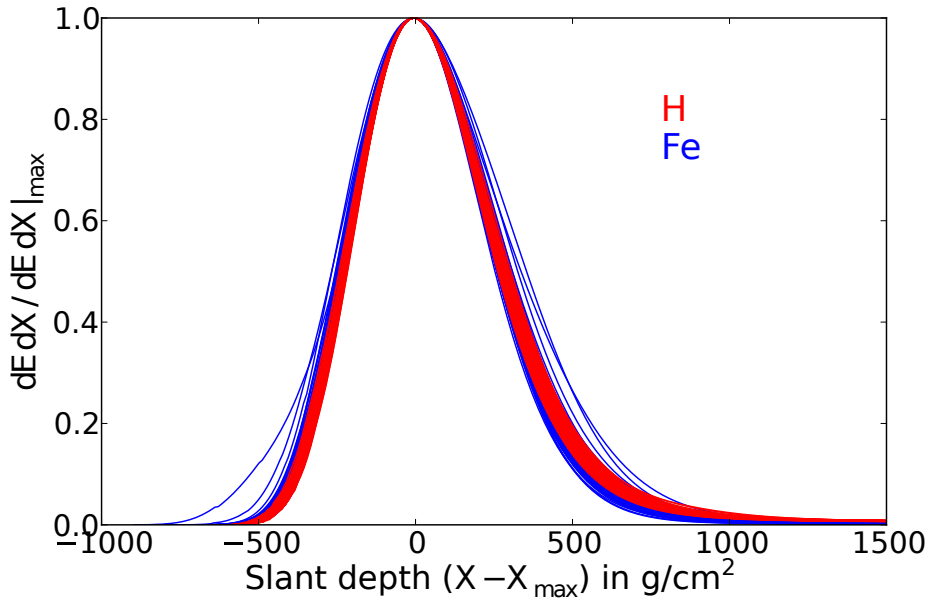

Figure 4.18: Shifted energy deposit shower profiles from Conex simulations with Sibyll2.1 for $\log(E/\text{eV}) = 16.9 - 17.0$. Shower maximum is set to 0 and the peak values are normalized to 1. H showers are shown in blue, Fe showers are shown in red.

k values. As non of the interaction models can be preferred about the others, these differences are taken into account in the chosen constraint parameters. From the Conex simulations of Sibyll2.1 and post-LHC interaction models EPOS LHC and QgsjetII-04, it is derived, that the k-constraint values for a mixed 50%:50% H:Fe chemical composition can be divided into two different parameter sets, which are given by

$$k^c_{LHC} = (415.9 + 9.24 \cdot \log(E_{cal}/\text{eV}))\,\text{g/cm}^2, \quad (4.10)$$

$$k^c_{Sib} = (397.7 + 9.59 \cdot \log(E_{cal}/\text{eV}))\,\text{g/cm}^2, \quad (4.11)$$

$$\sigma_{k^c} = 14.0\,\text{g/cm}^2. \quad (4.12)$$

Due to their similar results EPOS LHC and QgsjetII-04 are combined to a single constraint value set namely $(k^c_{LHC}, \sigma_{k^c})$. The Siyll2.1 values $(k^c_{Sib}, \sigma_{k^c})$ are used standalone. The mixed composition is chosen to make no a priori assumption on the chemical composition during the shower reconstruction. As shown in chapter 4.1, in this thesis both constraint value sets are used to analyze the data with nearly the same number of events.

The minimization function of the Gaisser-Hillas function in equation 3.10 is changed to

$$\chi^2 = \chi^2(dE/dX_{max}, X_{max}, \lambda, X_0) + \left(\frac{\lambda - \lambda^c}{\sigma_{\lambda^c}}\right)^2 + \left(\frac{X_0 - X_0^c}{\sigma_{X_0^c}}\right)^2 + \left(\frac{k - k^c}{\sigma_{k^c}}\right)^2, \quad (4.13)$$

with the constraining values X_0^c, $\sigma_{X_0^c}$,λ^c and σ_{λ^c}, which are given in table 4.5. The number of reconstructed events with this constraint is comparable to the reconstructed events without

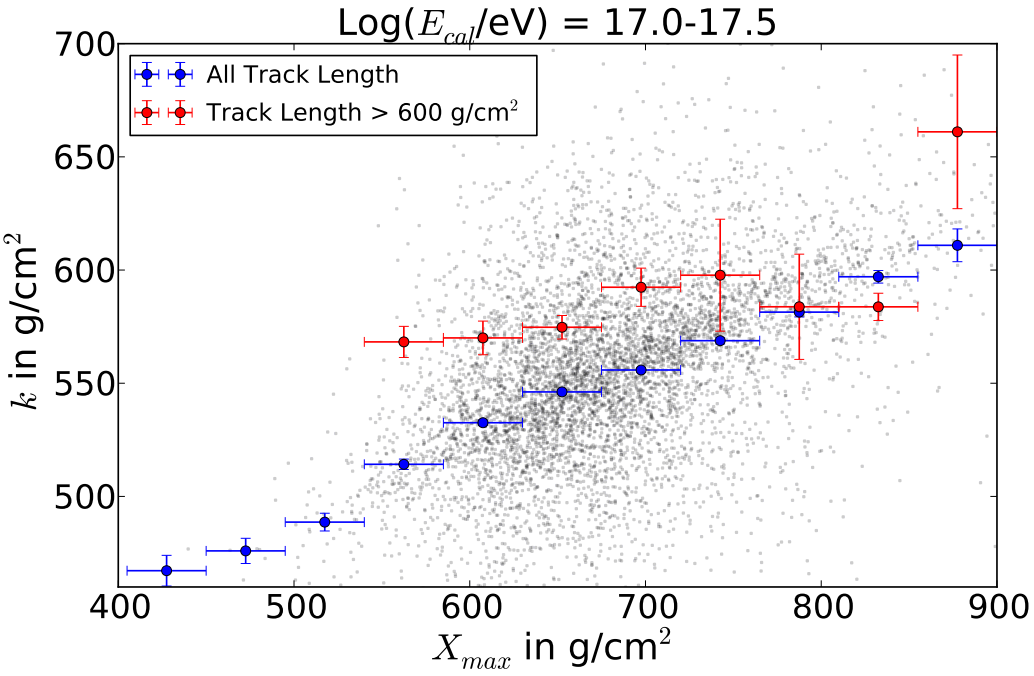

Figure 4.19: Universality k vs. reconstructed X_{max} for energies $\log(E/\text{eV}) = 17.0 - 17.5$ from the ICRC 2015 data set [111]. Blue markers represent the mean k of all selected events. Red markers represent the mean k of events with track lengths $> 600\,\text{g/cm}^2$.

	λ^c	σ_{λ^c}	X_0	$\sigma_{X_0^c}$
Values in g/cm^2	61	13	-121	172

Table 4.5: Standard constraint values for the Gaisser-Hillas fit in equation 4.13 used in Offline.

the universality constraint. In the next chapters, the effect of this k constraint on the energy bias, the X_{max} bias and X_{max} resolution is shown, which is derived from RealMC.

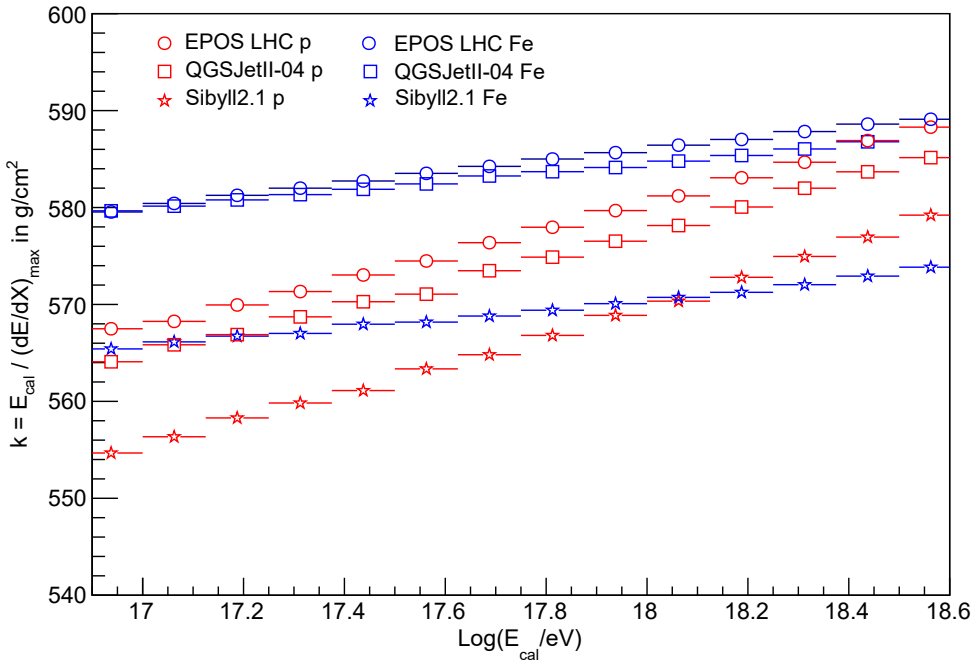

Figure 4.20: Universality k against calorimetric energy from Conex simulation for different primaries and interaction models.

4.3.2 Energy Bias and Resolution

The relative mean energy bias between reconstructed (rec) and generated (gen) calorimetric energy E_{cal} is given by

$$\langle E_{bias} \rangle = \left\langle \frac{E_{cal}^{rec} - E_{cal}^{gen}}{E_{cal}^{rec}} \right\rangle . \tag{4.14}$$

As already described in the previous chapter, the additional constraint of the universality k is applied during the simulation in equation 4.13. An additional improvement of the relative energy bias is achieved, due to the application of the 'lateral width correction' [125] on the simulated data, with an optical halo parametrization designed for FD simulations [124]. The 'lateral width correction' is needed during the reconstruction of the FD data, due to some not simulated optical issues of the telescopes. Due to the implementation of the correction also on simulated data, the relative energy bias in simulation is roughly reduced by $\sim 1\%$.
The relative energy bias has a small dependency on the chosen simulated primary, but to make no assumption on the chemical composition of the cosmic rays the RealMC described in table 4.4b is used for the relative energy bias determination. In figure 4.21, the relative energy bias for the standard HECO Monte Carlo reconstruction used at the ICRC 2015 data set and the new k-constraint reconstruction used in this thesis are shown as a function of E_{cal}. The energy bias is reduced relatively by more than 50%. In figure 4.22, the relative energy bias as a function of the generated X_{max} is shown and the previous strong dependence of the energy bias on the shower maximum X_{max} is gone.

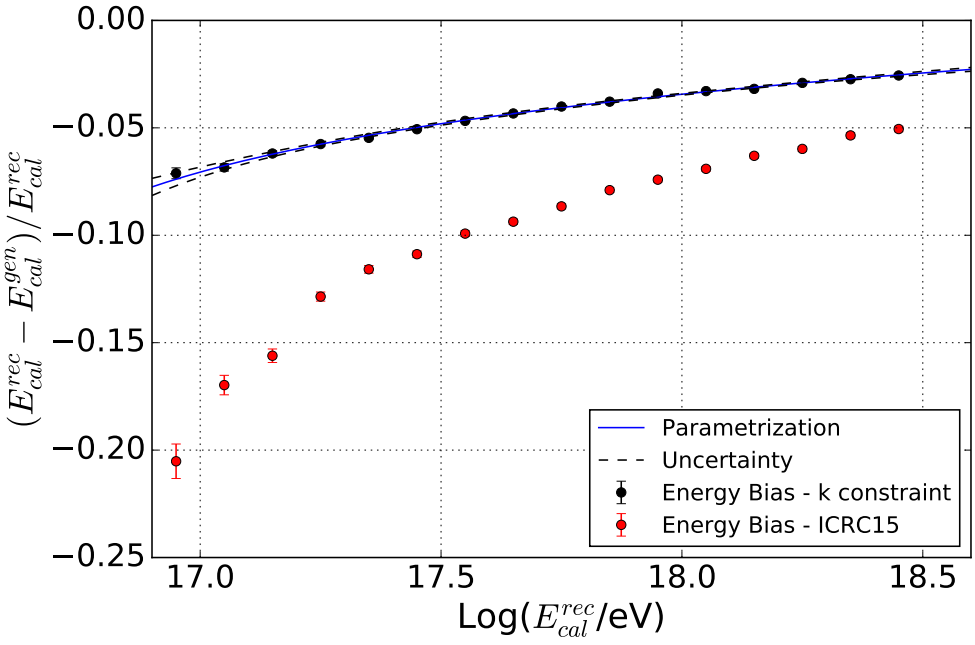

Figure 4.21: Relative energy bias as a function of $\log(E_{cal}^{rec}/\mathrm{eV})$ derived from RealMC studies with a parametrization including the fitting uncertainties and compared to ICRC15 RealMC data set.

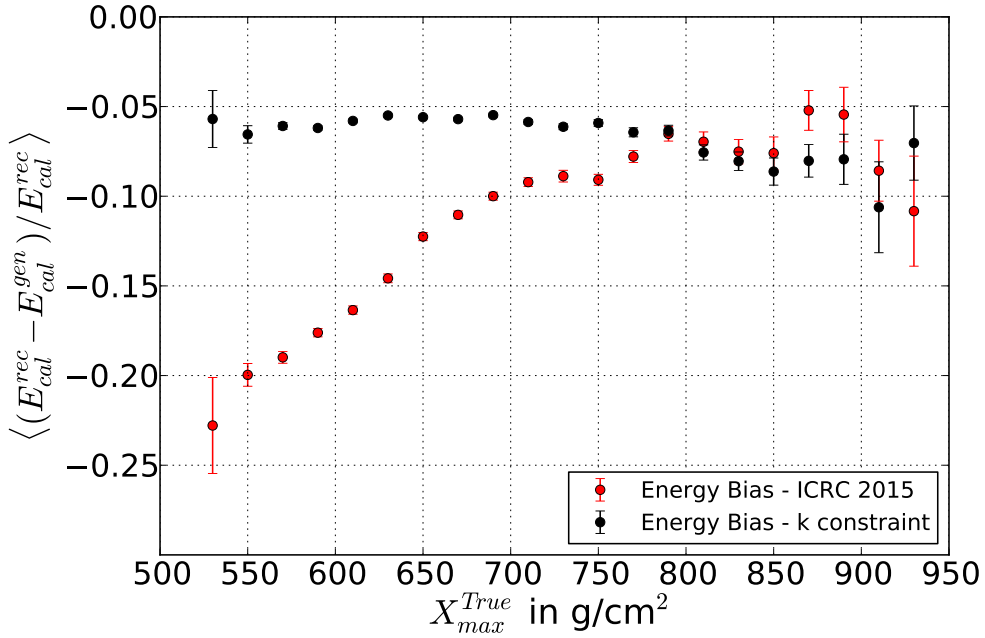

Figure 4.22: Relative energy bias against the generated X_{max} for air showers with energies $\log(E/\text{eV}) \leq 17.5$ derived from RealMC studies and compared to ICRC15 RealMC data set.

The energy resolution is shown in figure 4.23 and the new profile reconstruction shows also a strong improvement. As the observed energy is on average reconstructed lower than the

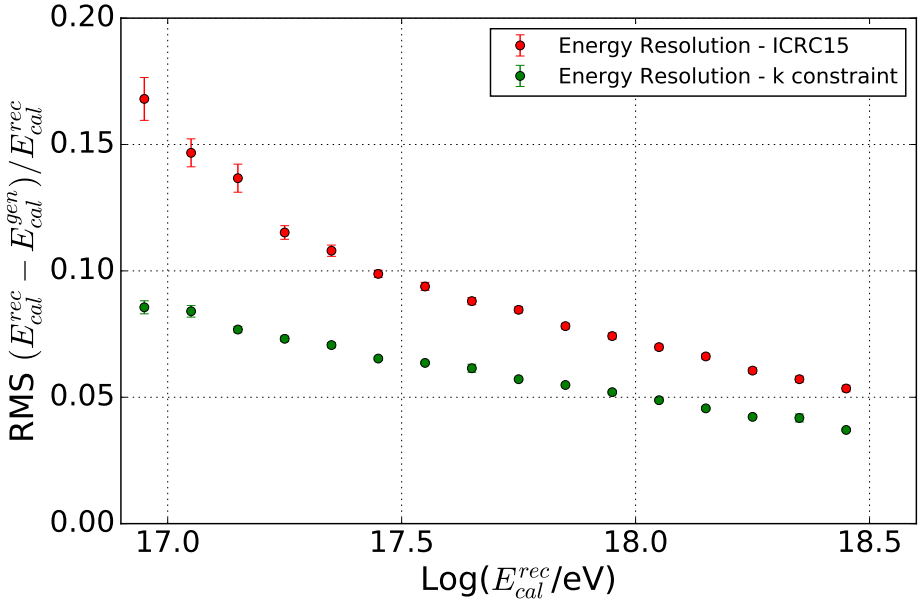

Figure 4.23: Energy resolution of HECO as a function of $\log(E_{cal}^{rec}/\text{eV})$ derived from RealMC studies and compared to ICRC15 RealMC data set.

true energy, an event migration to the lower energy bins occurs. To correct for this effect a parametrization of the energy bias is used. The parametrization is given by the empirical function

$$\langle E_{bias}(\log E_{cal}^{rec})\rangle = -0.05 + 0.08 \cdot \log(\log(E_{cal}^{rec}/\mathrm{eV}) - 16.43). \tag{4.15}$$

To convert the E_{cal}^{rec} into the total energy E^{true} the following relation is used

$$E^{true} = E_{cal}^{rec} \cdot f_{invis} \cdot f_{bias}(E_{cal}^{rec}), \tag{4.16}$$

where the correction factor is given by

$$f_{bias}(E_{cal}^{rec}) = 1 - \langle E_{bias}(\log E_{cal}^{rec})\rangle. \tag{4.17}$$

This correction of the reconstructed energy is used in the following chapters.

4.3.3 X_{max} Bias and Detector Resolution

To describe the detector resolution and potential Monte Carlo biases, the air shower maximum X_{max} is studied by simulation and reconstruction. The X_{max} bias and detector resolution have a small dependency on the chosen simulated primary, but to make no assumption on the chemical composition of the cosmic rays, the RealMC described in table 4.4b is used in this study. The distribution of the differences between the reconstructed and the generated X_{max} is investigated. This difference is given by

$$X_{bias} = X_{max}^{rec} - X_{max}^{gen}. \tag{4.18}$$

As shown in figure 4.24, the mean reconstruction bias follows a linear parametrization, which is given by

$$\langle X_{bias} \rangle (E_{cal}) = (-1.62 - 0.46 \cdot (\log(E_{cal}/\mathrm{eV}) - 16.03))\,\mathrm{g/cm^2}. \tag{4.19}$$

Besides this mean bias also the detector resolution $\sigma_{Det}(E_{cal})$ is given by the spread of the

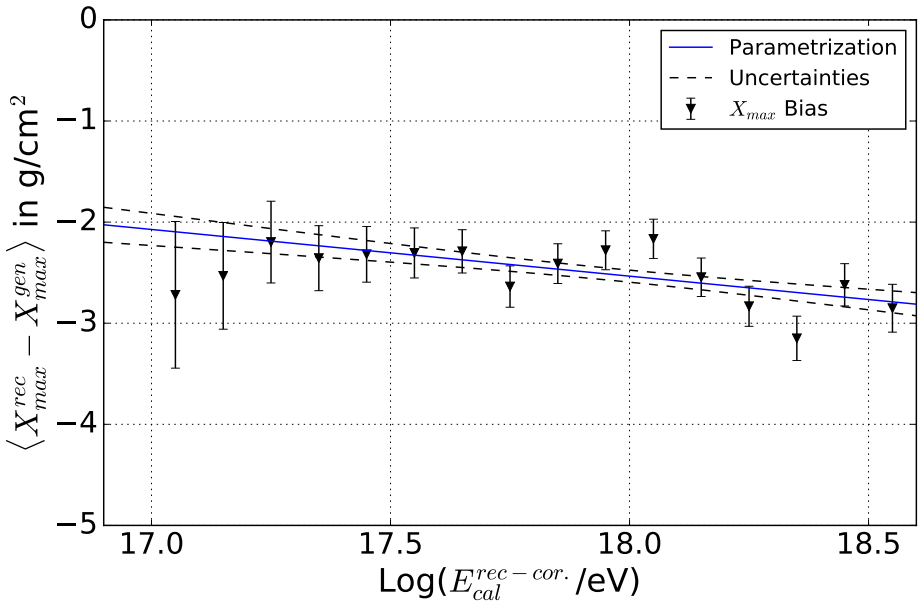

Figure 4.24: Reconstruction bias of X_{max} as a function of $\log(E_{cal}^{rec-cor.}/eV)$ derived from RealMC studies with a parametrization including the fitting uncertainties.

distributions per energy bin derived from equation 4.18. This detector resolution is independent of the intrinsic shower to shower fluctuations of extensive air showers and can be used to correct the measured spread of the final data X_{max} distributions.
The detector resolution is shown in figure 4.25, together with an energy dependent parametrization given by the empirical function

$$\sigma_{Det}(E_{cal}) = (4.93 + 3.82 \cdot (\log(E_{cal}/\mathrm{eV}) - 19.79)^2)\,\mathrm{g/cm^2}. \tag{4.20}$$

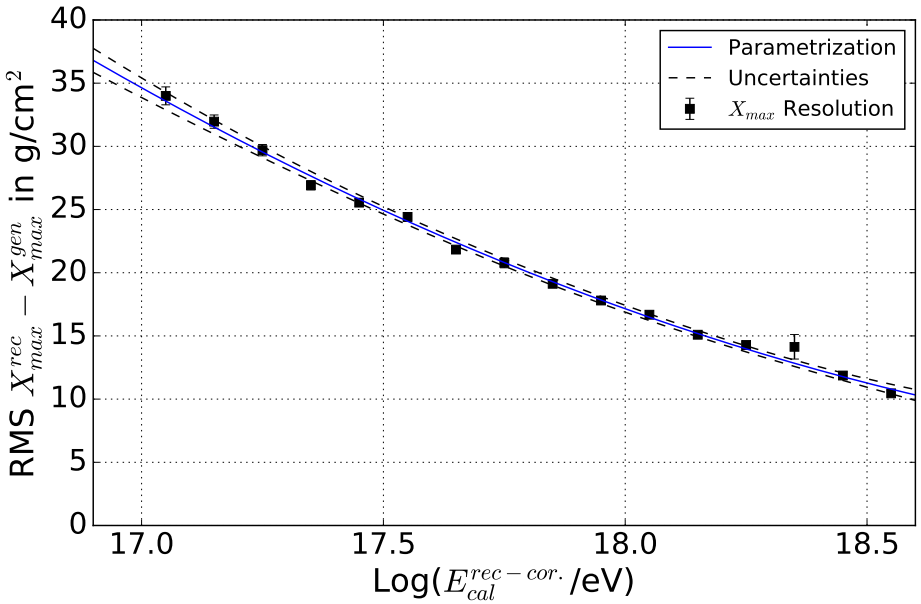

Figure 4.25: Detector resolution of X_{max} as a function of $\log(E_{cal}^{rec-cor.}/eV)$ derived from RealMC studies with a parametrization including the fitting uncertainties.

The measured air shower maximum X_{max} is corrected for $\langle X_{bias} \rangle$ in the following chapters, if not specified otherwise.

4.3.4 Detector X_{max}-Acceptance

Even in the case of the fiducial FOV quality selection, the probability to detect and select an air shower is not the same for all values of X_{max} [41]. To study the detector acceptance of HECO, the flat X_{max} RealMC described in table 4.4a is used. The simulated showers are selected with the same selection criteria as the data. The acceptance as a function of X_{max} is calculated from the ratio of selected to generated events. To first approximation, the shape of the longitudinal shower profile is universal and therefore not dependent on the primary particle or the details of the first interaction [126]. Therefore, the acceptance is in first order only depending on the calorimetric energy E_{cal} and X_{max}.
The relative X_{max}-acceptance of the FD telescopes can be parametrized empirically by an exponential rising flank, a constant central region and an exponential falling flank,

$$\epsilon_{rel}(X_{max}) = \begin{cases} e^{+\frac{X_{max}-X_1}{\lambda_1}} & X_{max} \leq X_1, \\ 1 & X_1 < X_{max} \leq X_2, \\ e^{-\frac{X_{max}-X_2}{\lambda_2}} & X_{max} > X_2, \end{cases} \tag{4.21}$$

with the fit parameters $X_1, \lambda_1, X_2, \lambda_2$. An example of this parametrization for the energy bin $\log(E/\text{eV}) = 17.7 - 17.8$ is shown in figure 4.26. The results for the other energy bins are shown in the appendix A.2.1. As this fit is very fragile and the flat Monte Carlo statistics are not sufficient enough, the fit was simplified by fixing the X_1 and X_2 values to the fiducial FOV cut values given in the equations 4.6 and 4.7, which leads in first order to reasonable results. This method works reasonably well for energies above $\log(E/\text{eV}) = 17.4$. Each fit parameter is parametrized by a 2 degree polynomial as a function of energy given by

$$p_i(\log(E/\text{EeV})) = p_{i0} + p_{i1} \cdot \log(E/\text{EeV}) + p_{i2} \cdot \log(E/\text{EeV})^2 \text{ for } i = \lambda_1, \lambda_2, \tag{4.22}$$

where the parameters p_{i0}, p_{i1} and p_{i2} are given in table 4.6. These parametrizations are shown

i	p_{i0} in g/cm^2	p_{i1} in g/cm^2	p_{i2} in g/cm^2
λ_1	381.46	225.10	131.48
λ_2	129.73	91.52	-7.16

X_1	given in eq. 4.7
X_2	given in eq. 4.6

Table 4.6: Parametrization constants for X_{max} acceptance derived from flat X_{max} RealMC.

for X_1 and X_2 in figure 4.27 and for λ_1 and λ_2 in figure 4.28. As told before, the X_1 and X_2 values are fixed and have therefore no error-bars, but these values can be released and fitted with an increased MC statistics in future analyses.
However, in the lowest studied energy bins, the acceptances have no flat plateau region. In this region the virtual HECO is dominated by HEAT events and possibly the differences in the sensitivity between HEAT and Coihueco telescopes become visible. This feature is still under investigation but the fitted acceptances with equation 4.21 do not describe the

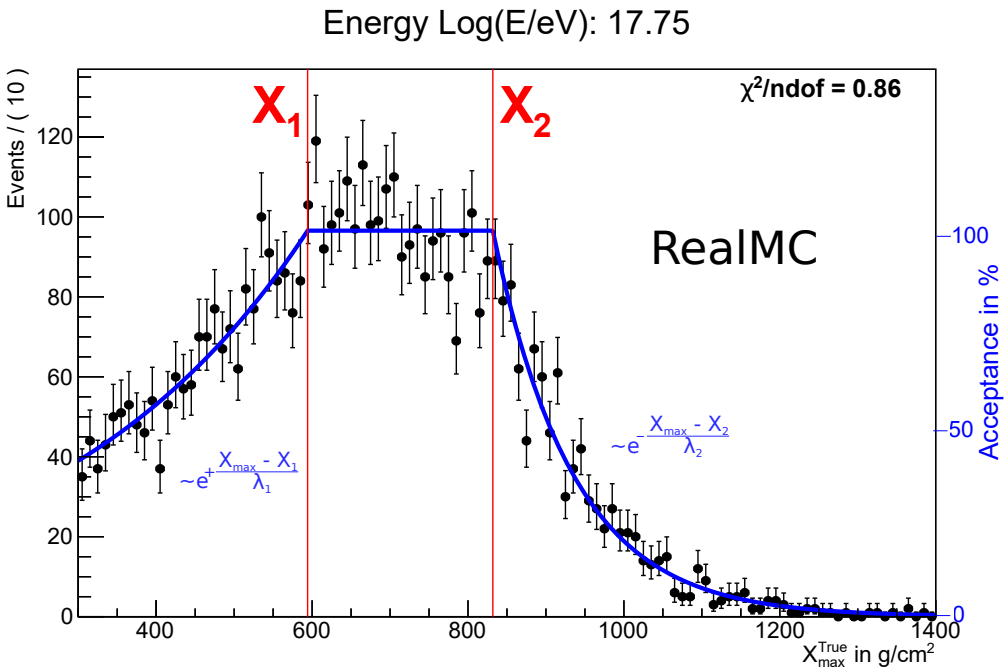

Figure 4.26: X_{max} distribution with acceptance function fit derived from flat X_{max} RealMC including fiducial FOV boundaries.

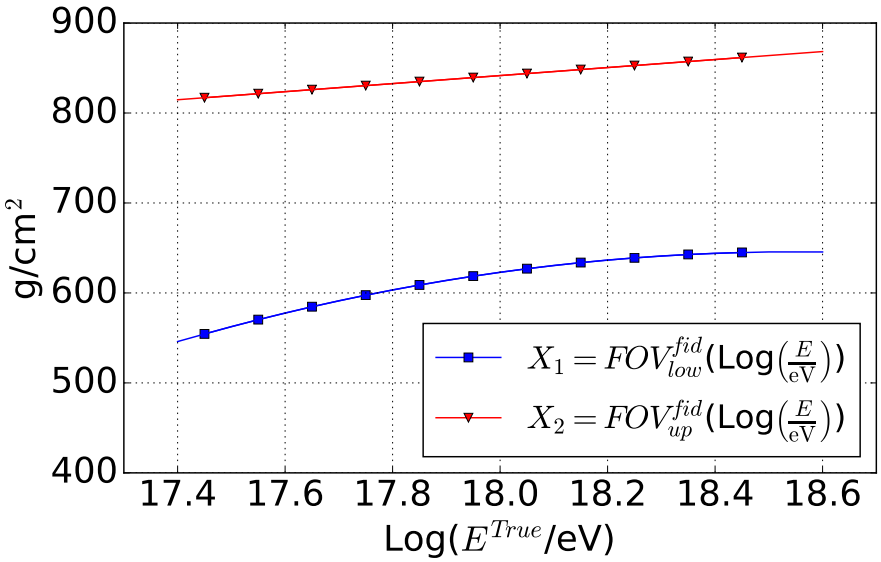

Figure 4.27: Acceptance range parametrization of X_1 and X_2 derived from flat X_{max} RealMC. In this case the values are fixed by the fiducial FOV boundaries.

Monte-Carlo data very well, which is shown in figure 4.29. As the knowledge of the correct acceptance is needed to weight the measured X_{max} values, a new method is used to describe

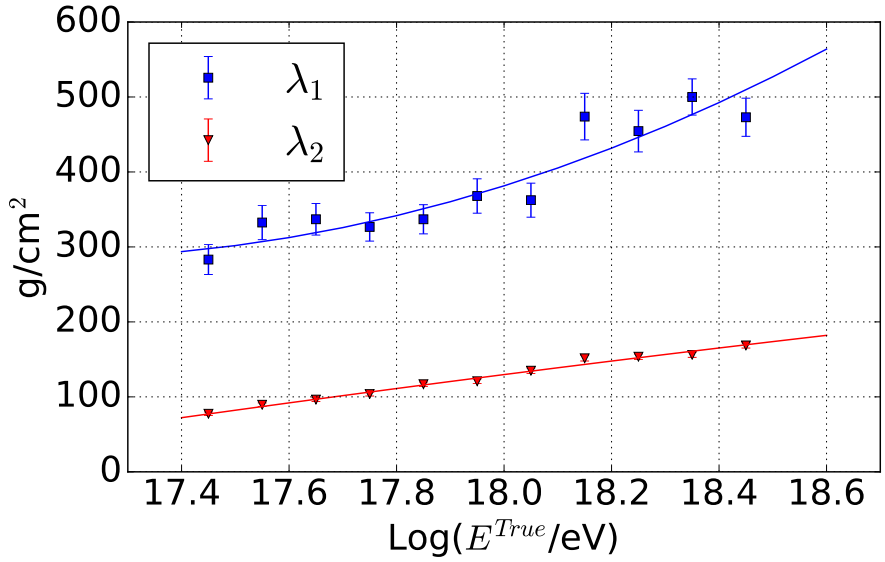

Figure 4.28: Acceptance parametrization fit of λ_1 and λ_2 derived from flat X_{max} RealMC.

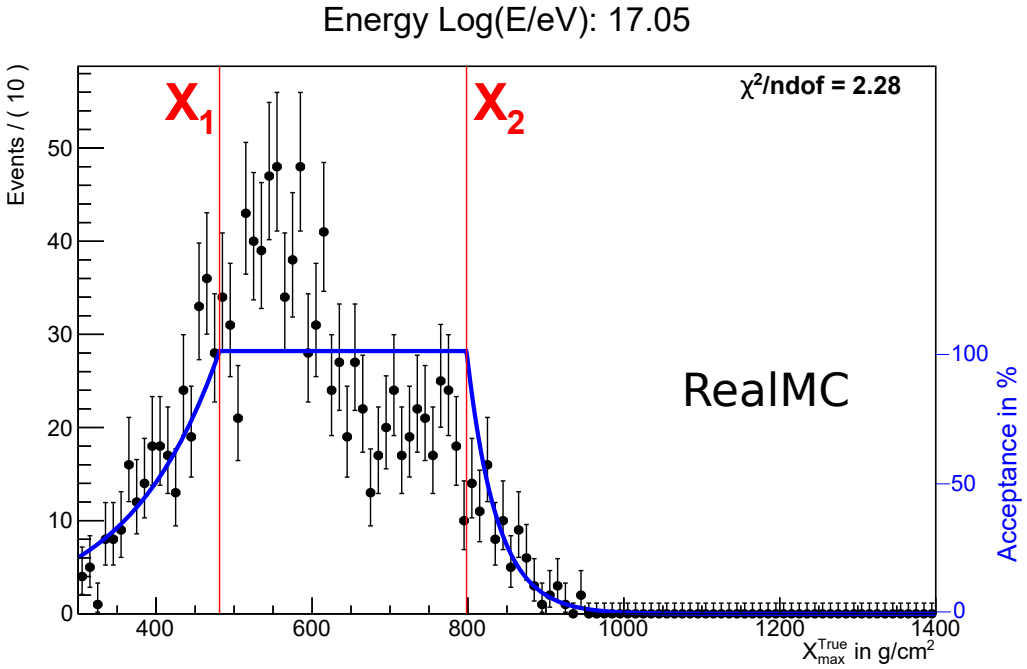

Figure 4.29: X_{max} distribution with wrong acceptance function fit derived from flat X_{max} RealMC including fiducial FOV boundaries.

the acceptance in the lowest energy bins. For this ansatz the kernel estimation model [127] of the RooFit [128] package is used. The selected X_{max} values are used to create an empirical probability distribution function (p.d.f.). Each value of the unbinned data set is represented

by a Gaussian p.d.f. with a certain width. All p.d.f. are then summed up to a superposition model by an adaptive kernel function depending on the local event density to get a smooth p.d.f. as acceptance function. The result for the lowest energy bin is shown in figure 4.30. This

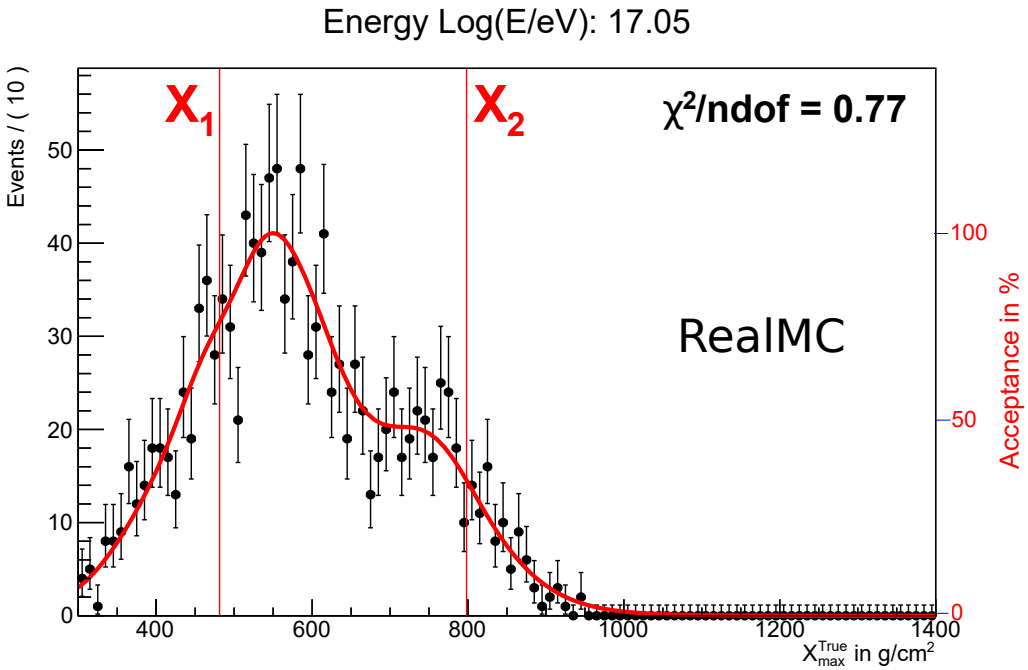

Figure 4.30: X_{max} distribution with kernel [127] acceptance function fit derived from flat X_{max} RealMC including fiducial FOV boundaries.

function shows a much better description of the detector acceptance than the regular acceptance function. The results for the other energy bins are shown in the appendix A.2.2. As this kernel model is not describable by a parametrization function of energy the fitted normalized p.d.f. is used as a template in every bin to calculated each event's relative acceptance $\epsilon_{rel}(X_{max})$. This kernel method is also applicable to the other energy bins, but the results are consistent with the 'normal' acceptance.

4.3.5 Calculation of the X_{max} Moments

To compare the measured X_{max} values with theoretical predictions, the easiest step is to calculate the moments $\langle X_{max} \rangle$ and $\sigma_{X_{max}}$ of the X_{max} distribution.
As the detector acceptance is not uniform, the selected X_{max} values get treated according to the determined detector acceptance, by assigning the inverse of the relative acceptance as weight by

$$w(X_{max}) = \frac{1}{\epsilon_{rel}(X_{max})}, \tag{4.23}$$

where $\epsilon_{rel}(X_{max})$ is calculated by equation 4.21 for the normal acceptance correction and by a template function for the lowest energy bins. The unbiased moments are then calculated by

the weighted X_{max} values. The mean of the X_{max} distribution is given by

$$\langle X_{max} \rangle = \frac{\sum_i w_i \cdot X_{max,i}}{\sum_i w_i}. \tag{4.24}$$

To calculate the spread of the weighted distribution, the second non central moment is needed, which is given by

$$\langle X^2_{max} \rangle = \frac{\sum_i w_i \cdot (X_{max,i})^2}{\sum_i w_i}. \tag{4.25}$$

The unbiased weighted variance is given by

$$V'_{X_{max}} = \frac{(\sum_i w_i)^2}{(\sum_i w_i)^2 - \sum_i w_i^2} \left(\langle X^2_{max} \rangle - \langle X_{max} \rangle^2 \right). \tag{4.26}$$

According to [129], the variances of $\langle X_{max} \rangle$ and $V'_{X_{max}}$ are given by

$$\sigma^2_{\langle X_{max} \rangle} = \frac{V'_{X_{max}}}{N} \tag{4.27}$$

$$\sigma^2_{V'_{X_{max}}} = \frac{1}{N} \left(m_4 - \frac{N-3}{N-1} \left(V'_{X_{max}} \right)^2 \right), \tag{4.28}$$

where N and the fourth central moment m_4 are given due to the weights by

$$N = \frac{(\sum_i w_i)^2}{\sum_i w_i^2}, \tag{4.29}$$

$$m_4 = \frac{\sum_i w_i \left(X_{max} - \langle X_{max} \rangle \right)^4}{\sum_i w_i}. \tag{4.30}$$

The variance of the X_{max} distribution includes the resolution $\widehat{Res}$ of the X_{max} measurements by subtracting it in quadrature from the unbiased weighted variance. The corrected spread of the distribution is given by

$$\sigma_{X_{max}} = \sqrt{V'_{X_{max}} - \widehat{Res}^2}. \tag{4.31}$$

The spread of the unbiased spread is given due to error propagation [117] by

$$\Delta_{\sigma'_{X_{max}}} = \sqrt{\frac{\sigma^2_{V'_{X_{max}}}}{4 V'_{X_{max}}}}. \tag{4.32}$$

Including the resolution subtraction in error propagation leads to the spread of the distribution spread, which is given by

$$\sigma_{\sigma_{X_{max}}} = \frac{\sqrt{V'_{X_{max}}}}{\sigma_{X_{max}}} \Delta_{\sigma'_{X_{max}}}. \tag{4.33}$$

4.4 End-to-End Monte Carlo Analysis

Before studying the high quality and unbiased selected air shower data of the Pierre Auger Observatory, Monte Carlo studies with a known chemical composition are made to check the whole analysis sequence. The used MC sample parameters are shown in table 4.4b. Three different scenarios are studied, namely a pure H, pure Fe and a mixed composition consisting of 50%H:50%Fe. For each of these scenarios the fiducial FOV is determined as described in chapter 4.1.3.6. The fiducial FOV boundaries for the three scenarios as a function of energy are shown in figure 4.31.

With this fiducial FOV cut the complete analysis sequence is performed on each of the sce-

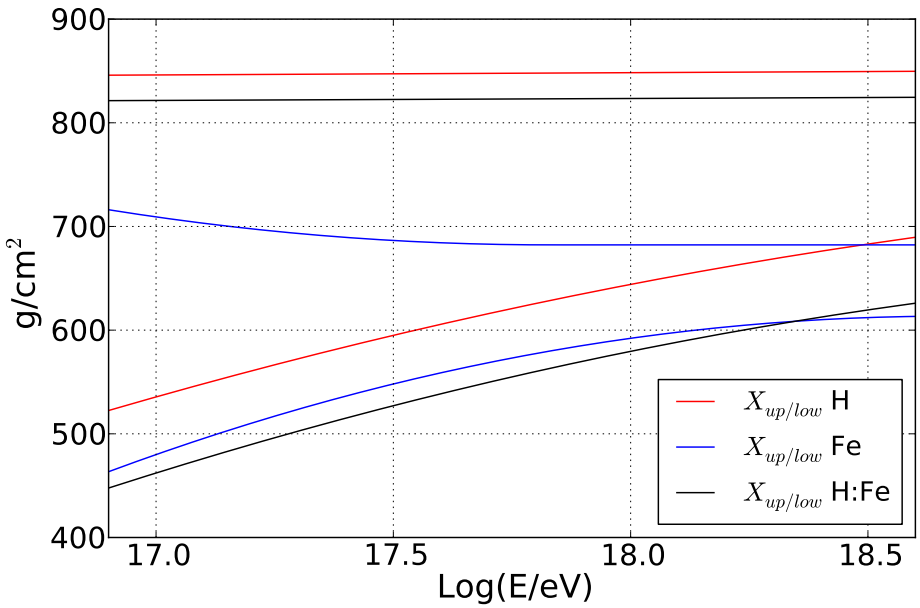

Figure 4.31: Fiducial field of view parametrization of the Monte Carlo studies for the end-to-end analysis study for the pure H, pure Fe and a mixed 50%H:50%Fe composition scenarios based on Sibyll2.1 RealMC. For each of these scenarios the fiducial FOV is determined as described in chapter 4.1.3.6.

narios, which means the bias corrections on energy and X_{max} as well as the detector resolution determination and the acceptance calculation. During the determination of these values, no assumptions on the chemical composition are made by using the RealMC air showers, shown in table 4.4b. In the acceptance determination, the normal assumption of a flat acceptance is used for every energy bin, except for the lowest five energy bins where the kernel method is used.

The first two moments of the MC X_{max} distribution are calculated following the method shown in chapter 4.3.5. As these scenarios are based on RealMC, the biases on energy and X_{max} derived from MC are fully corrected. The $\langle X_{max} \rangle$ and $\sigma_{X_{max}}$ moments after the whole analysis sequence are compared to the generated moments in figures 4.32 and 4.33. To illustrate the ef-

fect of the different acceptance assumption, a comparison of the moments with flat acceptance and kernel acceptance is shown. The moments of the flat acceptance are shown as yellow points for the first five bins. These points show strong deviation to the generated values both in the $\langle X_{max} \rangle$ and the $\sigma_{X_{max}}$ distributions, whereas the calculated moments using the kernel method are closer to the true values. However, there are still biases in the reconstructed moments.

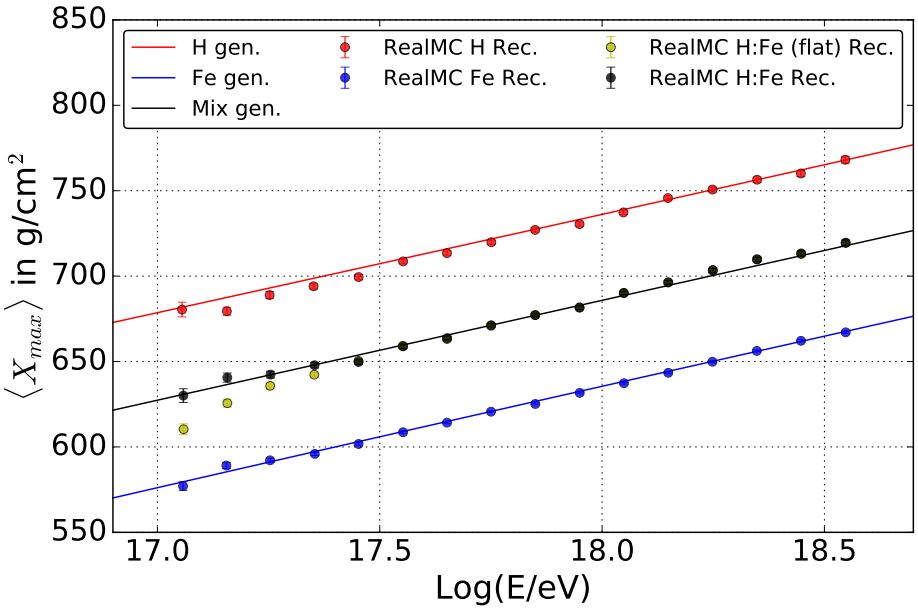

Figure 4.32: Mean of the X_{max} distributions in the End-to-End analysis for the pure H, pure Fe and 50%H:50%Fe Mix scenarios compared to the expected values. A kernel method acceptance in the first five bins is used in the pure and mixed scenarios in red, blue and black. The Mix scenario is also analyzed with a flat acceptance assumption in yellow.

The residuals of the reconstructed to the generated $\langle X_{max} \rangle$ for the mixed H:Fe scenario are shown in figure 4.34 using the flat acceptance in yellow and the kernel acceptance in the first five bins in black. The residuals are spread around 0 for the $\langle X_{max} \rangle$ and show only a small dependency on the reconstructed energy in case of the kernel method acceptance correction. In case of the flat acceptance correction a strong bias in the lowest bins is present.
The End-to-End bias on $\langle X_{max} \rangle$ for the kernel method is parametrized by a linear function of energy given by

$$X_{End2End}(\log(E/\mathrm{eV})) = (-0.66 - 3.47 \cdot (\log(E/\mathrm{eV}) - 18.0))\,\mathrm{g/cm^2}. \tag{4.34}$$

As this End-to-End study includes simulations of air showers, the bias can happen due to insufficiencies of the simulation and the reconstruction, that are not present in the data reconstruction. As a conservative approach the reconstructed X_{max} will be corrected half of this bias after the data reconstructed to compensate the effect by

$$X_{max}^{cor} = X_{max}^{rec} + \frac{1}{2} X_{End2End} \tag{4.35}$$

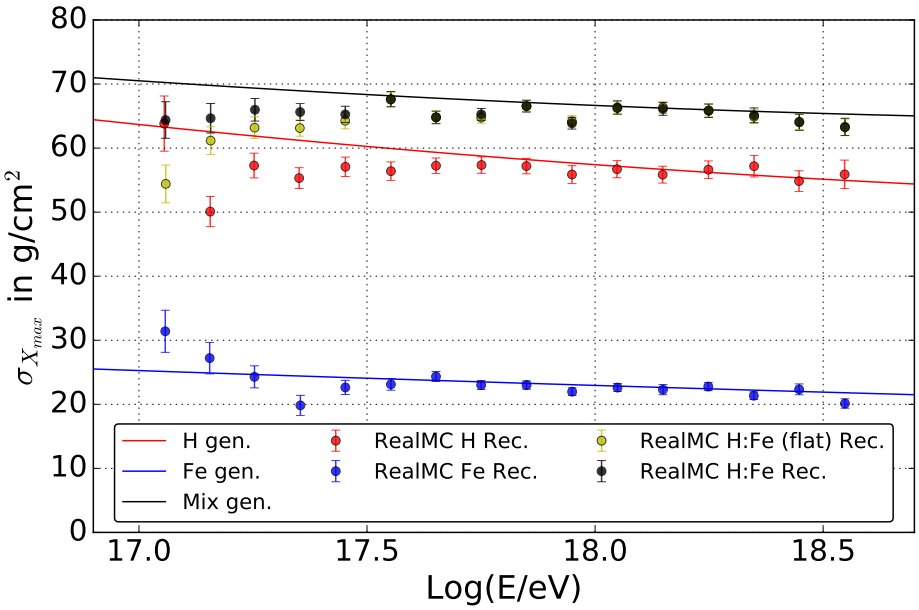

Figure 4.33: Spread of the X_{max} distributions in the End-to-End analysis for the pure H, pure Fe and 50%H:50%Fe Mix scenarios compared to the expected values. A kernel method acceptance in the first five energy bins is used in the pure and mixed scenarios in red, blue and black. The Mix scenario is also analyzed with a flat acceptance assumption in yellow.

The other half of this bias is taken into the systematic uncertainties as

$$\delta(X_{max})_{End2End} = ^{+X_{End2End}/2}_{-X_{End2End}/2} . \tag{4.36}$$

Also the residuals of the calculated $\sigma_{X_{max}}$ moments show a systematic uncertainty in comparison to the generated moments. For the mixed H:Fe scenario, which has the largest number of events in the lowest energy bins, this is shown in figure 4.35 using the flat acceptance assumption as yellow points and the kernel acceptance assumption in the first five bins as black points. The bias on the $\sigma_{X_{max}}$ moments is parametrized as a function of the energy given by

$$\sigma_{X_{max},End2End}(\log(E/\mathrm{eV})) = (1.44 - 2.35 \cdot (\log(E/\mathrm{eV}) - 18.0))\,\mathrm{g/cm^2}. \tag{4.37}$$

As this bias is taken as one-sided systematic uncertainty on the $\sigma_{X_{max}}$ moments as

$$\delta(\sigma_{X_{max}})_{End2End} = ^{+\sigma_{X_{max},End2End}}_{0} . \tag{4.38}$$

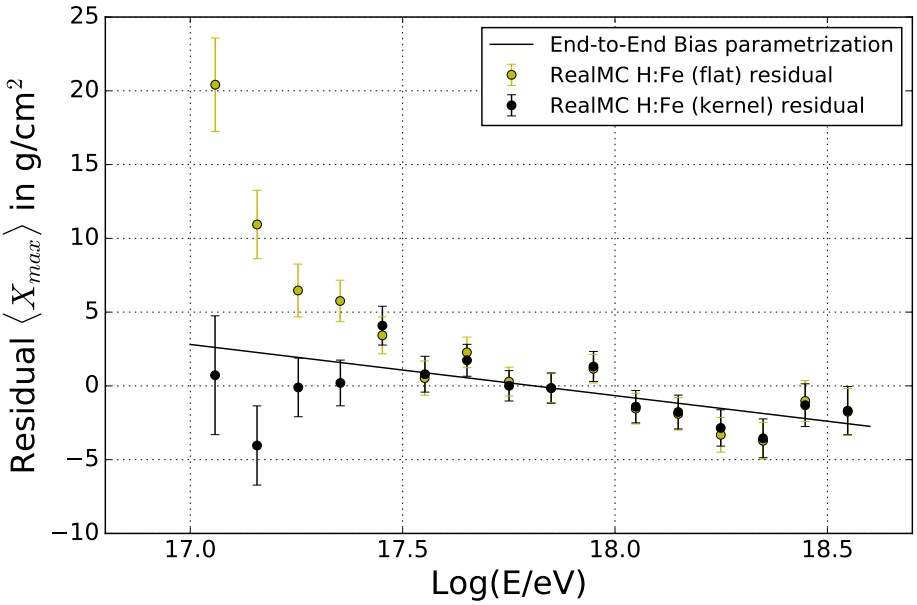

Figure 4.34: $\langle X_{max} \rangle$ residuals and parametrization fit for the mixed End-to-End scenario. Yellow points represent the residuals with an assumed flat acceptance in the all energy bins. Black points represent the residuals with a kernel method estimated acceptance in the first five energy bins.

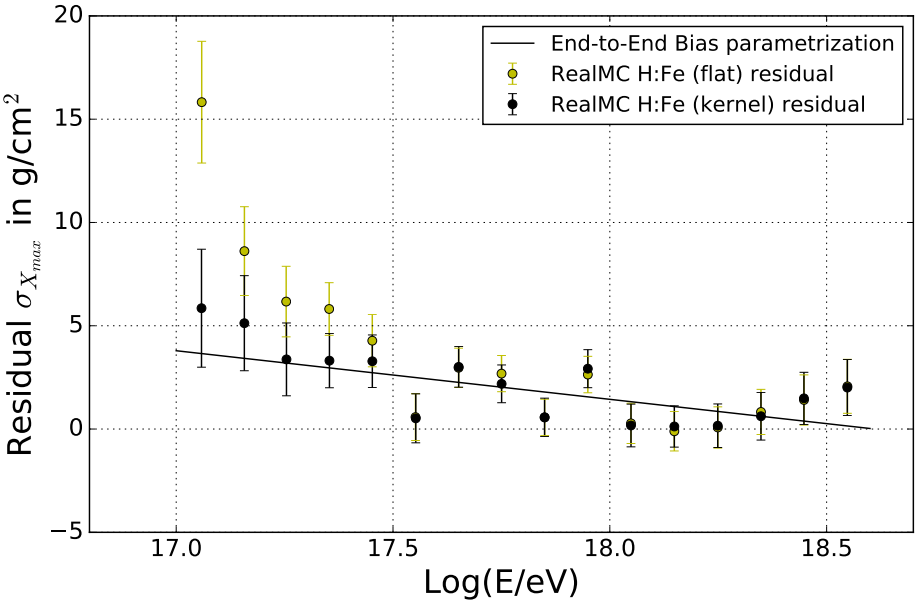

Figure 4.35: $\sigma_{X_{max}}$ residuals and parametrization fit for the mixed End-to-End scenario. Yellow points represent the residuals with an assumed flat acceptance in the all energy bins. Black points represent the residuals with a kernel method estimated acceptance in the first five energy bins.

4.5 Corrections, Resolution and Systematic Uncertainties

For the estimation of the systematic uncertainties of the air shower data, in this analysis several factors need to be taken into account. In the following chapter, these effects will be described. Also several effects on the X_{max} resolution will be discussed.

4.5.1 Energy Corrections and Systematic Uncertainty

The energy scale uncertainty of the Pierre Auger Observatory described in chapter 3.3.2 was given as $\delta E_{\text{scale}} \approx \pm 14\%$. Since in this analysis, the energy calibration of the Coihueco telescopes was shifted to have a better agreement with the HEAT telescopes, an additional uncertainty $\delta E_{\text{shift}} = ^{+5.3\%}_{0\%}$ has to be added to the total uncertainty. In chapter 4.3.2, an energy bias $f_{bias}(E_{cal})$ was found in the RealMC, which must be corrected to reconstruct the true energy. Since RealMC consist of a simulation part and a reconstruction part, this bias is not necessarily present in the reconstructed telescope data. The bias can happen due incompatibilities or shortcomings of the air shower simulation and reconstruction. Therefore, only half of this factor is corrected after the HECO data reconstruction, leading to a symmetrical systematic uncertainties $\delta E_{\text{bias}} = ^{+f_{bias}/2}_{-f_{bias}/2}$. The energy E^{true} used in this thesis is given by

$$E^{true} = E^{rec} \cdot \frac{1}{2} f_{bias}{}^{+f_{bias}/2}_{-f_{bias}/2}. \tag{4.39}$$

With the universality constraint described in chapter 4.3.1, the energy estimation is affected by a constraint of the interaction model. Although the k-constraint is in a similar range for all used models and primaries, there are some systematic differences. This systematic is studied by comparing the reconstructed events of the data sets using the universality constraint k^c_{LHC} and k^c_{sib} given in the equations 4.11 and 4.12. After the quality selection, each shower is compared to the same shower with the different constraint parametrization. The relative shower-to-shower differences of the reconstructed data sets are calculated by

$$\Delta E = \frac{E_{k_{Sib}} - E_{k_{LHC}}}{E_{k_{Sib}}}, \tag{4.40}$$

where $E_{k_{Sib}}$ is the reconstructed energy from the k^c_{sib} constraint and $E_{k_{LHC}}$ is the reconstructed energy from the k^c_{LHC} constraint. The relative shower-to-shower comparison and the parametrization of the systematic are shown in figure 4.36, where the event by event comparison is shown as blue dots and the mean values of the energy bins are shown as red dots. A quadratic polynomial is used to parametrize this relative bias by

$$\delta E_{\text{k}} = -0.488 + 0.048 \cdot \log(E/\text{eV}) - 0.001 \cdot \log(E/\text{eV})^2. \tag{4.41}$$

These four relative systematic uncertainties form the total systematic uncertainties by

$$\delta E_{\text{Tot}} = \sqrt{\delta E^2_{\text{scale}} + \delta E^2_{\text{shift}} + \delta E^2_{\text{bias}} + \delta E^2_{\text{k}}}, \tag{4.42}$$

where the effects are considered uncorrelated and therefore are summed in quadrature. The upper and lower systematic uncertainties on the energy as a function of the energy is shown in figure 4.37.

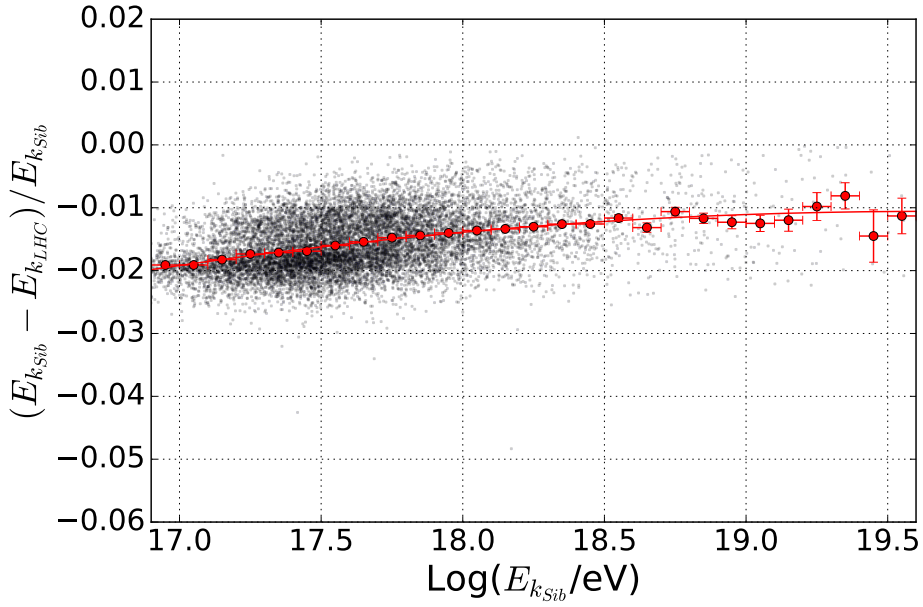

Figure 4.36: Event by event comparison of the energy reconstruction using different universality constraints k^c_{sib} and k^c_{LHC} given in equation 4.11 and 4.12. Blue dots represent the relative differences of the reconstructed shower. Red dots represent the mean values in each energy bin. Red line represents the parametrization of this systematic uncertainty.

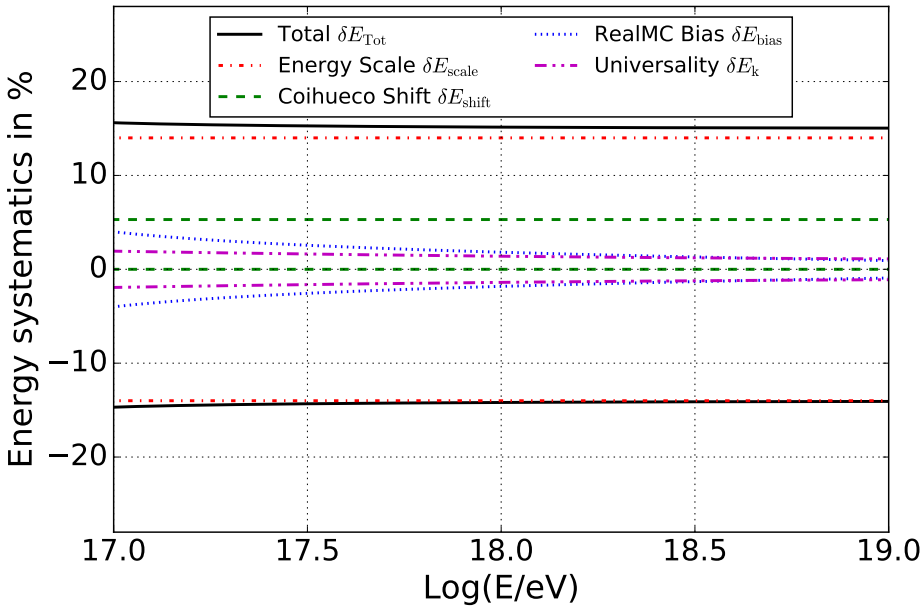

Figure 4.37: Summary of the systematic uncertainties of the HECO energy reconstruction.

4.5.2 X_{max} Corrections, Systematic Uncertainty and Resolution

To correct and analyze the measured X_{max}-distributions as a function of energy and compare them to Monte Carlo predictions, it is important to understand the systematic effects that affect this variable and the corresponding expected resolution. The following chapters will briefly describe the used corrections, systematic biases and the additional resolution effects by the detector, atmosphere and analysis.

4.5.2.1 RealMC Correction, Uncertainty and Resolution

The reconstruction bias of the RealMC described in chapter 4.3.3 shows that the mean deviation between simulation and reconstruction ($\langle X_{max}^{rec} - X_{max}^{true} \rangle$) is always negative, which is shown in figure 4.24. It is unclear, if this bias is an effect of the reconstruction sequence or a simulation/reconstruction sequence issue. Therefore, the reconstructed X_{max} value is corrected with half of the analysis bias. The corrected X_{max} value is given by

$$X_{max}^{cor} = X_{max}^{rec} + \frac{1}{2}\langle X_{bias} \rangle \tag{4.43}$$

where X_{bias} is a function of energy given in equation 4.19. A symmetrical systematic uncertainty of half of this bias is also taken into account as

$$\delta(X_{max})_{\text{bias}} = ^{+\langle X_{bias} \rangle /2}_{-\langle X_{bias} \rangle /2} . \tag{4.44}$$

In chapter 4.3.3 also the detector resolution as a function of energy is parametrized in equation 4.20, which is shown in figure 4.25. For the further analysis the detector resolution of X_{max} derived from RealMC is given as

$$Res_{\text{MC}} = \sigma_{Det} \, ^{+\text{fit uncer.}}_{-\text{fit uncer.}}, \tag{4.45}$$

where the uncertainties are taken from the error propagation of the parametrization uncertainties.

4.5.2.2 Universality Bias

Due to the universality constraint described in chapter 4.3.1, a systematic bias is introduced in the X_{max} reconstruction by the two constraint parameter sets used in this analysis based on the interaction models. The event by event differences of the reconstructed X_{max} from both data sets are calculated by

$$\Delta X_{max} = X_{max,k_{sib}} - X_{max,k_{LHC}}, \tag{4.46}$$

These calculated event by event differences are shown in figure 4.38. The mean values per energy bin are shown as cyan dots and show the small systematic bias. In first order, a linear function is used to parametrize this systematic bias by

$$\Delta X_{\text{k}} = (6.76 - 0.45 \cdot \log(E/\text{eV}))\,\text{g/cm}^2. \tag{4.47}$$

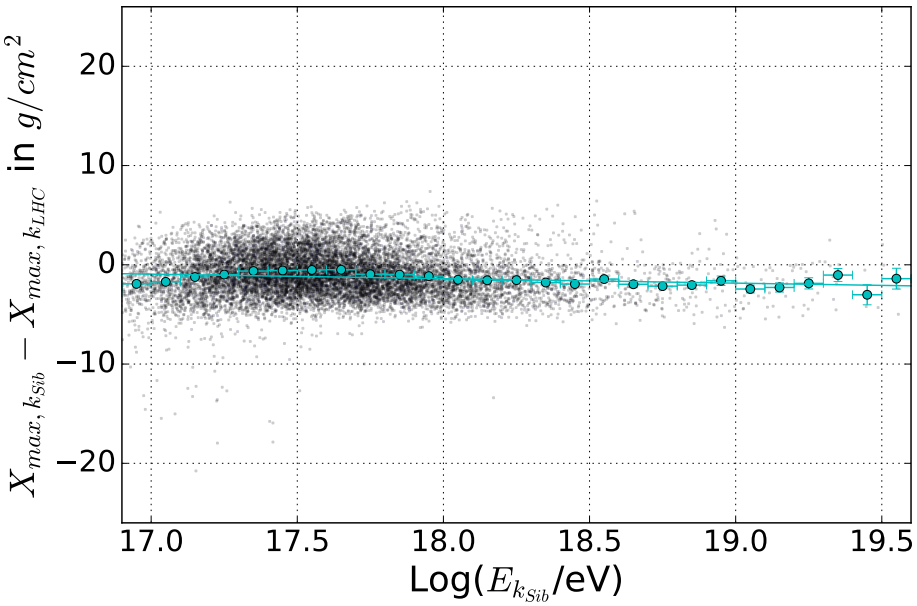

Figure 4.38: Comparison of the reconstructed X_{max} using different universality constraints based on equation 4.11 and 4.12. Blue dots represent the differences of event by event comparison. Cyan dots represent the mean values in each energy bin. Cyan line represents the linear parametrization of this systematic bias.

As non interaction model can be preferred, the systematic bias is taken into account as a symmetrical systematic uncertainty on the reconstructed X_{max} as

$$\delta X_{\mathrm{k}} = \pm \Delta X_{\mathrm{k}}. \tag{4.48}$$

Compared to the other systematic uncertainties, the universality uncertainty has the smallest value in the energy range of this thesis, which is shown later in figure 4.45.

4.5.2.3 Atmospheric Uncertainties and Resolution

As shown in chapters 3.2.4 and 3.3.2, the atmospheric conditions are constantly monitored at the Pierre Auger Observatory and taken into account during the energy and X_{max} reconstruction. The uncertainties of these measurements are taken into account as systematic uncertainties of the X_{max} measurements and additional X_{max} resolution contributions. The development of these atmospheric effects as a function of the energy is shown in figure 4.39 for the systematic X_{max} uncertainties and in figure 4.40 for the X_{max} resolution contributions. The following paragraphs describe the different effects which are studied.

4.5.2.3.1 Atmospheric Conditions

The influence of the atmospheric conditions (temperature, pressure, density) has an impact on the molecular attenuation. This effect is taken into account during the data reconstruction by using the atmospheric conditions from Global Data Assimilation System (GDAS). The

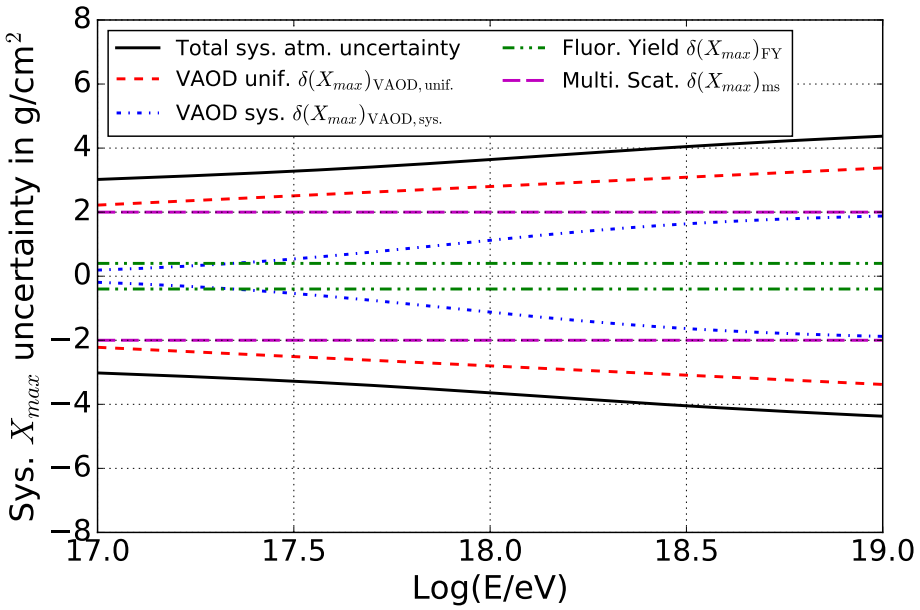

Figure 4.39: Systematic atmospheric uncertainties on the X_{max} measurements from the Vertical Aerosol Optical Depth (VAOD), fluorescence yield and multiple scattering uncertainties. Black line represents the square of the sum of these uncertainties in quadrature.

reconstruction of the air shower can also be made by taking the atmospheric conditions from balloon soundings. The influence of the molecular atmosphere on the X_{max} resolution is derived from the spread of the differences between both shower reconstructions. According to [86, 130], the contribution of the molecular atmosphere to the X_{max} resolution is given by

$$Res_{\mathrm{molAtm}} = (2.0 + 0.75 \cdot (\log(E/\mathrm{eV}) - 18))\,\mathrm{g/cm^2}. \tag{4.49}$$

4.5.2.3.2 Aerosols

The effects from aerosols are studied by measuring the Vertical Aerosol Optical Depth (VAOD) above the Pierre Auger Observatory. The resulting known systematic uncertainties will be described briefly in the following chapter.

Statistical Uncertainty of VAOD

The VAOD used in the reconstruction, is derived from measurement of the CLF and XLF. These measurements are averaged every hour and stored in the aerosol database. The mean and the variance of the hourly VAODs are used during the profile reconstruction and the uncertainties are propagated through to the longitudinal profile. At low energies, the distance to the shower is small and Mie scattering is negligible, therefore the effects are smaller. At high energies, the fluctuations saturate because of the limited size of the SD array. From the study in [130], the averaged effect on the variance on X_{max} as a function of energy is given by

$$\left\langle \sigma(X_{max})^2_{\mathrm{VAOD,stat.}} \right\rangle = 12 \left(\mathrm{g/cm^2}\right)^2 \cdot \left(e^{\frac{17.9-\log(E/\mathrm{eV})}{0.28}} + 1\right)^{-1}. \tag{4.50}$$

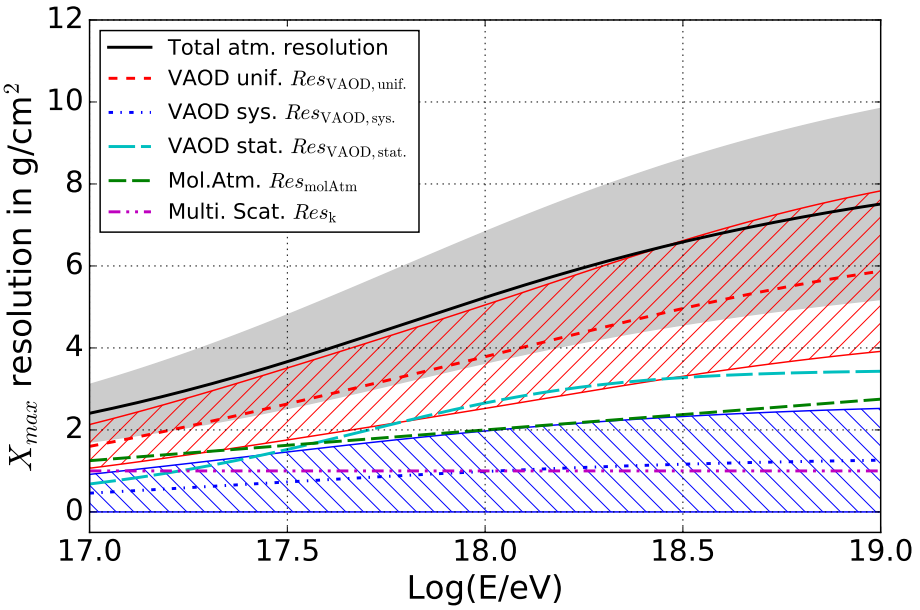

Figure 4.40: Contributions of the measured atmospheric conditions to the X_{max} resolution from the Vertical Aerosol Optical Depth (VAOD),atmospheric condition and multiple scattering. Black line represents the combination of this resolution contribution in quadrature. The shaded area represents the uncertainty on the resolution determination.

The contribution of this effect to the X_{max} resolution is given by

$$Res_{\mathrm{VAOD,stat.}} = \sqrt{\left\langle \sigma(X_{max})^2_{\mathrm{VAOD,stat.}} \right\rangle}. \tag{4.51}$$

Horizontal VAOD Uniformity

As the VAOD measurement only determines the direction from CLF/XLF to the FD telescopes, the calculations are based on the assumption of horizontal uniformity of the aerosol layers. With this assumption, it is possible to extend the calculation of the Mie attenuation to regions of the array that are not monitored by CLF/XLF. To study the systematic uncertainty and variation of the X_{max} measurement from this simplification, the air shower data were re-reconstructed using the VAOD profile of different FD stations. In [130], the largest systematic uncertainty and the spread of the X_{max} reconstruction as a function of energy are given as

$$\delta(X_{max})_{\mathrm{VAOD,unif.}} = \pm 2.8 + 0.58 \cdot (\log(E/\mathrm{eV}) - 18)\,\mathrm{g/cm^2} \tag{4.52}$$

and

$$\sigma(X_{max})_{\mathrm{VAOD,unif.}} = \sqrt{\frac{\left(14 \cdot \left(e^{\frac{17.8-\log(E/\mathrm{eV})}{0.65}} + 1\right)^{-1}\right)^2 - 2 \cdot \left\langle \sigma(X_{max})^2_{\mathrm{VAOD,stat.}} \right\rangle}{2}}\,\mathrm{g/cm^2}. \tag{4.53}$$

Since the re-reconstructed shower with the aerosol data of a different FD station is less representative than using the correct data, the variance could be overestimated. The assumption is that the true contribution of the horizontal non-uniformity of the VAOD on the X_{max} resolution is between $\sigma(X_{max})_{\text{VAOD,unif.}}/2$ and $\sigma(X_{max})_{\text{VAOD,unif.}}$. Therefore, the used contribution to the X_{max} resolution of this effect is given by

$$Res_{\text{VAOD,unif.}} = \frac{3}{4} \cdot \sigma(X_{max})_{\text{VAOD,unif.}}^{+\sigma(X_{max})_{\text{VAOD,unif.}}/4}_{-\sigma(X_{max})_{\text{VAOD,unif.}}/4}. \tag{4.54}$$

VAOD Systematic Uncertainties

The correlated systematic uncertainties of the laser energy, FD calibration and the choice of the reference nights are also taken into account for VAOD systematics. Therefore, the data are re-reconstructed with the VAODs changed for $\pm\sigma$ of these uncertainties. From [130] the parametrization of the systematic uncertainties and the spread of the X_{max} measurement as a function of energy are given by

$$\delta(X_{max})_{\text{VAOD,sys.}} = \pm 2 \cdot \left(e^{\frac{17.9-\log(E/\text{eV})}{0.4}} + 1\right)^{-1} \text{g/cm}^2 \tag{4.55}$$

and

$$\sigma(X_{max})_{\text{VAOD,sys.}} = 2.7 \cdot \left(e^{\frac{17.4-\log(E/\text{eV})}{0.6}} + 1\right)^{-1} \text{g/cm}^2. \tag{4.56}$$

It is unclear if these changes are simply statistical fluctuations of the X_{max} reconstruction due to fitting the air shower profile with slightly different attenuation corrections. Therefore, a conservative approach is used by assigning only half of this fluctuation as contribution to the resolution of X_{max} with a $\pm\sigma(X_{max})_{\text{VAOD,sys.}}/2$ uncertainty given by

$$Res_{\text{VAOD,sys.}} = \frac{1}{2}\sigma(X_{max})_{\text{VAOD,sys.}}^{+\sigma(X_{max})_{\text{VAOD,sys.}}/2}_{-\sigma(X_{max})_{\text{VAOD,sys.}}/2}. \tag{4.57}$$

4.5.2.3.3 Fluorescence Yield

As described in chapter 3.2.4, the Pierre Auger Observatory uses the fluorescence yield of the AIRFLY collaboration. According to [130], the systematic uncertainty on the X_{max} reconstruction is given by

$$\delta(X_{max})_{\text{FY}} = \pm 0.4\,\text{g/cm}^2. \tag{4.58}$$

4.5.2.3.4 Multiple Scattering

The systematics on X_{max} from the multiple scattering correction is estimated by changing the default Roberts multi scattering model [95] to the alternative Pekala et al. model [131]. The systematic uncertainties are given in [132] by

$$\delta(X_{max})_{\text{ms}} \leq \pm 2\,\text{g/cm}^2 \Rightarrow \delta(X_{max})_{\text{ms}} = \pm 2\,\text{g/cm}^2 \tag{4.59}$$

and the correspondent contribution to the X_{max} resolution from [133] is given by

$$\sigma(X_{max})_{\text{ms}} \leq 1\,\text{g/cm}^2 \Rightarrow Res_{\text{ms}} = 1\,\text{g/cm}^2. \tag{4.60}$$

4.5.2.4 Detector Uncertainties

At the Pierre Auger Observatory, the status of the detector is monitored on a regular basis. For X_{max} studies, the effects of the telescope alignment, the pixel calibration and the timing between SD and FD are important for the reconstruction of high quality air showers.

4.5.2.4.1 Telescope Alignment

A precise knowledge of the FD alignment is important for the measurement of X_{max}. A misaligned telescope will drastically introduce a systematic bias onto the height of the shower maximum. To measure the alignment of the FD telescopes, a cross calibration with showers seen by FD and SD is performed [134]. There are also methods that use star tracks in the camera [135, 136] and CLF events [137, 138] to study the alignment.
In case of the combined eye HECO, a misalignment of HEAT and Coihueco could lead to a systematic difference at the shower detector plane (SDP) determination for showers crossing both eyes. The systematic uncertainties get bigger at lower energies. At energies below $10^{17.5}$ eV, HECO becomes dominant over the standard telescopes and the increasing uncertainties are emerging. This is shown in the figures 4.41a and 4.41b. The parametrization of the systematic

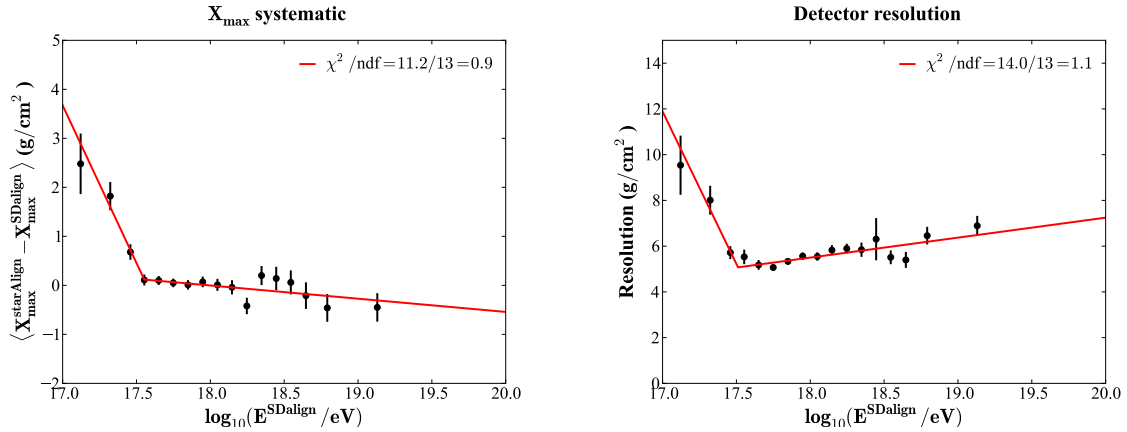

(a) Systematic uncertainties of X_{max} due to different alignment methods.

(b) Contribution of the different alignment methods to the X_{max} resolution.

Figure 4.41: Study of the X_{max} differences by the SD alignment (SDalign) and star alignment (starAlign) methods [110].

X_{max} uncertainties as a function of energy is given by

$$\Delta(X_{max})_{\text{align}} = \begin{cases} (0.12 - 6.43 \cdot (\log(E/\text{eV}) - 17.55))\,\text{g/cm}^2 & \text{if } \log(E/\text{eV}) < 17.55 \\ (0.12 - 0.27 \cdot (\log(E/\text{eV}) - 17.55))\,\text{g/cm}^2 & \text{otherwise} \end{cases} \tag{4.61}$$

and the spread is given by

$$\sigma(X_{max})_{\text{align}} = \begin{cases} (5.07 - 13.34 \cdot (\log(E/\text{eV}) - 17.51))\,\text{g/cm}^2 & \text{if } \log(E/\text{eV}) < 17.51 \\ (5.07 - 0.87 \cdot (\log(E/\text{eV}) - 17.51))\,\text{g/cm}^2 & \text{otherwise} \end{cases} . \tag{4.62}$$

The alignment of the FD telescopes is derived from the SD cross calibration. However, it is unclear which method is accurate. Therefore, half of the bias in equation 4.61 is corrected during the X_{max} measurement and the other half is taken as systematic uncertainty. As the uncertainties are summed up in quadrature, the absolute value of $\Delta(X_{max})_{\text{align}}$ is considered as

$$\delta(X_{max})_{\text{align}} = {}^{+|\Delta(X_{max})_{\text{align}}|/2}_{-|\Delta(X_{max})_{\text{align}}|/2}\ \text{g/cm}^2. \tag{4.63}$$

The contribution to the X_{max} resolution is given by

$$Res_{\text{align}} = \frac{1}{2}\sigma(X_{max})_{\text{align}}\ {}^{+\sigma(X_{max})_{\text{align}}/2}_{-\sigma(X_{max})_{\text{align}}/2}\ \text{g/cm}^2. \tag{4.64}$$

4.5.2.4.2 Pixel Calibration

Uncertainties of the pixel calibration only affect X_{max} if there is an elevation dependent bias in the nightly relative camera calibration constants of the 'CalA' (described in chapter 3.2.3). From [117, 130] it is known that from various updates of the CalA database no significant changes on X_{max} were induced. As a conservative approach, the systematic uncertainty of the calibration [130] is assumed to be

$$\delta(X_{max})_{\text{cal}} \leq \pm 1\,\text{g/cm}^2. \tag{4.65}$$

4.5.2.4.3 Time Calibration

Differences in the timing synchronization between SD and FD lead to different geometry reconstructions and therefore differences in X_{max}. From [117, 139], the largest systematic uncertainty on the X_{max} reconstruction is given by

$$\delta(X_{max})_{\delta t} \leq \pm 3.5\,\text{g/cm}^2. \tag{4.66}$$

4.5.2.5 Correction Biases

Several corrections are applied during the reconstruction process of X_{max}. The resulting systematic uncertainties will be described briefly in the following subsections.

4.5.2.5.1 Lateral width correction

The 'lateral width correction' [125] is a phenomenological parametrization of the light outside the studied light track of the camera and is applied on the air shower data during the reconstruction. This also accounts for the large-halo effect due to light reflections from the camera surface [140]. The magnitude of this correction as a function of energy is given

$$\Delta_{\text{LWcorr}} = 14.8 \cdot \left(e^{\frac{\log(E/\text{eV})-18.68}{0.43}} + 1\right)^{-1} \text{g/cm}^2. \tag{4.67}$$

It was shown in recent studies [141], that a simple implementation of the measured point spread function into the simulation is not adequate enough to describe this effect. When the 'lateral width correction' is applied on simulation, a reconstruction bias of X_{max} occurs [130]. The resulting bias is corrected for the regular FD telescopes by

$$X'_{max} = X_{max} - b_{\text{LWcorr}}, \tag{4.68}$$

where the bias as a function of energy is given by

$$b_{\mathrm{LWcorr}} = 6.5 \cdot \left(e^{\frac{\log(E/\mathrm{eV})-18.23}{0.41}} + 1 \right)^{-1} \mathrm{g/cm^2}. \tag{4.69}$$

For the regular FD telescope the systematic uncertainty is given by

$$\delta(X_{max})_{\mathrm{LWcorr,FD}} = ^{+b_{\mathrm{LWcorr}}}_{-(\Delta_{\mathrm{LWcorr}}-b_{\mathrm{LWcorr}})} . \tag{4.70}$$

Since the correction Δ_{LWcorr} and the subsequent reconstruction bias b_{LWcorr} is only valid and parametrized for the regular FD stations and their energy range, it is still under investigation in the HECO analysis chain by the hybrid reconstruction task of the Pierre Auger collaboration [124]. The regular FD telescopes and the HEAT telescopes have the same optical system and therefore the lateral width correction is also used in this thesis.

4.5.2.5.2 Coihueco Energy Calibration Adjustment

Due to the energy shift of the Coihueco telescopes described in chapter 4.1.2, systematic differences on the X_{max} reconstruction occur. The average differences on X_{max} and the resolution are shown in the figures 4.42a and 4.42b. The parametrizations of these differences as a function

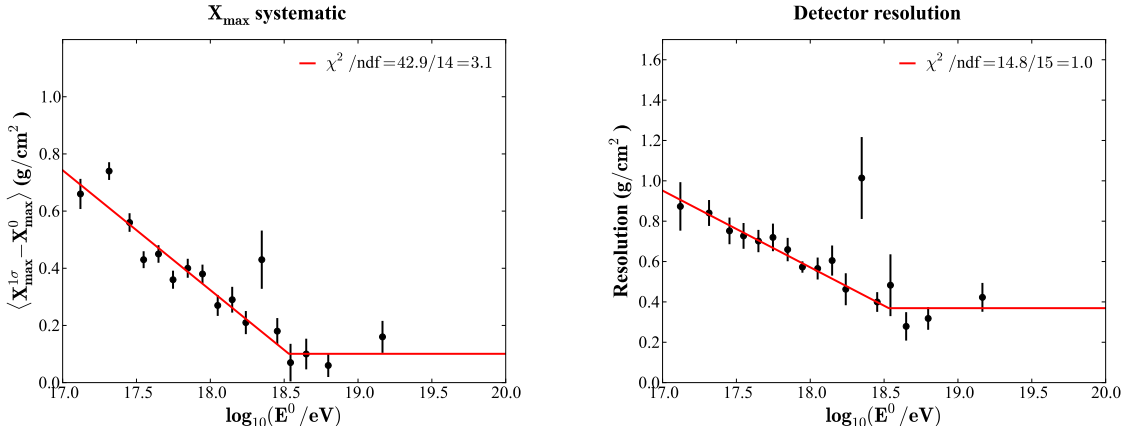

(a) Systematic uncertainty on X_{max} by the energy calibration shift.

(b) Contribution to the X_{max} resolution by the energy calibration shift.

Figure 4.42: Study of the X_{max} differences by the energy calibration shift of the Coihueco telescopes [110].

of energy [110] are given by

$$calAdj = \pm \begin{cases} 0.1 - 0.42 \cdot (\log(E/\mathrm{eV}) - 18.53) & \text{if } \log(E/\mathrm{eV}) < 18.53 \\ 0.1 & \text{otherwise} \end{cases} , \tag{4.71}$$

$$\sigma_{calAdj} = \pm \begin{cases} 0.37 - 0.38 \cdot (\log(E/\mathrm{eV}) - 18.53) & \text{if } \log(E/\mathrm{eV}) < 18.53 \\ 0.37 & \text{otherwise} \end{cases} . \tag{4.72}$$

This parametrization is used as one-sided systematic uncertainty given by

$$\delta(X_{max})_{\text{calAdj}} = ^{+|calAdj|}_{-0} \text{ g/cm}^2. \tag{4.73}$$

The contribution to the resolution is given by

$$Res_{\text{calAdj}} = 0.^{+\sigma_{calAdj}}_{-0} \text{g/cm}^2. \tag{4.74}$$

4.5.2.5.3 HECO vs. Coihueco X_{max} Data Comparison

The reconstructed HECO events consist of 3 different event classes. The first two event classes of HECO use only the telescopes of Coihueco or only the telescopes of HEAT. This HECO events reconstruct the same values as the single telescope event reconstruction. The third event class uses the combination of the Coihueco and the HEAT telescopes. The telescope crossing events extend single reconstructed FD station events, e.g. a Coihueco event is extended by the data of a HEAT telescope.

The energy distribution of the different HECO event classes of the data used in this thesis is shown in figure 4.43a. The relative event fractions of the events classes are shown in figure 4.43b. These figures show the evolution of the different event classes per energy. The fraction of HEAT only events is decreasing, whereas the Coihueco only events is increasing as a function of energy. Over the whole energy range the fraction of the telescope crossing event class is considerable large. As this reconstruction is different from the standard reconstruction of the single FD stations a cross check is made to analyze for systematic uncertainties. In the energy range from $\log(E/\text{eV}) = 18.0 - 18.4$, high quality air shower events are reconstructed in $\overline{\text{Off}}\underline{\text{line}}$ separately with Coihueco and the virtual HECO. This energy range is used as a control region to find systematic differences as Coihueco is very efficient here. The same quality selection is made on both data sets, HECO and Coihueco. In figure 4.44a the shower to shower comparison of the data set is shown divided into the different event classes. The differences of the reconstructed X_{max} of HECO and Coihueco is nearly zero if the same telescopes are used. The minor differences of the X_{max} results are due to reconstructing the same raw data with different start parameters.

The telescope crossing event class shows a large spread in the X_{max} differences and the mean of the differences in this event class is systematically shifted. On average Coihueco reconstructs the shower maximum with a larger X_{max}. The spread of the reconstructed X_{max} is also seen in the RealMC data, which is shown in figure 4.44b. The systematic shift between the different reconstructions is not reproducible in the RealMC. As it is unknown which telescope reconstructions is the correct one and the effect is not seen in the RealMC, the average difference in the control region between reconstructed X_{max} of HECO, where HECO events consist of telescope crossing events, and Coihueco is given as

$$\Delta_{adhoc} = \langle X_{max,HECO} - X_{max,CO} \rangle = -4.05\,\text{g/cm}^2, \tag{4.75}$$

This adhoc-shift in one of the three event classes is still under investigation by the mass composition task of the Pierre Auger collaboration [122] and in this thesis used as one-sided

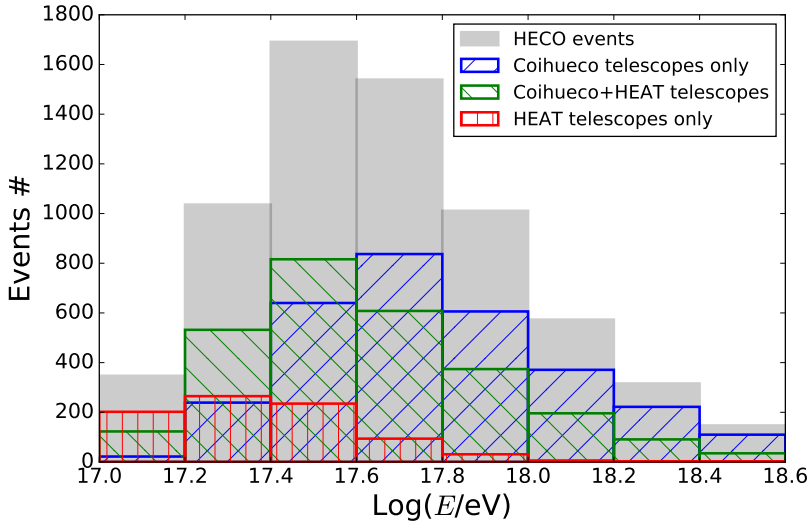

(a) Energy distribution of the different event classes of the HECO events.

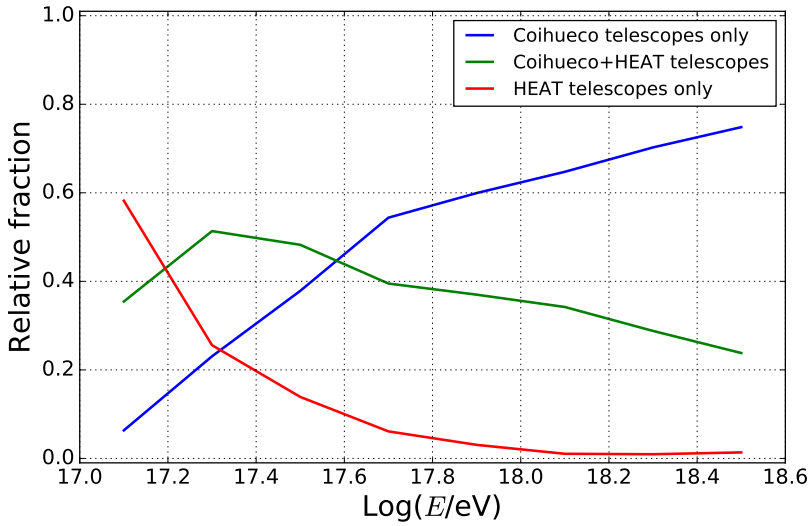

(b) Evolution of the relative fraction of the different event classes as a function of energy.

Figure 4.43: Different event classes of HECO events after the complete quality selection. Events seen with Coihueco telescopes are shown in blue. Events seen with HEAT telescopes are shown in red. Events seen with Coihueco and HEAT telescopes are shown in green.

conservative systematic uncertainty of the HECO events in this thesis given by

$$\delta X_{\Delta_{adhoc}} = {}^{+|\Delta_{adhoc}|}_{0} \, . \tag{4.76}$$

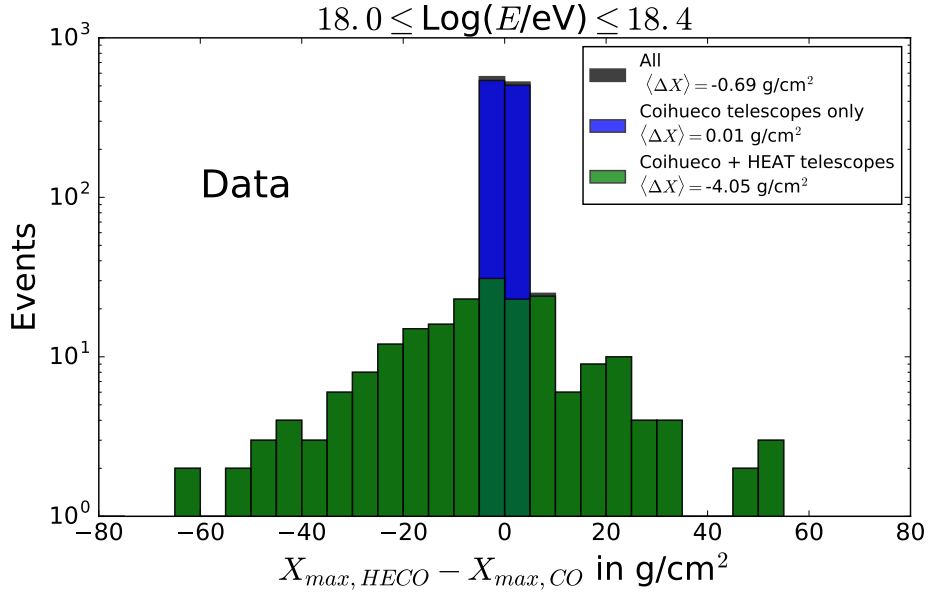

(a) Shower to shower comparison of reconstructed HECO and Coihueco X_{max} in the reconstructed data set.

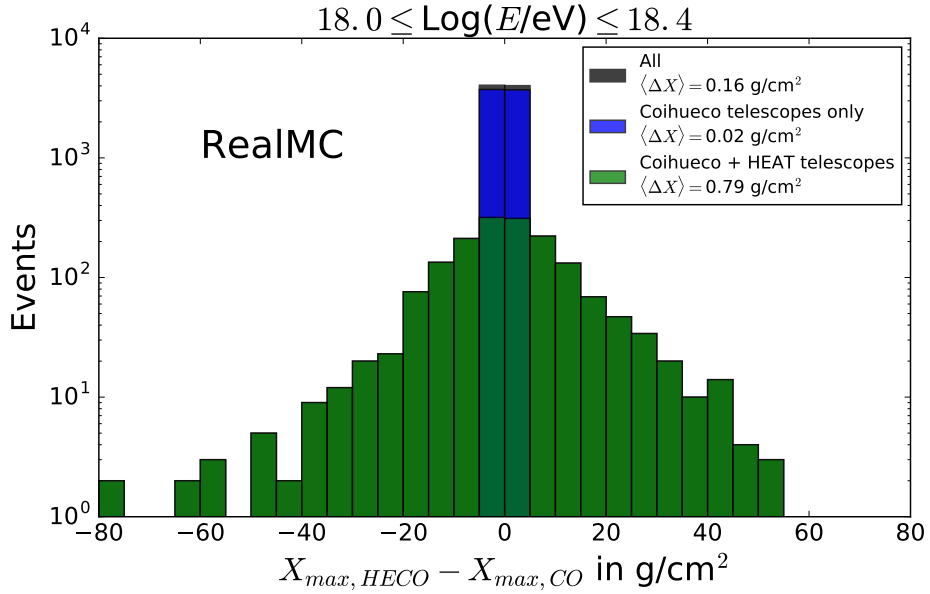

(b) Shower to shower comparison of reconstructed HECO and Coihueco X_{max} in the reconstructed Monte Carlo data set.

Figure 4.44: Shower to shower comparison of reconstructed HECO and Coihueco X_{max}. Differences of the events seen with Coihueco telescopes only are shown in blue. Events seen with Coihueco+HEAT telescopes are shown in green. The average differences for each event classes is given in the legend.

4.6 Summary of Applied X_{max} Corrections and Resolution Components

From this point on, the reconstructed X_{max} value from air shower data uses the following correction to get the best possible reconstruction of the shower maximum:

$$X_{max} = X_{max}^{rec} - \frac{1}{2}\langle X_{bias}\rangle - \frac{1}{2}X_{End2End} + \frac{1}{2}\Delta(X_{max})_{\text{align}} - b_{LW}. \tag{4.77}$$

The total systematic uncertainties of X_{max} are given by

$$\delta X_{Tot} = \sqrt{\delta X^2_{\text{atmos}} + \delta X^2_{\text{cal}} + \delta X^2_{rec} + \delta X^2_{\text{k}} + \delta X^2_{\Delta_{adhoc}}}, \tag{4.78}$$

with

$$\begin{aligned}
\delta X^2_{\text{atmos}} &= \delta(X_{max})^2_{\text{VAOD,unif.}} + \delta(X_{max})^2_{\text{VAOD,sys.}} + \delta(X_{max})^2_{\text{FY}} + \delta(X_{max})^2_{\text{ms}}, && (4.79)\\
\delta X^2_{\text{cal}} &= \delta(X_{max})^2_{\text{cal}} + \delta(X_{max})^2_{\delta t} + \delta(X_{max})^2_{\text{align}}, && (4.80)\\
\delta X^2_{rec} &= \delta(X_{max})^2_{\text{bias}} + \delta(X_{max})^2_{End2End} + \delta(X_{max})^2_{\text{LWcorr}} + \delta(X_{max})^2_{\text{calAdj}}. && (4.81)
\end{aligned}$$

The resulting upper and lower systematic uncertainties of X_{max} as a function of energy are shown in figure 4.45.

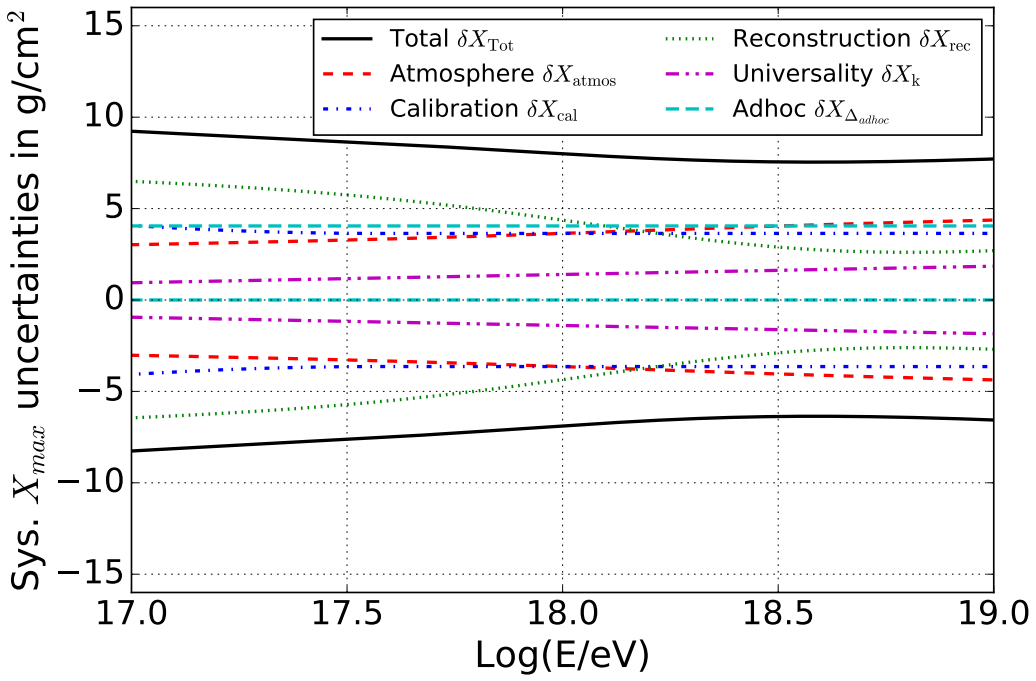

Figure 4.45: Summary of systematic uncertainties of the X_{max} reconstruction as a function of energy.

For the comparison of the theoretical predictions of the intrinsic shower to shower fluctuations,

the measured spread of the X_{max} distribution needs to be corrected for the total measurement X_{max} resolution according to equation 4.31. This total X_{max} resolution Res_{Tot} includes all detector, atmosphere and analysis resolution component and their uncertainties. As the single components are assumed to be uncorrelated, Res_{Tot} is given by

$$Res_{\mathrm{Tot}} = \sqrt{Res^2_{\mathrm{det}} + Res^2_{\mathrm{atmos}}}, \tag{4.82}$$

with

$$\begin{aligned} Res^2_{\mathrm{det}} &= Res^2_{\mathrm{MC}} + Res^2_{\mathrm{align}} + Res^2_{\mathrm{calAdj}}, & (4.83)\\ Res^2_{\mathrm{atmos}} &= Res^2_{\mathrm{molAtm}} + Res^2_{\mathrm{VAOD,stat.}} + Res^2_{\mathrm{VAOD,unif.}} + Res^2_{\mathrm{VAOD,sys.}} + Res^2_{\mathrm{ms}}. & (4.84) \end{aligned}$$

The upper and lower systematic uncertainties of the X_{max} resolution are assumed uncorrelated. The systematic uncertainty of the measured X_{max} spread derived from the End-to-End analysis in chapter 4.4 is also included here. The total uncertainty is summed up in quadrature and given by

$$\delta Res_{\mathrm{Tot}} = \sqrt{\delta Res^2_{\mathrm{det}} + \delta Res^2_{\mathrm{atmos}} + \delta(\sigma_{X_{max}})_{End2End}}, \tag{4.85}$$

with

$$\begin{aligned} \delta Res^2_{\mathrm{det}} &= \delta Res^2_{\mathrm{MC}} + \delta Res^2_{\mathrm{align}} + \delta Res^2_{\mathrm{calAdj}}, & (4.86)\\ \delta Res^2_{\mathrm{atmos}} &= \delta Res^2_{\mathrm{VAOD,unif.}} + \delta Res^2_{\mathrm{VAOD,sys.}}. & (4.87) \end{aligned}$$

The total resolution including the given systematic uncertainties for HECO is shown in figure 4.46.

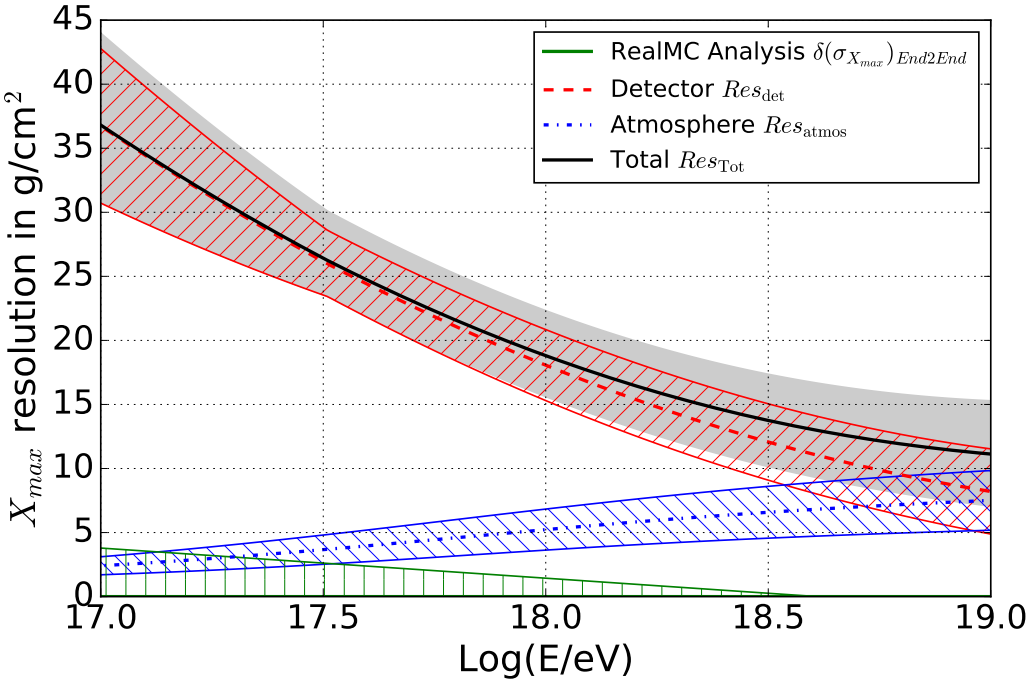

Figure 4.46: Combined resolution components of the X_{max} reconstruction as a function of energy. The shaded areas represent the systematic uncertainties of these resolution components. The systematic uncertainty of the measured X_{max} spread derived from the End2End analysis in chapter 4.4 is shown in green.

Chapter 5

X_{max} Data Studies

For the final validation of the selected data set, a comparison of the final data set and RealMC data set is presented in chapter 5.1. After all quality checks and bias corrections the unbiased data set can be used to analyze the chemical composition of UHECRs by calculating the X_{max}-moments as a function of energy. This is presented in chapter 5.2. Also the chemical composition fractions are fitted based on the simulation parametrization, which will be discussed in chapter 5.3.

5.1 Data and Monte Carlo Shower Geometry Comparison

As an independent test of compatibility of the selected data and the RealMC described in table 4.4b, the distributions of the shower geometry parameters are used. Both data sets are selected using the same quality criteria. The investigated parameters are the perpendicular distance from the shower axis to the telescope R_p, which is defined in figure 3.25, and the zenith angle of the shower. An example for a low energy bin of $\log(E/\text{eV}) = 17.1 - 17.2$ is shown in figure 5.1. The R_p distribution in figure 5.1a shows a small deviation in the falling tail of the distribution

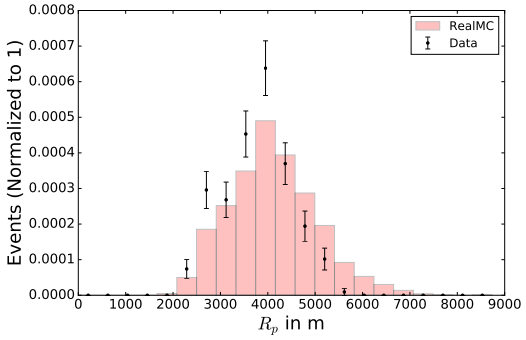

(a) Comparison of the R_p distribution of RealMC and data.

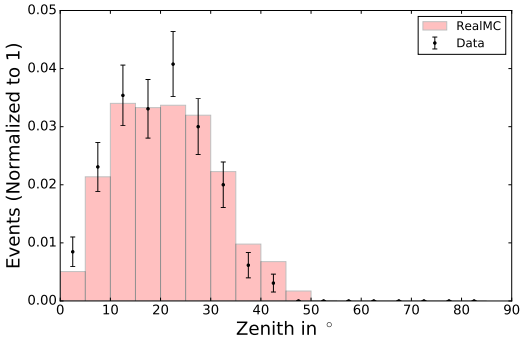

(b) Comparison of the zenith angle distribution of RealMC and data.

Figure 5.1: Perpendicular distance from the shower axis to the telescope R_p and zenith angle distribution of reconstructed air showers with energies of $\log(E/\text{eV}) = 17.1 - 17.2$. Both data sets are normalized to 1 for the comparison. RealMC distributions are represented in red. Reconstructed HECO data sets are show in black including Poisson error bars.

in the comparison of the data and the RealMC. The zenith distribution in figure 5.1b of the same energy bin shows also a small discrepancy at large zenith angles between the data and

the RealMC. Due to the current statistics the data points have large error bars so this could be a statistical issue. In figure 5.2 the distributions of the events with $\log(E/\text{eV}) = 17.9 - 18.0$ are shown. The R_p and the zenith angle distribution show a reasonable agreement between data and RealMC. The distributions for the whole studied energy range is given in appendix E.

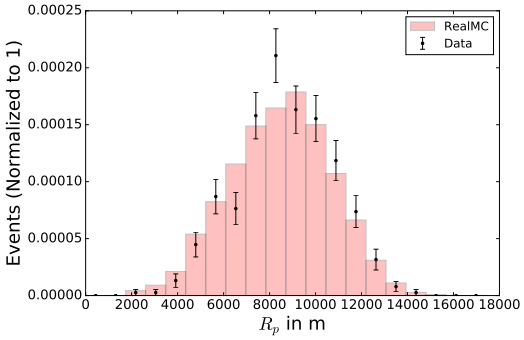

(a) Comparison of the R_p distribution of RealMC and data.

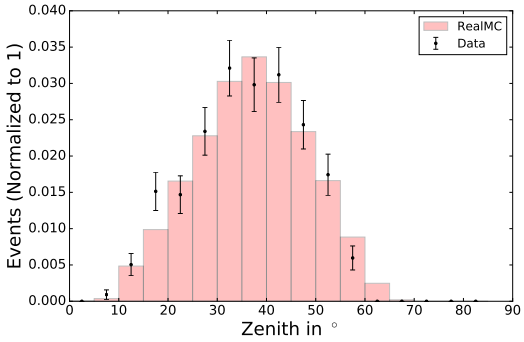

(b) Comparison of the zenith angle distribution of RealMC and data.

Figure 5.2: Perpendicular distance from the shower axis to the telescope R_p and zenith angle distribution of reconstructed air showers with energies of $\log(E/\text{eV}) = 17.9 - 18.0$. Both data sets are normalized to 1 for the comparison. RealMC distributions are represented in red. Reconstructed HECO data sets are show in black including Poisson error bars.

Except the lowest 4 energy bins with the lowest statistics and the largest detector resolution, the RealMC and the data distributions agree well within the statistical uncertainties.

5.2 X_{max}-Moments

As discussed in chapter 4.3.1, in this thesis a constraint on the shower profile based on interaction models is introduced. As none of the interaction models can be ignored, this leads to two reconstructed data sets of the same raw data showers using k_{LHC} and k_{Sib} variables from the equations 4.11 and 4.12. The moments of the X_{max}-distribution are calculated for both data sets and are shown in figure 5.3. Both data sets agree very well and only small fluctuations are present. These fluctuations are induced by the fitting routine with the different constraints and therefore small fluctuations during the event selection process. To make a comparison with other data sets easier, the weighted average of the given data points is used in the following plots.
These final HECO moments are compared to the standard FD Coihueco only X_{max}-moments in figure 5.4. For the Coihueco moments the same reconstruction and analysis procedure is used as for the HECO moments. The results from HECO and Coihueco agree well within their uncertainties. The systematic uncertainty described in chapter 4.5.2.5.3 leads to a small systematic shift. The $\langle X_{max} \rangle$ HECO moments are $\sim 1 - 2\,\text{g/cm}^2$ lower than the Coihueco moments. This effect is still under investigation by the Pierre Auger collaboration [122]. The $\sigma_{X_{max}}$ moments of HECO and Coihueco are in good agreement with each other within their

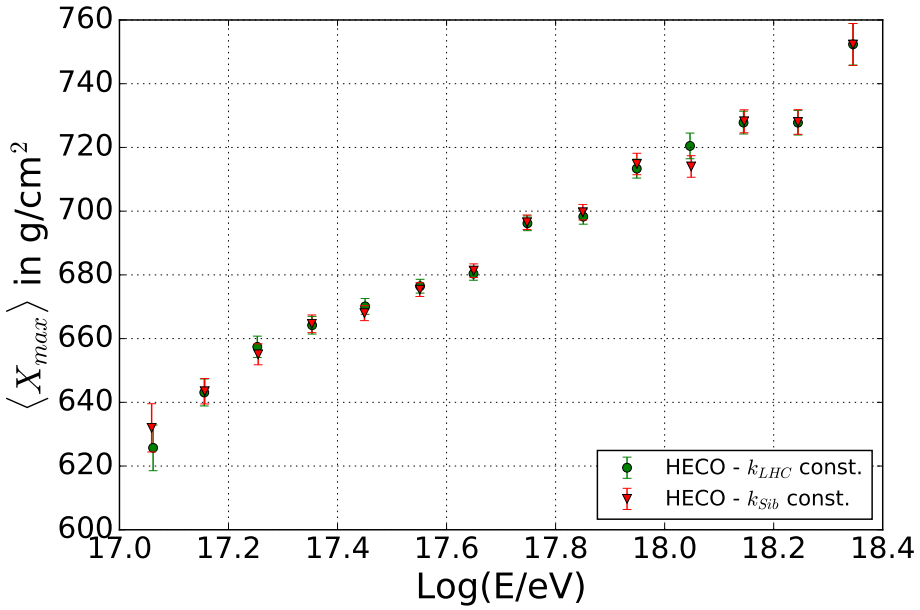

(a) Calculated $\langle X_{max} \rangle$ of the HECO data set.

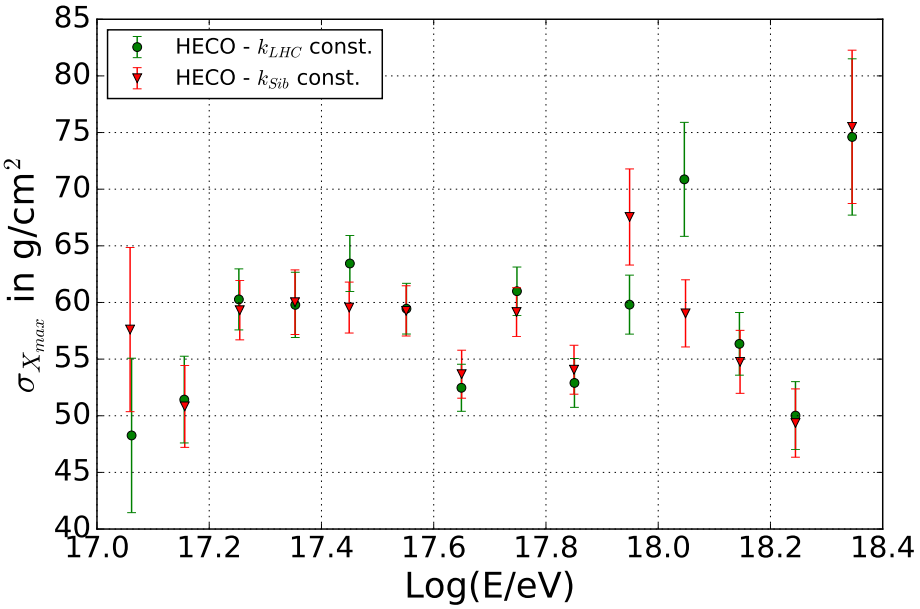

(b) Calculated $\sigma_{X_{max}}$ of the HECO data set.

Figure 5.3: Comparison of the X_{max} moments calculated with different reconstruction profile constraints as described in chapter 4.3.1.

uncertainties. The first two X_{max}-moments for the standard FD telescopes in an extended time period from December 2004 to December 2012 were already calculated and published in 2014 in PRD [41] and this data set is also used for a comparison. The HECO reconstruction

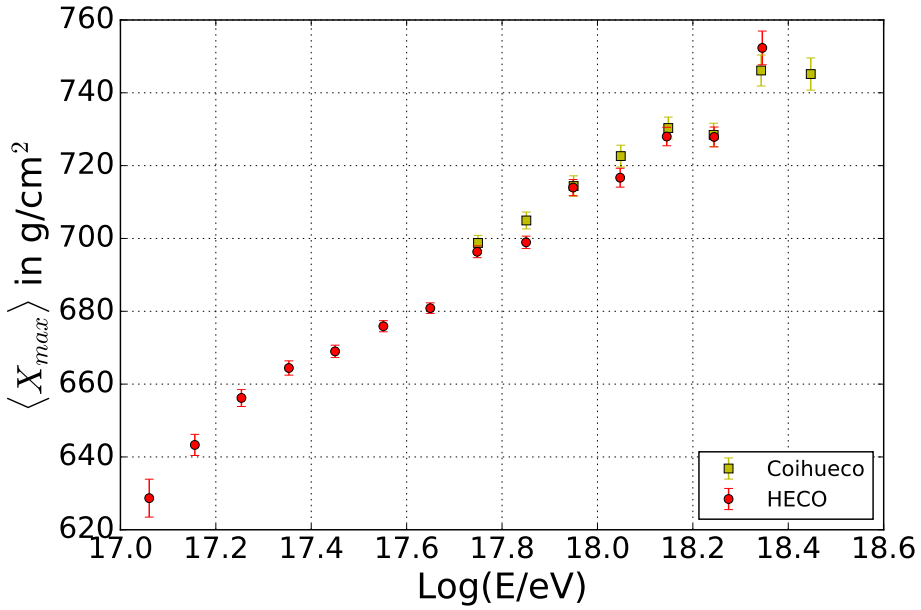

(a) Calculated $\langle X_{max} \rangle$ of the HECO data set compared to Coihueco only data set.

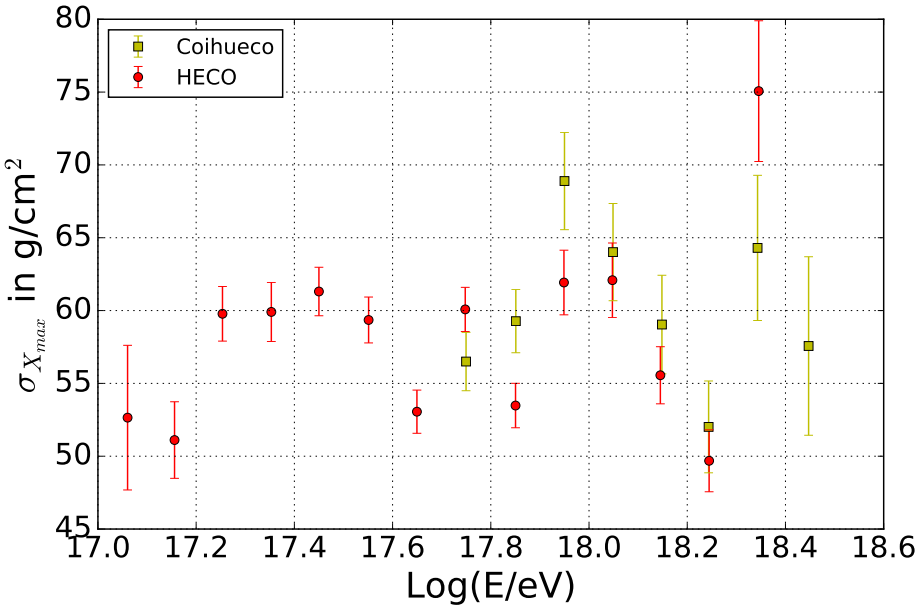

(b) Calculated $\sigma_{X_{max}}$ of the HECO data set compared to Coihueco only data set.

Figure 5.4: Comparison of the X_{max} moments calculated with HECO and Coihueco only.

module sequence is different from the standard reconstruction used in [41]. The result is shown in figure 5.5a, where the reconstructed moments from the different module sequence are compared. The $\langle X_{max} \rangle$ of Coihueco using the HECO module sequence is systematic lower than the results of the standard reconstruction. The residuals of these moments are shown in figure

5.5b and show that this shift is constant in energy with a difference of

$$\Delta = (6.32 \pm 1.16)\,\mathrm{g/cm^2}. \tag{5.1}$$

As the Coihueco moments are only an subset of the Auger PRD raw data from 2010 to 2012 and only include a single FD station, this shift could be due to some unknown systematic bias. This issue is also still under investigation by the Pierre Auger collaboration [123].

The evolution of the HECO $\langle X_{max} \rangle$ and $\sigma_{X_{max}}$ as a function of energy compared to the previous results of the Pierre Auger Observatory is shown in the figures 5.6 and 5.7. The calculated HECO moments are joining the PRD results within the systematic uncertainties very well. The adhoc shift of the HECO moments to match the PRD results, which is performed in [111], is not applied in this thesis, but it is included in the systematic uncertainties. The comparison to the results of other experiments is shown in figure 5.8. These experimental data are taken from the Yakutsk [142, 143], Hires/MIA [144], Hires [145], TA [146, 147] and LOFAR [148] publications. The Hires and TA publications give only the observed air shower maximum $\langle X_{max}^{obs.} \rangle$ including their detector reconstruction effects. For this comparison the results are shifted by a Δ factor to account for this effect by calculating the differences of the proton expectations with and without their detector [51]. The HECO $\langle X_{max} \rangle$ nicely describes the trend in the air shower maximum also seen by the other experiments. In the studied energy range from $\log(E/\mathrm{eV}) = 17.0 - 18.4$ the chemical composition seems to get lighter with increasing energy compared to the predictions from current interaction models.

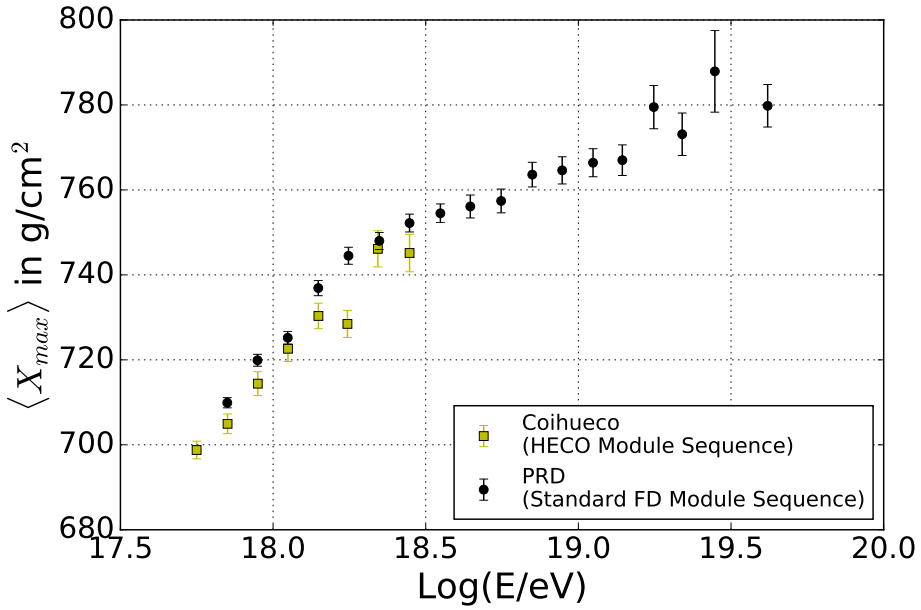

(a) The average air shower maximum $\langle X_{max} \rangle$ including statistical uncertainties as a function of energy of the Auger PRD results and Coihueco only.

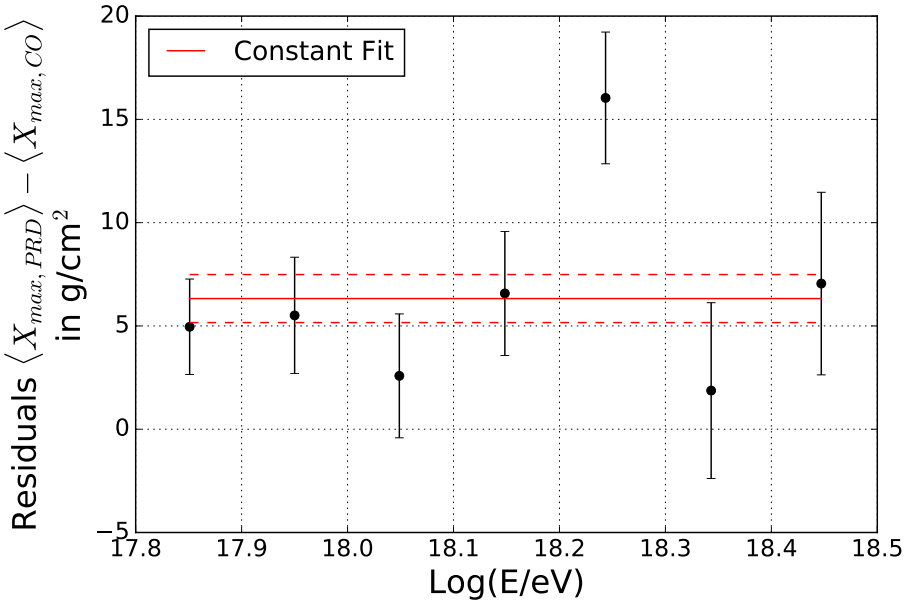

(b) Residuals of the Auger PRD results [41] to the Coihueco only $\langle X_{max} \rangle$. The difference is constant in energy, which is represented as red line.

Figure 5.5: Comparison of the X_{max}-moments calculated with Coihueco only compared to the previous results of the Pierre Auger Observatory [41]. Coihueco only data consists of a subset of the PRD raw data but reconstructed using a different module sequence.

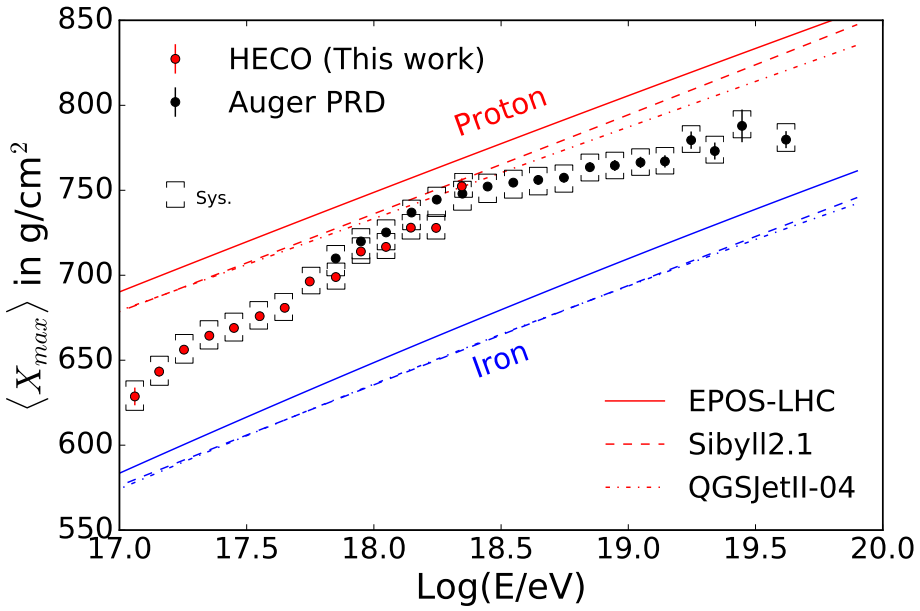

Figure 5.6: The average air shower maximum $\langle X_{max} \rangle$ including statistical and systematic uncertainties of the HECO data set as a function of energy, compared to the previous results of the Pierre Auger Observatory [41]. Expected values of pure proton and iron primaries from simulations by the current interaction models are shown as lines.

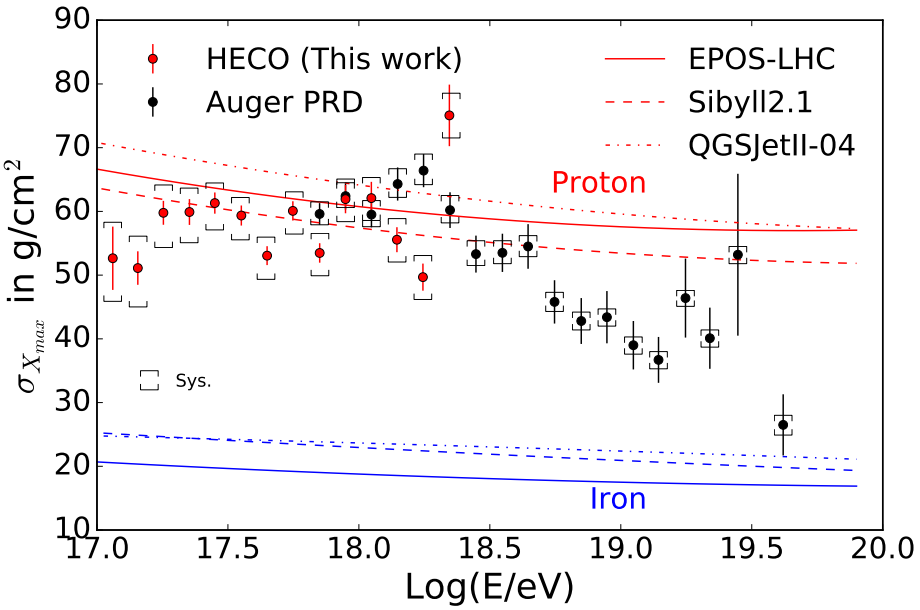

Figure 5.7: The spread of the air shower maximum $\sigma_{X_{max}}$ including statistical and systematic uncertainties of the HECO data set as a function of energy, compared to the previous results of the Pierre Auger Observatory [41]. Expected values of pure proton and iron primaries from simulations by the current interaction models are shown as lines.

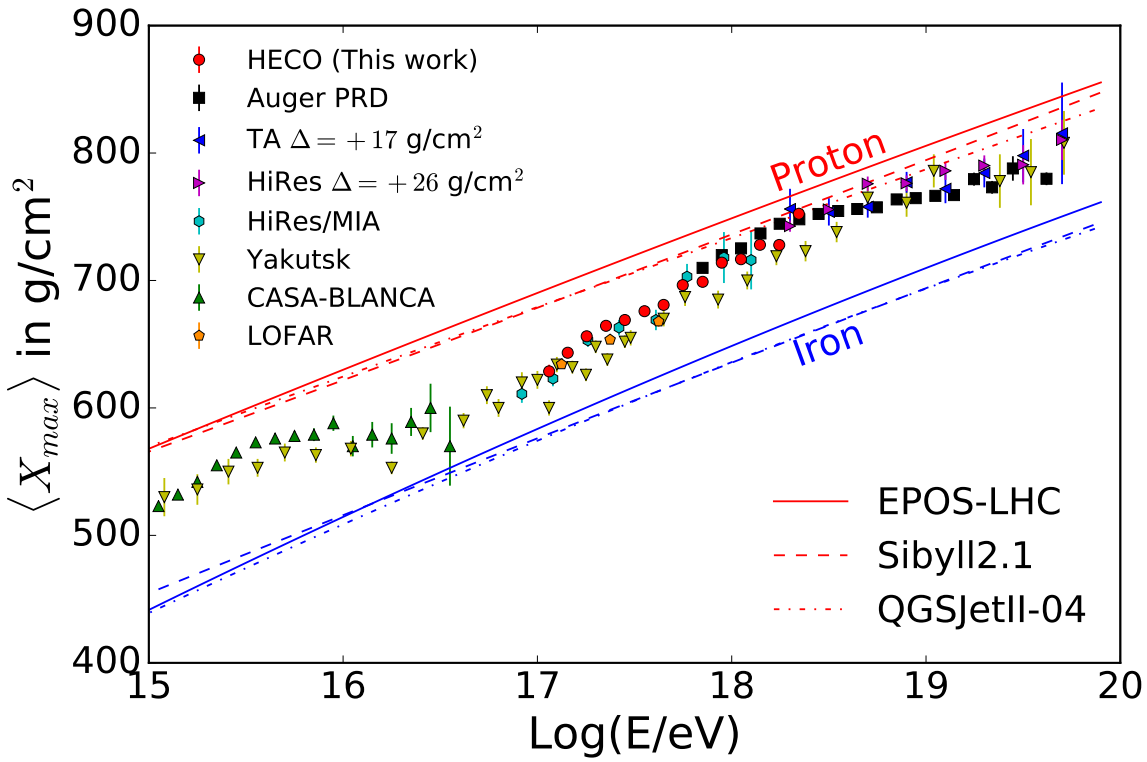

Figure 5.8: The average air shower maximum $\langle X_{max} \rangle$ including statistical uncertainties of different air shower experiments in the energy range $\log(E/\text{eV}) = 15 - 20$. Expected values of proton and iron primaries from simulations by the current interaction models are shown as lines. These experimental data are taken from Pierre Auger [41], Yakutsk [142, 143], Hires/MI A[144], Hires [145], TA [146, 147] and LOFAR [148] publications.

5.3 X_{max}-Distribution Parametrization

As already shown in the chapter 5.2, the X_{max}-distributions from Monte Carlo simulations of different interaction models differ in the mean value and in the spread of the distribution for every primary and energy. Recent measurements of the Pierre Auger Observatory [41, 42] indicate that cosmic rays are not composed of a pure primary composition in the UHECRs energy range, but are composed of a mixture of different primaries. A mixed composition can be seen as a superposition of X_{max}-distributions from different elementary groups. In this thesis, the exemplary groups are hydrogen (H), helium (He), nitrogen (N) and iron (Fe) primaries. As nuclei with atomic masses greater than iron have lower abundance in the measured cosmic ray composition (see figure 2.3). Also due to the logarithmic dependency of X_{max} on the atomic mass A given in equation 2.23, air showers induced by those particles with $A > 56$ have similar development to iron shower. With the knowledge of the position and the shape of the X_{max}-distribution for different primaries and an unbiased data set, it is possible to derive the fraction of the elementary groups producing this distribution. These fractions should not be mistaken for the real chemical composition of the cosmic rays, as each component stands for a group of different primaries, i.e. nitrogen stands for elements with similar atomic masses like carbon and oxygen.

5.3.1 Gumbel Parametrization

The X_{max}-distribution can be parametrized as a function of energy and atomic mass. As underlying function of the distribution, a generalized Gumbel distribution [149] is used, which is given by

$$G(X_{max}) = G_0 \cdot \left[e^{-z-e^{-z}}\right]^{\lambda}, z = \frac{X_{max} - \mu}{\sigma}, \tag{5.2}$$

where G_0 is the normalization factor, μ is the position of the distribution's maximum and the parameters λ and σ are shape parameters.
The empirical parametrization [150] for the Gumbel parameters are derived from Conex simulations based on EPOS LHC, QgsjetII-04 and Sibyll2.1 for primaries with a given energy E and atomic mass A. It is given by

$$\mu(A;E) = p_{0_\mu} + p_{1_\mu} \log(E/E_0) + p_{2_\mu} \log^2(E/E_0), \tag{5.3}$$
$$\lambda(A;E) = p_{0_\lambda} + p_{1_\lambda} \log(E/E_0), \tag{5.4}$$
$$\sigma(A;E) = p_{0_\sigma} + p_{1_\sigma} \log(E/E_0), \tag{5.5}$$

with the parameters

$$p_{0_{\mu,\lambda,\sigma}} = a_{0_{\mu,\lambda,\sigma}} + a_{1_{\mu,\lambda,\sigma}} \ln(A) + a_{2_{\mu,\lambda,\sigma}} \ln^2(A), \tag{5.6}$$
$$p_{1_{\mu,\lambda,\sigma}} = b_{0_{\mu,\lambda,\sigma}} + b_{1_{\mu,\lambda,\sigma}} \ln(A) + b_{2_{\mu,\lambda,\sigma}} \ln^2(A), \tag{5.7}$$
$$p_{2_\mu} = c_{0_\mu} + c_{1_\mu} \ln(A) + c_{2_\mu} \ln^2(A). \tag{5.8}$$

The parameter values for the interaction models are given in table 5.1.

QgsjetII-04	a_0	a_1	a_2	b_0	b_1	b_2
μ	761.383	-11.719	-1.372	57.344	-1.731	0.309
σ	35.221	12.335	-2.889	0.307	-1.147	0.271
λ	0.673	0.694	-0.007	0.060	-0.019	0.017
EPOS LHC	a_0	a_1	a_2	b_0	b_1	b_2
μ	775.589	-7.047	-2.427	57.589	-0.743	0.214
σ	29.403	13.553	-3.154	0.096	-0.961	0.150
λ	0.563	0.711	0.058	0.039	0.067	-0.004
Sibyll2.1	a_0	a_1	a_2	b_0	b_1	b_2
μ	770.104	-15.873	-0.960	58.668	-0.124	-0.023
σ	31.717	1.335	-0.601	-1.912	0.007	0.086
λ	0.683	0.278	0.012	0.008	0.051	0.003

QgsjetII-04	c_0	c_1	c_2
μ	-2.346	0.348	-0.086
EPOS LHC	c_0	c_1	c_2
μ	-0.820	-0.169	-0.027
Sibyll2.1	c_0	c_1	c_2
μ	-1.423	0.977	-0.191

Table 5.1: Parameters for the Gumbel parametrization of the X_{max} distributions of ultra high energy nuclei derived from Conex simulations [150].

The parameters as a function of energy and atomic mass are shown in figure 5.9 and an example of the X_{max}-distribution for the primaries H, He, N and Fe based on this Gumbel parametrization is shown in figure 5.10. To check this parametrization sets 2000 Conex air

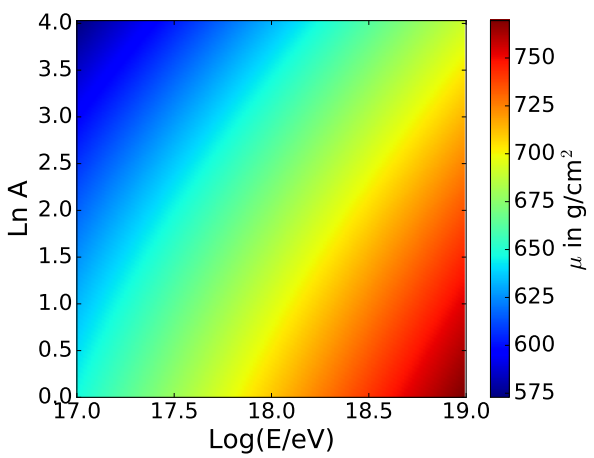

(a) Maximum of the Gumbel distribution μ.

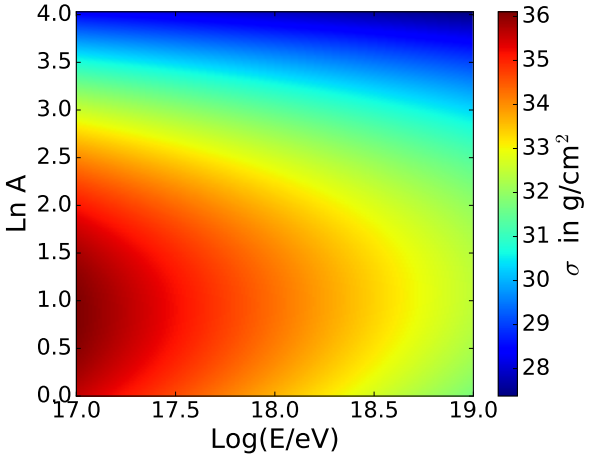

(b) Spread of the Gumbel distribution σ.

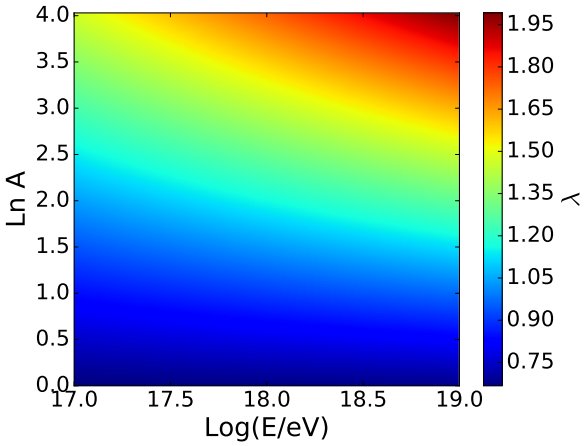

(c) Shape parameter of the Gumbel distribution λ.

Figure 5.9: Gumbel parameter [150] as a function of energy E and atomic mass A derived from Conex simulations with Sibyll2.1.

showers are generated in 0.1 bin steps between $\log(E/\text{eV}) = 17.0 - 18.5$ with EPOS LHC for H, He, N, Al and Fe. The primary Al showers are chosen here because they are not used during the determination of the parametrization constants [150] and they are used to show that this Gumbel parametrization is valid for all elements up to Fe. A direct comparison for a single energy bin of H Conex air showers and the Gumbel parametrization prediction is shown in figure 5.11. Here only the normalization of the Gumbel parametrization is adjusted to the Conex data set. The $\chi^2/ndof$ and the residuals show that the description of the X_{max}-distribution with the Gumbel parametrization is reasonable for H primaries in this energy bin. To check that this parametrization is also valid for other energies and primaries, the $\chi^2/ndof$ values

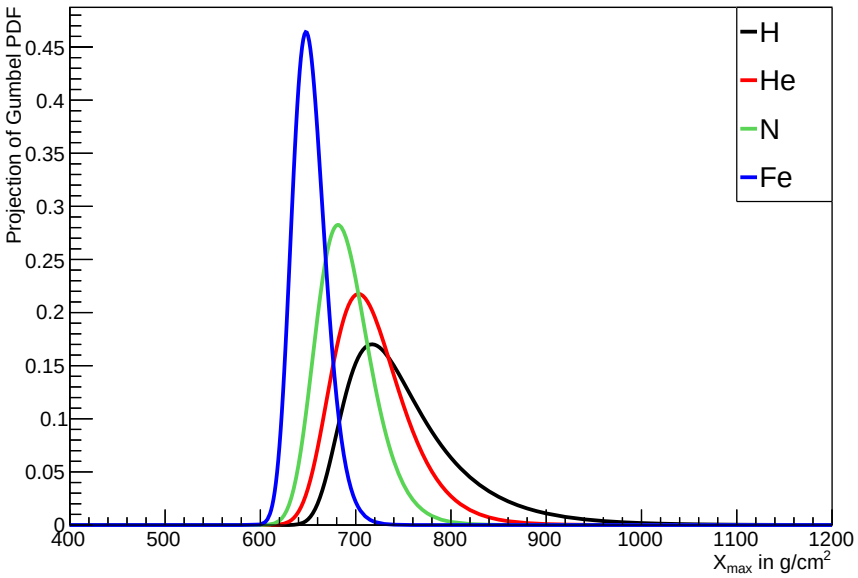

Figure 5.10: Example of Gumbel parametrization of X_{max}-distributions for H, He, N and Fe primaries at an energy of 10^{18}eV simulated with EPOS LHC.

from the comparison of the simulated Conex X_{max}-distributions and the according Gumbel parametrizations are used. In figure 5.12 these $\chi^2/ndof$ values are shown depending on the primary energy E and the logarithm of the atomic mass A. All $\chi^2/ndof$ are in an acceptable range and show that the Gumbel parametrization is a valid description of X_{max}-distributions. The according X_{max}-distributions and residuals for all tested Conex samples are given in appendix C.

This parametrization is valid for an ideal detector with a perfect X_{max}-resolution. In case of the Pierre Auger Observatory, also the actual X_{max}-resolution and acceptance of HECO have to be taken into account. The resolution is applied via a numerical convolution of the Gumbel parametrization and a Gaussian. An example of a X_{max}-distribution with and without the detector resolution of $30\,\mathrm{g/cm^2}$ is shown in figure 5.13.

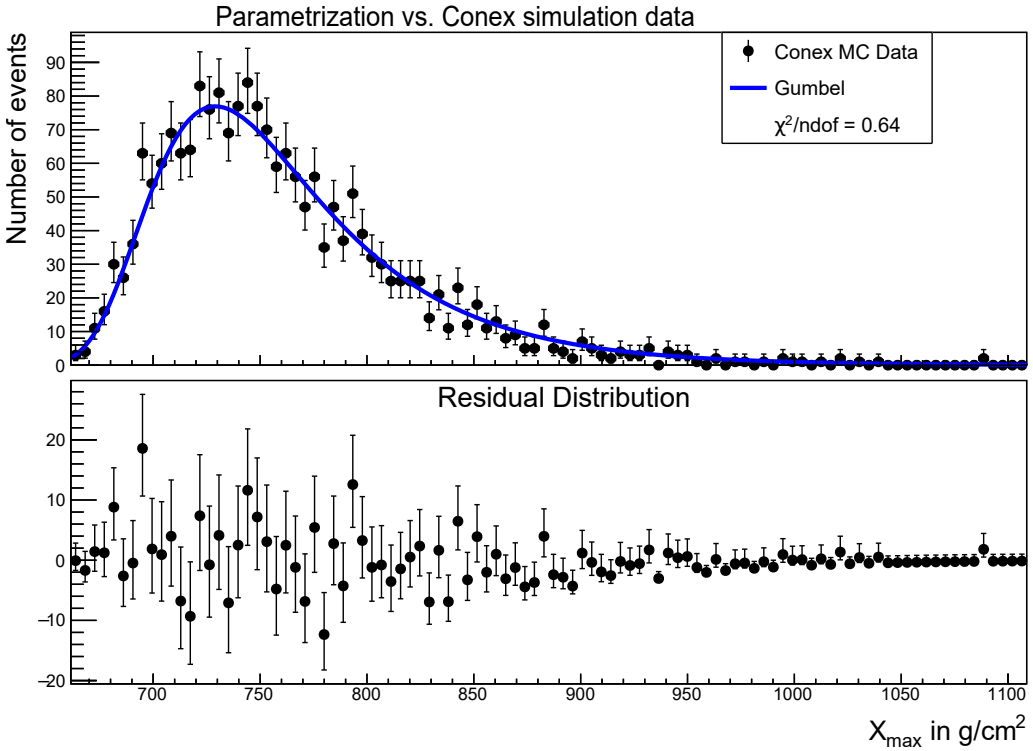

Figure 5.11: Upper plot: Gumbel parametrization of the X_{max}-distribution for H air showers at an energy of $10^{18.2}$eV compared to the X_{max} values of 2000 H Conex air showers simulated with EPOS LHC. The normalization of the Gumbel parametrization is adjusted to the Conex data. Lower plot: Residuals of the simulated Conex X_{max}-distribution with the Gumbel parametrization.

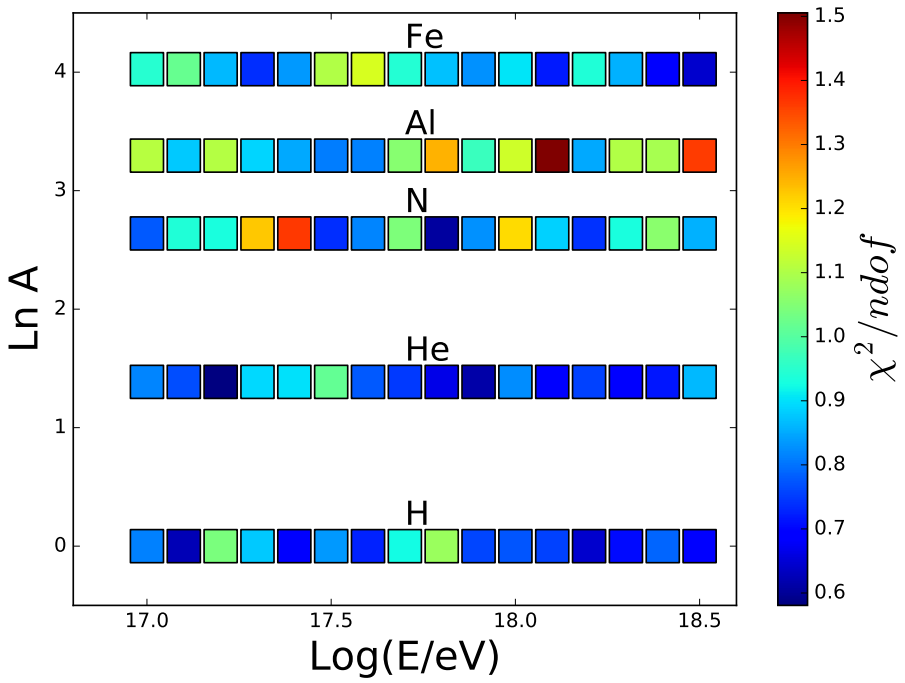

Figure 5.12: $\chi^2/ndof$ from the comparison of simulated Conex air showers with EPOS LHC and the Gumbel parametrization of the X_{max}-distribution. The according X_{max}-distributions and residuals for all tested Conex samples are given in appendix C

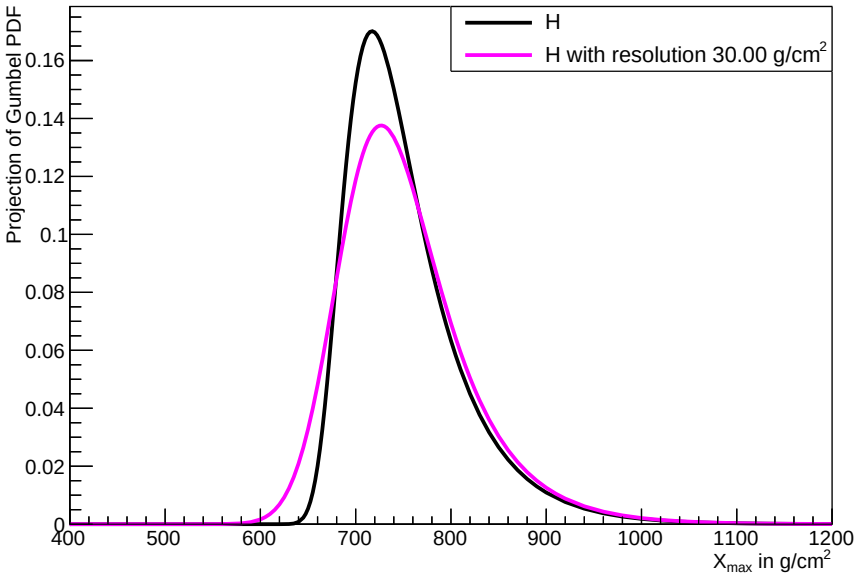

Figure 5.13: Gumbel parametrization of an EPOS LHC X_{max}-distribution for a H primary at an energy of 10^{18}eV compared to the same distribution with convoluted detector resolution of $30\,\mathrm{g/cm^2}$.

5.4 Chemical Composition Fit

The $X_{max} = x_1, ..., x_n$ values are distributed according to an underlying p.d.f. of the chemical composition $f(x; \mathbf{\Theta})$, which is the probability density to find a shower maximum $x = X_{max}$ if chemical composition parameter set of cosmic rays is $\mathbf{\Theta} = (\Theta_1, ..., \Theta_m)$ assuming a given interaction model and the fluorescence detector of the Pierre Auger Observatory. As cosmic ray induced air showers are uncorrelated events, the number of observations n itself is Poisson distributed with a mean value ν. Therefore, the likelihood function of the X_{max}-distribution is given by

$$L(\nu, \mathbf{\Theta}) = \frac{\nu^n}{n!} e^{-\nu} \prod_{i=1}^{n} f(x_i; \mathbf{\Theta}) = \frac{e^{-\nu}}{n!} \prod_{i=1}^{n} \nu f(x_i; \mathbf{\Theta}). \tag{5.9}$$

This function is called an extended likelihood function [151]. This p.d.f. is a superposition of the different known primary particle parametrizations and given by

$$f(x_i; \mathbf{\Theta}) = \sum_{j}^{m} \Theta_j f_j(x_i). \tag{5.10}$$

The parameters Θ_j are not independent in this case, but their sum is constrained to unity. Instead of replacing one coefficient by $1 - \sum_{j=1}^{m-1} \Theta_j$, this constraint is treated in a more symmetrical way by calculating the log-likelihood of the data sample as

$$\ln L(\nu, \mathbf{\Theta}) = -\nu + \sum_{i=1}^{n} \ln \left(\sum_{j}^{m} \nu \, \Theta_j f_j(x_i) \right), \tag{5.11}$$

where an additive term $\ln(n!)$ is neglected, as the estimation of the parameters only depend on the derivatives of $L(\nu, \mathbf{\Theta})$ [151]. Now, the expected numbers of events of type j are defined as $\mu_j = \nu \, \Theta_j$ and the log-likelihood function can be written as

$$\ln L(\boldsymbol{\mu}) = -\sum_{j=1}^{m} \mu_j + \sum_{i=1}^{n} \ln \left(\sum_{j}^{m} \mu_j f_j(x_i) \right), \tag{5.12}$$

with $\boldsymbol{\mu} = (\mu_1, ..., \mu_m)$. The parameters $\boldsymbol{\mu}$ are then no longer subject to a constraint on Θ_j and give a direct estimator for the number of events of type j. In case of the X_{max}-distributions the used p.d.f. is the Gumbel distribution described in chapter 5.3.1 with $f_j(x_i) = G_j(E, X_{max})$, where j represents the used primary group, for example $j = (H, He, N, Fe)$ in case of a 4-component fit. To calculate the uncertainties of the fit results the profile of the likelihood function is used to get the confidence intervals. With the profile likelihood method a multidimensional likelihood function is reduced to a function depending only on one interesting parameter [152]. In this thesis the 68% and the 95% confidence ranges of the chemical composition fractions are calculated for each primary group by treating the other groups as nuisance parameters. This method considers correlations of the parameters and also provides a good sampling of the parameter space for the confidence intervals, even at the boundaries.

5.4.1 Fit of Chemical Composition on Monte Carlo Data

The method to fit the chemical composition is first tested on Monte Carlo data sets generated with the Gumbel parametrizations for different primaries. For this MC study, the fitting procedure of root [153] and especially the Roofit [128] package are used.
The chemical composition of the MC test sample is based on the H3a model [154] from predicted cosmic ray fluxes for H, He, CNO group, MgSi group and Fe primaries. This model provides a prediction of the different UHECRs chemical composition fractions for every energy bin. In this Monte Carlo data set, the X_{max} values are simulated by using Gumbel parametrization [150] of the EPOS LHC [61, 62] interaction model for an ideal detector. The number of events per energy bin is chosen to be similar to the current statistics of the final HECO data set, namely $\approx$ 1000 events for each energy bin. The MC data set is analyzed with 3 different fit scenarios with different primary groups.

First a 5-component fit with the generated primaries is applied to the simulated data to show the capability of this method to reconstruct the correct primary composition, when using the correct primary parameter set. An example of a Gumbel fit result is shown in figure 5.14. The MC data are reconstructed very well by the extended log likelihood fit. However, the true

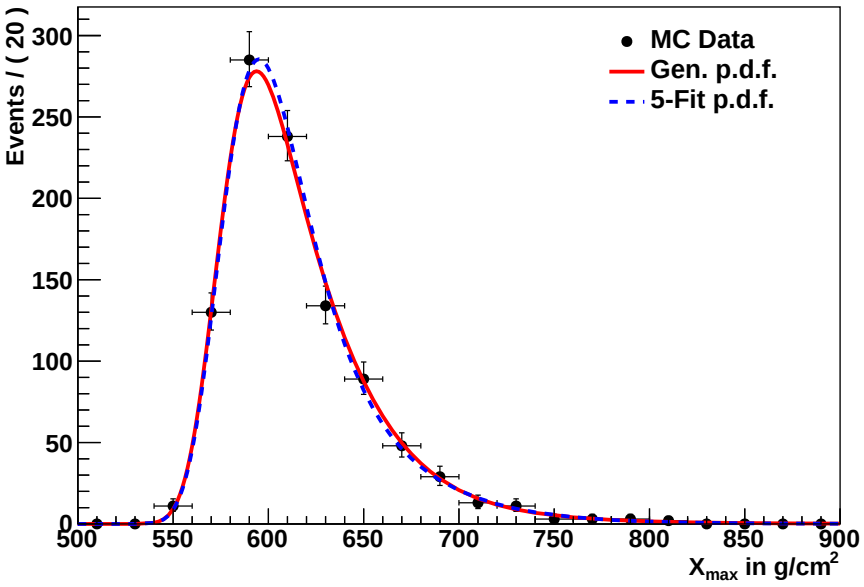

Figure 5.14: Fit result for one energy bin of simulated X_{max}-distribution (red line) based on the H3a model [154] analyzed with a 5-component Gumbel parametrization (blue dashed line) including H, He, N, Si and Fe.

primary composition for the HECO data is not known and the fit result is depending on the chosen primaries of the fit. Therefore, the same MC sample is analyzed again with different assumptions on the primary distribution to illustrate the issues of such an analysis method.

The simplest test is a 2-component fit consisting of a mixture of a H and Fe Gumbel parametrizations, which is a extreme scenario, and a result of this fit is shown in figure 5.15. As expected, the 5-component scenario is not described by the 2-component fit as clear deviations from the MC data and the fit result are visible.

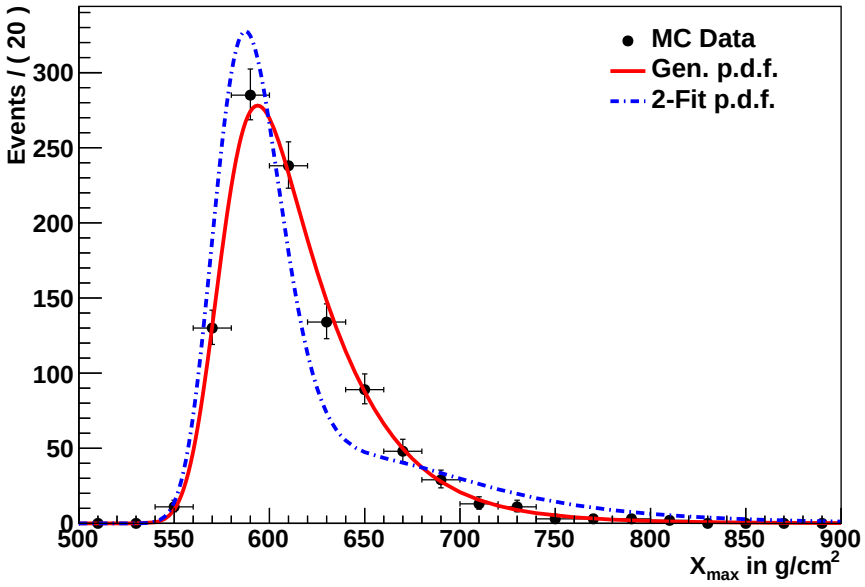

Figure 5.15: Fit result for one energy bin of simulated chemical composition of cosmic rays based on the H3a model [154] analyzed with a 2-component Gumbel parametrization.

A more realistic assumption, is to apply a 4-component Gumbel parametrization based on H, He, N and Fe. An example of the resulting fit is shown in figure 5.16. This fit describes the data points almost as good as the 5-component fit.

The MC truth and the fitting results over the whole simulated energy range of the 5-component fit including the confidence limits are shown in figure 5.17. The 69% and 95% confidence limits are computed by a profile log likelihood study[152]. The fit results describe the MC truth very well inside the expected uncertainties. The fit results of 2-component fit over the whole energy range are shown in figure 5.18. As shown previously the 2-component fit cannot describe the MC truth in this scenario accurately. The fit results of the 4-component fit over the whole energy range are shown in figure 5.19. The plot shows that the missing Si primary component is fragmented into the fraction of the neighborhood components N and Fe, as they have a similar shape. Even if the true composition is not reconstructed correctly, the fitting method gives a very good result on the superior composition classification light, medium or heavy composition.

The number and the chosen primary components are therefore very crucial to get a reasonable primary composition result. It is also important not to overshot the complexity of the

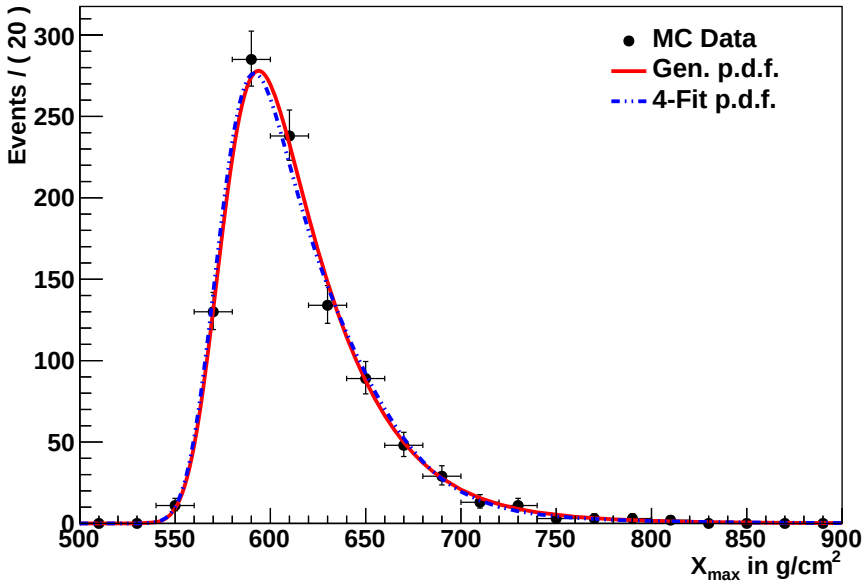

Figure 5.16: Fit result for one energy bin of simulated chemical composition of cosmic rays based on the H3a model [154] analyzed with a 4-component Gumbel parametrization.

fitted composition as the fit uncertainties of course increase with additional free parameters.

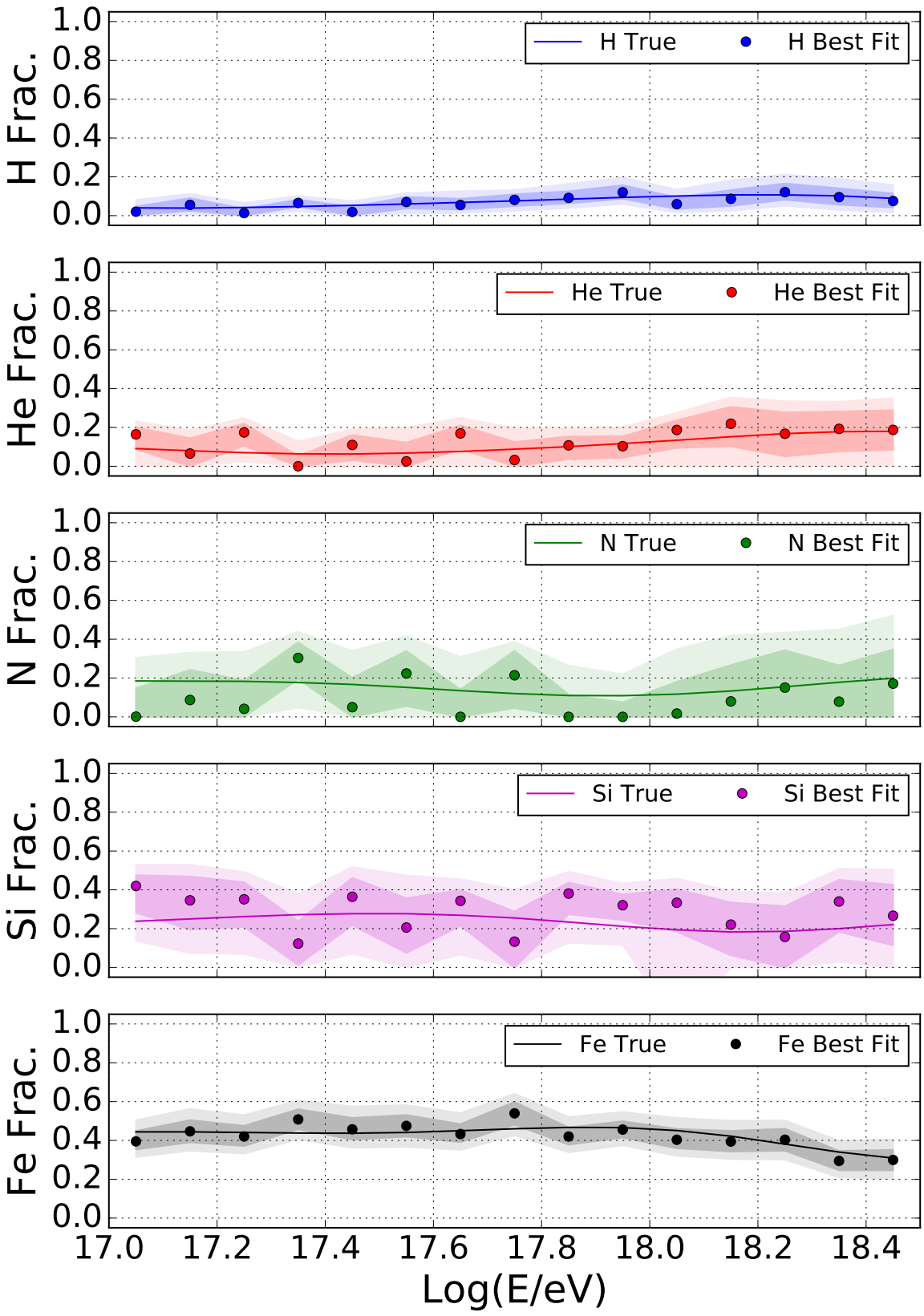

Figure 5.17: Reconstruction of simulated chemical composition of cosmic rays based on the H3a model [154] analyzed with a 5-component Gumbel parametrization. Contours give the 68% and 95% confidence levels derived from profile log likelihood studies. The MC truth is illustrated as a solid line.

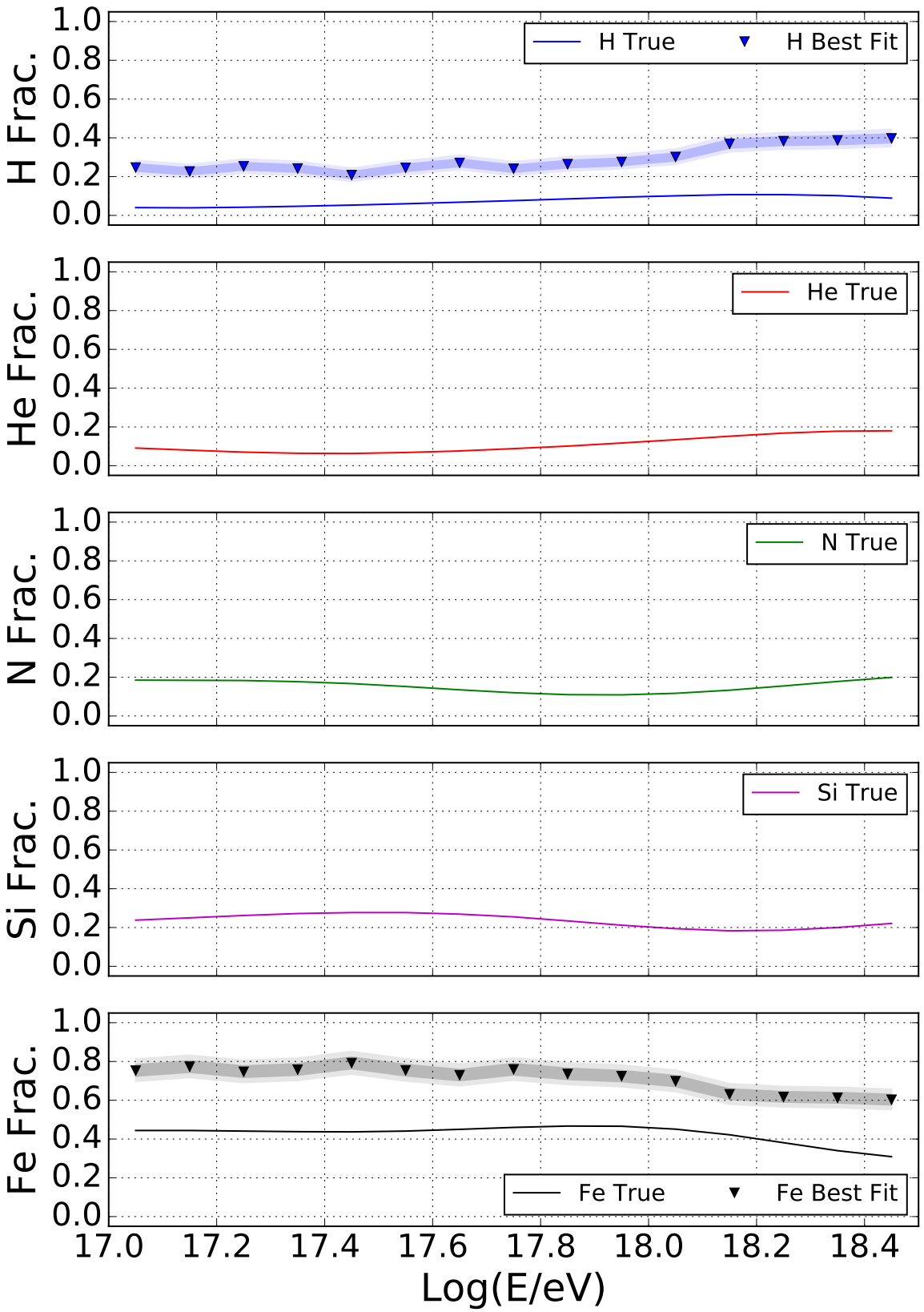

Figure 5.18: Reconstruction of simulated chemical composition of cosmic rays based on the H3a model [154] analyzed with a 2-component Gumbel parametrization. Contours give the 68% and 95% confidence levels derived from profile log likelihood studies. The MC truth is illustrated as a solid line.

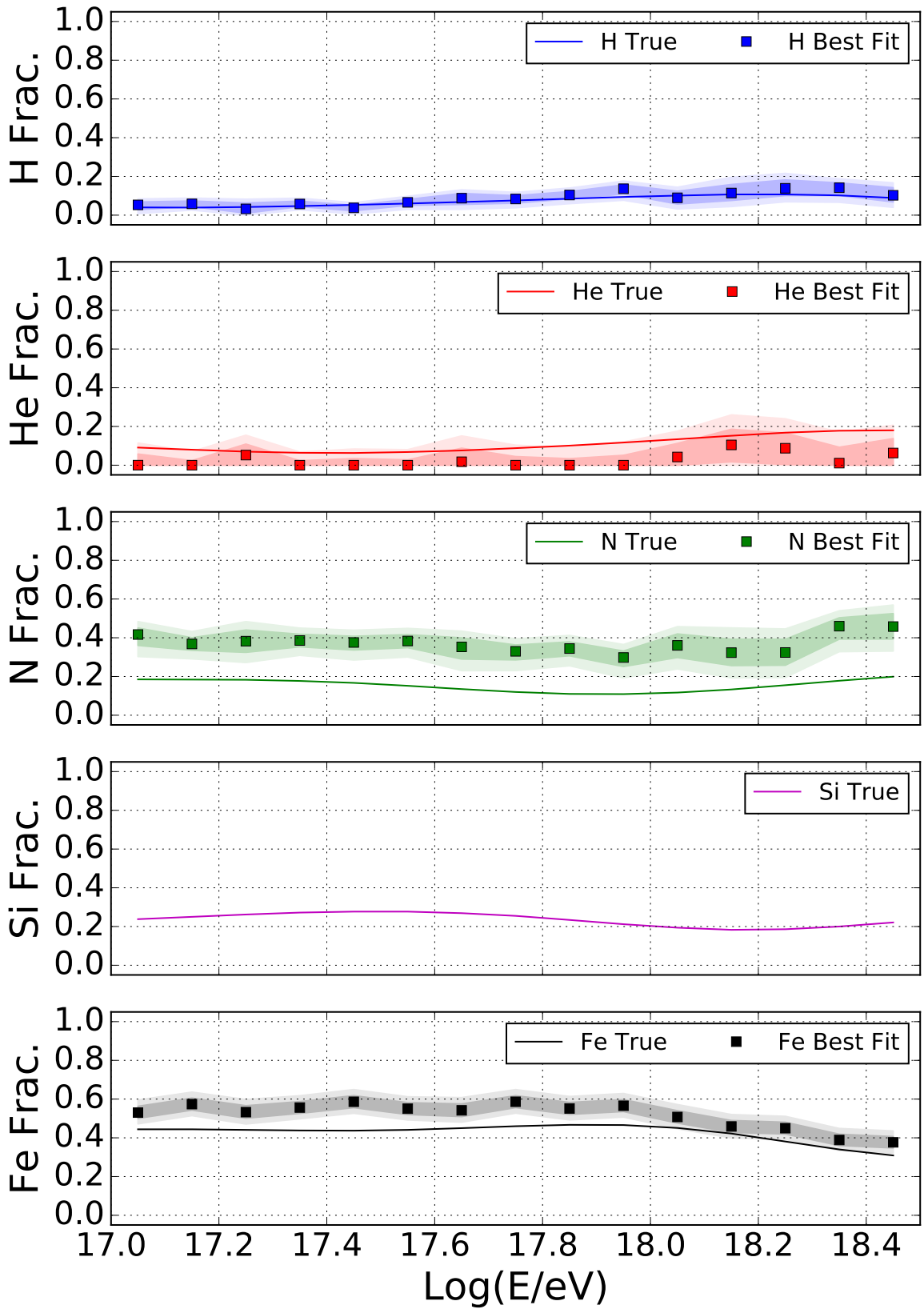

Figure 5.19: Reconstruction of simulated chemical composition of cosmic rays based on the H3a model [154] analyzed with a 4-component Gumbel parametrization. Contours give the 68% and 95% confidence levels derived from profile log likelihood studies. The MC truth is illustrated as a solid line.

5.4.2 Goodness-of-fit and P-value Determination

The previous chapter shows the importance of the choice of the primary composition for the fit method. The extended log likelihood in formula 5.12 provides a method for the parameter estimation, but it does not give directly a method for the estimation of the goodness-of-fit of this analysis. For the evaluation of this goodness-of-fit of the chemical composition fit with the Gumbel parametrization, MC studies are used to calculate the negative log likelihood *nll* distribution of the parametrization using equation 5.12.

To do this, the fit results from the previous chapter are used to generate many MC data sets with the same number of events as the original data set. These MC data sets are re-analyzed again with the same fit routine. By comparing the fit negative log likelihood *nll* value of the fit result to the distribution of these MC data sets [151], the P-value for the fit is given by the integrals

$$P = \frac{1}{n_{MC}} \int_{-\infty}^{nll_{fit}} nll \, d(nll), \tag{5.13}$$

with the number of MC fits n_{MC}.

The fit results shown in figure 5.15 for the 2-component fit, in figure 5.16 for the 4-component fit and in figure 5.14 for the 5-component fit are now used to generate MC data sets for the negative log likelihood *nll* distributions. In these examples, the distributions are derived by a total of 1000 MC data sets per energy bin. The resulting negative log likelihood *nll* distributions for the 5-component fit are shown in the figures 5.20, for the 2-component fit in figure 5.21 and for the 4-component fit in figure 5.22. The P-values for all fit results shown in the previous chapter are shown in figure 5.23. As shown previously the 2-component fit results are not describing the data set and the calculated P-values are low. Only due to the limited statistics of the X_{max} values, the 2-component scenario is not ruled out by the P-values completely. The *nll* of the 4-component and 5-component fit results are compared to the *nll* test distributions in a reasonable domain. The 5-component fit results have slightly better P-values, but this is expected as they use the correct primary parameter set for this scenario. Although, there are 5-components inside the MC data set the 4-component fit delivers reasonable results for the given primary groups. As the fitted fraction results depends strongly on the given number of events, the number of fitted primaries should preferably sample the chemical composition range equally, to get reasonable fraction results for a limited number of primary groups. To conclude, the 4-component fit is adequate for the analysis of cosmic ray data with limited statistics.

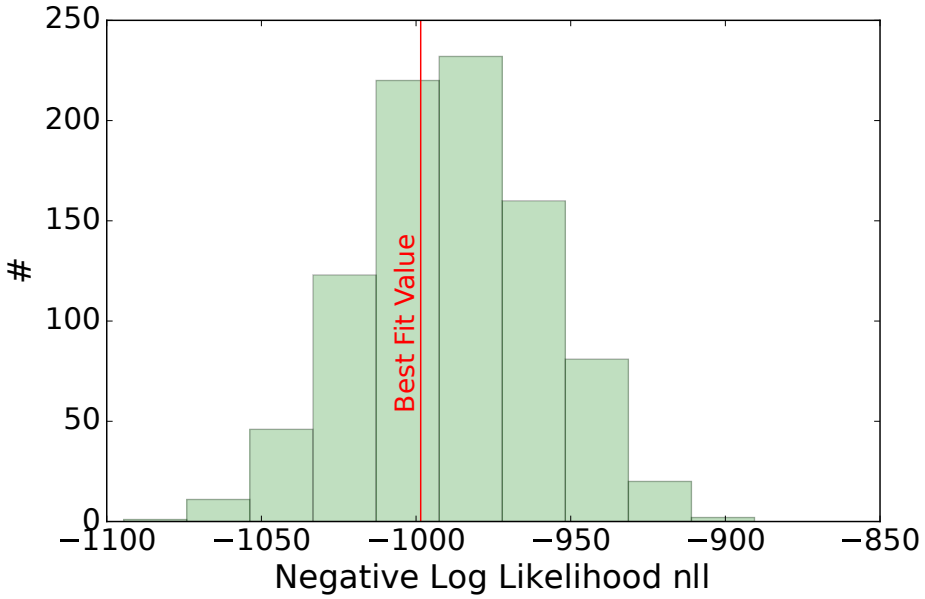

Figure 5.20: Negative log likelihood *nll* distributions of the fit result of simulated chemical composition of cosmic rays based on the H3a model [154] analyzed with the 5-component Gumbel parametrization shown in figure 5.14. The red line indicates the position of the *nll* values for the best fit.

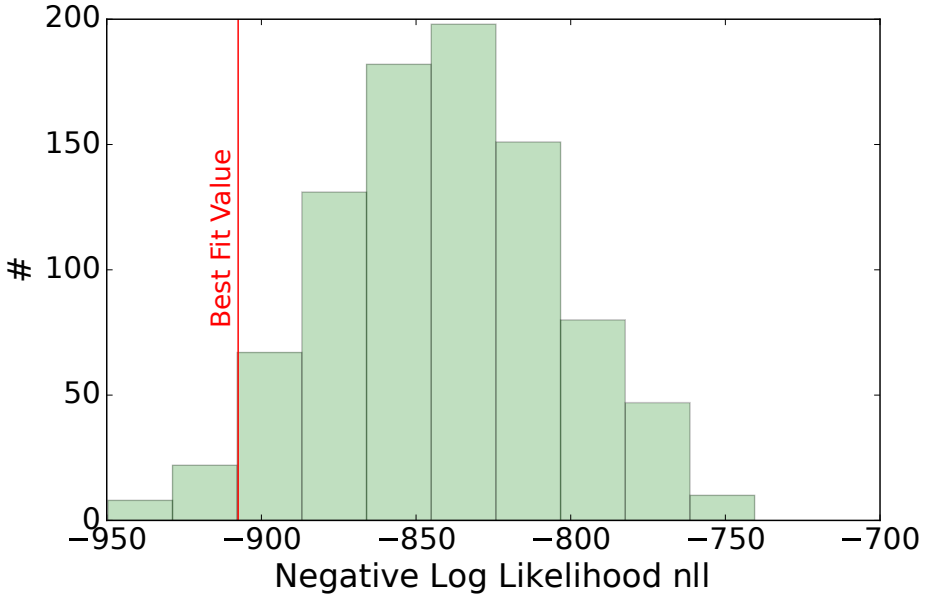

Figure 5.21: Negative log likelihood *nll* distributions of the fit result of simulated chemical composition of cosmic rays based on the H3a model [154] analyzed with the 2-component Gumbel parametrization shown in figure 5.15. The red line indicates the position of the *nll* values for the best fit.

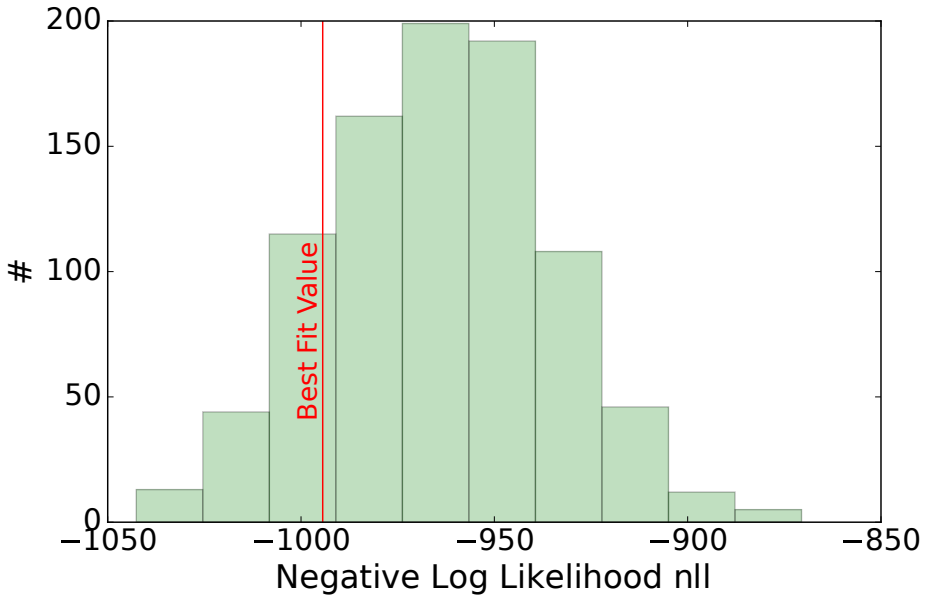

Figure 5.22: Negative log likelihood *nll* distributions of the fit result of simulated chemical composition of cosmic rays based on the H3a model [154] analyzed with the 4-component Gumbel parametrization shown in figure 5.16. The red line indicates the position of the *nll* values for the best fit.

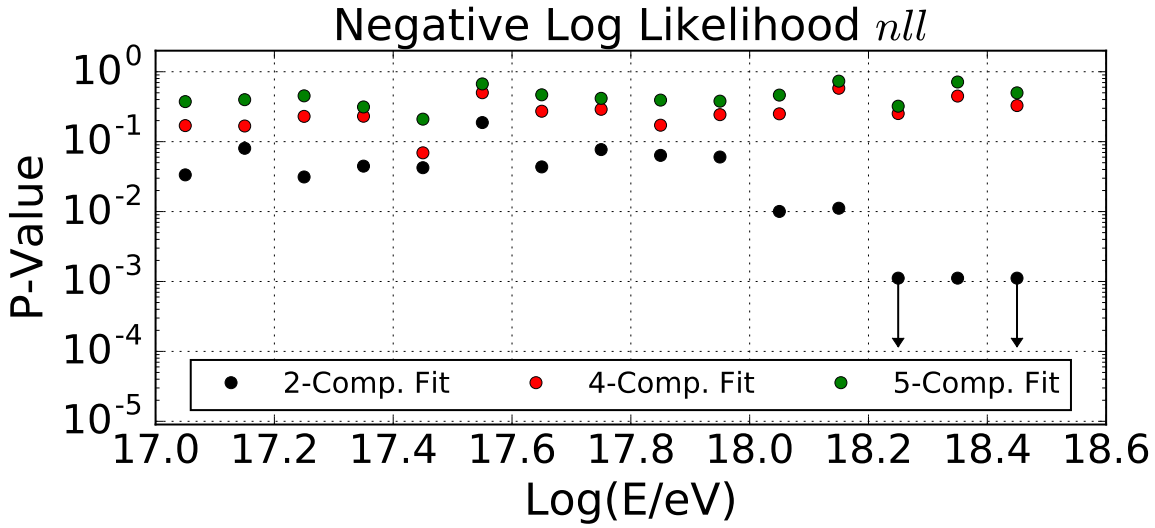

Figure 5.23: P-values calculated for the fits in figures 5.17, 5.18 and 5.19 by the *nll* distribution of MC data set fit. Arrows indicating the upper limit of the calculated P-value.

5.5 Chemical Composition Fraction from X_{max}-Distributions

This thesis extends the energy range down of the fitted fractions to 10^{17} eV. Therefore, a comparison to recently published fractions of the Pierre Auger collaboration [42] is made. A similar method for the standard telescopes with the Gumbel statistics on the X_{max}-distributions of the air shower data from ICRC 2011 and ICRC 2013 was performed by M. Urban in [155, 156].

As shown in the previous chapter, the 4-component fit is sufficient enough for the qualitative analysis of the chemical composition. The HECO X_{max}-distribution used in the moment calculation in chapter 5.2 are analyzed with a Gumbel parametrization and an extended likelihood function. An example for the X_{max}-distribution for the energy bin $\log(E/\text{eV}) = 17.4 - 17.5$ with a fraction fit with EPOS LHC is shown in figure 5.24. This fit includes the total X_{max}-resolution and the detector acceptance. The distributions and the fits of the other energy bins of all interaction models are shown in the appendix D. The fit results for the studied energy

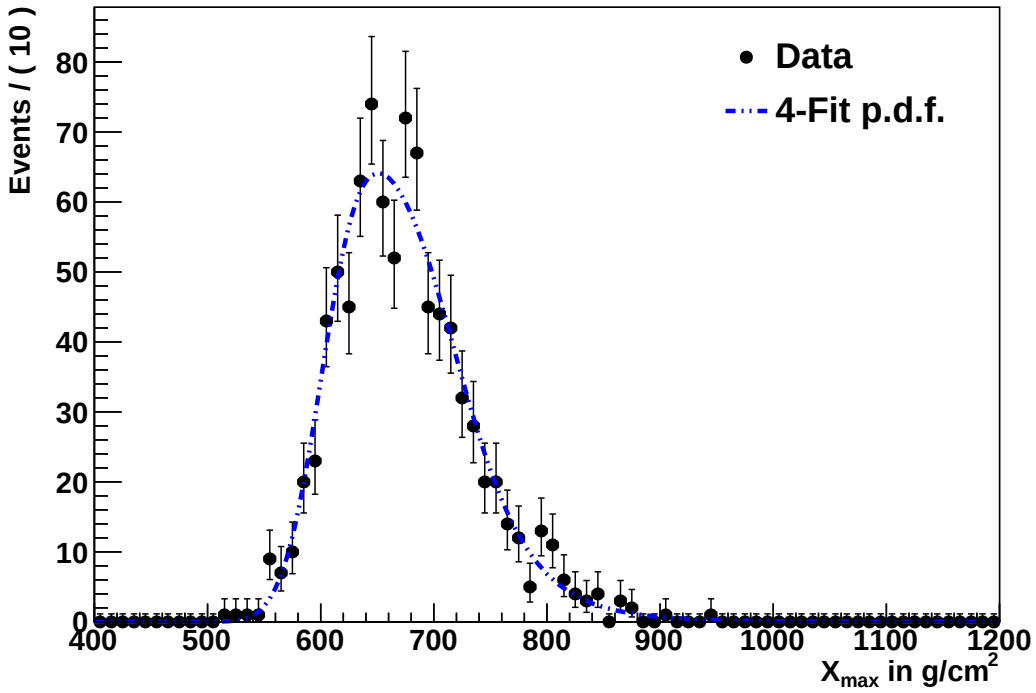

Figure 5.24: HECO X_{max}-distribution for $\log(E/\text{eV}) = 17.4 - 17.5$ analyzed with a 4-component Gumbel parametrization simulated with the EPOS LHC interaction model. Total X_{max}-resolution and detector acceptance are included.

bins are shown in figure 5.25 for Sibyll2.1, in figure 5.26 for QgsjetII-04 and 5.27 for EPOS LHC. These figures include 68% and 95% confidence limits derived from profile likelihood studies [152], which is described in the previous chapter.

The considered sources of systematic uncertainties are the energy uncertainty δE_{Tot}, which is described in chapter 4.5.1, total systematic uncertainty δX_{Tot} and the resolution uncertainty δRes_{Tot} of the X_{max} measurements, which are described in chapter 4.6. To account for this systematic uncertainties, the Gumbel parametrizations of the primaries are shifted up to $\pm\delta$ of the energy and X_{max} systematic uncertainties. This is done for all possible combinations and the data are re-analyzed. As the composition fit is not expected to evolve monotonically due to the shift of these uncertainties, the range between -δ and δ is scanned in $0.2\,\sigma$ steps. After these scans, the largest deviation from the best fit result is taken as the systematic uncertainty of the fraction fit. The calculated P-values show good agreement of the fit and the data.

All interaction models show a mixed composition of nitrogen and iron like nuclei at the starting point of 10^{17}eV in this study with only minor contributions of hydrogen. Due to the low event statistics and the large X_{max} detector resolution, the uncertainties of these fraction are large. All models show the same continuous rising fraction of the light element groups like hydrogen and helium with increasing energy. This indicates a change in the composition of the cosmic rays. At the end of the analyzed energy range at $10^{18.3}$eV, the composition seems to be dominated by cosmic rays consisting of hydrogen and helium like nuclei.

In this context, the HECO results are compared to the chemical composition fraction results of the standard FD telescopes [42]. These analyses use a similar method in the determination of the primary fractions. Instead of a parametrization of the X_{max}-distribution, template histograms for every energy bin and every primary from large MC studies are produced. With these templates a superposition model is created to fit the primary fractions. This fit method is also based on likelihood minimization. The comparison of both analyses is shown in figure 5.28 for Sibyll2.1, in figure 5.29 for QgsjetII-04 and in figure 5.30 for EPOS LHC. The HECO fraction results attached nicely to the regular FD results inside the given statistical and systematic uncertainties. The large component of heavy elements at 10^{17} eV shown in all interaction models supports the hypothesis of an iron 'knee' in the galactic cosmic ray component and the rising fractions of light elements support the assumption of a transition from galactic to extra galactic component, which is nearly completed at $10^{18.3}$ eV.

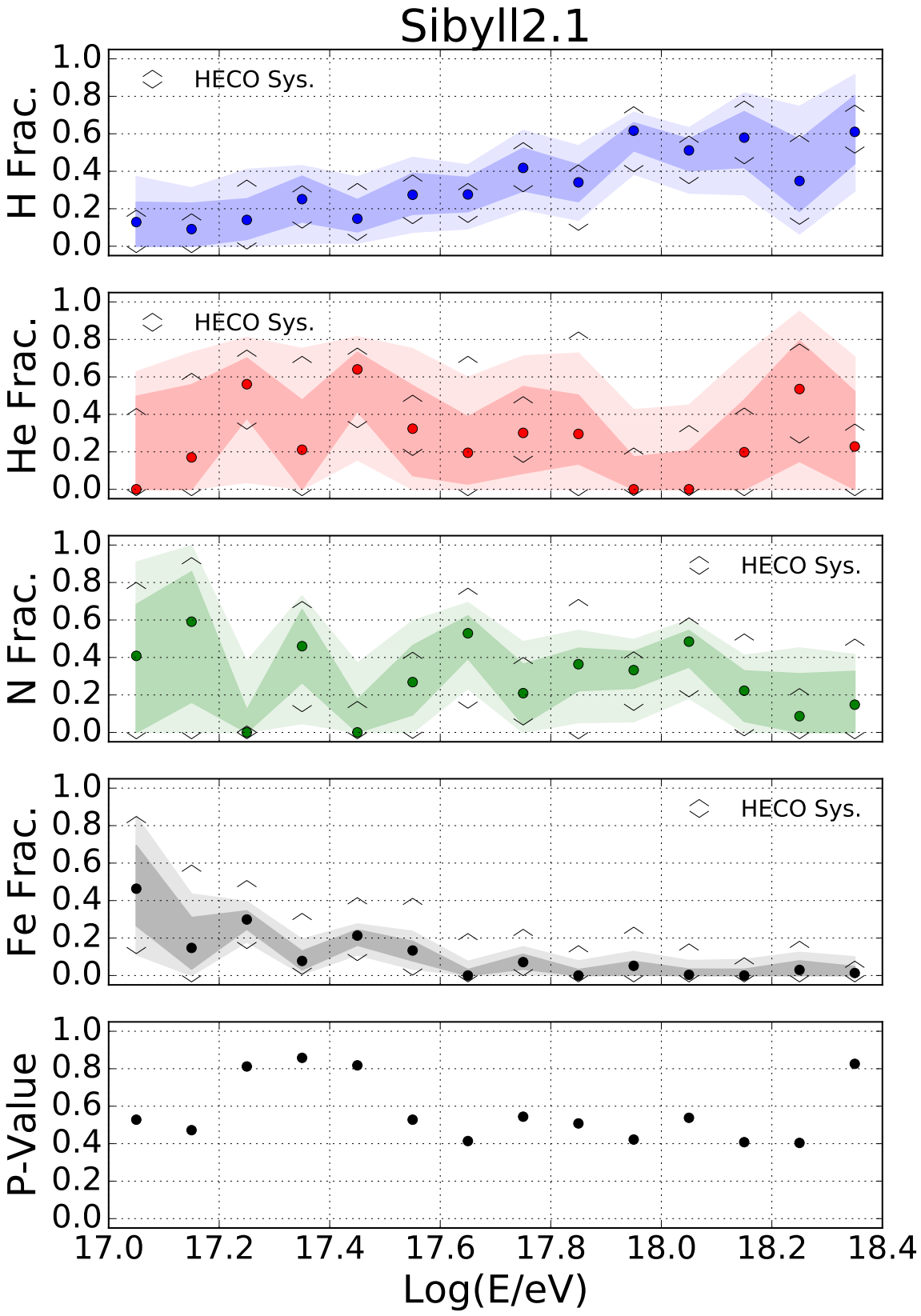

Figure 5.25: Reconstruction of chemical composition of cosmic rays analyzed with a 4-component Gumbel parametrization with Sibyll2.1 including systematic uncertainties. Contours give the 68% and 95% confidence levels derived from profile log likelihood studies. P-values are calculated with Monte Carlo studies of the *nll*-distribution.

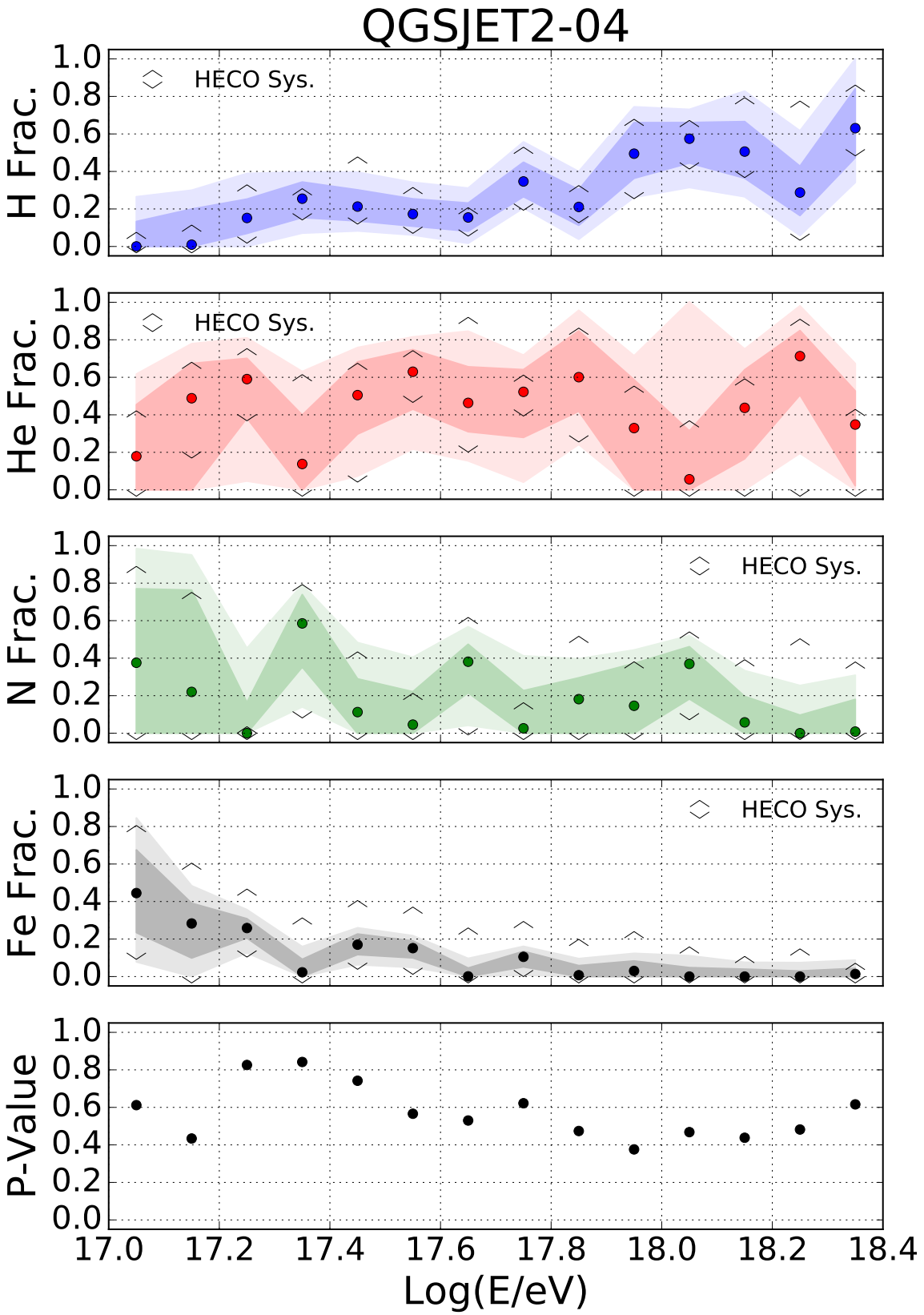

Figure 5.26: Reconstruction of chemical composition of cosmic rays analyzed with a 4-component Gumbel parametrization with QgsjetII-04 including systematic uncertainties. Contours give the 68% and 95% confidence levels derived from profile log likelihood studies. P-values are calculated with Monte Carlo studies of the *nll*-distribution.

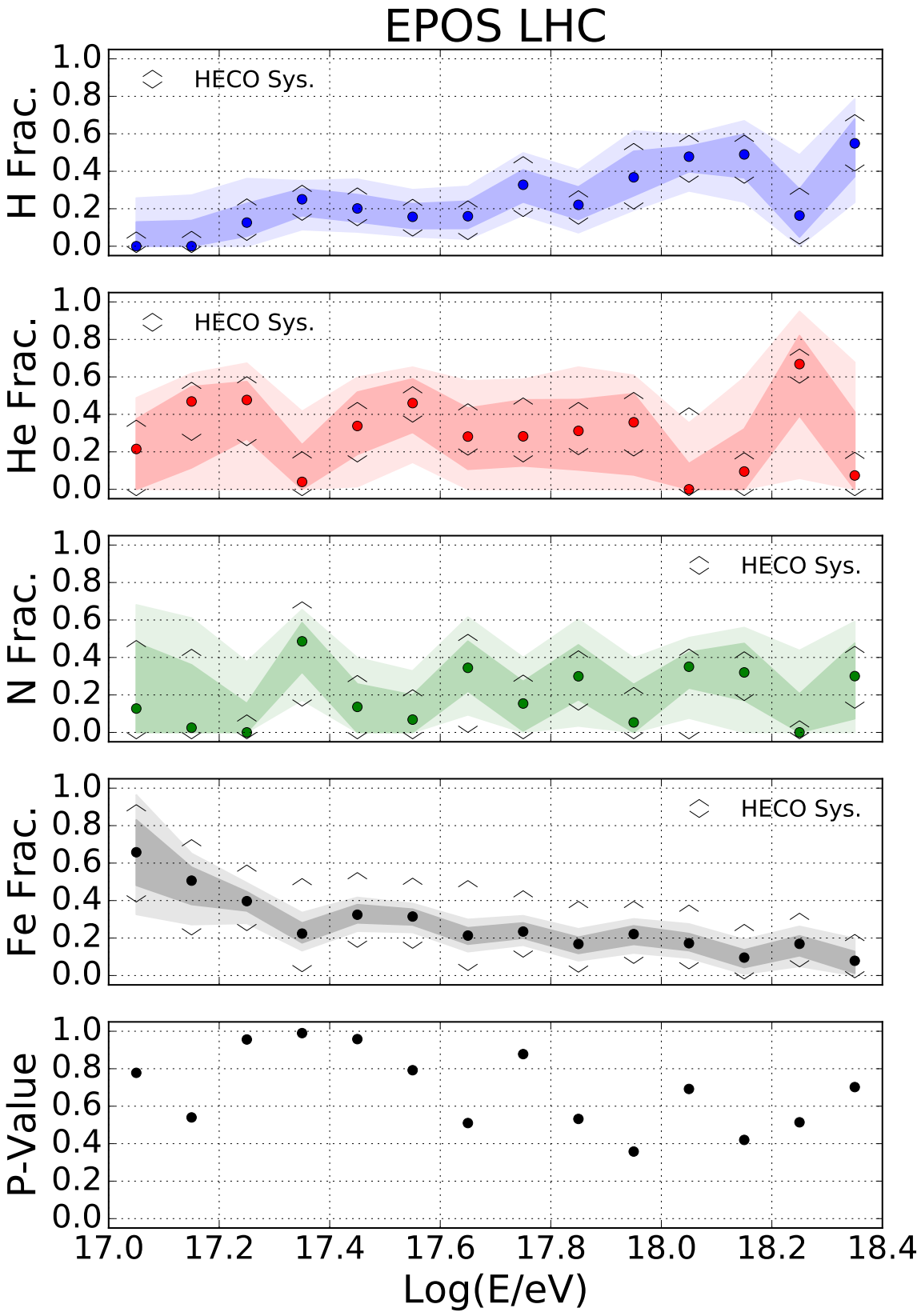

Figure 5.27: Reconstruction of chemical composition of cosmic rays analyzed with a 4-component Gumbel parametrization with EPOS LHC including systematic uncertainties. Contours give the 68% and 95% confidence levels derived from profile log likelihood studies. P-values are calculated with Monte Carlo studies of the *nll*-distribution.

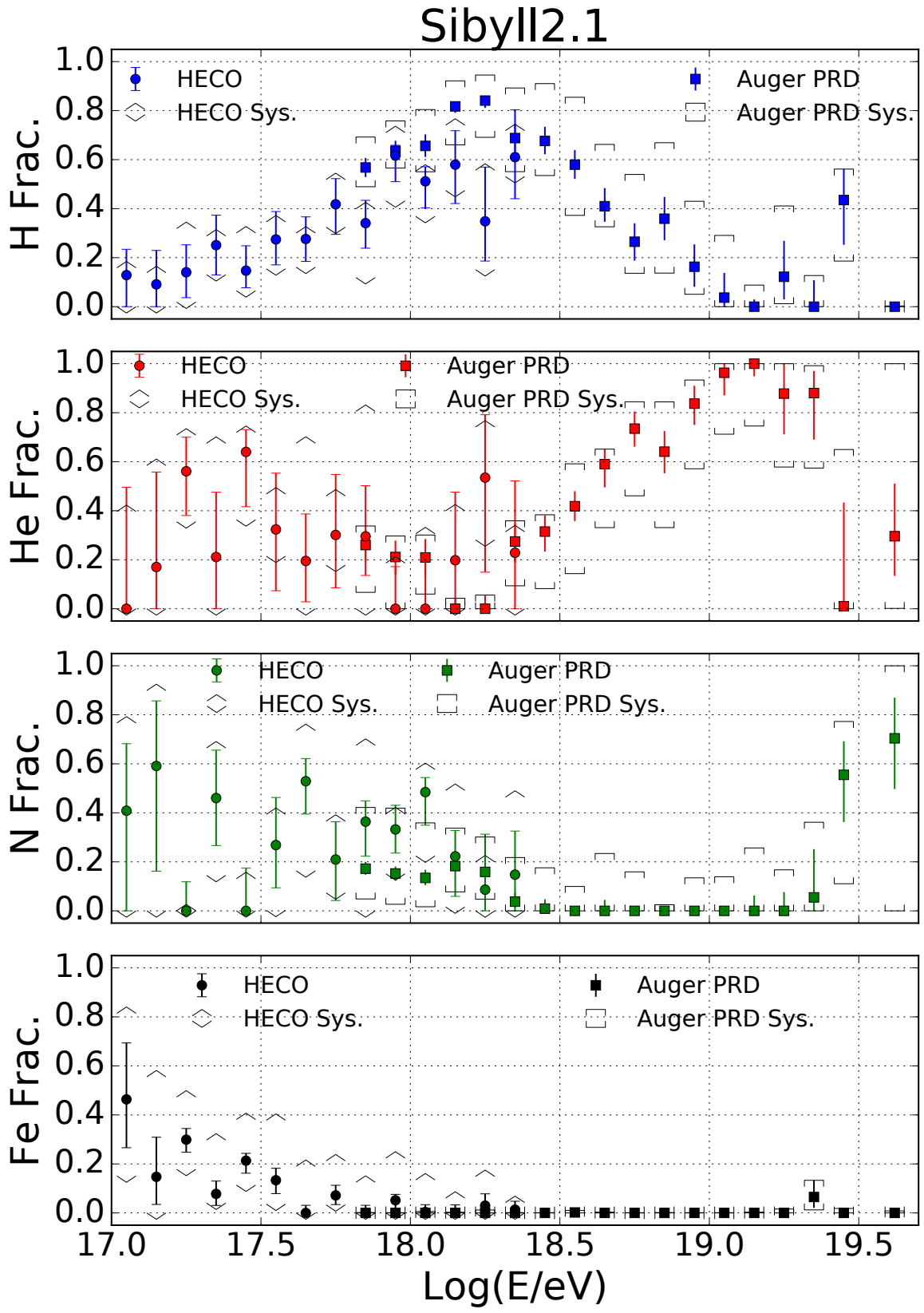

Figure 5.28: Reconstruction of chemical composition of cosmic rays analyzed with a 4-component Gumbel parametrization with Sibyll2.1 compared to the Pierre Auger fraction results [42]. Systematic uncertainties are shown for both data sets.

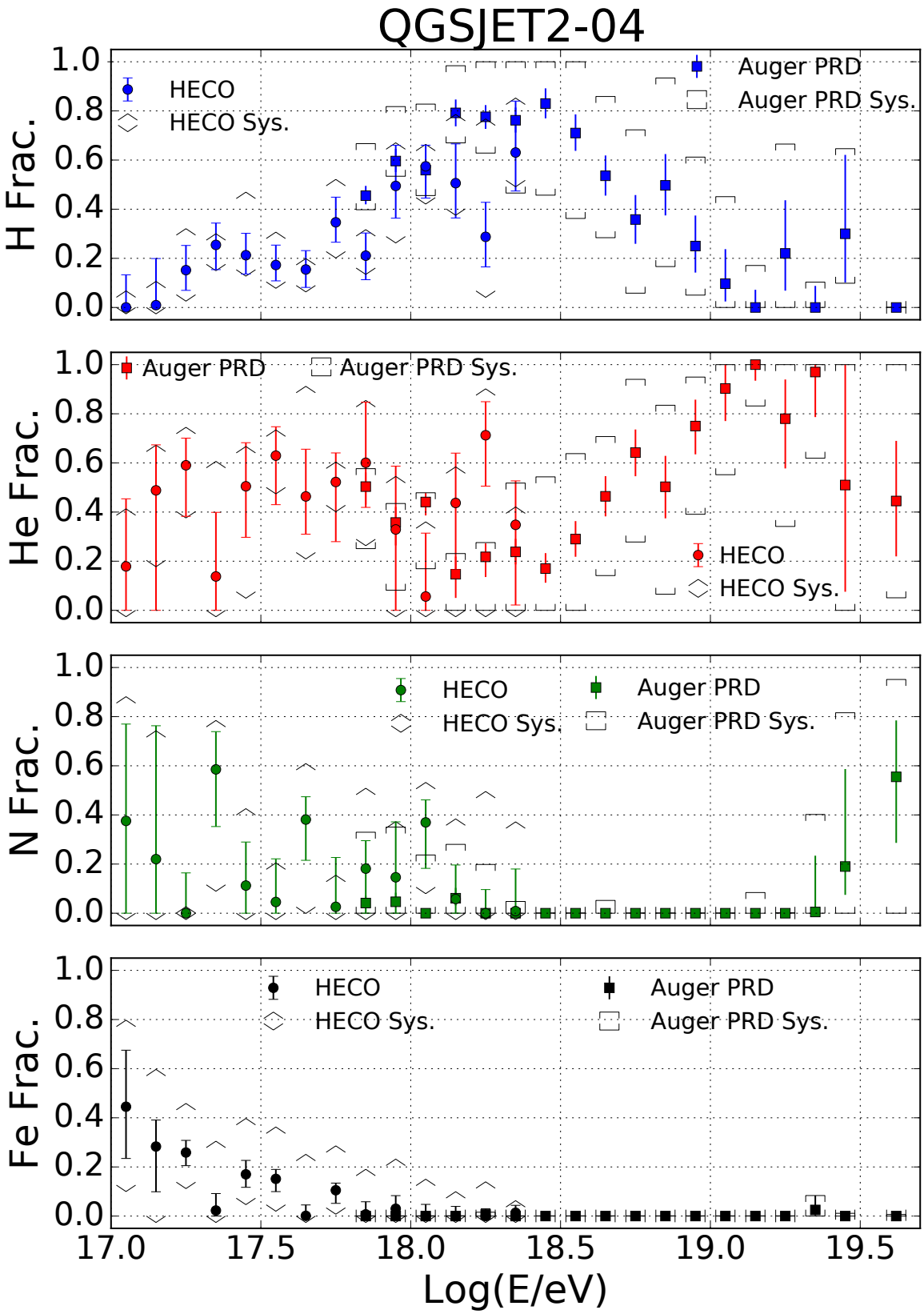

Figure 5.29: Reconstruction of chemical composition of cosmic rays analyzed with a 4-component Gumbel parametrization with QgsjetII-04 compared to the Pierre Auger fraction results [42]. Systematic uncertainties are shown for both data sets.

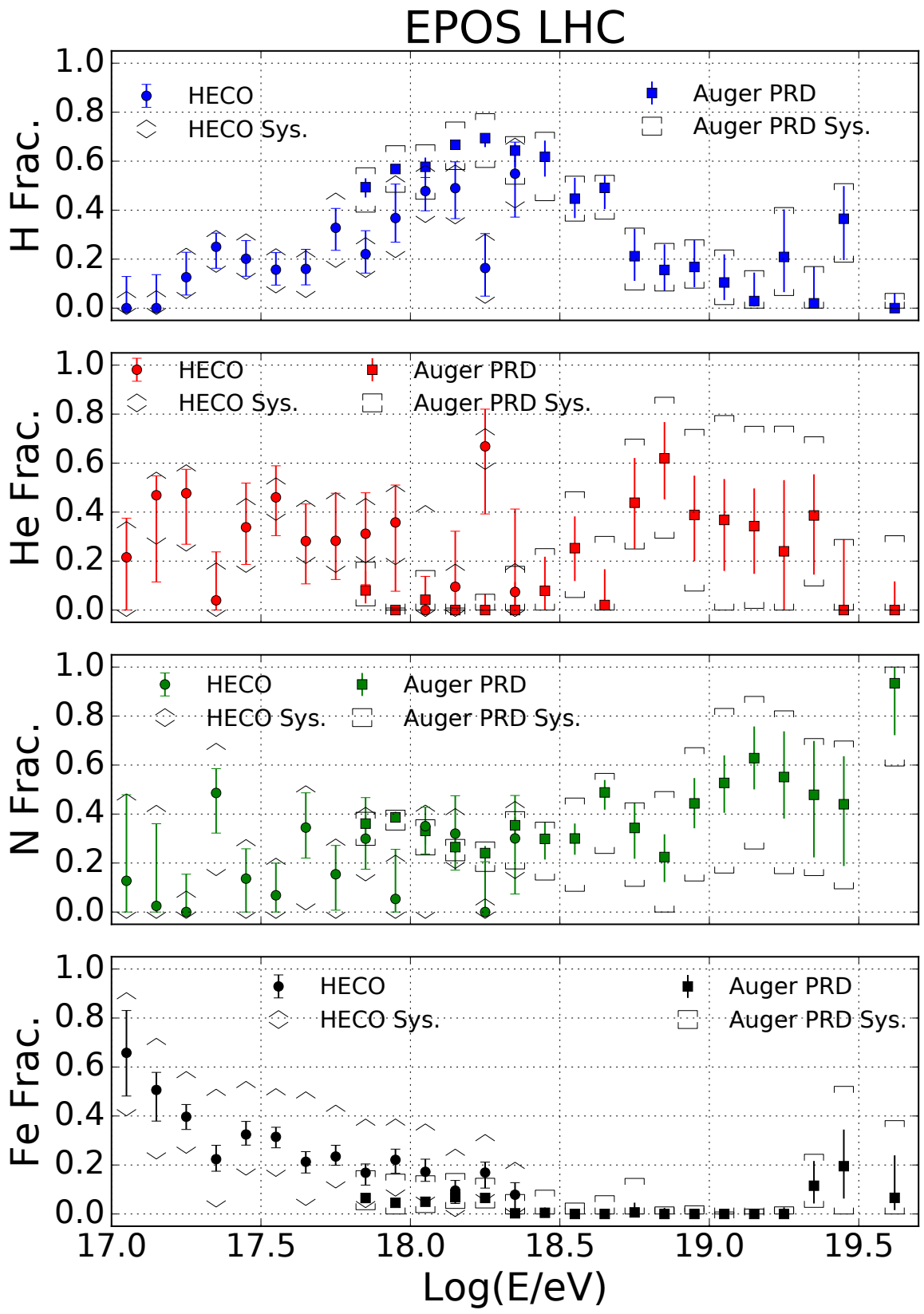

Figure 5.30: Reconstruction of chemical composition of cosmic rays analyzed with a 4-component Gumbel parametrization with EPOS LHC compared to the Pierre Auger fraction results [42]. Systematic uncertainties are shown for both data sets.

Chapter 6

Summary and Outlook

The goal of this thesis was the measurement of the chemical composition of UHECRs in the energy region of the expected transition from galactic to extra galactic cosmic rays. This was achieved by measuring the position of the extensive air shower maximum X_{max} in the atmosphere with the fluorescence detector of the Pierre Auger Observatory in the energy range from 10^{17} eV to $10^{18.4}$ eV for the time range from June 2010 to August 2012. Due to the combination of HEAT and Coihueco fluorescence telescopes, the virtual telescope HECO was used to measure high quality air shower profiles with a high accuracy.

The HECO reconstruction sequence was tested with various simulation studies and highly improved by adding an additional constraint to the profile reconstruction based on the universality approach from current interaction models. Reconstruction biases on the energy and the X_{max} determination were studied and corrected for. The systematic uncertainties introduced by these correction were significantly reduced compared to previous analyses. The detector acceptance was determined with a time dependent detector simulation for the whole energy range and every measured event was accordingly weighted. The lowest studied energy bins showed a still not understood acceptance distribution, but by using the kernel estimation method these bins were analyzable in this study. This was shown by validating the analysis method and the detector with Monte Carlo based analyses for different chemical compositions. The analysis showed a good reconstruction performance over the whole energy range. The systematic uncertainties of the fluorescence events were studied in detail. A new systematic uncertainty was found in the reconstructed data for the cosmic ray events that were detected in HEAT and Coihueco telescopes simultaneously.

The moments from the X_{max}-distribution $\langle X_{max} \rangle$ and $\sigma_{X_{max}}$ were calculated and compared to theoretical predictions from current interaction models. In the studied energy range the moments showed a change in the chemical composition from intermediate atomic masses at 10^{17} eV to a light composition at $10^{18.4}$ eV. A comparison with the results from other Auger analyses and other experiments showed a good agreement of the thesis results inside the statistical and systematical uncertainties. A comparison between this thesis and the Auger PRD results showed a constant systematical difference of the $\langle X_{max} \rangle$. This difference was introduced due to the use of a different reconstruction module sequences for the special HECO reconstruction.

A more detailed study of the chemical composition was presented with a new analysis method using the shape of the reconstructed X_{max}-distributions. By using parametrizations

from simulated primaries from current interaction models based on Gumbel statistics, the chemical composition of different elementary groups as a function of the energy were fitted. The fraction results of the elementary group were tested on simulations for the determination of the optimal number of fit components. The analysis of the shape of the X_{max}-distributions with this method showed a rather heavy chemical composition consisting of nitrogen or iron like primaries at low energies around 10^{17} eV that changed to a light composition at $10^{18.4}$ eV consisting of hydrogen or helium like cosmic rays. The findings of this thesis were in good agreement inside the statistical and systematical uncertainties with the previous published fraction results of the Pierre Auger Collaboration. The change in the chemical composition with increasing energy could be an indication of the transition from galactic to extra galactic cosmic ray components. Using the fraction results from this thesis in combination with the Auger PRD fractions several theoretical cosmic ray source scenarios like the 'ankle' or the 'dip' model can be disfavored as they require a hydrogen dominated composition up to the highest energies. A mixed composition scenario for cosmic rays is therefore in favor by the current reconstructed X_{max} data of the Pierre Auger Observatory. The results shown in this thesis can be used in the future in global fits to constrain possible cosmic ray scenarios and help understanding the physical processes of UHECRs.

The presented analysis in this thesis can be improved by extending the time range of the data set to the maximal time possible to reduce statistical fluctuations and this will allow to reduce the lower energy boundary to $10^{16.5}$ and even below. Also a dedicated detector study for HEAT and the virtual telescope HECO should be performed to find the reason for the systematic shift between the HECO and the Auger PRD results. Additional an extensive study of the telescope alignment using all possible methods, e.g. tilt monitoring, star tracking and SD event alignment, should be performed to reduce known systematic uncertainties in the lowest energy bins. The profile reconstruction should be improved by calculating the universality k constraint for the most recent interaction models including Sibyll2.3. Also with an increased event statistics, the universality constraint can be made independent of the interaction model predictions by using the measured k factor from high quality air showers with very long track length. Additionally, the HECO data set should also be used in the calculation of the hybrid energy spectrum. A composition change is normally also present in the spectral index of the energy spectrum.

These possible improvements are beyond the scope of this thesis and left for future analysis.

Appendices

Appendix A

Parametrization

A.1 Fiducial Field of View Cut

A.1.1 HECO only data set (Sibyll2.1 constraint)

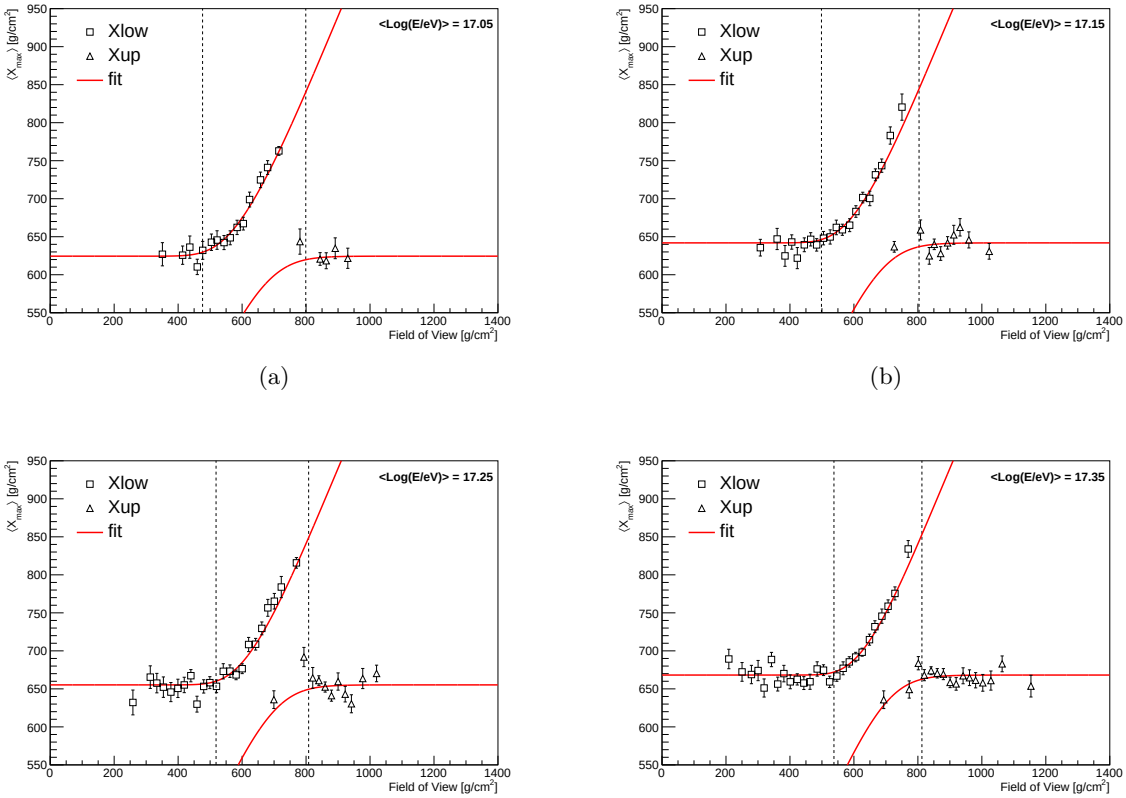

(a) (b)

(c) (d)

Figure A.1: Fiducial field of view fitting routine.

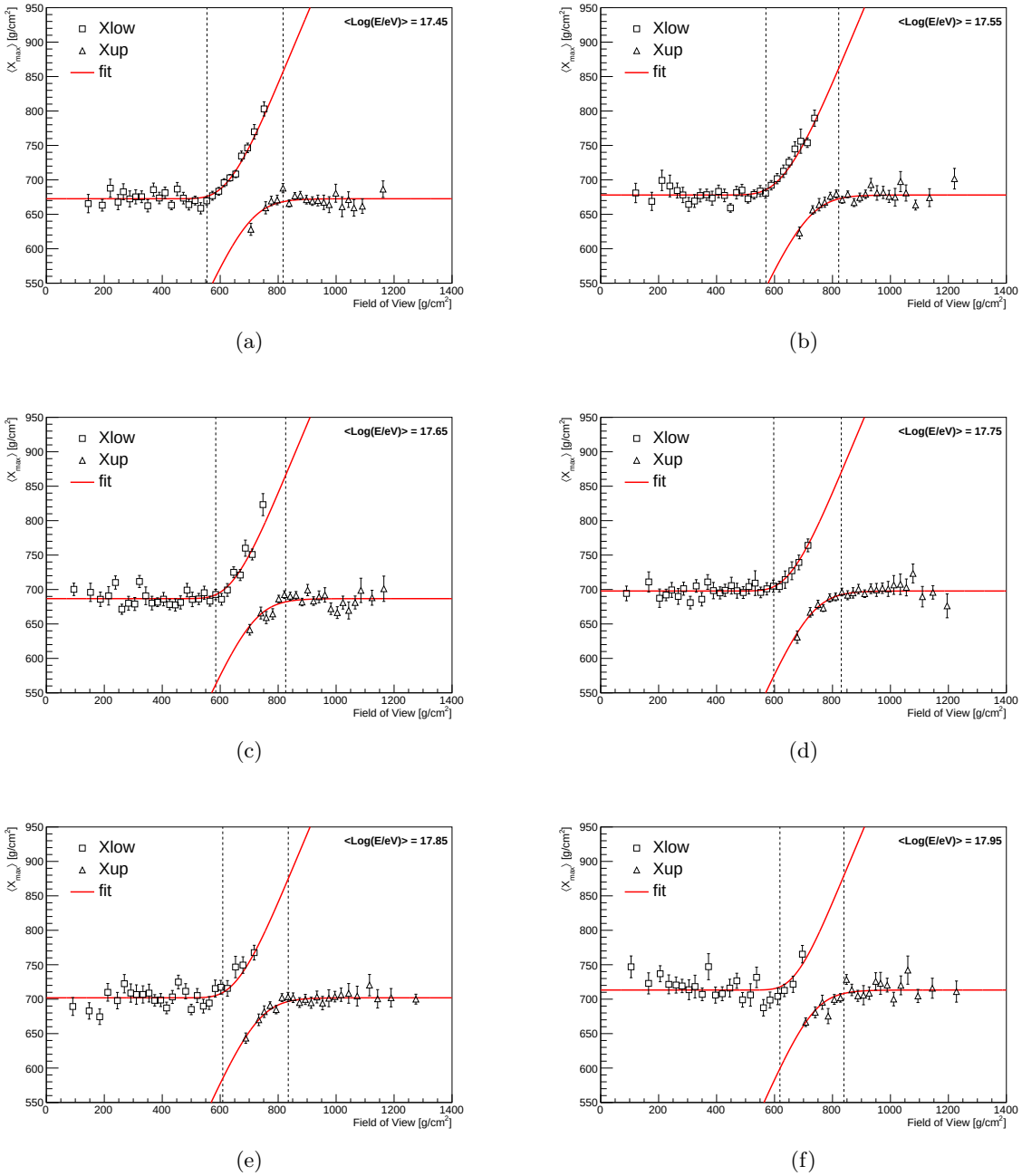

(a) (b) (c) (d) (e) (f)

Figure A.2: Fiducial field of view fitting routine.

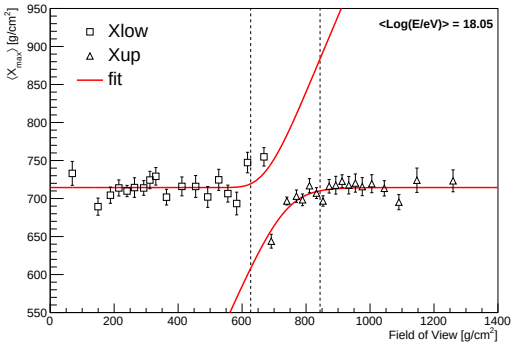

(a)

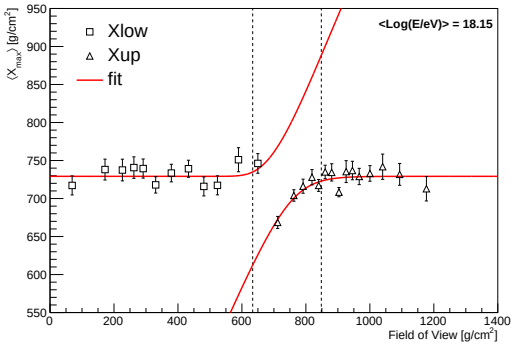

(b)

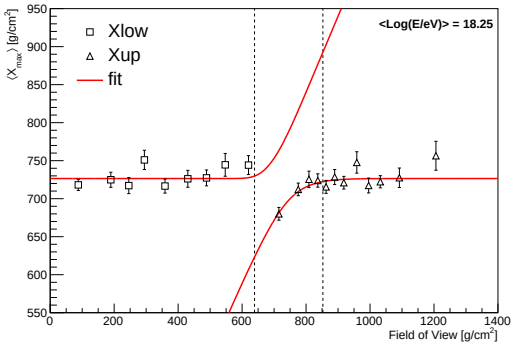

(c)

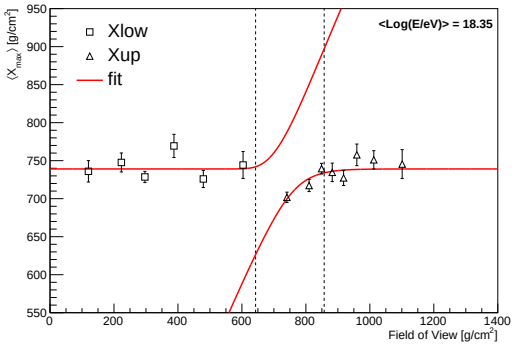

(d)

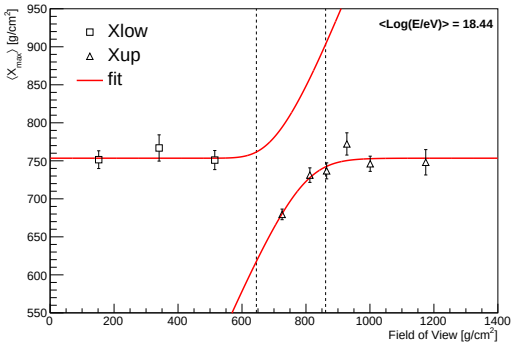

(e)

Figure A.3: Fiducial field of view fitting routine.

A.1.2 HECO only data set (LHC constraint)

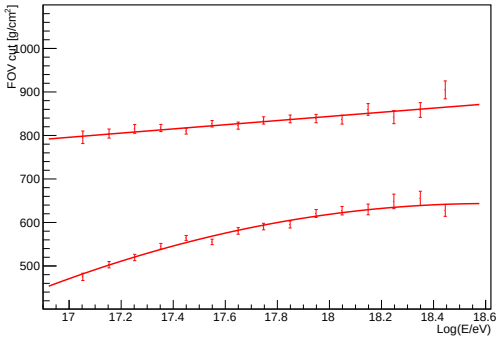

Figure A.4: Fiducial FOV parametrization based on the HECO data set with the LHC constraint.

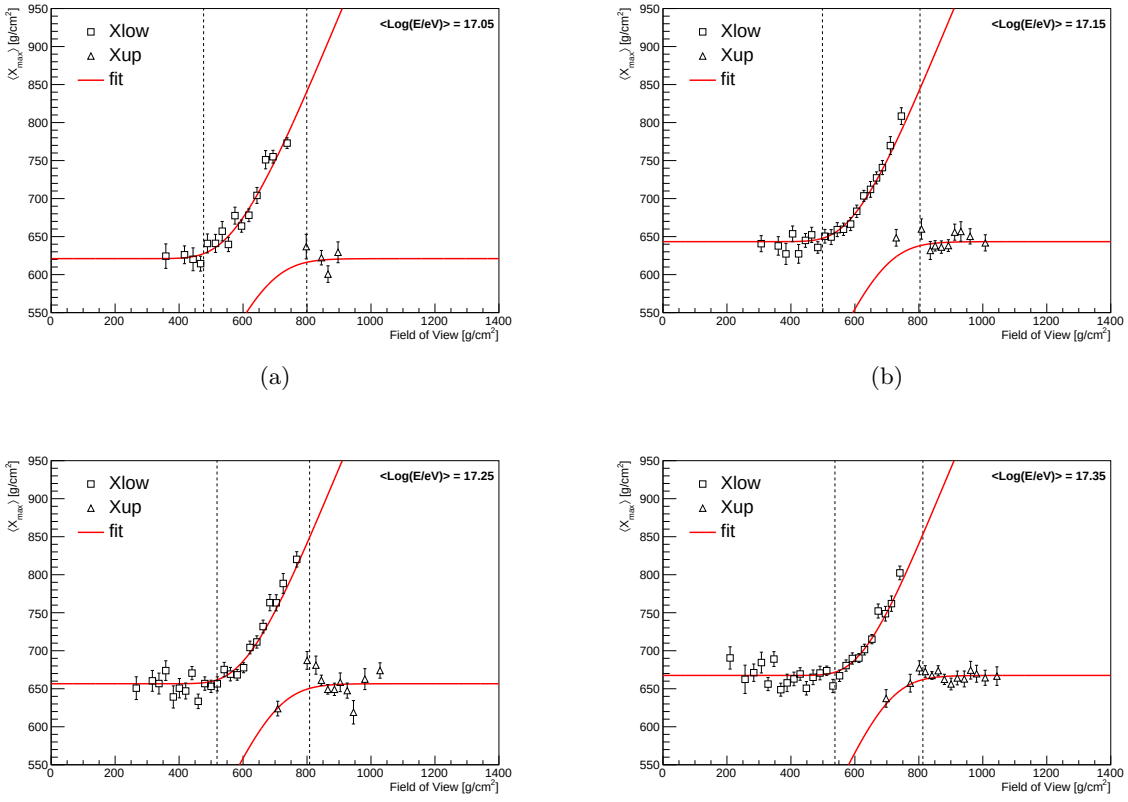

(a) (b) (c) (d)

Figure A.5: Fiducial field of view fitting routine.

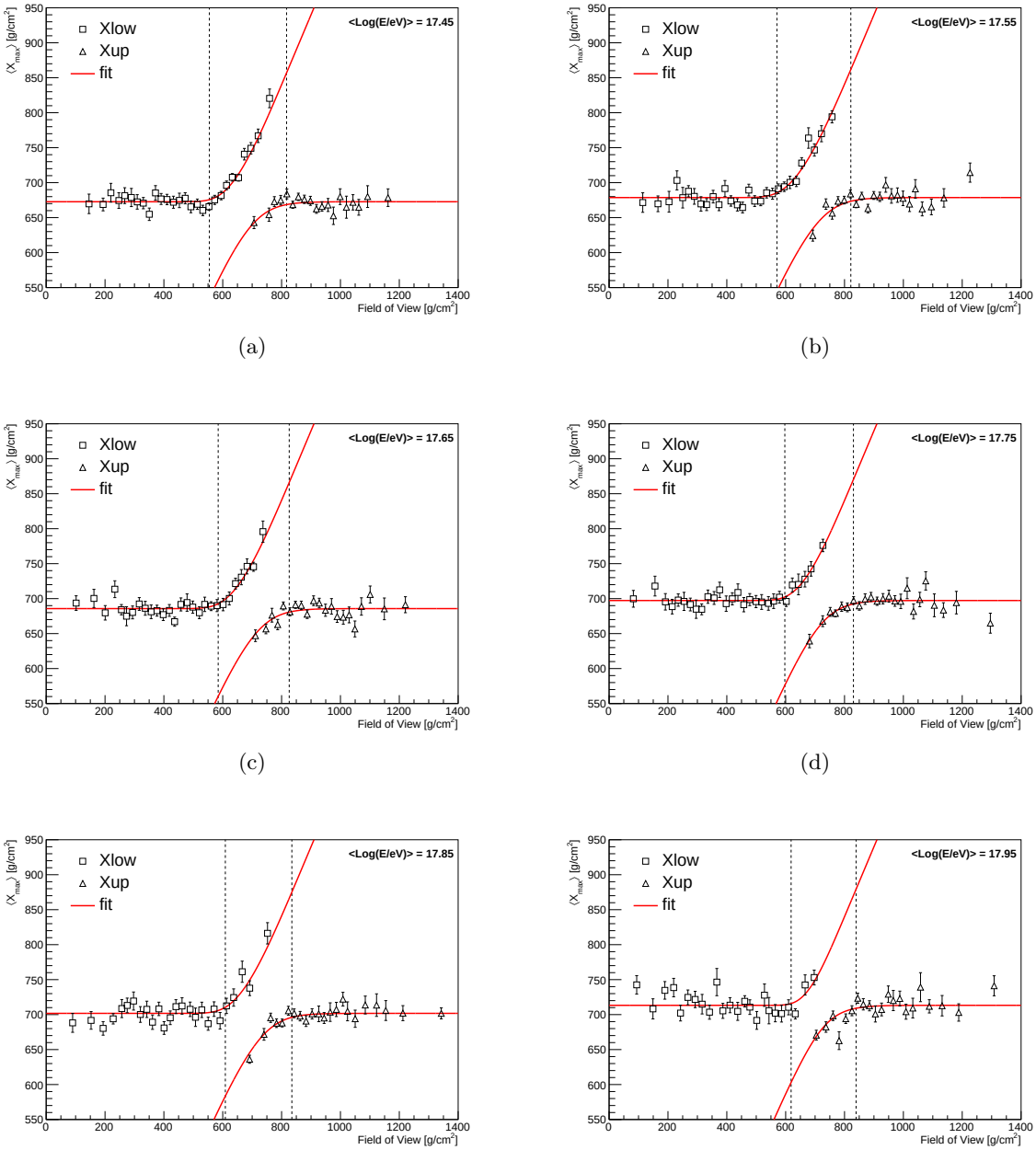

(a) (b) (c) (d) (e) (f)

Figure A.6: Fiducial field of view fitting routine.

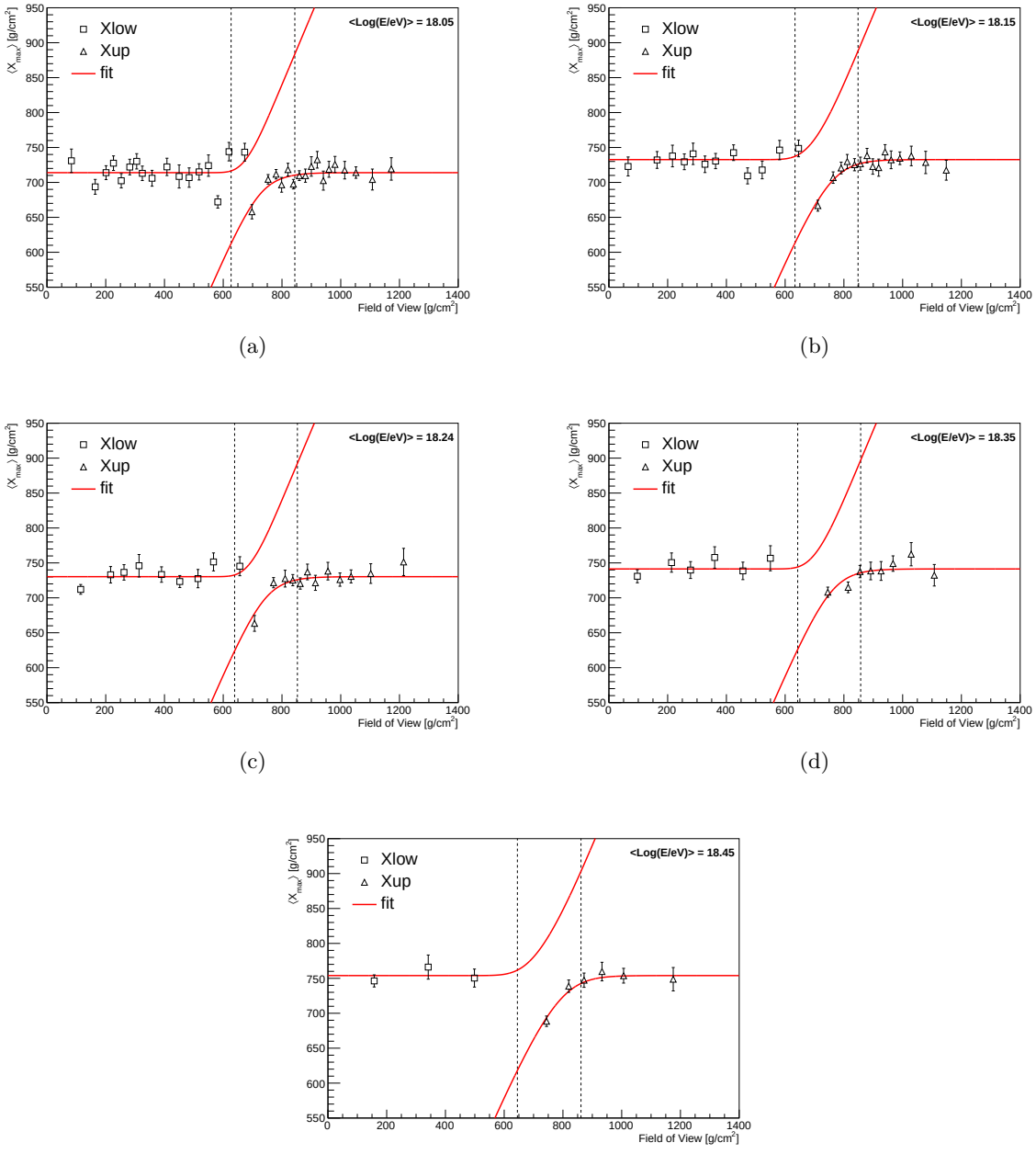

(a) (b) (c) (d) (e)

Figure A.7: Fiducial field of view fitting routine.

A.2 Acceptance

A.2.1 Normal acceptance model

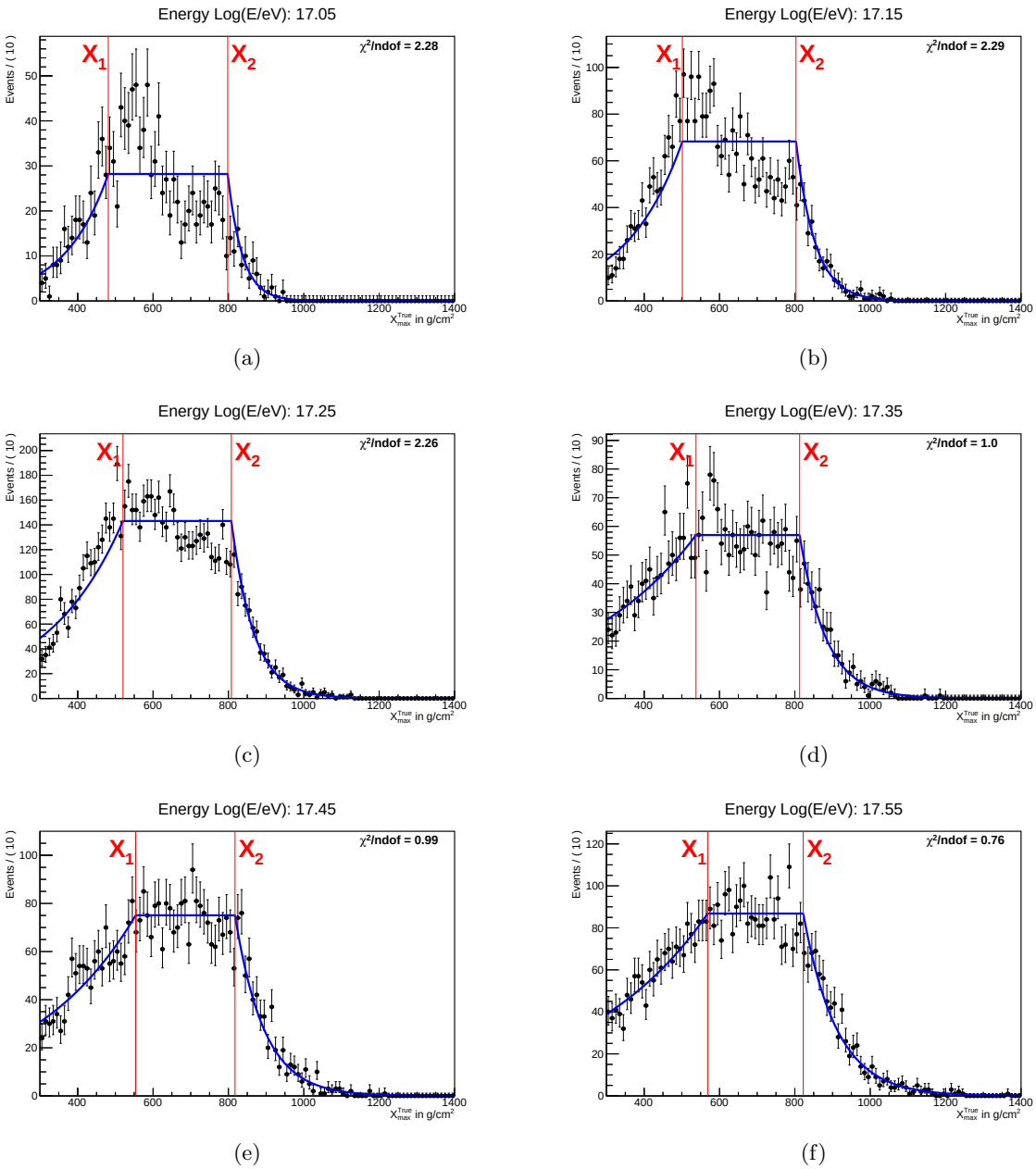

Figure A.8: HECO X_{max} acceptance fitted with normal method.

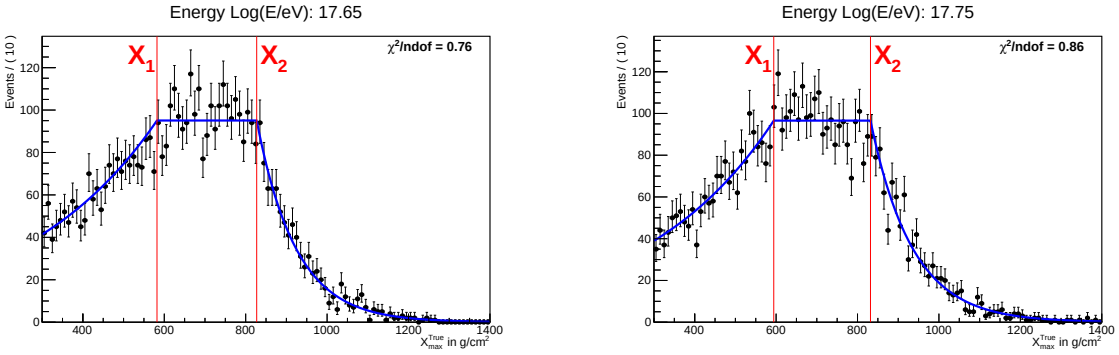

(a)

(b)

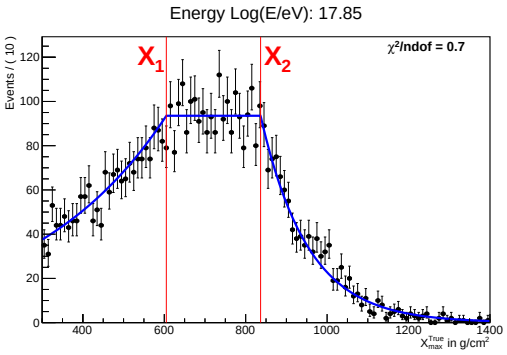

(c)

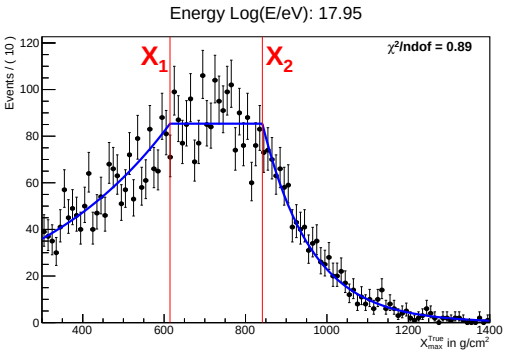

(d)

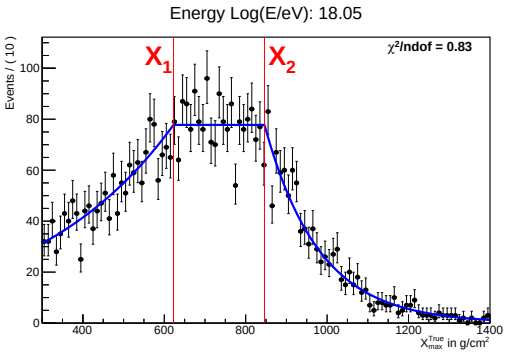

(e)

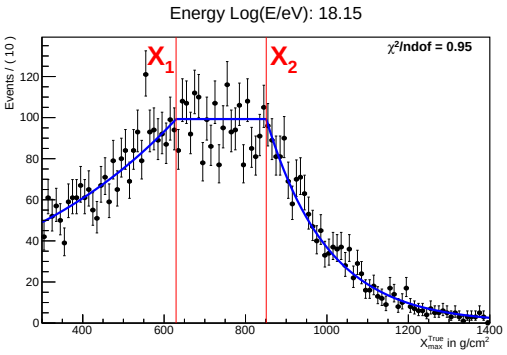

(f)

Figure A.9: HECO X_{max} acceptance fitted with normal method.

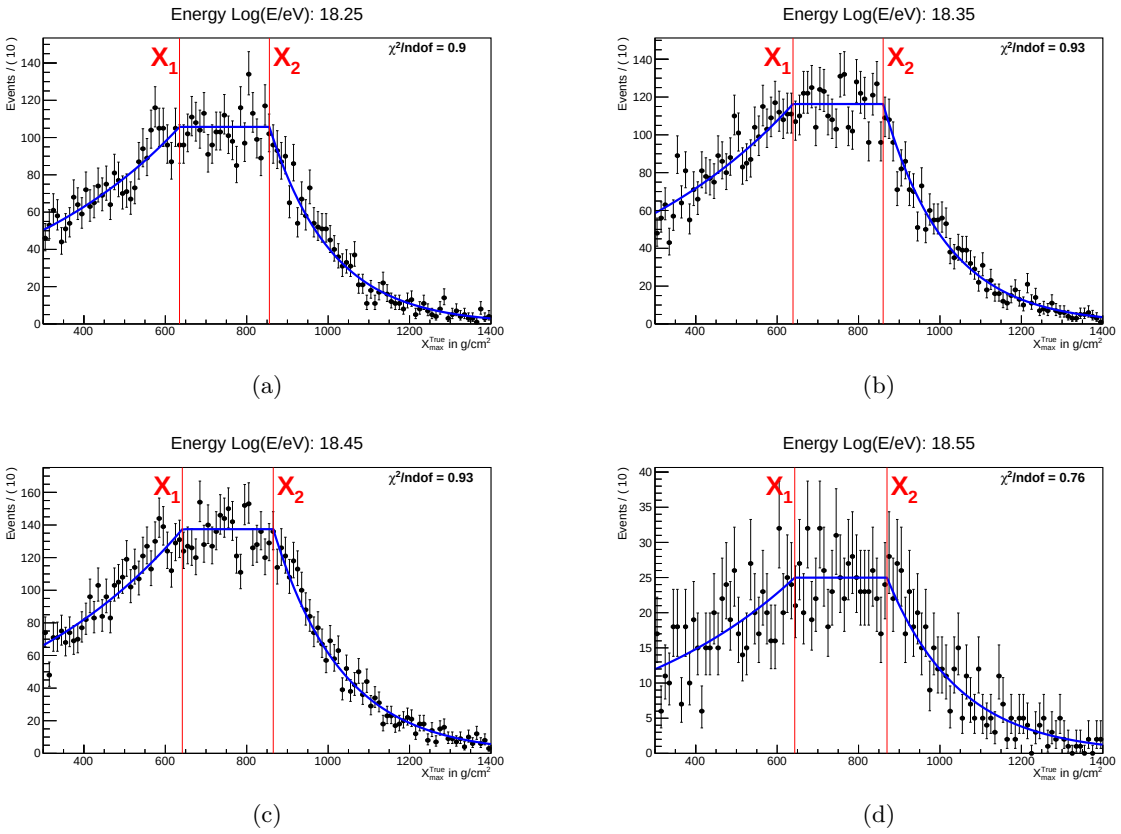

Figure A.10: HECO X_{max} acceptance fitted with normal method.

A.2.2 Kernel estimation model

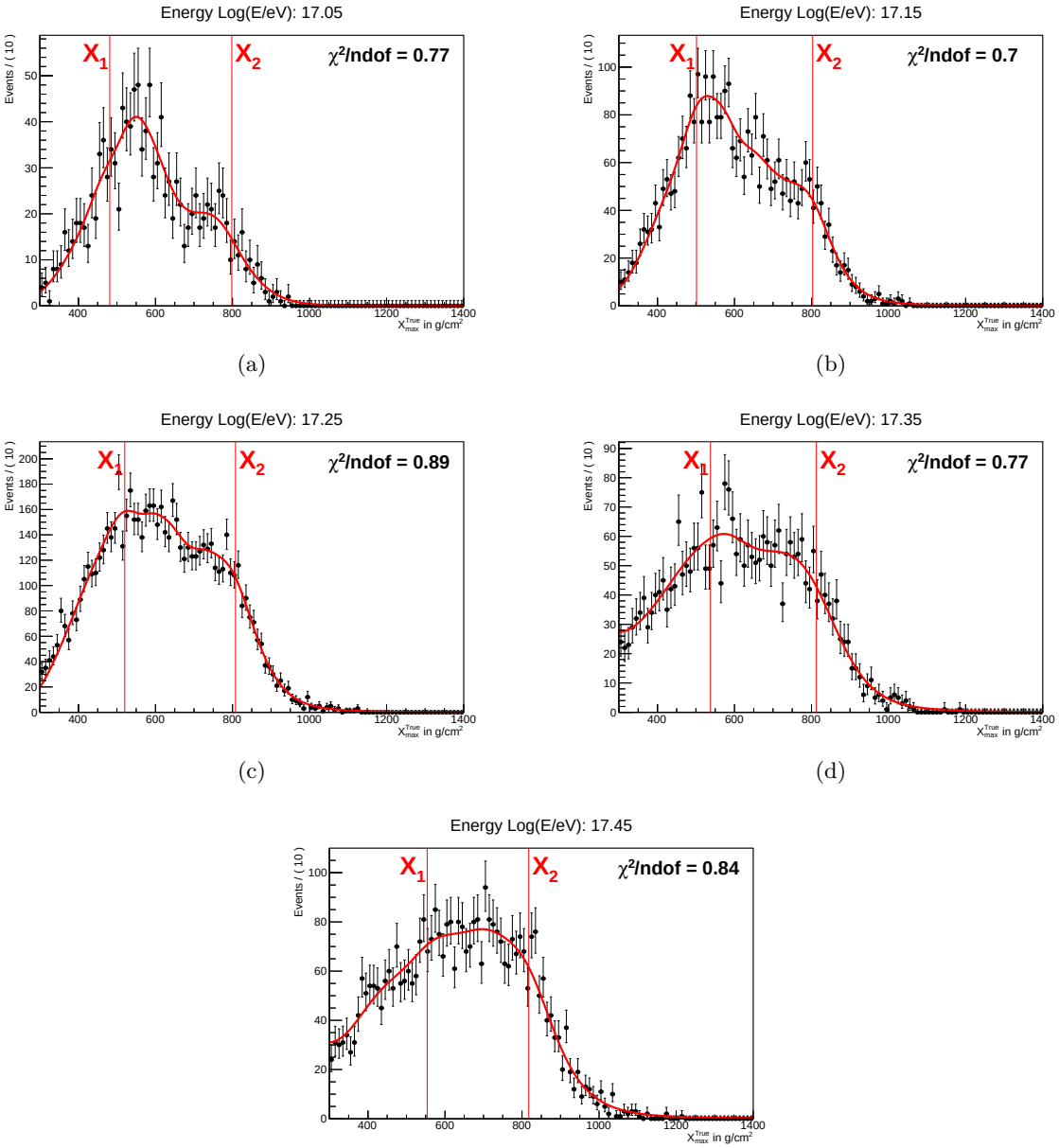

Figure A.11: HECO X_{max} acceptance fitted with kernel method.

Appendix B

Long Time Stability Tilt Monitoring

Designation	located at
Inc Sensor 1	left side of the shutter
Inc Sensor 2	top middle of the mirror
Inc Sensor 3	top of the camera
Inc Sensor 4	base of the camera

Table B.1: HEAT bay 1 inclination sensors points.

Designation	Measures distance between
Dist Sensor 1	center of the mirror to a point beneath the camera
Dist Sensor 2	top right of mirror to top right of the camera
Dist Sensor 3	top left of mirror to top left of the camera
Dist Sensor 4	bottom left of the mirror to the left side of the shutter

Table B.2: HEAT bay 1 distance sensors points.

Designation	located at
Inc Sensor 1	base of the camera
Inc Sensor 2	top middle of the mirror
Inc Sensor 3	left side of the shutter
Inc Sensor 4	top of the camera

Table B.3: HEAT bay 3 inclination sensors points.

Designation	Measures distance between
Dist Sensor 1	center of the mirror to a point beneath the camera
Dist Sensor 2	top left of mirror to top left of the camera
Dist Sensor 3	bottom left of the mirror to the left side of the shutter
Dist Sensor 4	top right of mirror to top right of the camera

Table B.4: HEAT bay 3 distance sensors points.

B.1 HEAT Bay 1

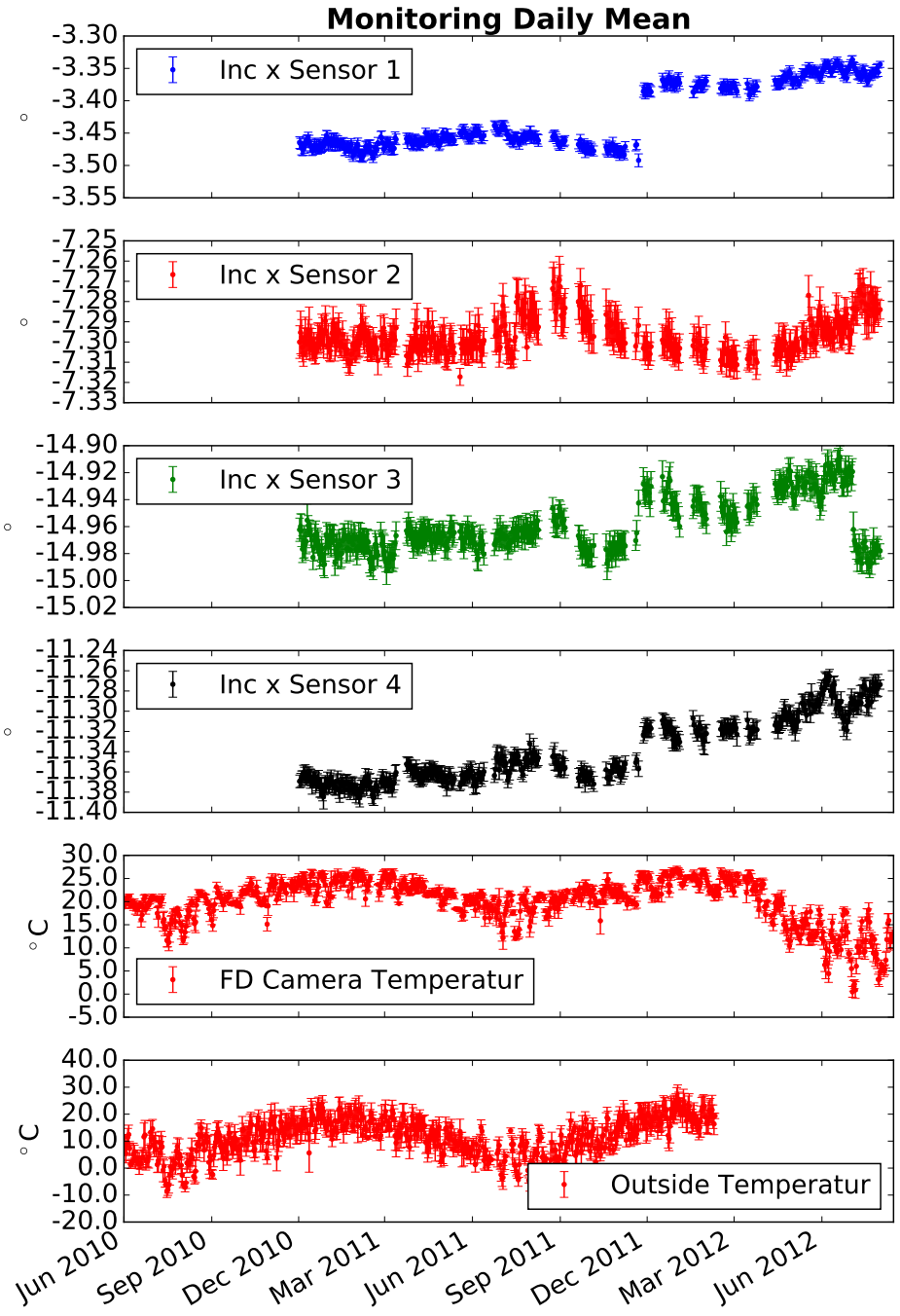

Figure B.1: Daily mean values of the inclination sensors of the x-axis in HEAT bay 1, the outside temperature at the Coihueco weather station and inside temperature measured at the PMT camera.

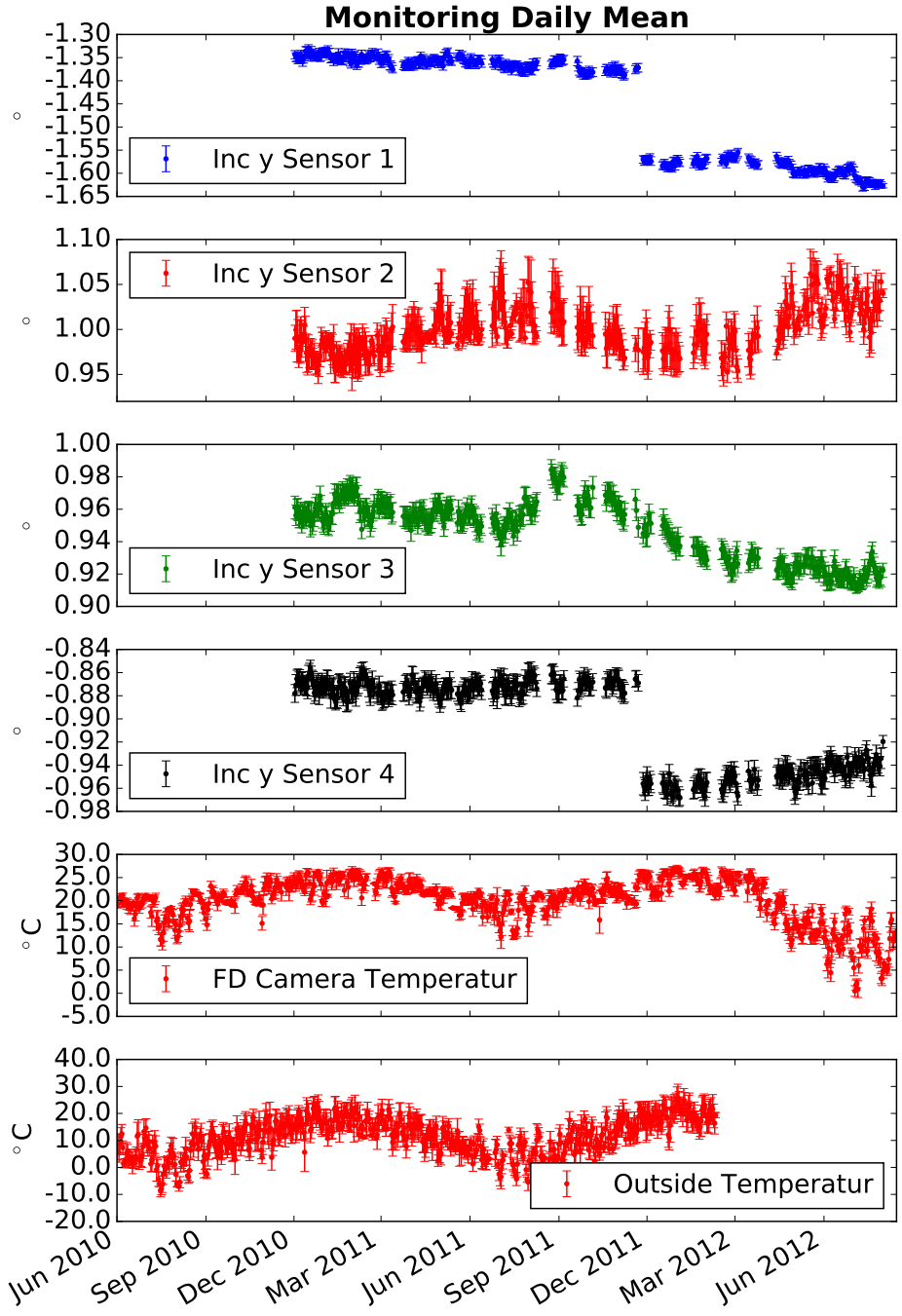

Figure B.2: Daily mean values of the inclination sensors of the y-axis in HEAT bay 1, the outside temperature at the Coihueco weather station and inside temperature measured at the PMT camera.

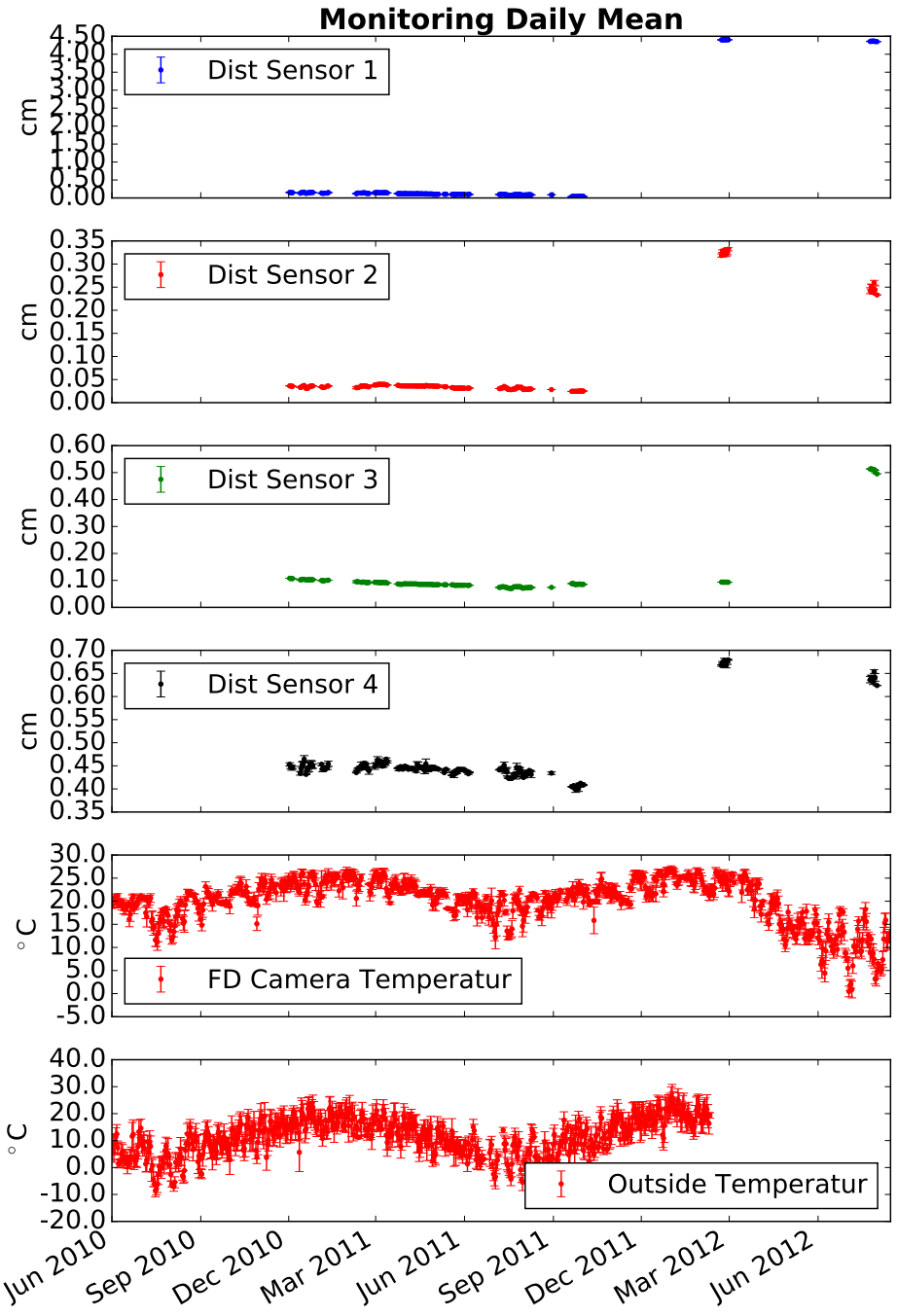

Figure B.3: Daily mean values of the distance sensors in HEAT bay 1, the outside temperature at the Coihueco weather station and inside temperature measured at the PMT camera.

B.2 HEAT Bay 3

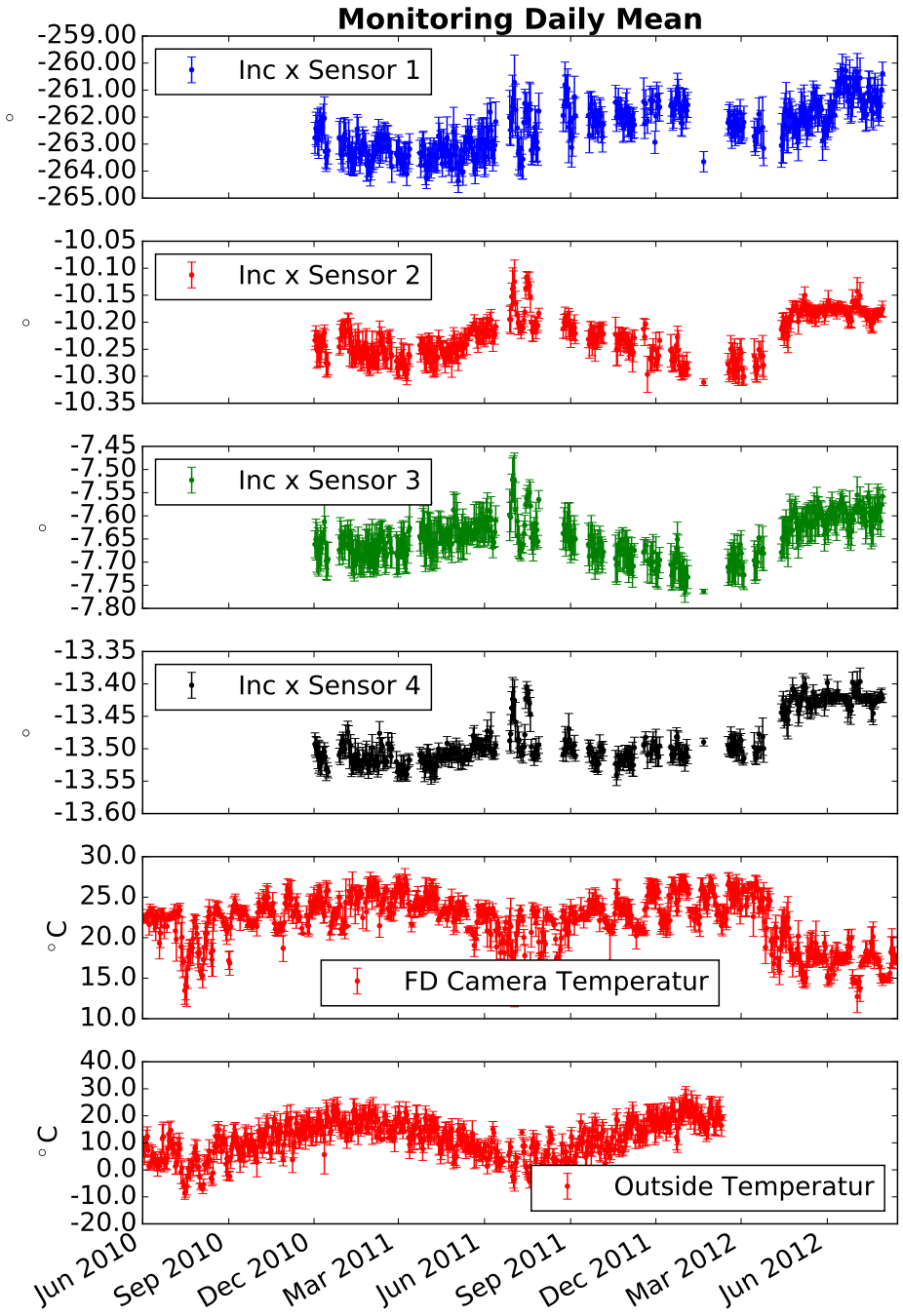

Figure B.4: Daily mean values of the inclination sensors of the x-axis in HEAT bay 3, the outside temperature at the Coihueco weather station and inside temperature measured at the PMT camera.

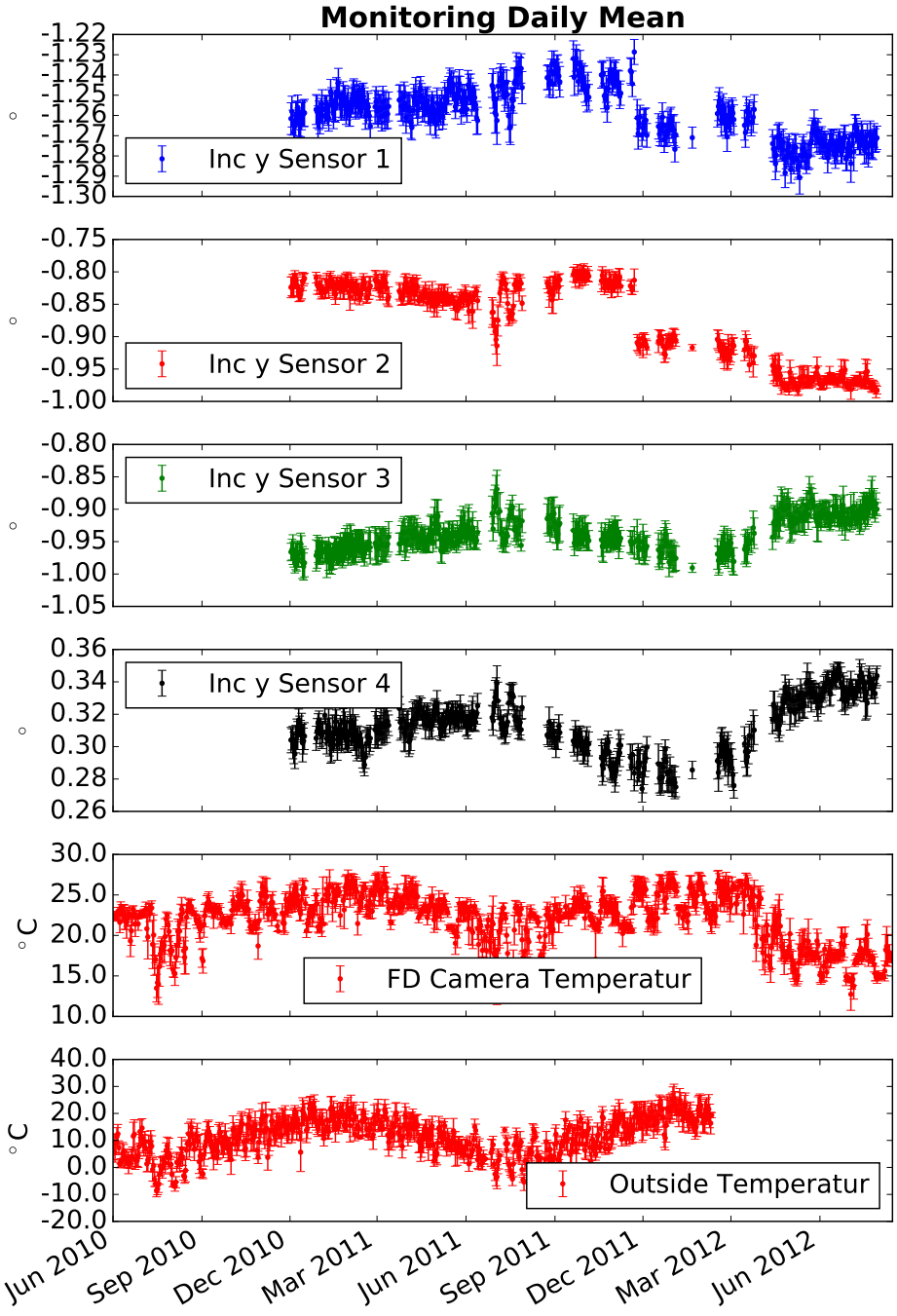

Figure B.5: Daily mean values of the inclination sensors of the y-axis in HEAT bay 3, the outside temperature at the Coihueco weather station and inside temperature measured at the PMT camera.

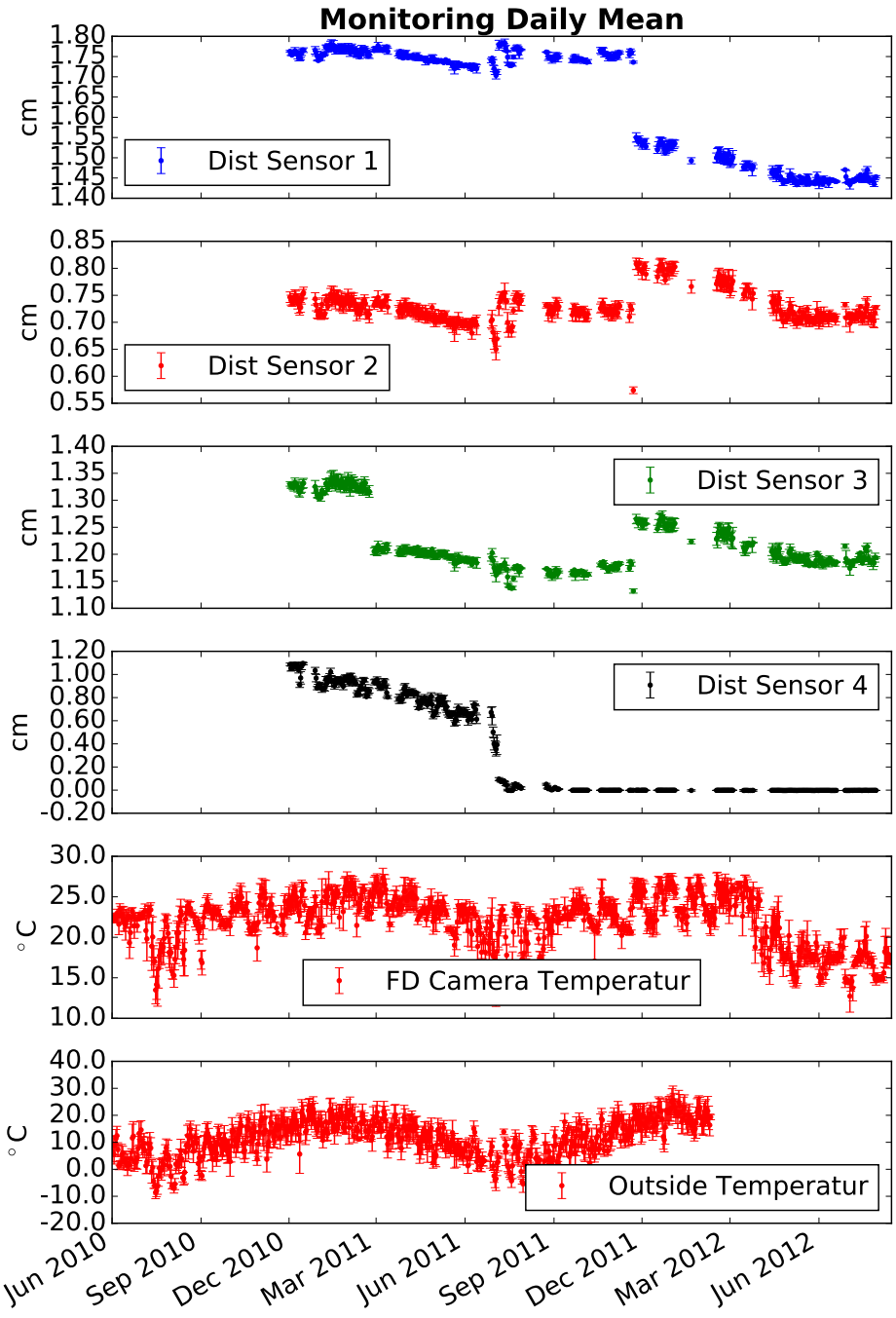

Figure B.6: Daily mean values of the distance sensors in HEAT bay 3, the outside temperature at the Coihueco weather station and inside temperature measured at the PMT camera.

Appendix C

Gumbel Parametrization Comparison with Conex Monte Carlo

C.1 Conex H primary

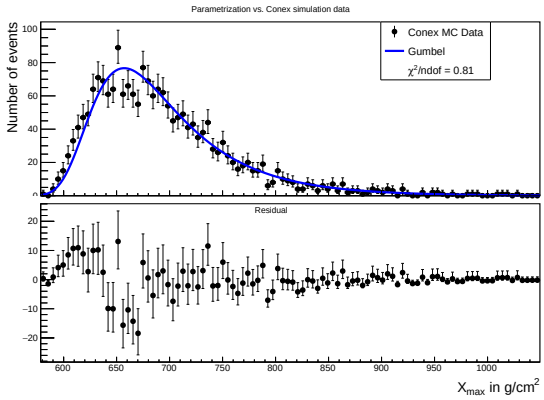

(a) $\log(E/\text{eV}) = 17.0$

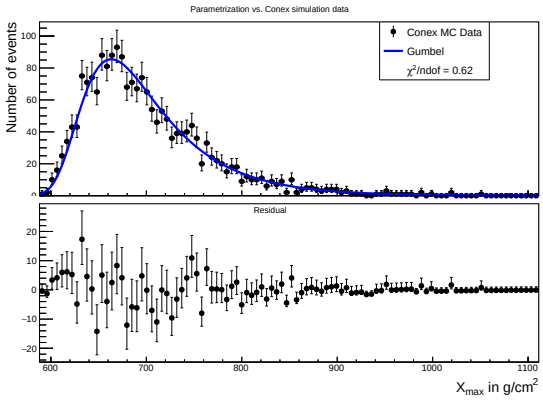

(b) $\log(E/\text{eV}) = 17.1$

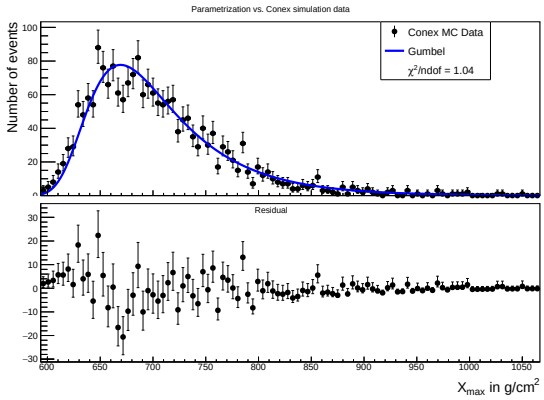

(c) $\log(E/\text{eV}) = 17.2$

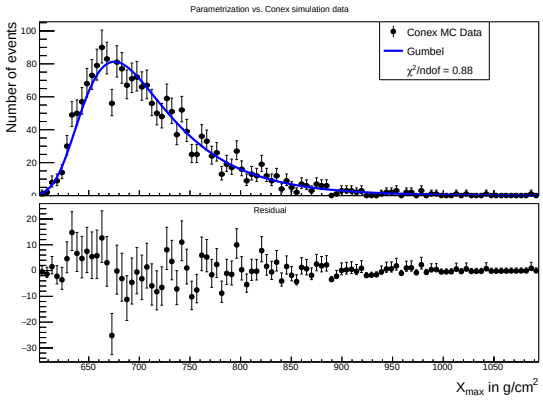

(d) $\log(E/\text{eV}) = 17.3$

Figure C.1: X_{max}-distribution of 2000 H primary Conex air showers with EPOS LHC compared with Gumbel parametrization[150].

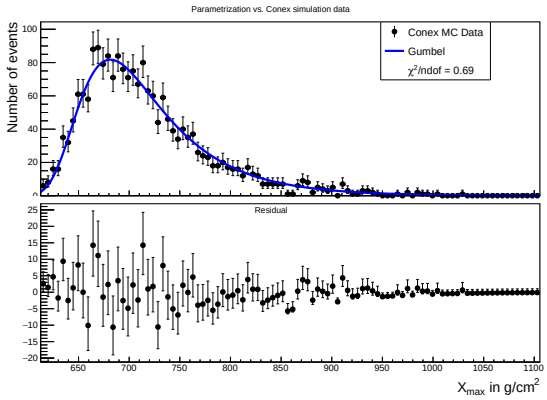

(a) $\log(E/\text{eV}) = 17.4$

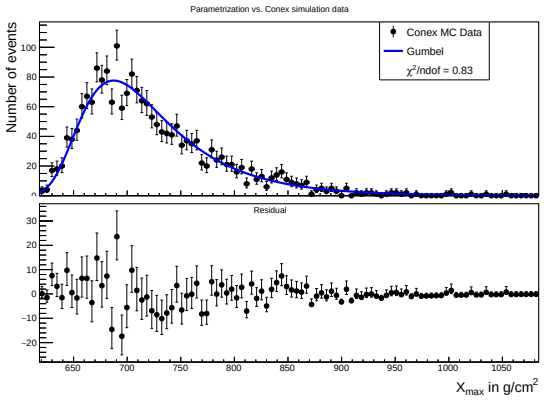

(b) $\log(E/\text{eV}) = 17.5$

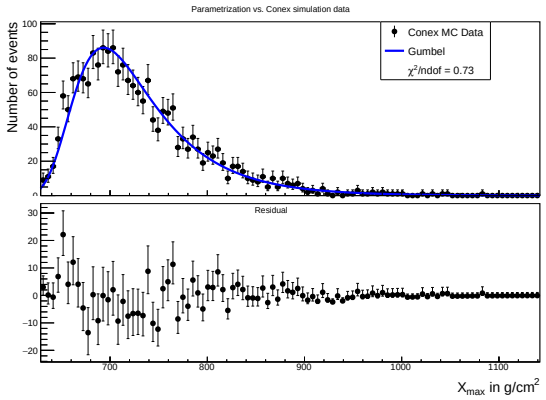

(c) $\log(E/\text{eV}) = 17.6$

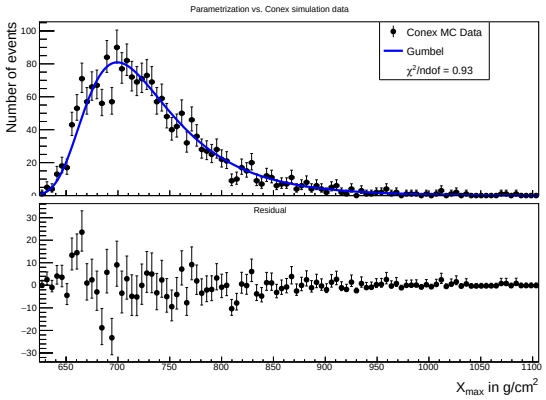

(d) $\log(E/\text{eV}) = 17.7$

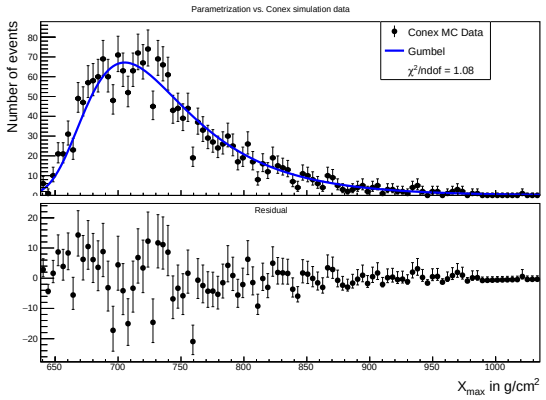

(e) $\log(E/\text{eV}) = 17.8$

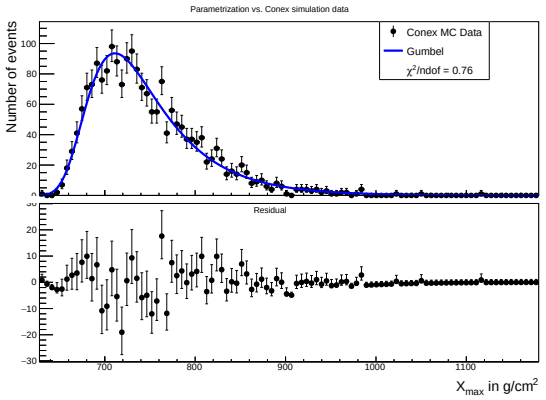

(f) $\log(E/\text{eV}) = 17.9$

Figure C.2: X_{max}-distribution of 2000 H primary Conex air showers with EPOS LHC compared with Gumbel parametrization[150].

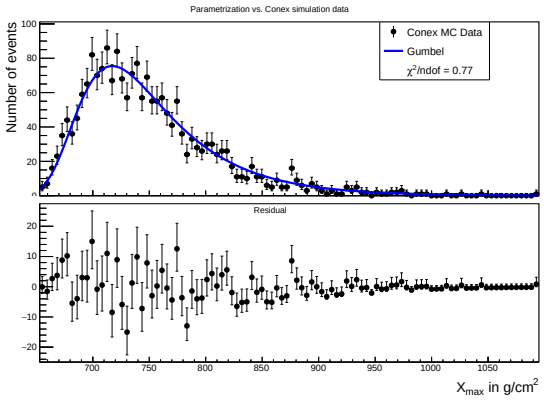

(a) $\log(E/\mathrm{eV}) = 18.0$

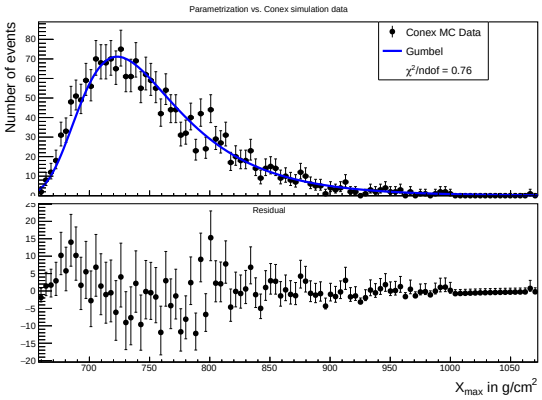

(b) $\log(E/\mathrm{eV}) = 18.1$

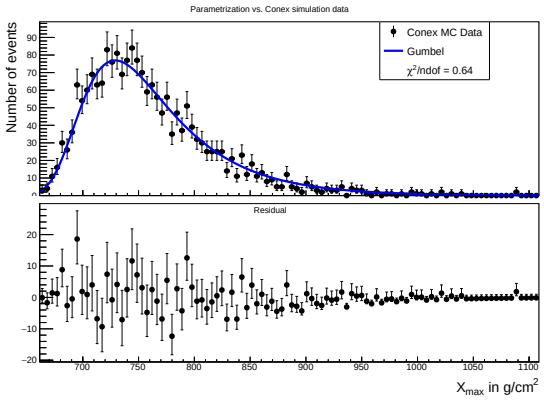

(c) $\log(E/\mathrm{eV}) = 18.2$

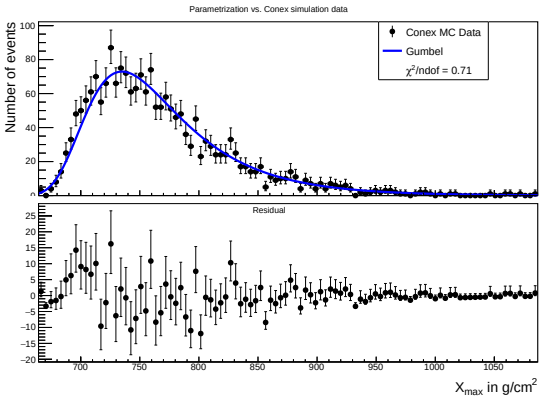

(d) $\log(E/\mathrm{eV}) = 18.3$

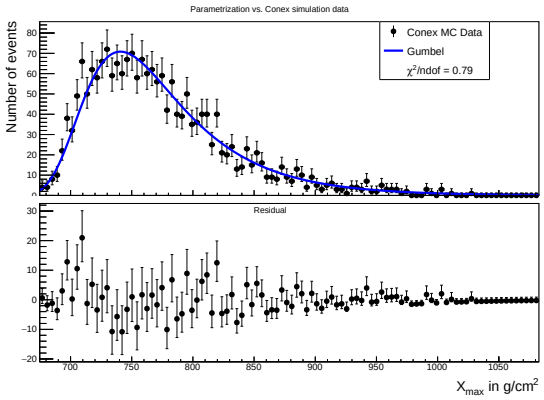

(e) $\log(E/\mathrm{eV}) = 18.4$

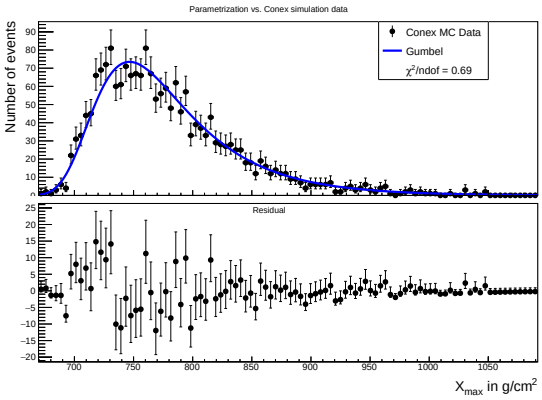

(f) $\log(E/\mathrm{eV}) = 18.5$

Figure C.3: X_{max}-distribution of 2000 H primary Conex air showers with EPOS LHC compared with Gumbel parametrization[150].

C.2 Conex He primary

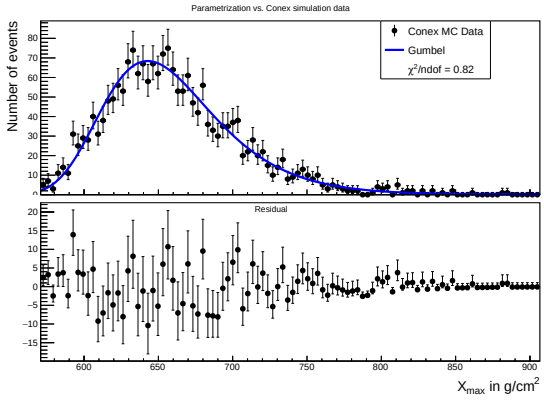

(a) $\log(E/\text{eV}) = 17.0$

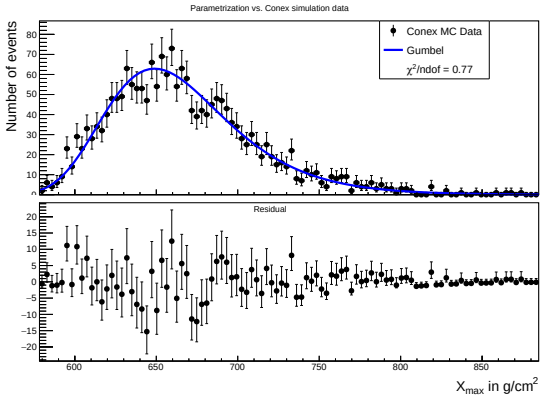

(b) $\log(E/\text{eV}) = 17.1$

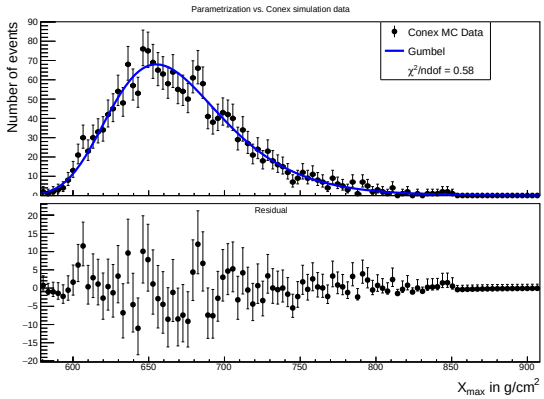

(c) $\log(E/\text{eV}) = 17.2$

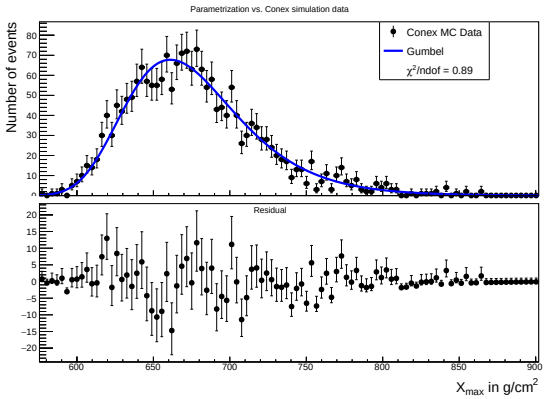

(d) $\log(E/\text{eV}) = 17.3$

Figure C.4: X_{max}-distribution of 2000 He primary Conex air showers with EPOS LHC compared with Gumbel parametrization[150].

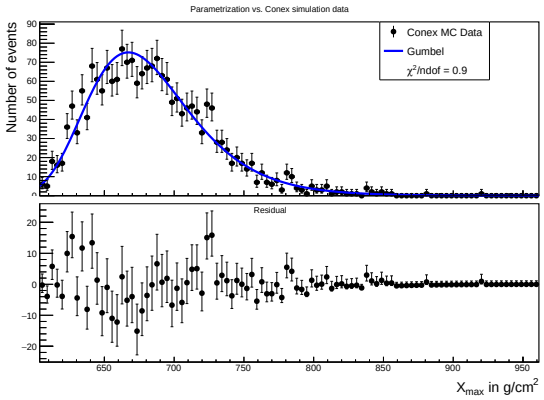

(a) $\log(E/\mathrm{eV}) = 17.4$

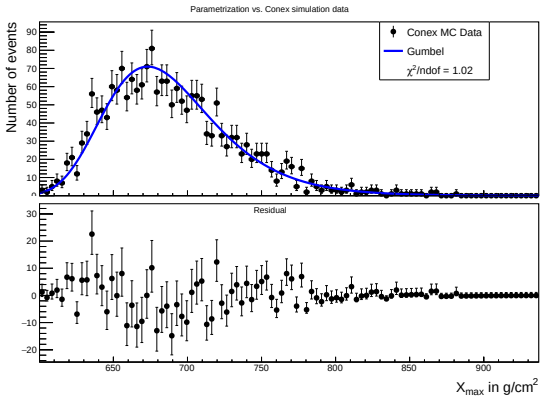

(b) $\log(E/\mathrm{eV}) = 17.5$

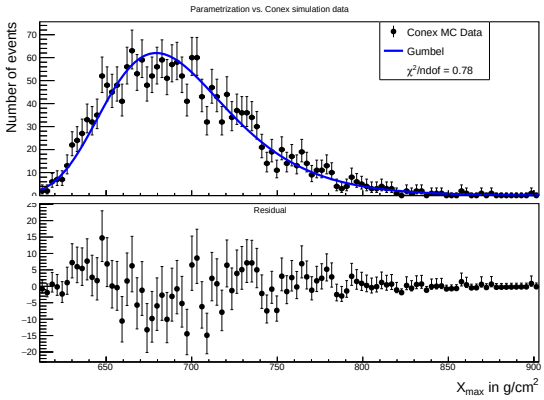

(c) $\log(E/\mathrm{eV}) = 17.6$

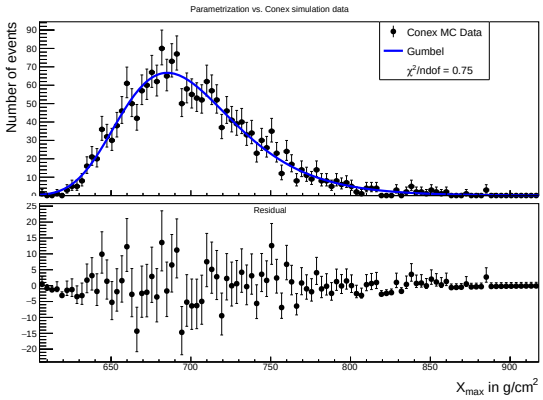

(d) $\log(E/\mathrm{eV}) = 17.7$

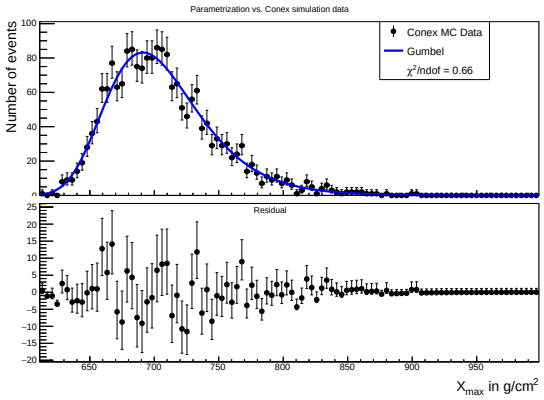

(e) $\log(E/\mathrm{eV}) = 17.8$

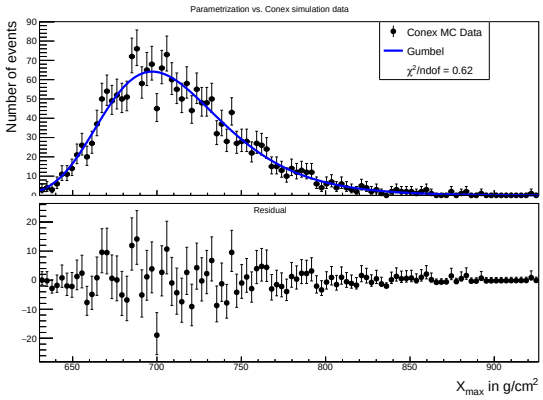

(f) $\log(E/\mathrm{eV}) = 17.9$

Figure C.5: X_{max}-distribution of 2000 He primary Conex air showers with EPOS LHC compared with Gumbel parametrization[150].

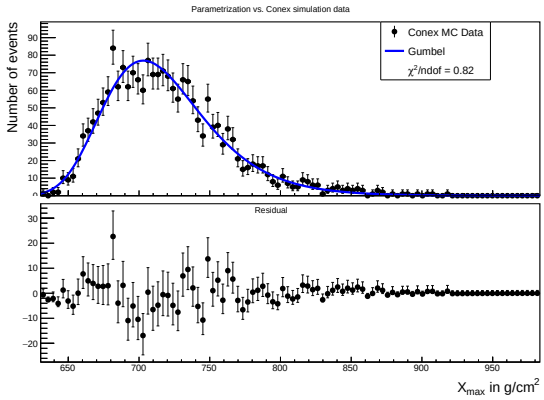

(a) $\log(E/\mathrm{eV}) = 18.0$

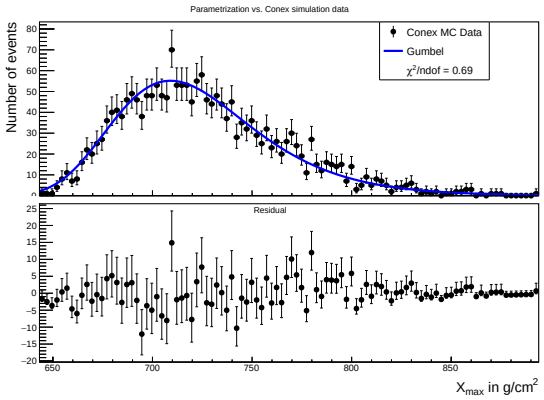

(b) $\log(E/\mathrm{eV}) = 18.1$

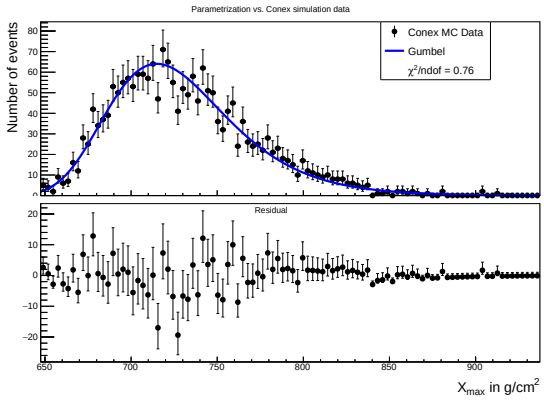

(c) $\log(E/\mathrm{eV}) = 18.2$

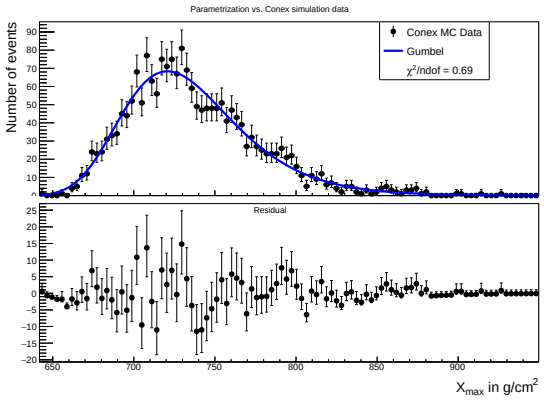

(d) $\log(E/\mathrm{eV}) = 18.3$

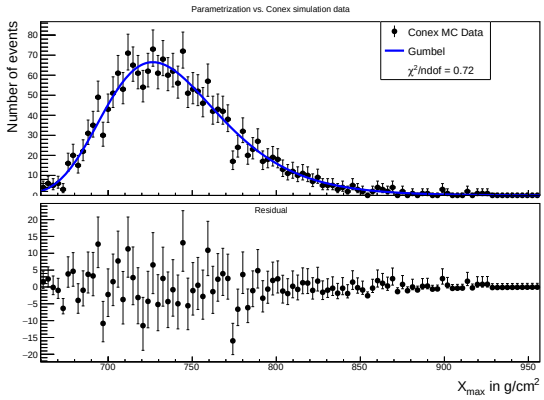

(e) $\log(E/\mathrm{eV}) = 18.4$

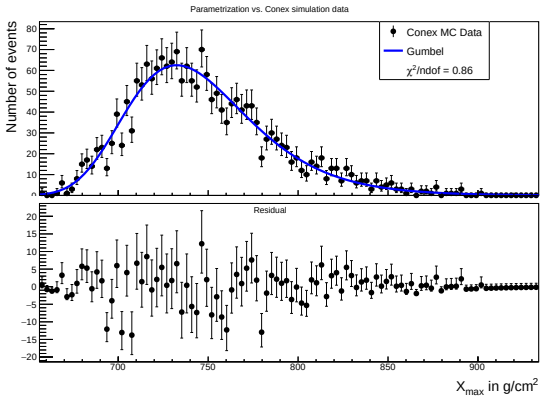

(f) $\log(E/\mathrm{eV}) = 18.5$

Figure C.6: X_{max}-distribution of 2000 He primary Conex air showers with EPOS LHC compared with Gumbel parametrization[150].

C.3 Conex N primary

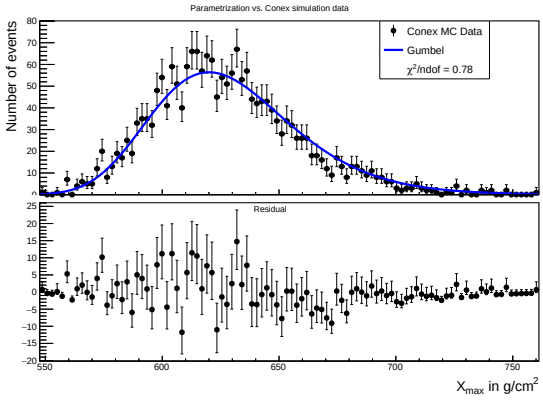

(a) $\log(E/\text{eV}) = 17.0$

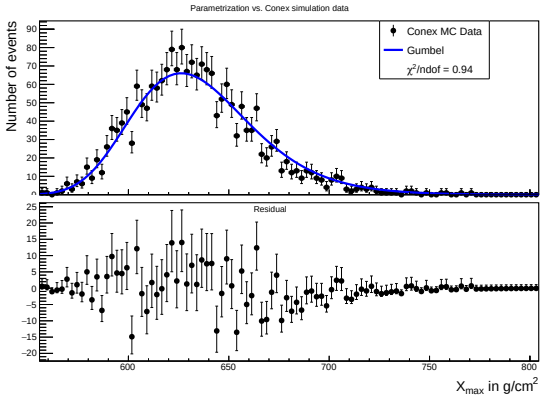

(b) $\log(E/\text{eV}) = 17.1$

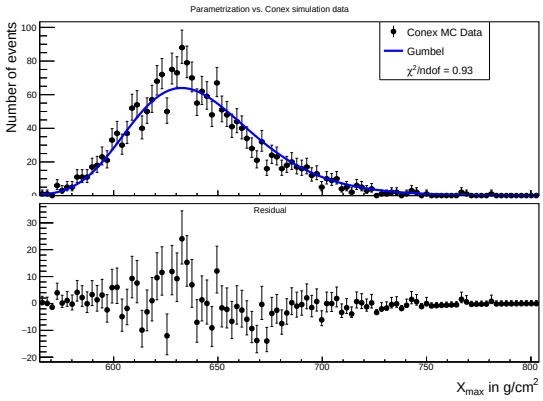

(c) $\log(E/\text{eV}) = 17.2$

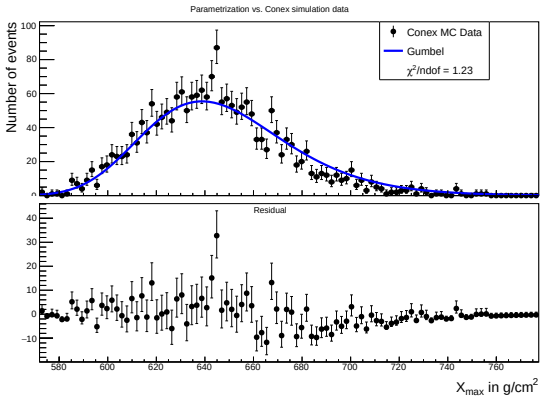

(d) $\log(E/\text{eV}) = 17.3$

Figure C.7: X_{max}-distribution of 2000 Al primary Conex air showers with EPOS LHC compared with Gumbel parametrization[150].

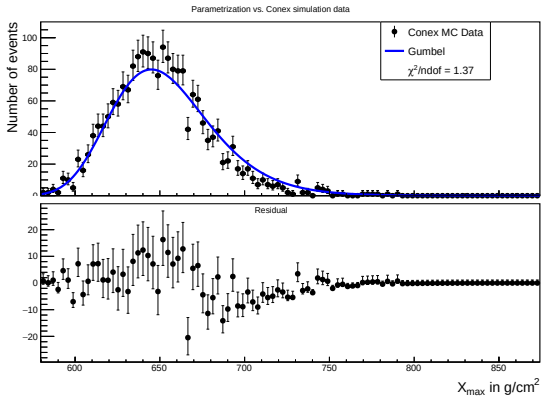

(a) $\log(E/\mathrm{eV}) = 17.4$

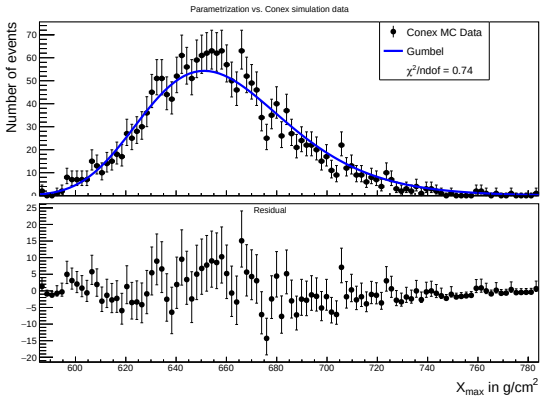

(b) $\log(E/\mathrm{eV}) = 17.5$

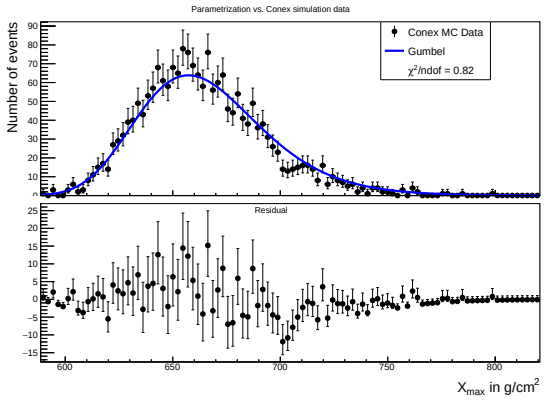

(c) $\log(E/\mathrm{eV}) = 17.6$

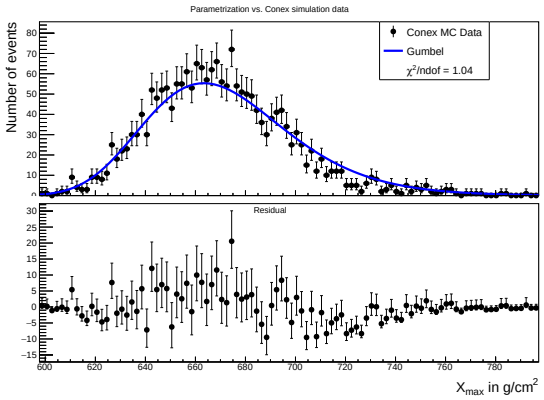

(d) $\log(E/\mathrm{eV}) = 17.7$

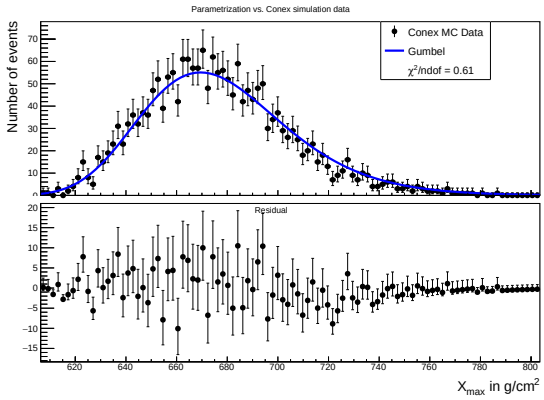

(e) $\log(E/\mathrm{eV}) = 17.8$

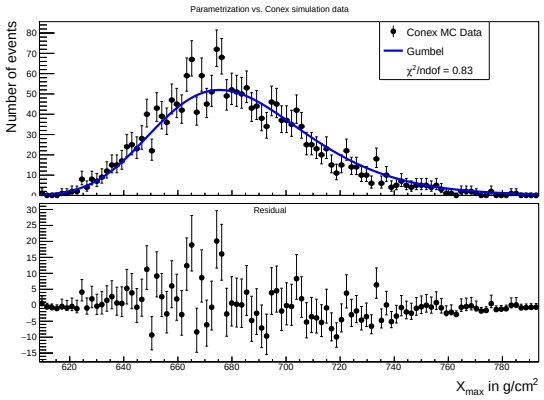

(f) $\log(E/\mathrm{eV}) = 17.9$

Figure C.8: X_{max}-distribution of 2000 N primary Conex air showers with EPOS LHC compared with Gumbel parametrization[150].

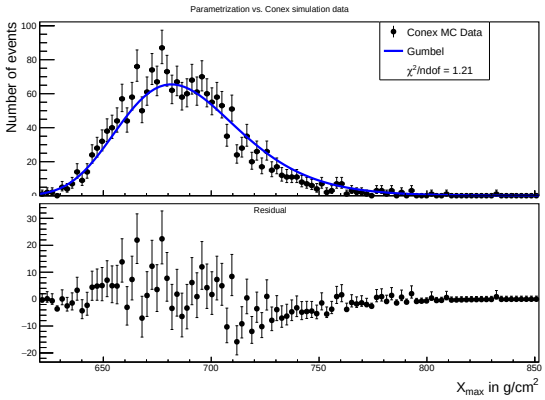

(a) $\log(E/\mathrm{eV}) = 18.0$

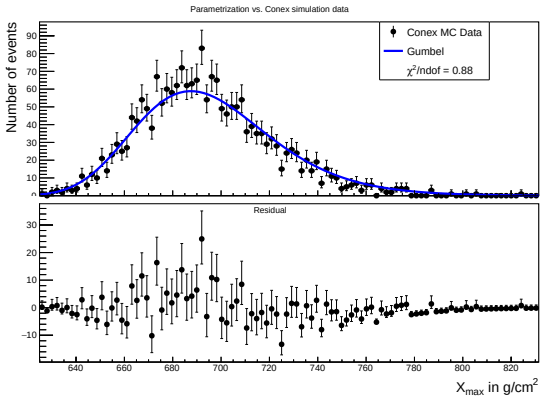

(b) $\log(E/\mathrm{eV}) = 18.1$

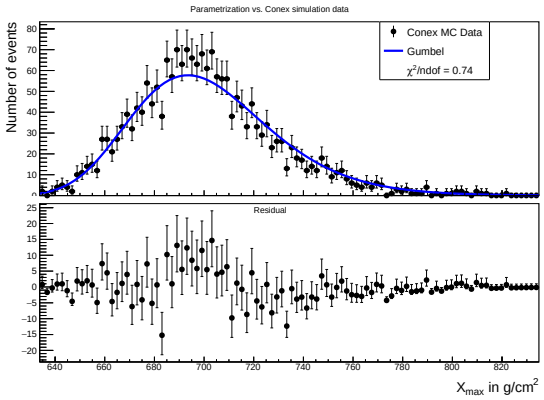

(c) $\log(E/\mathrm{eV}) = 18.2$

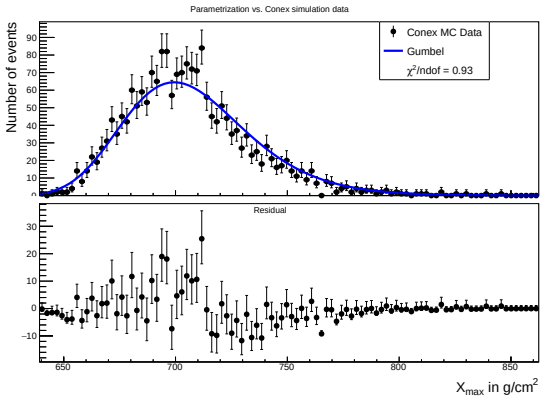

(d) $\log(E/\mathrm{eV}) = 18.3$

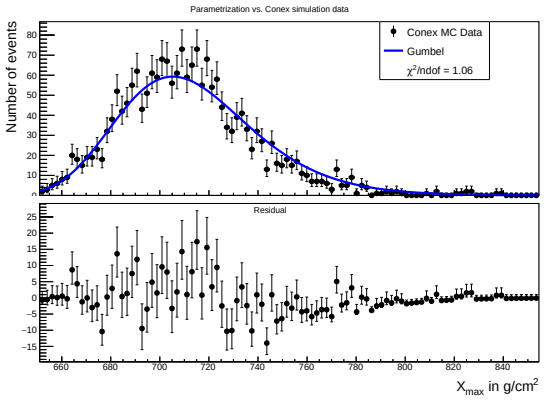

(e) $\log(E/\mathrm{eV}) = 18.4$

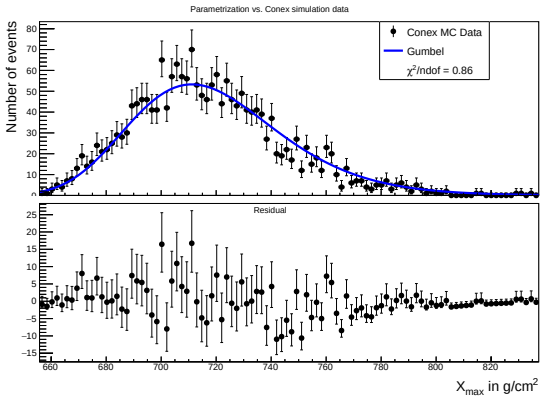

(f) $\log(E/\mathrm{eV}) = 18.5$

Figure C.9: X_{max}-distribution of 2000 N primary Conex air showers with EPOS LHC compared with Gumbel parametrization[150].

C.4 Conex Al primary

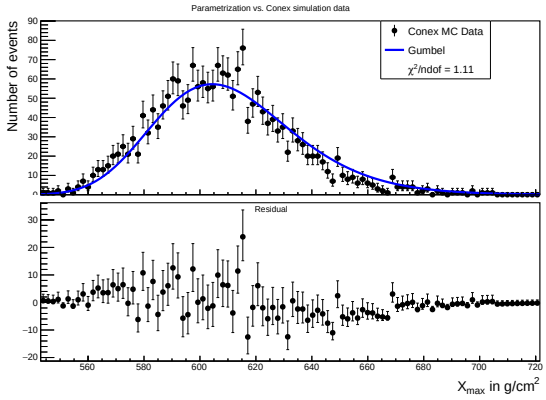

(a) $\log(E/\text{eV}) = 17.0$

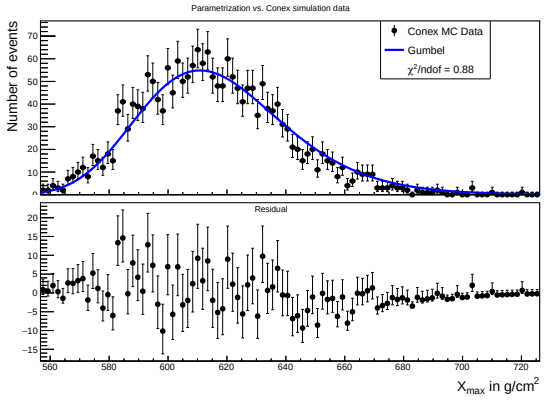

(b) $\log(E/\text{eV}) = 17.1$

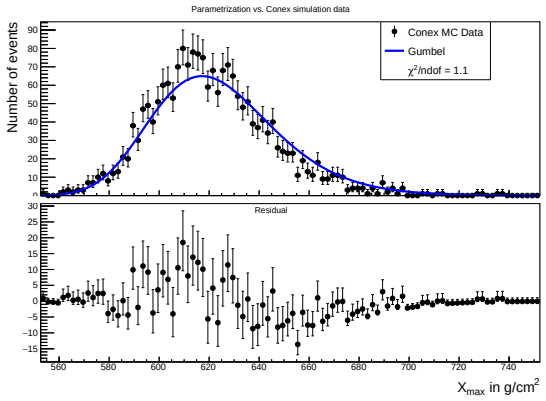

(c) $\log(E/\text{eV}) = 17.2$

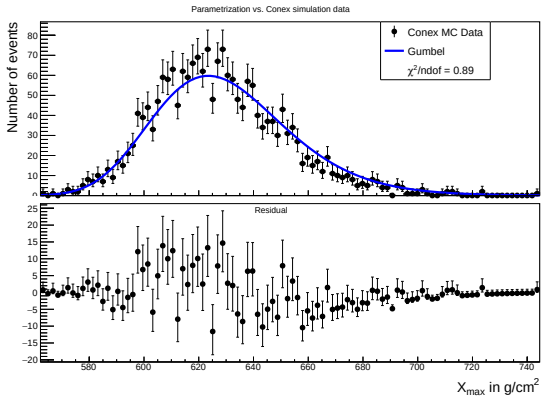

(d) $\log(E/\text{eV}) = 17.3$

Figure C.10: X_{max}-distribution of 2000 Al primary Conex air showers with EPOS LHC compared with Gumbel parametrization[150].

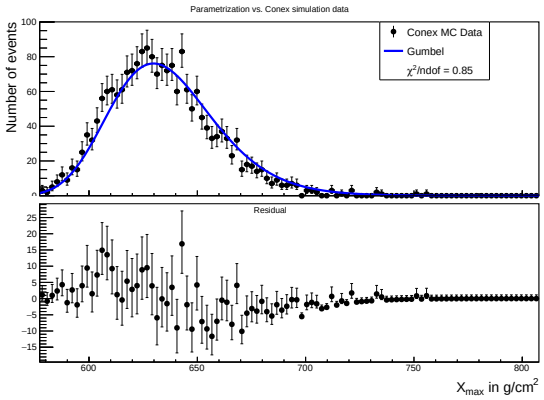

(a) $\log(E/\mathrm{eV}) = 17.4$

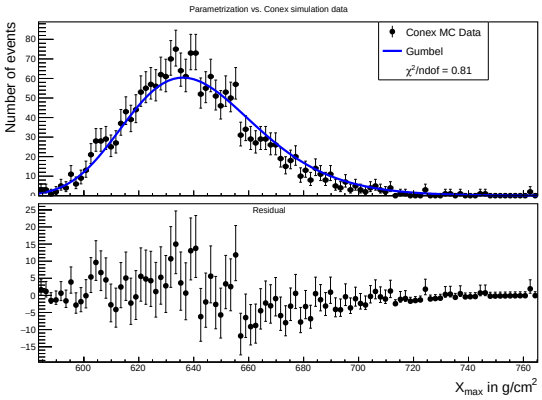

(b) $\log(E/\mathrm{eV}) = 17.5$

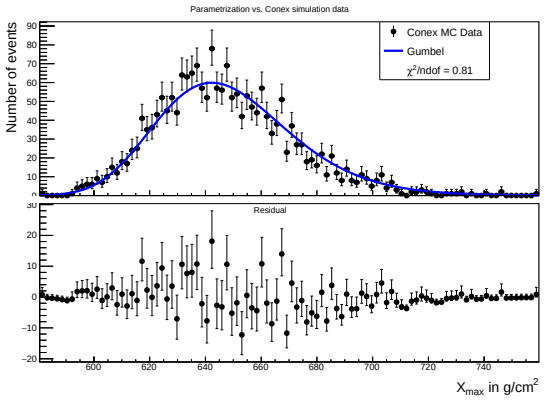

(c) $\log(E/\mathrm{eV}) = 17.6$

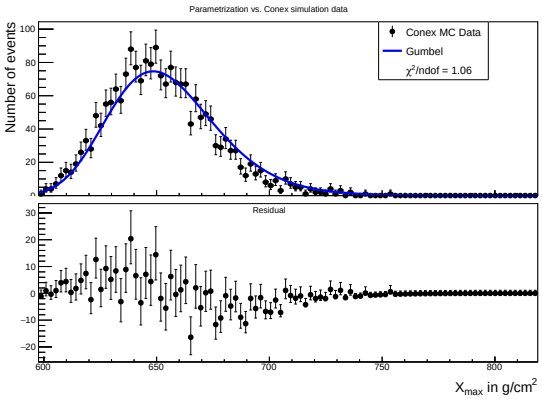

(d) $\log(E/\mathrm{eV}) = 17.7$

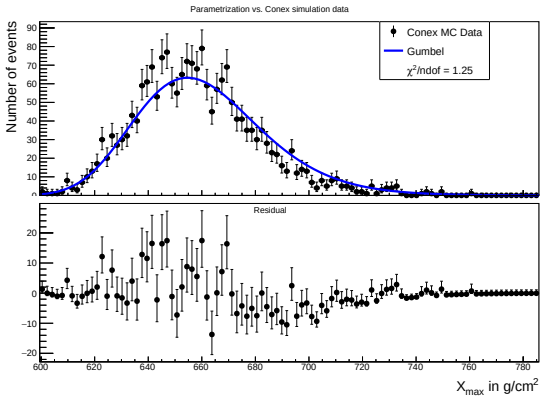

(e) $\log(E/\mathrm{eV}) = 17.8$

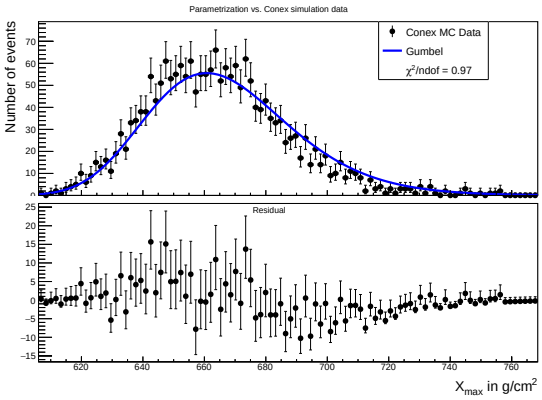

(f) $\log(E/\mathrm{eV}) = 17.9$

Figure C.11: X_{max}-distribution of 2000 Al primary Conex air showers with EPOS LHC compared with Gumbel parametrization[150].

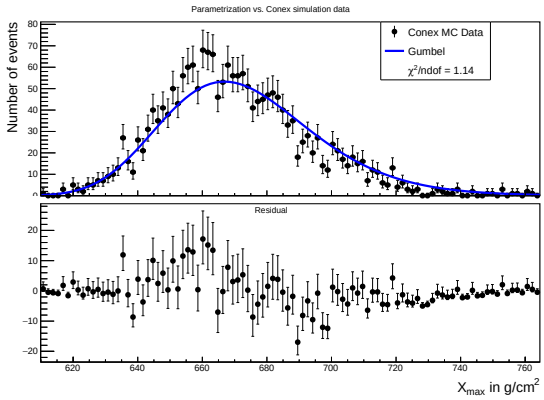

(a) $\log(E/\text{eV}) = 18.0$

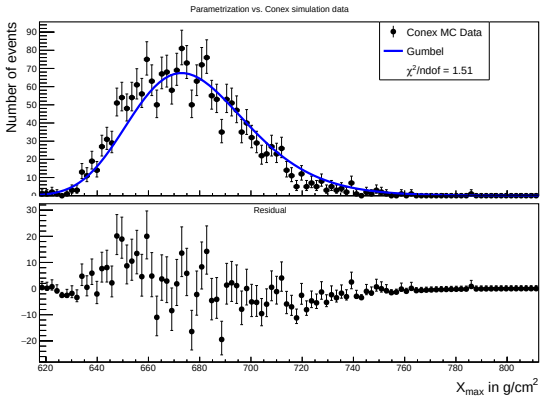

(b) $\log(E/\text{eV}) = 18.1$

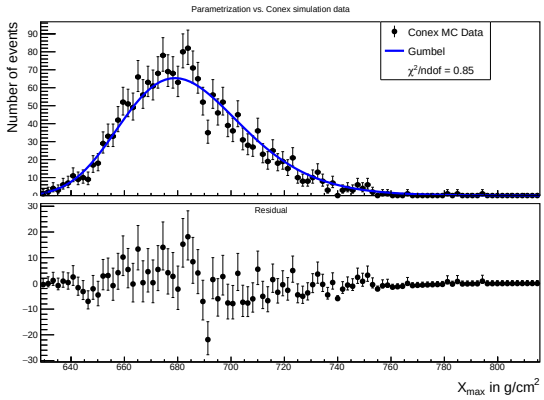

(c) $\log(E/\text{eV}) = 18.2$

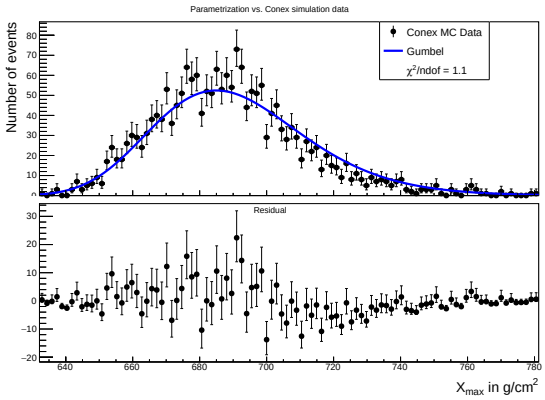

(d) $\log(E/\text{eV}) = 18.3$

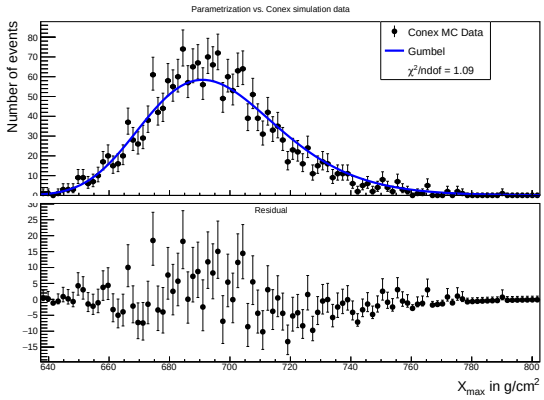

(e) $\log(E/\text{eV}) = 18.4$

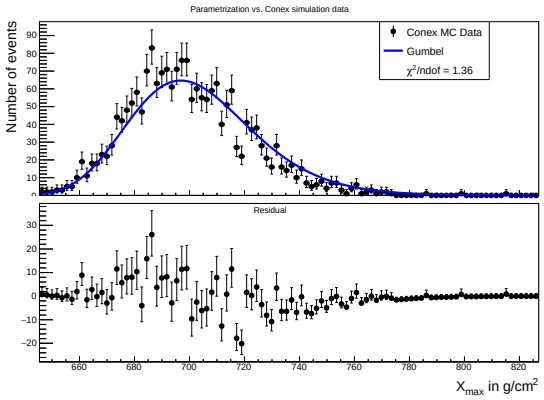

(f) $\log(E/\text{eV}) = 18.5$

Figure C.12: X_{max}-distribution of 2000 Al primary Conex air showers with EPOS LHC compared with Gumbel parametrization[150].

C.5 Conex Fe primary

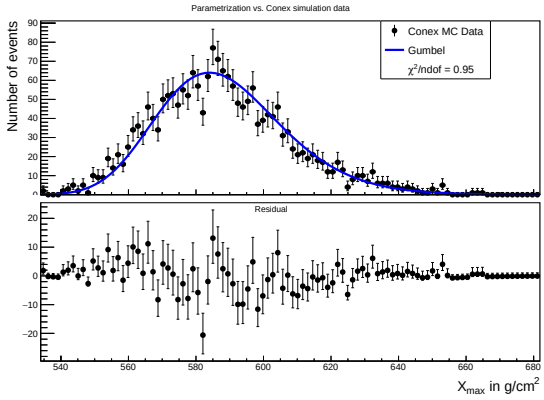

(a) $\log(E/\mathrm{eV}) = 17.0$

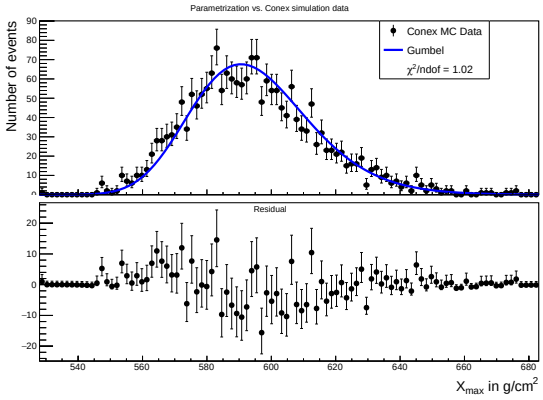

(b) $\log(E/\mathrm{eV}) = 17.1$

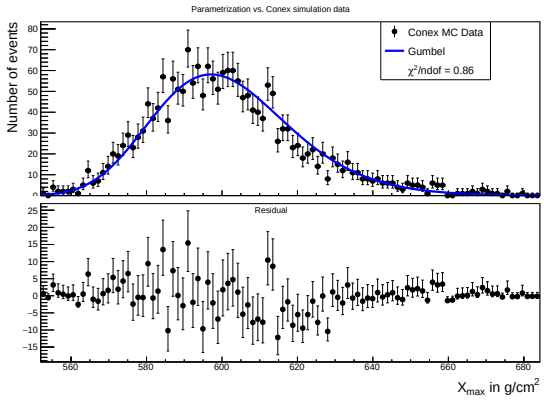

(c) $\log(E/\mathrm{eV}) = 17.2$

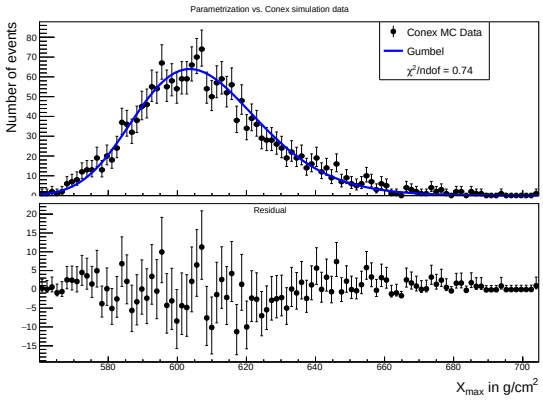

(d) $\log(E/\mathrm{eV}) = 17.3$

Figure C.13: X_{max}-distribution of 2000 Fe primary Conex air showers with EPOS LHC compared with Gumbel parametrization[150].

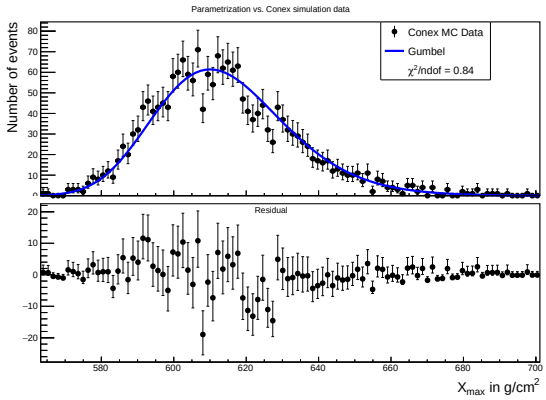

(a) $\log(E/\mathrm{eV}) = 17.4$

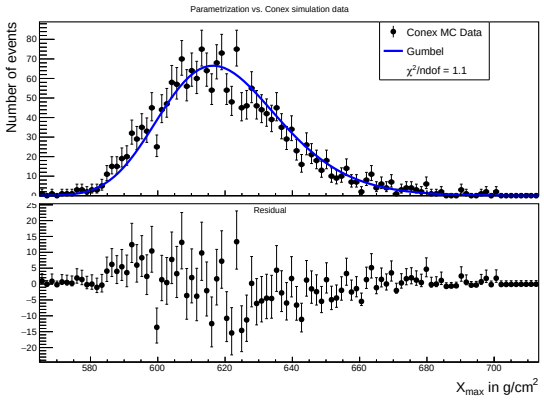

(b) $\log(E/\mathrm{eV}) = 17.5$

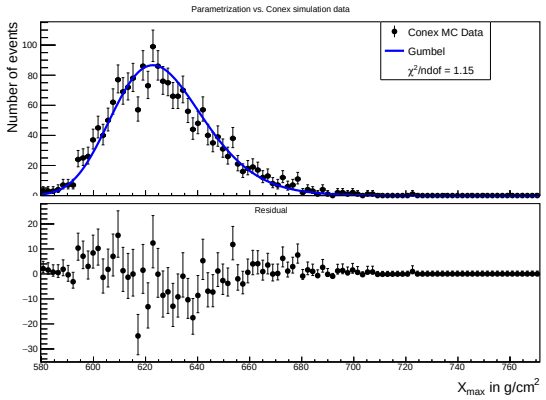

(c) $\log(E/\mathrm{eV}) = 17.6$

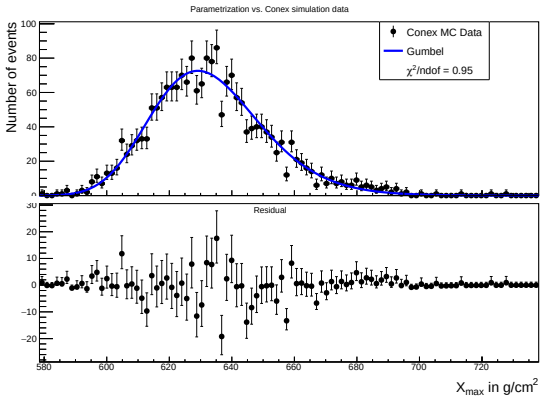

(d) $\log(E/\mathrm{eV}) = 17.7$

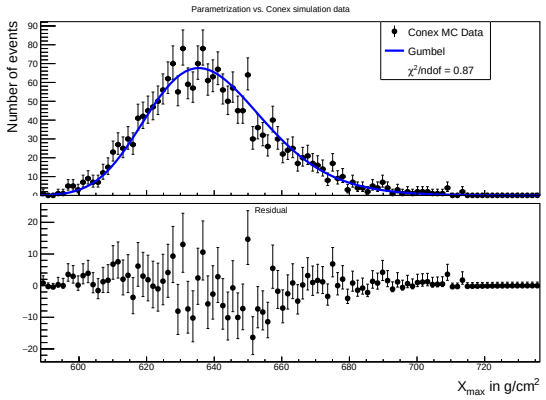

(e) $\log(E/\mathrm{eV}) = 17.8$

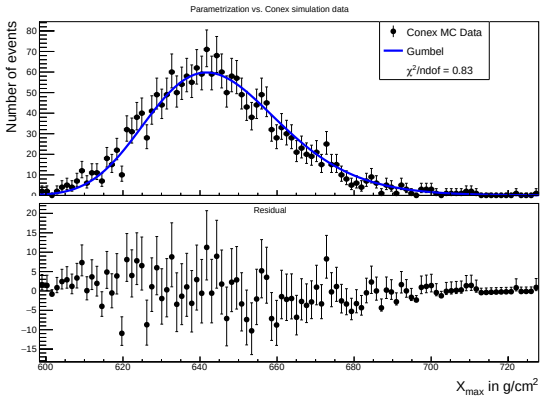

(f) $\log(E/\mathrm{eV}) = 17.9$

Figure C.14: X_{max}-distribution of 2000 Fe primary Conex air showers with EPOS LHC compared with Gumbel parametrization[150].

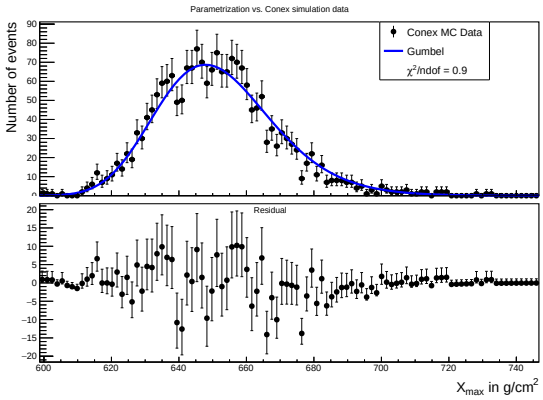

(a) $\log(E/\mathrm{eV}) = 18.0$

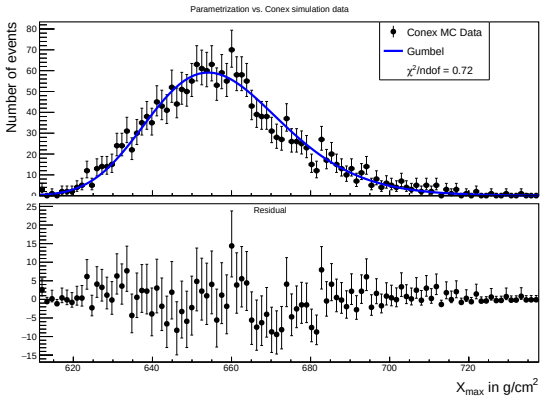

(b) $\log(E/\mathrm{eV}) = 18.1$

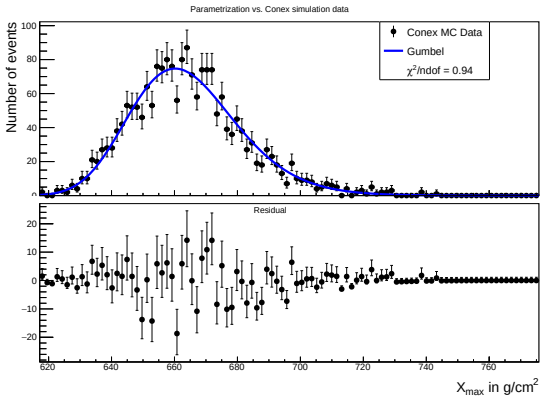

(c) $\log(E/\mathrm{eV}) = 18.2$

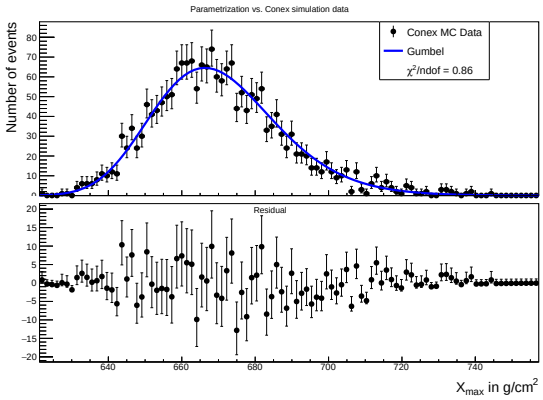

(d) $\log(E/\mathrm{eV}) = 18.3$

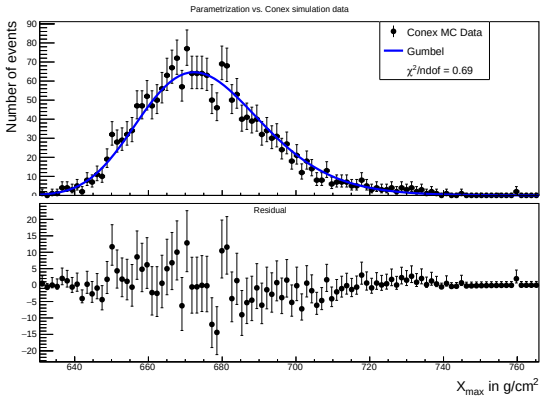

(e) $\log(E/\mathrm{eV}) = 18.4$

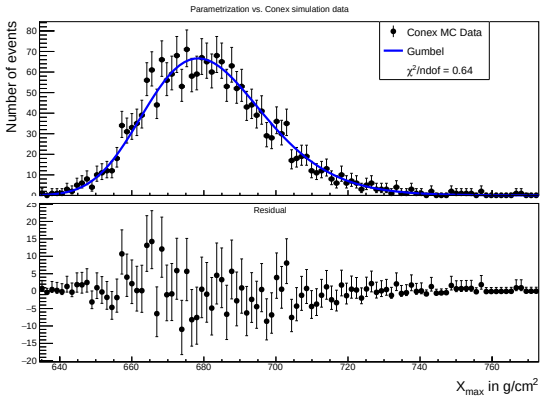

(f) $\log(E/\mathrm{eV}) = 18.5$

Figure C.15: X_{max}-distribution of 2000 Fe primary Conex air showers with EPOS LHC compared with Gumbel parametrization[150].

Appendix D

X_{max}-Distributions and Parametrization Fits

D.1 Epos-LHC Parametrization Fit

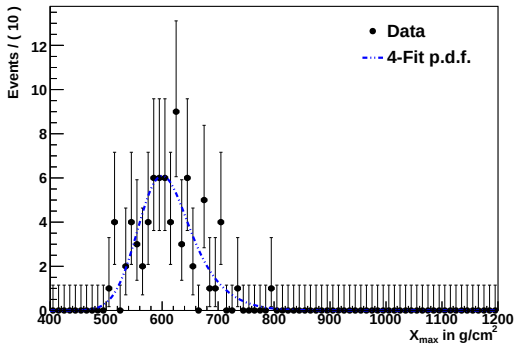

(a) $\log(E/\text{eV}) = 17.0 - 17.1$

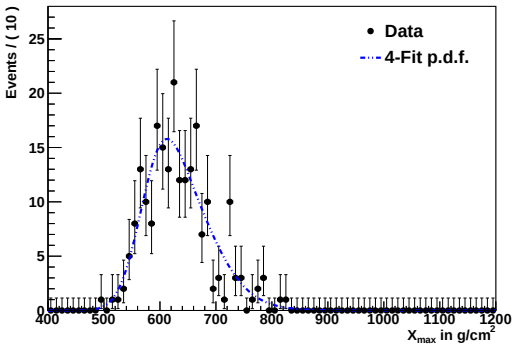

(b) $\log(E/\text{eV}) = 17.1 - 17.2$

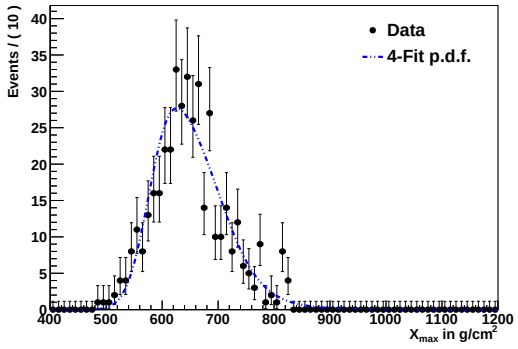

(c) $\log(E/\text{eV}) = 17.2 - 17.3$

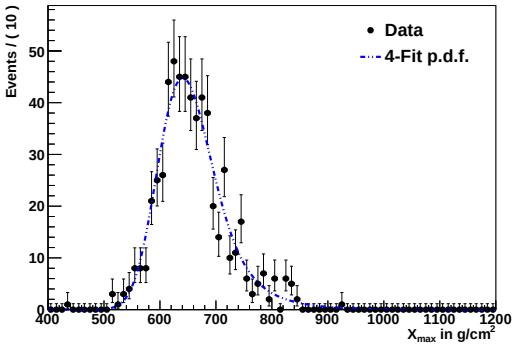

(d) $\log(E/\text{eV}) = 17.3 - 17.4$

Figure D.1: X_{max}-distribution of HECO data reconstructed with k_{LHC} constraint.

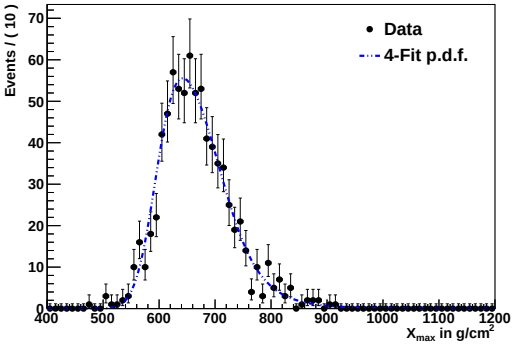

(a) $\log(E/\mathrm{eV}) = 17.4 - 17.5$

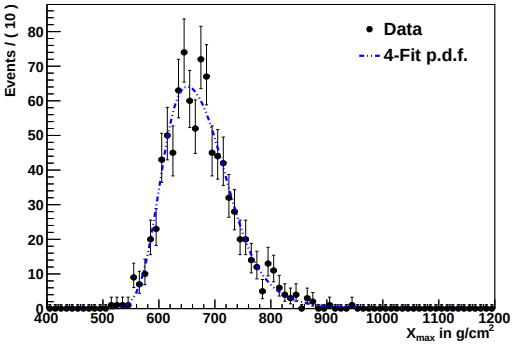

(b) $\log(E/\mathrm{eV}) = 17.5 - 17.6$

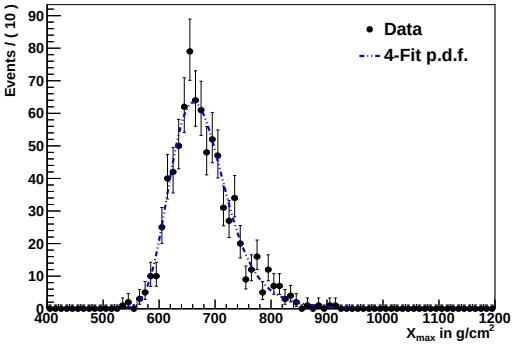

(c) $\log(E/\mathrm{eV}) = 17.6 - 17.7$

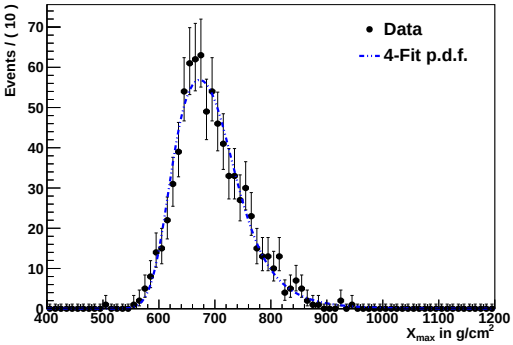

(d) $\log(E/\mathrm{eV}) = 17.7 - 17.8$

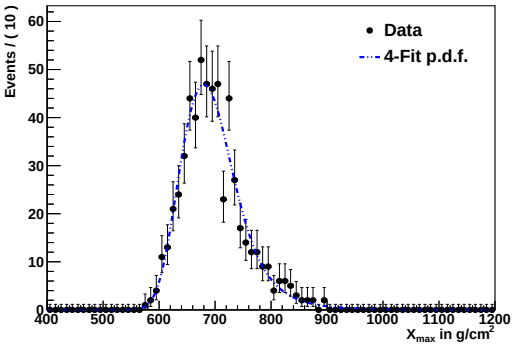

(e) $\log(E/\mathrm{eV}) = 17.8 - 17.9$

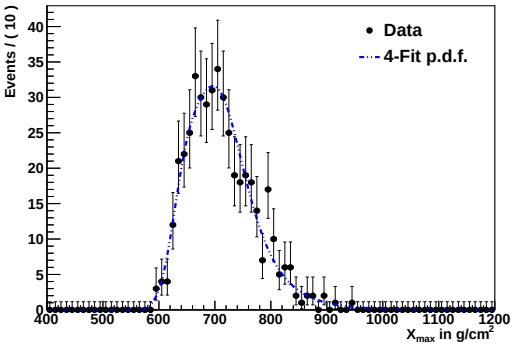

(f) $\log(E/\mathrm{eV}) = 17.9 - 18.0$

Figure D.2: X_{max}-distribution of HECO data reconstructed with k_{LHC} constraint.

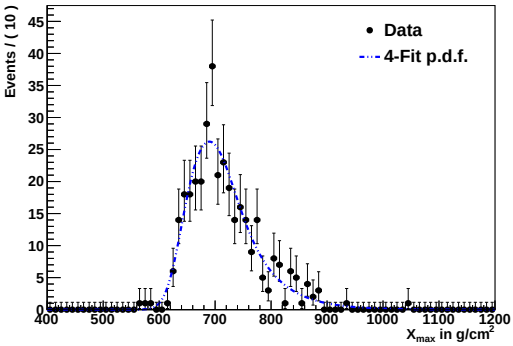

(a) $\log(E/\mathrm{eV}) = 18.0 - 18.1$

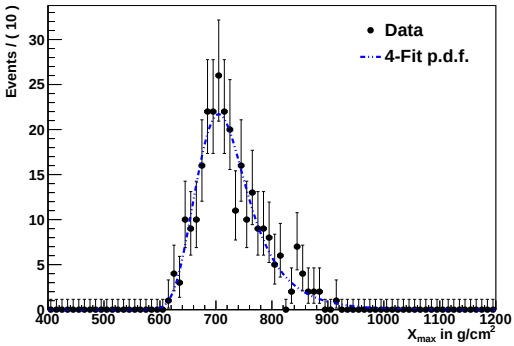

(b) $\log(E/\mathrm{eV}) = 18.1 - 18.2$

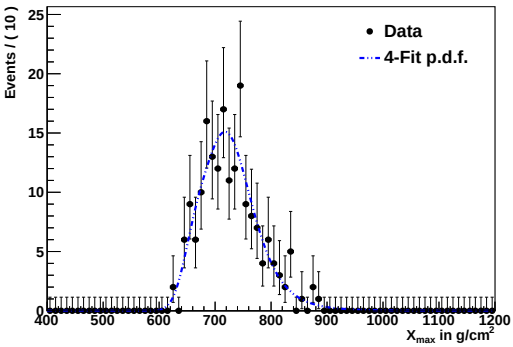

(c) $\log(E/\mathrm{eV}) = 18.2 - 18.3$

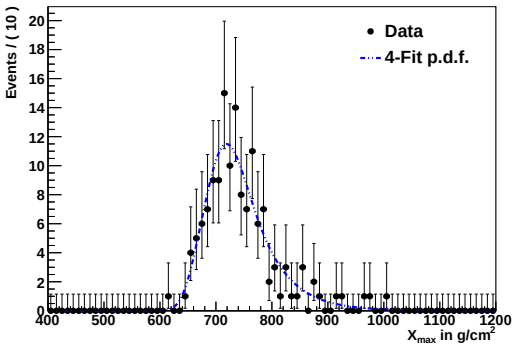

(d) $\log(E/\mathrm{eV}) = 18.3 - 18.4$

Figure D.3: X_{max}-distribution of HECO data reconstructed with k_{LHC} constraint.

D.2 QgsjetII-04 Parametrization Fit

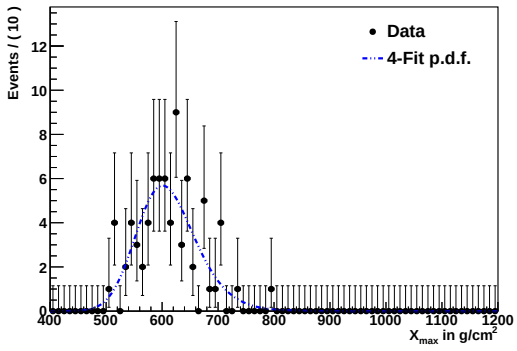

(a) $\log(E/\text{eV}) = 17.0 - 17.1$

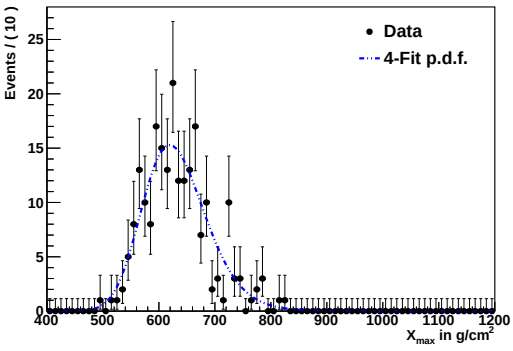

(b) $\log(E/\text{eV}) = 17.1 - 17.2$

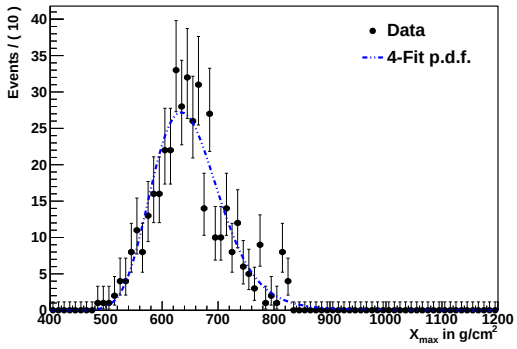

(c) $\log(E/\text{eV}) = 17.2 - 17.3$

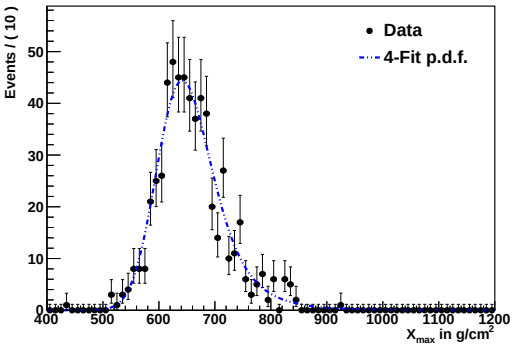

(d) $\log(E/\text{eV}) = 17.3 - 17.4$

Figure D.4: X_{max}-distribution of HECO data reconstructed with k_{LHC} constraint.

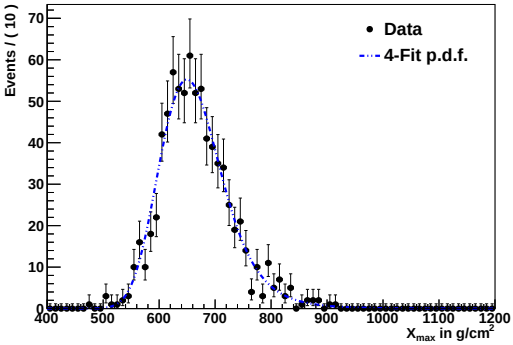

(a) $\log(E/\mathrm{eV}) = 17.4 - 17.5$

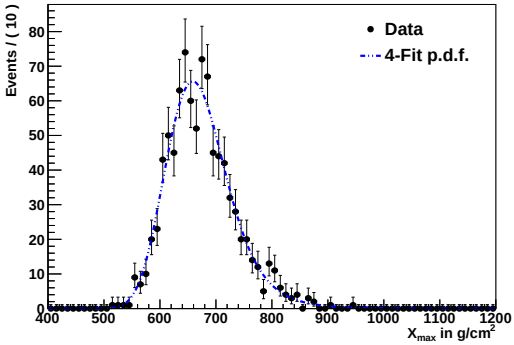

(b) $\log(E/\mathrm{eV}) = 17.5 - 17.6$

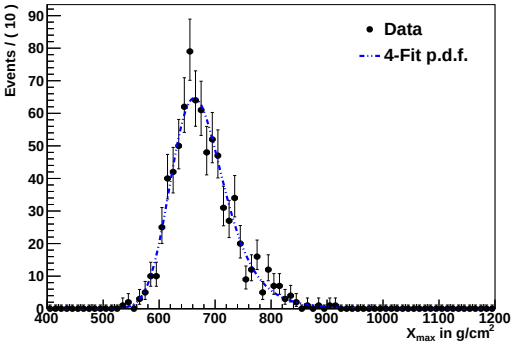

(c) $\log(E/\mathrm{eV}) = 17.6 - 17.7$

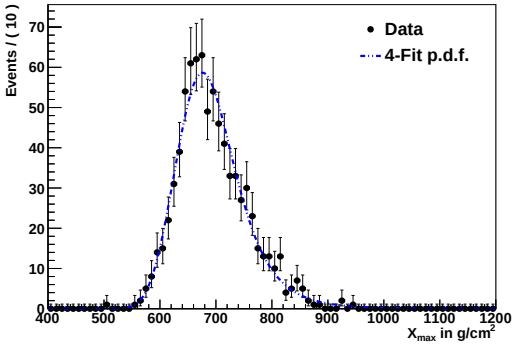

(d) $\log(E/\mathrm{eV}) = 17.7 - 17.8$

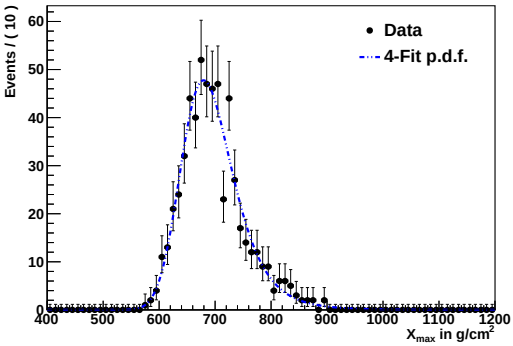

(e) $\log(E/\mathrm{eV}) = 17.8 - 17.9$

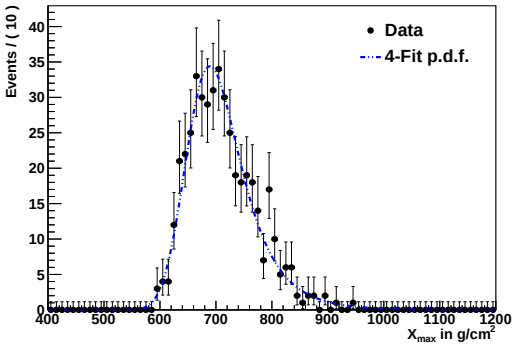

(f) $\log(E/\mathrm{eV}) = 17.9 - 18.0$

Figure D.5: X_{max}-distribution of HECO data reconstructed with k_{LHC} constraint.

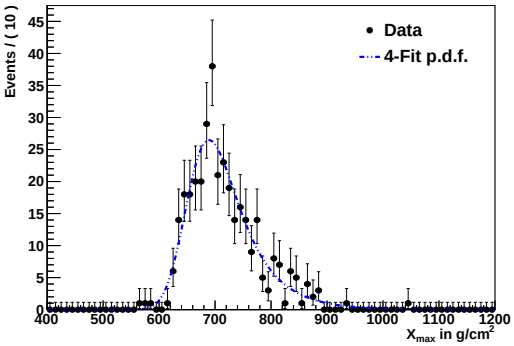

(a) $\log(E/\mathrm{eV}) = 18.0 - 18.1$

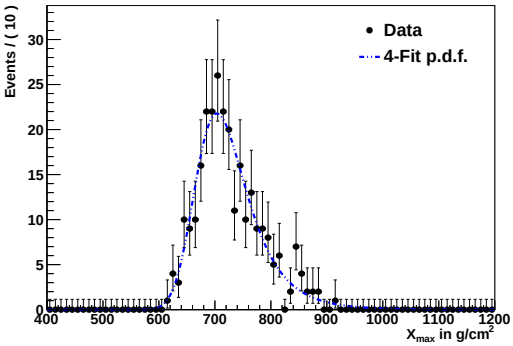

(b) $\log(E/\mathrm{eV}) = 18.1 - 18.2$

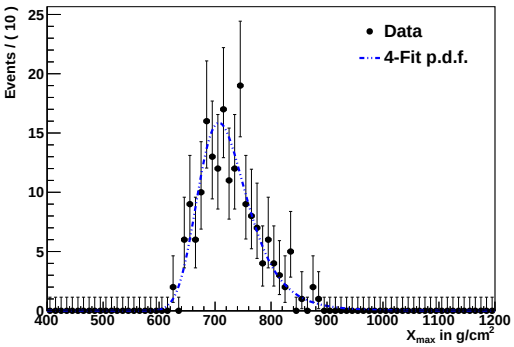

(c) $\log(E/\mathrm{eV}) = 18.2 - 18.3$

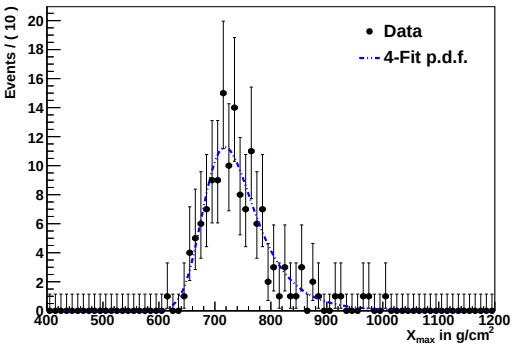

(d) $\log(E/\mathrm{eV}) = 18.3 - 18.4$

Figure D.6: X_{max}-distribution of HECO data reconstructed with k_{LHC} constraint.

D.3 Sibyll2.1 Parametrization Fit

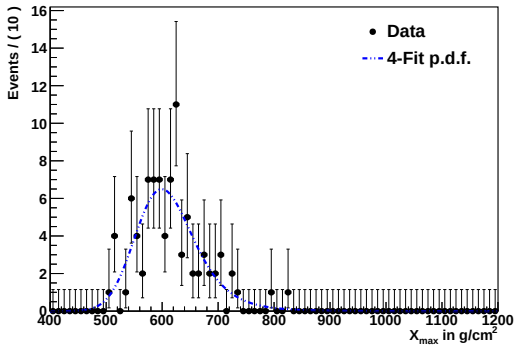

(a) $\log(E/\mathrm{eV}) = 17.0 - 17.1$

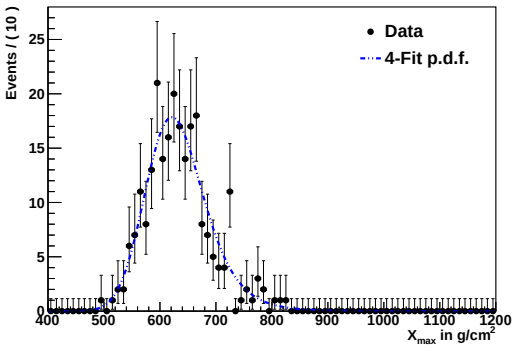

(b) $\log(E/\mathrm{eV}) = 17.1 - 17.2$

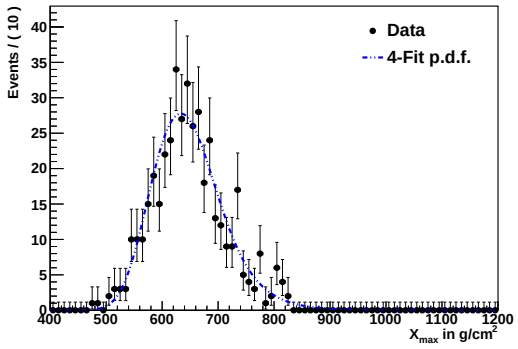

(c) $\log(E/\mathrm{eV}) = 17.2 - 17.3$

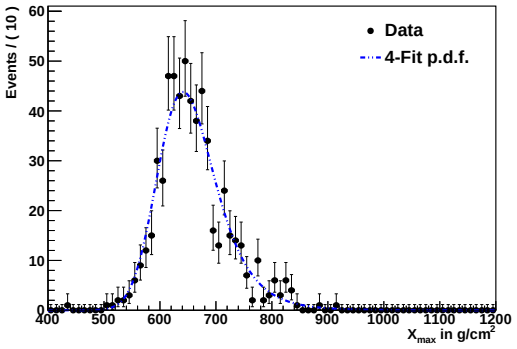

(d) $\log(E/\mathrm{eV}) = 17.3 - 17.4$

Figure D.7: X_{max}-distribution of HECO data reconstructed with k_{sib} constraint.

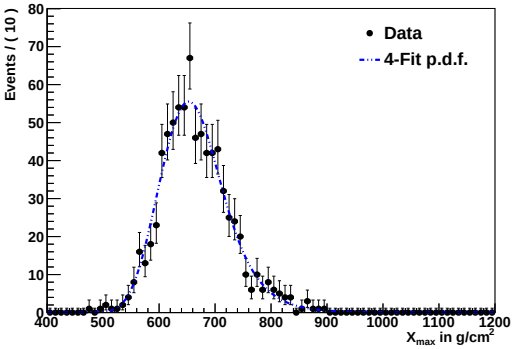

(a) $\log(E/\mathrm{eV}) = 17.4 - 17.5$

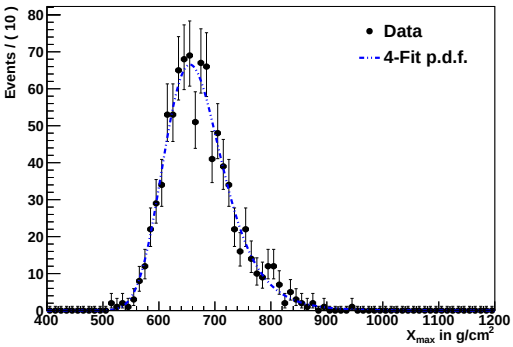

(b) $\log(E/\mathrm{eV}) = 17.5 - 17.6$

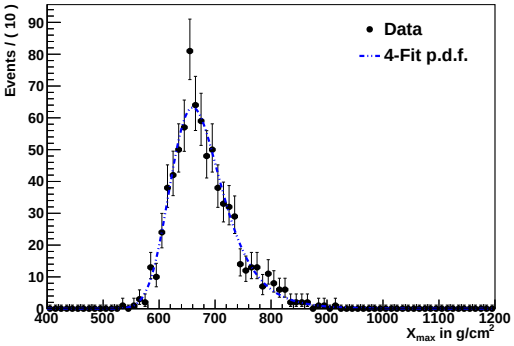

(c) $\log(E/\mathrm{eV}) = 17.6 - 17.7$

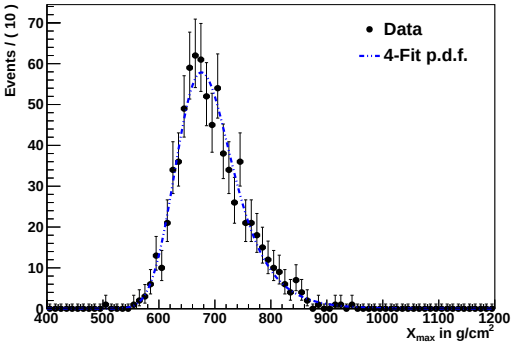

(d) $\log(E/\mathrm{eV}) = 17.7 - 17.8$

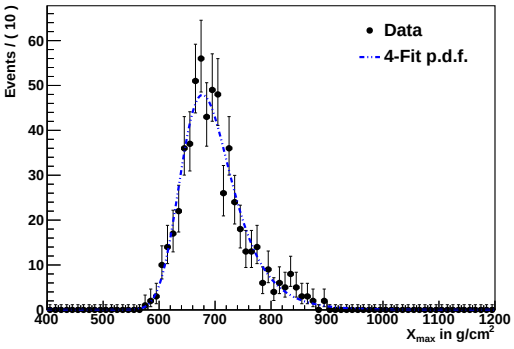

(e) $\log(E/\mathrm{eV}) = 17.8 - 17.9$

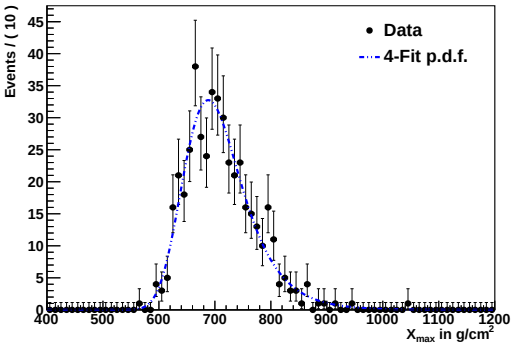

(f) $\log(E/\mathrm{eV}) = 17.9 - 18.0$

Figure D.8: X_{max}-distribution of HECO data reconstructed with k_{sib} constraint.

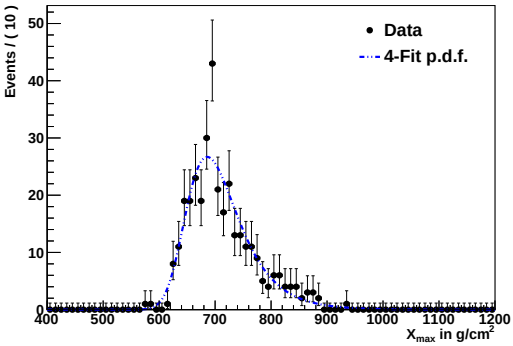

(a) $\log(E/\mathrm{eV}) = 18.0 - 18.1$

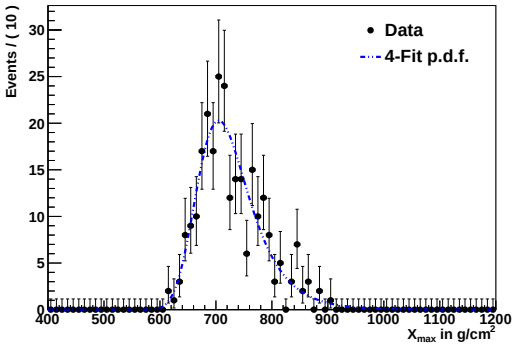

(b) $\log(E/\mathrm{eV}) = 18.1 - 18.2$

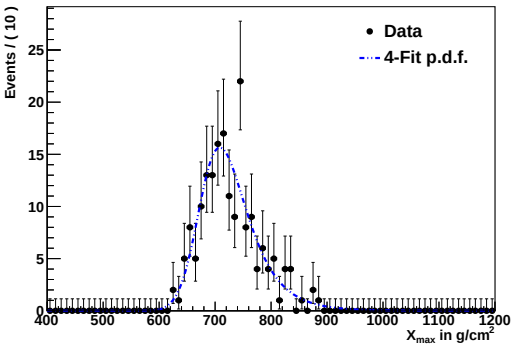

(c) $\log(E/\mathrm{eV}) = 18.2 - 18.3$

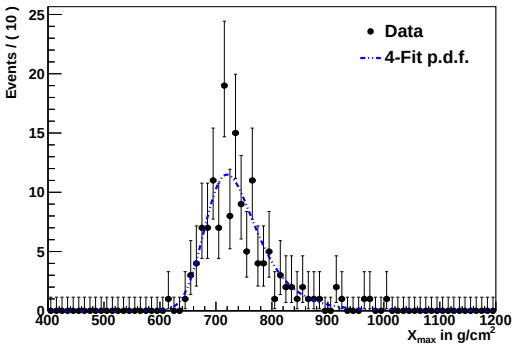

(d) $\log(E/\mathrm{eV}) = 18.3 - 18.4$

Figure D.9: X_{max}-distribution of HECO data reconstructed with k_{sib} constraint.

Appendix E

Validation of Data and RealMC

E.1 R_p Distribution

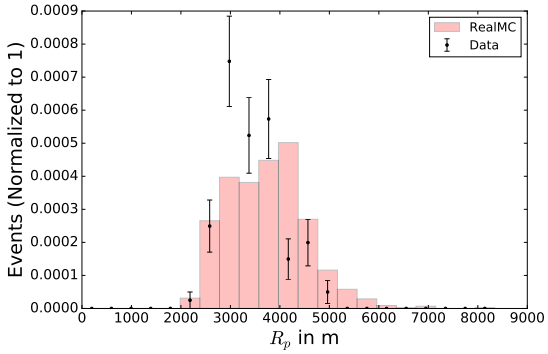

(a) $\log(E/\text{eV}) = 17.0 - 17.1$

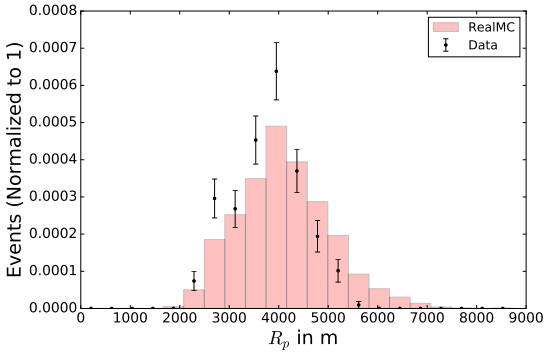

(b) $\log(E/\text{eV}) = 17.1 - 17.2$

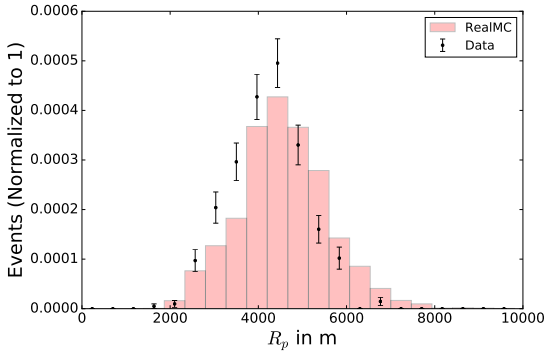

(c) $\log(E/\text{eV}) = 17.2 - 17.3$

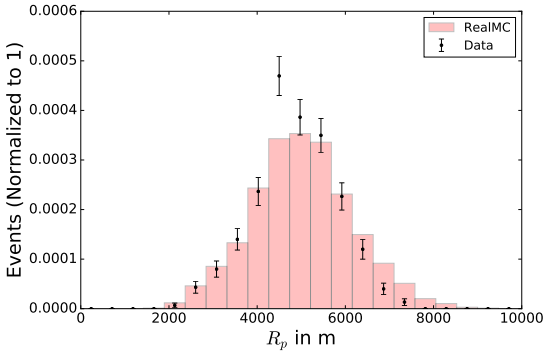

(d) $\log(E/\text{eV}) = 17.3 - 17.4$

Figure E.1: Comparison of the R_p distribution of data and RealMC. RealMC is represented in red. Reconstructed data is show in black.

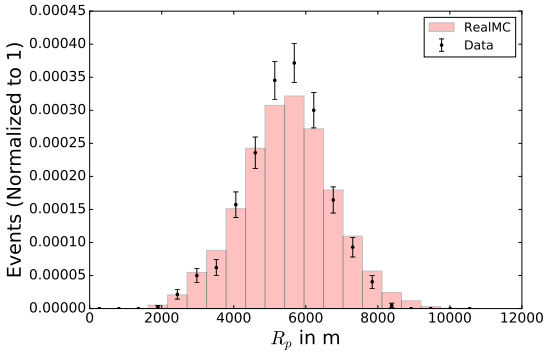

(a) $\log(E/\mathrm{eV}) = 17.4 - 17.5$

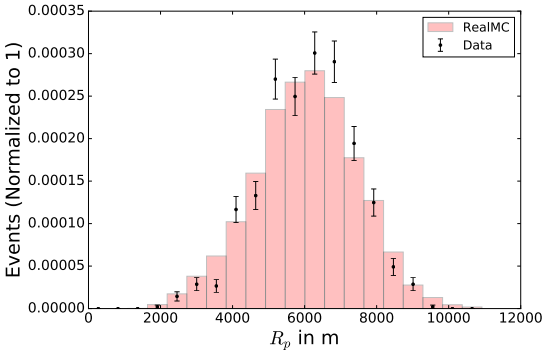

(b) $\log(E/\mathrm{eV}) = 17.5 - 17.6$

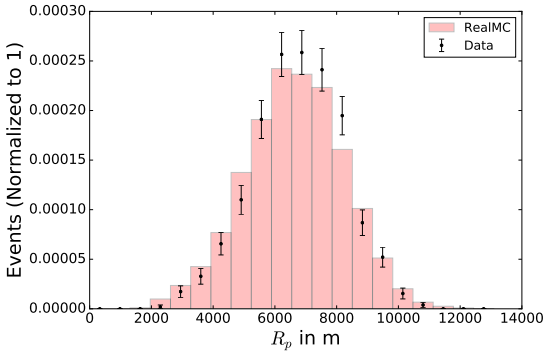

(c) $\log(E/\mathrm{eV}) = 17.6 - 17.7$

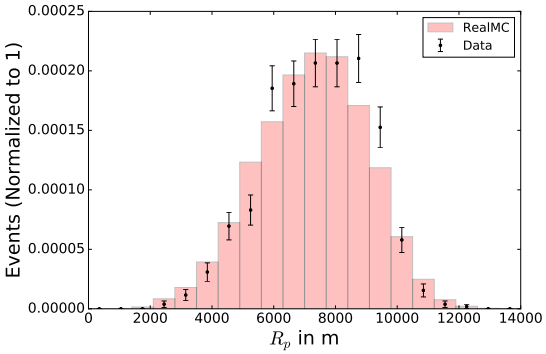

(d) $\log(E/\mathrm{eV}) = 17.7 - 17.8$

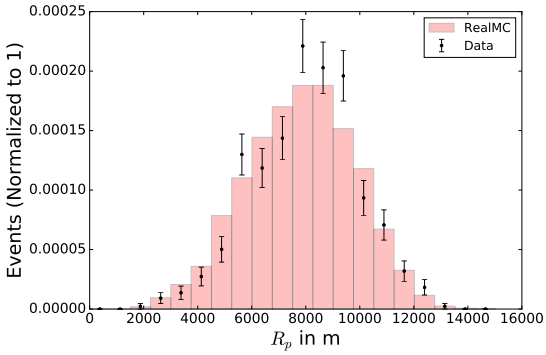

(e) $\log(E/\mathrm{eV}) = 17.8 - 17.9$

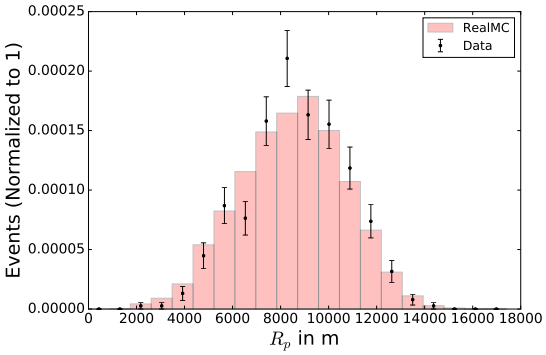

(f) $\log(E/\mathrm{eV}) = 17.9 - 18.0$

Figure E.2: Comparison of the R_p distribution of data and RealMC. RealMC is represented in red. Reconstructed data is show in black.

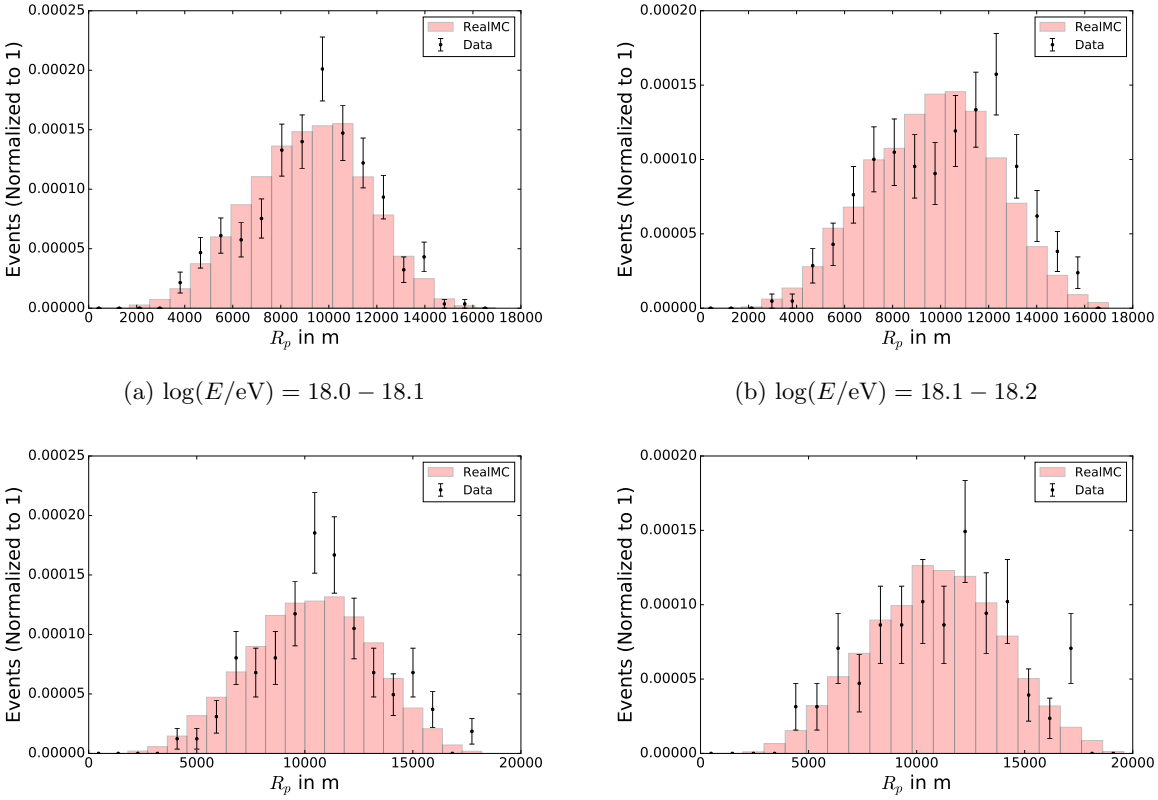

(a) $\log(E/\text{eV}) = 18.0 - 18.1$

(b) $\log(E/\text{eV}) = 18.1 - 18.2$

(c) $\log(E/\text{eV}) = 18.2 - 18.3$

(d) $\log(E/\text{eV}) = 18.3 - 18.4$

Figure E.3: Comparison of the R_p distribution of data and RealMC. RealMC is represented in red. Reconstructed data is show in black.

E.2 Zenith Angular Distribution

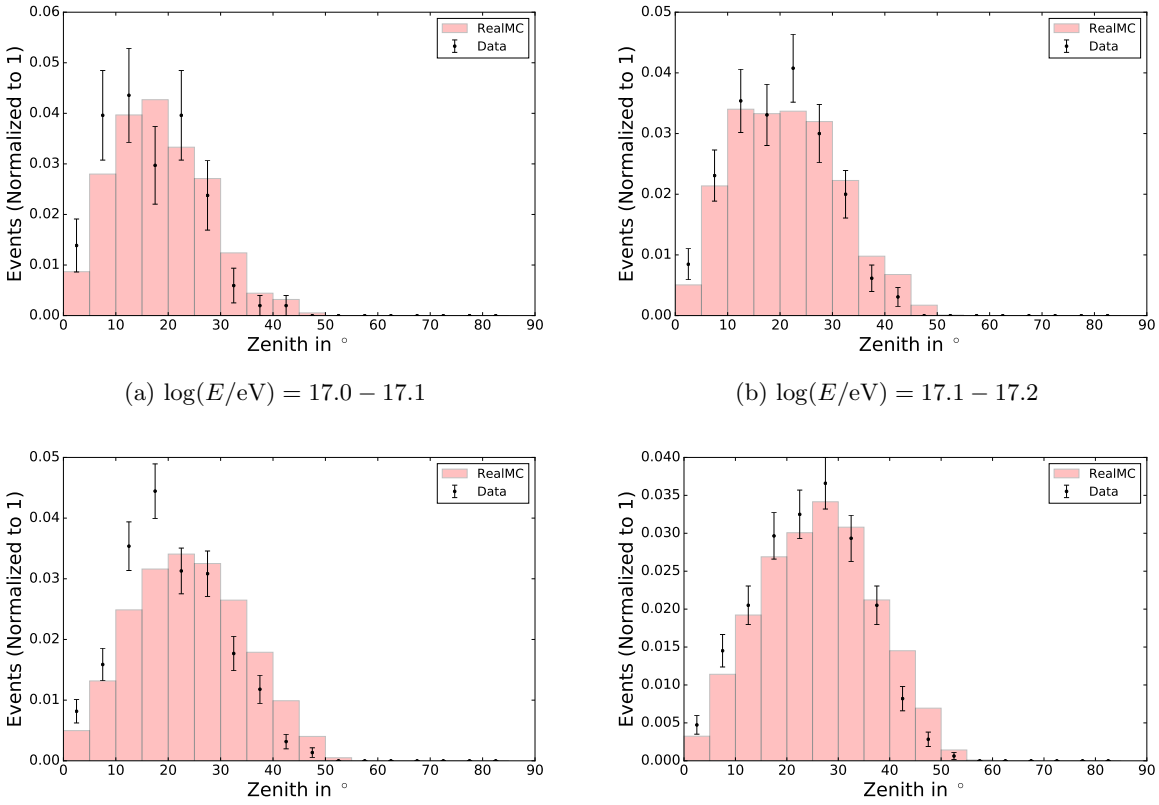

(a) $\log(E/\text{eV}) = 17.0 - 17.1$

(b) $\log(E/\text{eV}) = 17.1 - 17.2$

(c) $\log(E/\text{eV}) = 17.2 - 17.3$

(d) $\log(E/\text{eV}) = 17.3 - 17.4$

Figure E.4: Comparison of the zenith angular distribution of data and RealMC. RealMC is represented in red. Reconstructed data is show in black.

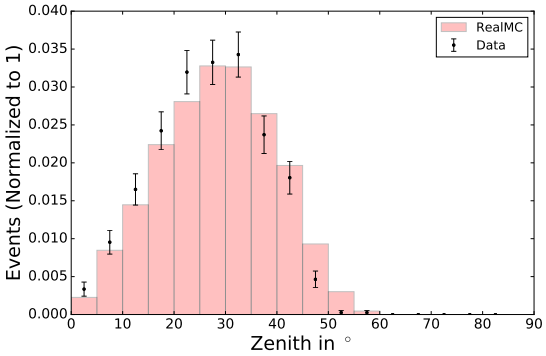

(a) $\log(E/\text{eV}) = 17.4 - 17.5$

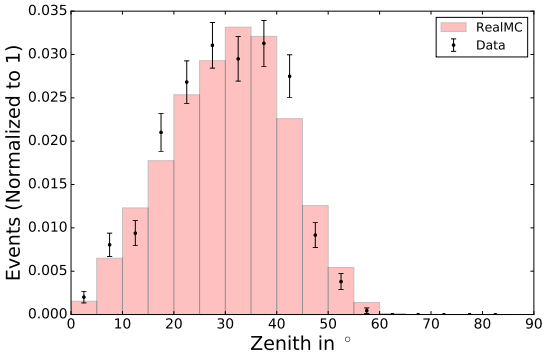

(b) $\log(E/\text{eV}) = 17.5 - 17.6$

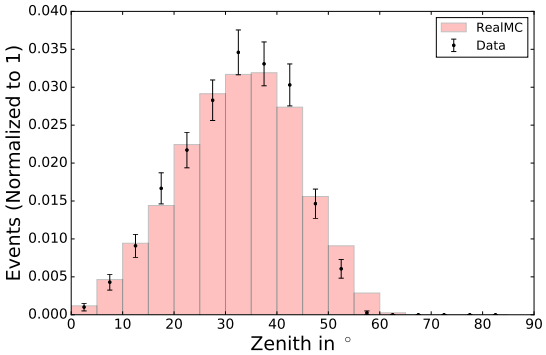

(c) $\log(E/\text{eV}) = 17.6 - 17.7$

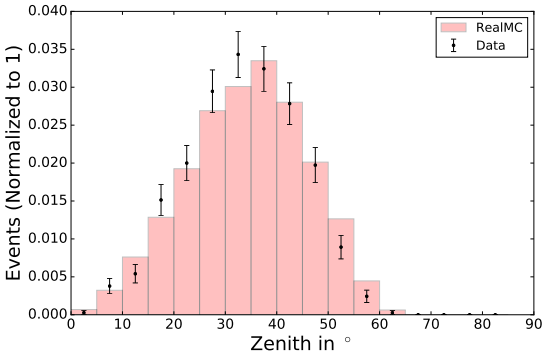

(d) $\log(E/\text{eV}) = 17.7 - 17.8$

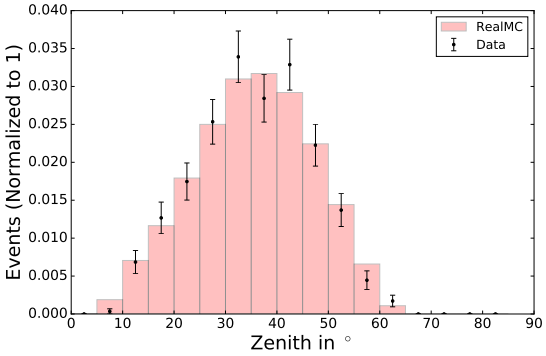

(e) $\log(E/\text{eV}) = 17.8 - 17.9$

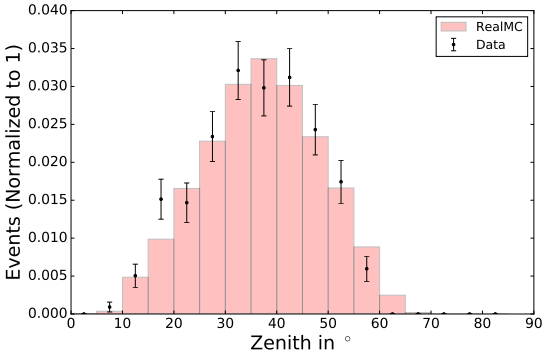

(f) $\log(E/\text{eV}) = 17.9 - 18.0$

Figure E.5: Comparison of the zenith angular distribution of data and RealMC. RealMC is represented in red. Reconstructed data is show in black.

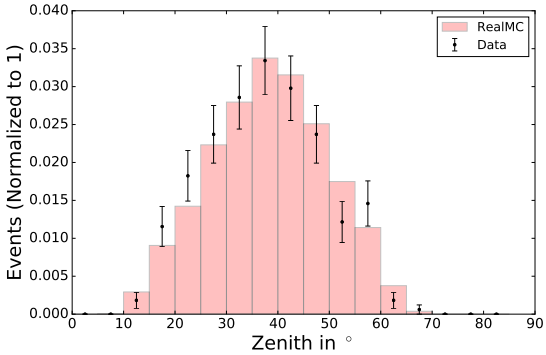

(a) $\log(E/\mathrm{eV}) = 18.0 - 18.1$

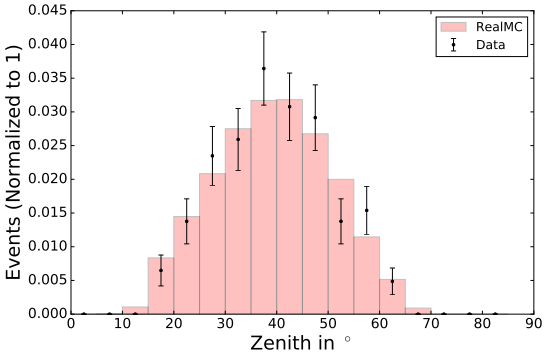

(b) $\log(E/\mathrm{eV}) = 18.1 - 18.2$

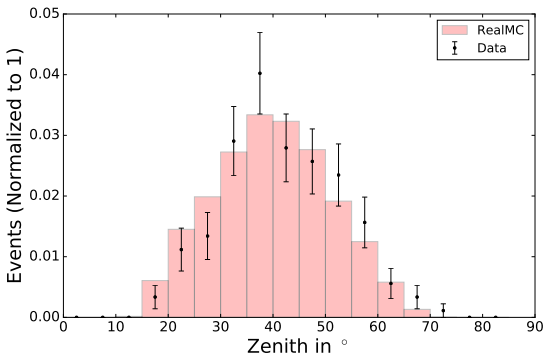

(c) $\log(E/\mathrm{eV}) = 18.2 - 18.3$

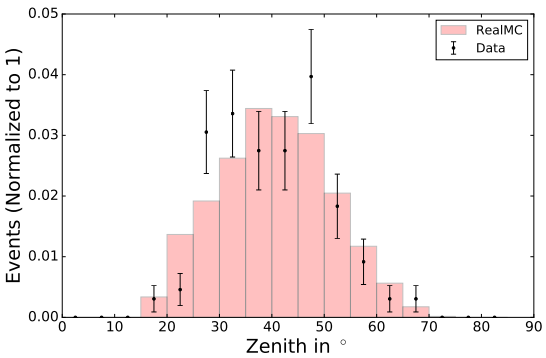

(d) $\log(E/\mathrm{eV}) = 18.3 - 18.4$

Figure E.6: Comparison of the zenith angular distribution of data and RealMC. RealMC is represented in red. Reconstructed data is show in black.

Appendix F

Data and Simulation Cut List

This chapter contains the cut lists for the event selection of the HECO air showers used in this thesis with the Offline [109] framework. These cuts are described in chapter 4.1.3 and are applied to the reconstructed data as well as to the simulated RealMC.

F.1 Eye

eyeCut	100000
heatOrientationUp	

F.2 Data Acquisition

badFDPeriodRejection	
skipSaturated	
noBadPixelsInPulse	
good10MHzCorrection	
minBackgroundRMSSimpleEyes	17 11111
minBackgroundRMSMergedEyes	17 6 11000

F.3 HECO

HeCoHasUpTime	
minPBrass	0.9
maxPBrassProtonIronDiff	0.05
RejectCDASVetoPeriods	100000 4
RejectFDASVetoPeriods	100000 4
RejectT3VetoPeriods	100000 4

F.4 Hybrid

hybridTankTrigger	2
maxZenithFD	85
minLgEnergyFD	1.e-20
maxCoreTankDist	1500

F.5 Reconstruction

XmaxErrorLessThenXmax	
maxDepthHole	30
profileChi2Sigma	5. -1.42

F.6 Atmosphere

hasMieDatabase	
maxVAOD	params: .1 nMinusOne: 100 0. 1.
cloudCut	

F.7 Field of View

xMaxObsInExpectedFOV	params: 40 20
fiducialFOV	

Bibliography

[1] V. F. Hess, "Über Beobachtungen der durchdringenden Strahlung bei sieben Freiballonfahrten," *Z. Phys.*, vol. 13, pp. 1084–1091, 1912.

[2] P. Auger, P. Ehrenfest, R. Maze, J. Daudin, and R. A. Fréon, "Extensive cosmic-ray showers," *Rev. Mod. Phys.*, vol. 11, pp. 288–291, Jul 1939.

[3] J. Linsley, "Evidence for a Primary Cosmic-Ray Particle with Energy 10^{20} eV," *Phys. Rev. Lett.*, vol. 10, pp. 146–148, Feb 1963.

[4] L. Evans and P. Bryant, "LHC Machine," *Journal of Instrumentation*, vol. 3, no. 08, p. S08001, 2008.

[5] J. Blümer, R. Engel, and J. R. Hörandel, "Cosmic rays from the knee to the highest energies," *Progress in Particle and Nuclear Physics*, vol. 63, no. 2, pp. 293 – 338, 2009.

[6] C. Patrignani *et al.*, "Review of Particle Physics," *Chin. Phys.*, vol. C40, no. 10, p. 100001, 2016.

[7] W. Baade and F. Zwicky, "Remarks on Super-Novae and Cosmic Rays," *Phys. Rev.*, vol. 46, pp. 76–77, Jul 1934.

[8] E. Fermi, "On the Origin of the Cosmic Radiation," *Phys. Rev.*, vol. 75, pp. 1169–1174, Apr 1949.

[9] V. L. Ginzburg and S. I. Syrovatsky, "Origin of cosmic rays," *International Cosmic Ray Conference*, vol. 1, p. 53, 1965.

[10] W. I. Axford, E. Leer, and G. Skadron, "The acceleration of cosmic rays by shock waves," *International Cosmic Ray Conference*, vol. 11, pp. 132–137, 1977.

[11] A. R. Bell, "The acceleration of cosmic rays in shock fronts. I," MNRAS, vol. 182, pp. 147–156, Jan. 1978.

[12] P. Blasi, "The Origin of Galactic Cosmic Rays," *Astron. Astrophys. Rev.*, vol. 21, p. 70, 2013.

[13] S. G. Lucek and A. R. Bell, "Non-linear amplification of a magnetic field driven by cosmic ray streaming," MNRAS, vol. 314, pp. 65–74, May 2000.

[14] R. Aloisio, V. Berezinsky, and A. Gazizov, "Transition from galactic to extragalactic cosmic rays," *Astroparticle Physics*, vol. 39, pp. 129–143, Dec. 2012.

[15] V. Berezinsky, "Extragalactic cosmic rays and their signatures," *Astroparticle Physics*, vol. 53, pp. 120 – 129, 2014.

[16] W. D. Apel *et al.*, "KASCADE-Grande measurements of energy spectra for elemental groups of cosmic rays," *Astroparticle Physics*, vol. 47, pp. 54 – 66, 2013.

[17] G. Giacinti, M. Kachelrieß, and D. V. Semikoz, "Escape model for Galactic cosmic rays and an early extragalactic transition," *Phys. Rev. D*, vol. 91, p. 083009, Apr 2015.

[18] J. R. Hörandel, "Cosmic rays from the knee to the second knee: 10^{14} to 10^{18} eV," *Mod. Phys. Lett.*, vol. A22, pp. 1533–1552, 2007.

[19] A. M. Hillas, "The Origin of Ultra-High-Energy Cosmic Rays," *Annual Review of Astronomy and Astrophysics*, vol. 22, no. 1, pp. 425–444, 1984.

[20] P. M. Bauleo and J. R. Martino, "The dawn of the particle astronomy era in ultra-high-energy cosmic rays," *Nature*, vol. 458, pp. 847–851, Apr 2009.

[21] J. Abraham *et al.*, "Correlation of the highest energy cosmic rays with nearby extragalactic objects," *Science*, vol. 318, pp. 938–943, 2007.

[22] J. Abraham *et al.*, "Correlation of the highest-energy cosmic rays with the positions of nearby active galactic nuclei," *Astroparticle Physics*, vol. 29, pp. 188–204, 2008. [Erratum: Astroparticle Physics 30,45(2008)].

[23] P. Abreu *et al.*, "Update on the correlation of the highest energy cosmic rays with nearby extragalactic matter," *Astroparticle Physics*, vol. 34, pp. 314–326, 2010.

[24] R. U. Abbasi *et al.*, "Search for Correlations between HiRes Stereo Events and Active Galactic Nuclei," *Astroparticle Physics*, vol. 30, pp. 175–179, 2008.

[25] T. Abu-Zayyad *et al.*, "Search for Anisotropy of Ultrahigh Energy Cosmic Rays with the Telescope Array Experiment," *Astrophys. J.*, vol. 757, p. 26, Sept. 2012.

[26] R. U. Abbasi *et al.*, "Indications of Intermediate-Scale Anisotropy of Cosmic Rays with Energy Greater Than 57 EeV in the Northern Sky Measured with the Surface Detector of the Telescope Array Experiment," *Astrophys. J.*, vol. 790, p. L21, 2014.

[27] A. Aab *et al.*, "Searches for Large-Scale Anisotropy in the Arrival Directions of Cosmic Rays Detected above Energy of 10^{19} eV at the Pierre Auger Observatory and the Telescope Array," *Astrophys. J.*, vol. 794, no. 2, p. 172, 2014.

[28] M. G. Aartsen *et al.*, "Search for correlations between the arrival directions of IceCube neutrino events and ultrahigh-energy cosmic rays detected by the Pierre Auger Observatory and the Telescope Array," *JCAP*, vol. 1601, no. 01, p. 037, 2016.

[29] R. U. Abbasi *et al.*, "First Observation of the Greisen-Zatsepin-Kuzmin Suppression," *Phys. Rev. Lett.*, vol. 100, p. 101101, Mar 2008.

[30] T. Abu-Zayyad *et al.*, "Energy Spectrum of Ultra-High Energy Cosmic Rays Observed with the Telescope Array Using a Hybrid Technique," *Astroparticle Physics*, vol. 61, pp. 93–101, 2015.

[31] J. Abraham *et al.*, "Observation of the Suppression of the Flux of Cosmic Rays above 4×10^{19} eV," *Phys. Rev. Lett.*, vol. 101, p. 061101, Aug 2008.

[32] K. Greisen, "End to the Cosmic-Ray Spectrum?," *Phys. Rev. Lett.*, vol. 16, pp. 748–750, Apr 1966.

[33] G. T. Zatsepin and V. A. Kuz'min, "Upper Limit of the Spectrum of Cosmic Rays," *Soviet Journal of Experimental and Theoretical Physics Letters*, vol. 4, p. 78, Aug. 1966.

[34] F. W. Stecker and M. H. Salamon, "Photodisintegration of ultrahigh-energy cosmic rays: A New determination," *Astrophys. J.*, vol. 512, pp. 521–526, 1999.

[35] K.-H. Kampert and P. Tinyakov, "Cosmic rays from the ankle to the cutoff," *Comptes Rendus Physique*, vol. 15, pp. 318–328, 2014.

[36] T. Wibig and A. W. Wolfendale, "At what particle energy do extragalactic cosmic rays start to predominate?," *J. Phys.*, vol. G31, pp. 255–264, 2005.

[37] A. M. Hillas, "Cosmic Rays: Recent Progress and some Current Questions," in *Conference on Cosmology, Galaxy Formation and Astro-Particle Physics on the Pathway to the SKA Oxford, England, April 10-12, 2006*, 2006.

[38] V. Berezinsky, A. Z. Gazizov, and S. I. Grigorieva, "Dip in UHECR spectrum as signature of proton interaction with CMB," *Phys. Lett.*, vol. B612, pp. 147–153, 2005.

[39] P. Sokolsky *et al.*, "Final Results from the High solution Flys Eye (HiRes) Experiment," *Nuclear Physics B - Proceedings Supplements*, vol. 212213, pp. 74–78, 2011.

[40] M. Fukushima, "Recent Results from Telescope Array," *EPJ Web Conf.*, vol. 99, p. 04004, 2015.

[41] A. Aab *et al.*, "Depth of maximum of air-shower profiles at the Pierre Auger Observatory. I. Measurements at energies above $10^{17.8}$ eV," *Phys. Rev. D*, vol. 90, p. 122005, Dec 2014.

[42] A. Aab *et al.*, "Depth of maximum of air-shower profiles at the Pierre Auger Observatory. II. Composition implications," *Phys. Rev. D*, vol. 90, p. 122006, Dec 2014.

[43] R. U. Abbasi *et al.*, "Pierre Auger Observatory and Telescope Array: Joint Contributions to the 34th International Cosmic Ray Conference (ICRC 2015)," *ArXiv e-prints*, 2015.

[44] D. Allard, E. Parizot, E. Khan, S. Goriely, and A. V. Olinto, "UHE nuclei propagation and the interpretation of the ankle in the cosmic-ray spectrum," *Astron. Astrophys.*, vol. 443, pp. L29–L32, Dec. 2005.

[45] D. Allard, "Extragalactic propagation of ultrahigh energy cosmic-rays," *Astroparticle Physics*, vol. 3940, pp. 33–43, 2012.

[46] R. Aloisio, V. Berezinsky, and P. Blasi, "Ultra high energy cosmic rays: implications of Auger data for source spectra and chemical composition," *JCAP*, vol. 1410, no. 10, p. 020, 2014.

[47] R. Aloisio, V. Berezinsky, and P. Blasi, "Ultra high energy cosmic rays: implications of Auger data for source spectra and chemical composition," *JCAP*, vol. 2014, p. 020, Oct 2014.

[48] V. Berezinsky, M. Kachelrieß, and A. Vilenkin, "Ultrahigh Energy Cosmic Rays without Greisen-Zatsepin-Kuzmin Cutoff," *Phys. Rev. Lett.*, vol. 79, pp. 4302–4305, Dec. 1997.

[49] G. Gelmini, O. E. Kalashev, and D. V. Semikoz, "GZK photons as ultra high energy cosmic rays," *J. Exp. Theor. Phys.*, vol. 106, pp. 1061–1082, 2008.

[50] C. T. Hill, "Monopolonium," *Nuclear Physics B*, vol. 224, no. 3, pp. 469–490, 1983.

[51] K.-H. Kampert and M. Unger, "Measurements of the cosmic ray composition with air shower experiments," *Astroparticle Physics*, vol. 35, pp. 660–678, May 2012.

[52] D. Heck, J. Knapp, J. Capdevielle, G. Schatz, and T. Thouw, "CORSIKA: A Monte Carlo Code to Simulate Extensive Air Showers," 1998.

[53] R. Engel, D. Heck, and T. Pierog, "Extensive air showers and hadronic interactions at high energy," *Annual Review of Nuclear and Particle Science*, vol. 61, no. 1, pp. 467–489, 2011.

[54] W. Heitler, *The Quantum Theory of Radiation*. Dover Books on Physics, Dover Publications, 1954.

[55] A. Letessier-Selvon and T. Stanev, "Ultrahigh energy cosmic rays," *Rev. Mod. Phys.*, vol. 83, pp. 907–942, Sep 2011.

[56] J. Matthews, "A Heitler model of extensive air showers," *Astroparticle Physics*, vol. 22, no. 56, pp. 387 – 397, 2005.

[57] J. Linsley and A. A. Watson, "Validity of scaling to 10^{20} ev and high-energy cosmic-ray composition," *Phys. Rev. Lett.*, vol. 46, pp. 459–463, Feb 1981.

[58] E.-J. Ahn, R. Engel, T. K. Gaisser, P. Lipari, and T. Stanev, "Cosmic ray interaction event generator SIBYLL 2.1," *Phys. Rev. D*, vol. 80, p. 094003, Nov 2009.

[59] S. Ostapchenko, "Monte Carlo treatment of hadronic interactions in enhanced Pomeron scheme: QGSJET-II model," *Phys. Rev. D*, vol. 83, p. 014018, Jan 2011.

[60] S. Ostapchenko, "Air shower development: impact of the LHC data," in *Proceedings, 32nd International Cosmic Ray Conference (ICRC 2011)*, vol. 2, p. 71, 2011.

[61] T. Pierog and K. Werner, "Muon production in extended air shower simulations," *Phys. Rev. Lett.*, vol. 101, p. 171101, Oct 2008.

[62] T. Pierog, I. Karpenko, J. Katzy, E. Yatsenko, and K. Werner, "EPOS LHC: test of collective hadronization with LHC data," *ArXiv e-prints*, 2013.

[63] D. d'Enterria, R. Engel, T. Pierog, S. Ostapchenko, and K. Werner, "Constraints from the first LHC data on hadronic event generators for ultra-high energy cosmic-ray physics," *Astroparticle Physics*, vol. 35, no. 2, pp. 98–113, 2011.

[64] A. Aab *et al.*, "The Pierre Auger Observatory Upgrade - Preliminary Design Report," *ArXiv e-prints*, Apr. 2016.

[65] I. Allekotte *et al.*, "The surface detector system of the Pierre Auger Observatory," *Nuclear Instruments and Methods in Physics Research Section A: Accelerators, Spectrometers, Detectors and Associated Equipment*, vol. 586, pp. 409–420, Mar. 2008.

[66] B. Keilhauer, *Investigation of Atmospheric Effects on the Development of Extensive Air Showers and their Detection with the Pierre Auger Observatory.* PhD thesis, Karlsruhe University, December 2003.

[67] A. Aab *et al.*, "The Pierre Auger Cosmic Ray Observatory," *Nuclear Instruments and Methods in Physics Research Section A: Accelerators, Spectrometers, Detectors and Associated Equipment*, vol. 798, pp. 172–213, 2015.

[68] J. Abraham *et al.*, "Trigger and aperture of the surface detector array of the Pierre Auger Observatory," *Nuclear Instruments and Methods in Physics Research A*, vol. 613, pp. 29–39, Jan. 2010.

[69] K. Kamata and J. Nishimura, "The Lateral and the Angular Structure Functions of Electron Showers," *Progress of Theoretical Physics Supplement*, vol. 6, pp. 93–155, 1958.

[70] K. Greisen, *Progress In Cosmic Ray Physics Vol. 3*, ch. The extensive air showers. North-Holland publishing C°, 1956.

[71] M. Ambrosio, C. Aramo, F. Guarino, D. DUrso, L. Valore, and A. Yushkov, "Total signal at 1000 meters as primary mass sensitive parameter," *Internal GAP-Note 2009-042*, 2009.

[72] J. Abraham *et al.*, "The Fluorescence Detector of the Pierre Auger Observatory," *Nuclear Instruments and Methods in Physics Research Section A: Accelerators, Spectrometers, Detectors and Associated Equipment*, vol. 620, pp. 227–251, Aug. 2010.

[73] J. Zorn, K. Daumiller, M. D. Rio, R. Engel, H.-J. Mathes, R. Smida, L. Tomankova, M. Unger, and D. Veberic, "The first measurement with the FD operated at a reduced PMT gain," *Internal GAP-Note*, 2015.

[74] H. Mathes *et al.*, "The HEAT Telescopes of the Pierre Auger Observatory. Status and First Data," in *Proceedings, 32nd International Cosmic Ray Conference (ICRC 2011)*, 2011.

[75] M. Straub, "Mass composition studies with the low energy extension HEAT at the Pierre Auger Observatory," Master's thesis, RWTH Aachen University, January 2012.

[76] C. Meurer and N. Scharf for the Pierre Auger Collaboration, "HEAT - a low energy enhancement of the Pierre Auger Observatory," *Astrophysics and Space Sciences Transactions*, vol. 7, no. 2, pp. 183–186, 2011.

[77] N. Scharf, *The energy spectrum of cosmic rays measured with the HEAT extension at the Pierre Auger Observatory.* PhD thesis, RWTH Aachen University, November 2013.

[78] D. Ravignani *et al.*, "Measurement of the energy spectrum of cosmic rays above 3×10^{17} eV using the AMIGA 750 m Surface Detector Array of the Pierre Auger Observatory," in *Proceedings, 33rd International Cosmic Ray Conference (ICRC 2013)*, 2013.

[79] J. C. de No, "Monitoring of Camera Positions for Auger Fluorescence Telescopes," Diploma thesis, RWTH Aachen University, March 2008.

[80] S. Schulte, *Autocorrelation Studies of the Arrival Directions of UHECRs measured by the Surface Detector of the Pierre Auger Observatory.* PhD thesis, RWTH Aachen University, July 2011.

[81] S. Cecchini and M. Spurio, "Atmospheric muons: experimental aspects," *Geoscientific Instrumentation, Methods and Data Systems Discussions*, vol. 2, pp. 603–641, Aug. 2012.

[82] P. Abreu *et al.*, "Techniques for measuring aerosol attenuation using the Central Laser Facility at the Pierre Auger Observatory," *Journal of Instrumentation*, vol. 8, no. 04, p. P04009, 2013.

[83] S. BenZvi *et al.*, "The Lidar system of the Pierre Auger Observatory," *Nuclear Instruments and Methods in Physics Research Section A: Accelerators, Spectrometers, Detectors and Associated Equipment*, vol. 574, no. 1, pp. 171–184, 2007.

[84] D. Mandat *et al.*, "AllSky camera for Pierre Auger Observatory - BGcam," *Internal GAP-Note 2011-008*, 2011.

[85] P. Abreu *et al.*, "Identifying clouds over the Pierre Auger Observatory using infrared satellite data," *Astroparticle Physics*, vol. 5052, pp. 92 – 101, 2013.

[86] P. Abreu *et al.*, "Description of atmospheric conditions at the Pierre Auger Observatory using the Global Data Assimilation System (GDAS)," *Astroparticle Physics*, vol. 35, no. 9, pp. 591–607, 2012.

[87] C. Tomasi, V. Vitale, B. Petkov, A. Lupi, and A. Cacciari, "Improved algorithm for calculations of rayleigh-scattering optical depth in standard atmospheres," *Appl. Opt.*, vol. 44, pp. 3320–3341, Jun 2005.

[88] C. M. Will, *Atmospheric Monitoring for Ground-Based Cosmic Ray Detectors*. PhD thesis, Karlsruhe Institute of Technology, June 2012.

[89] J. Abraham *et al.*, "A study of the effect of molecular and aerosol conditions in the atmosphere on air fluorescence measurements at the Pierre Auger Observatory," *Astroparticle Physics*, vol. 33, pp. 108–129, Mar. 2010.

[90] M. Buscemi *et al.*, "Update of the Aerosol Database May 2013," *Internal GAP-Note 2013-048*, 2013.

[91] M. Ave *et al.*, "Spectrally resolved pressure dependence measurements of air fluorescence emission with AIRFLY," *Nuclear Instruments and Methods in Physics Research Section A: Accelerators, Spectrometers, Detectors and Associated Equipment*, vol. 597, no. 1, pp. 41–45, 2008.

[92] M. Ave *et al.*, "Precise measurement of the absolute fluorescence yield of the 337 nm band in atmospheric gases," *Astroparticle Physics*, vol. 42, pp. 90–102, 2013.

[93] M. Giller, G. Wieczorek, A. Kacperczyk, H. Stojek, and W. Tkaczyk, "Energy spectra of electrons in the extensive air showers of ultra-high energy," *Journal of Physics G: Nuclear and Particle Physics*, vol. 30, no. 2, p. 97, 2004.

[94] F. Nerling, J. Blümer, R. Engel, and M. Risse, "Universality of electron distributions in high-energy air showers-Description of Cherenkov light production," *Astroparticle Physics*, vol. 24, no. 6, pp. 421–437, 2006.

[95] M. Roberts, "The role of atmospheric multiple scattering in the transmission of fluorescence light from extensive air showers," *Journal of Physics G: Nuclear and Particle Physics*, vol. 31, no. 11, p. 1291, 2005.

[96] D. Góra, R. Engel, D. Heck, P. Homola, H. Klages, J. Pękala, M. Risse, B. Wilczyńska, and H. Wilczyński, "Universal lateral distribution of energy deposit in air showers and its application to shower reconstruction," *Astroparticle Physics*, vol. 24, no. 6, pp. 484–494, 2006.

[97] M. Giller and G. Wieczorek, "Influence of the scattered Cherenkov light on the width of shower images as measured in the EAS fluorescence experiments," *Astroparticle Physics*, vol. 31, no. 3, pp. 212–219, 2009.

[98] T. K. Gaisser and A. M. Hillas, "Reliability of the method of constant intensity cuts for reconstructing the average development of vertical showers," *International Cosmic Ray Conference*, vol. 8, pp. 353–357, 1977.

[99] M. Unger, B. Dawson, R. Engel, F. Schüssler, and R. Ulrich, "Reconstruction of longitudinal profiles of ultra-high energy cosmic ray showers from fluorescence and Cherenkov light measurements," *Nuclear Instruments and Methods in Physics Research Section A: Accelerators, Spectrometers, Detectors and Associated Equipment*, vol. 588, no. 3, pp. 433–441, 2008.

[100] H. Barbosa, F. Catalani, J. Chinellato, and C. Dobrigkeit, "Determination of the calorimetric energy in extensive air showers," *Astroparticle Physics*, vol. 22, no. 2, pp. 159–166, 2004.

[101] A. G. Mariazzi *et al.*, "A new method for determining the primary energy from the calorimetric energy of showers observed in hybrid mode on a shower-by-shower basis," in *Proceedings, 32nd International Cosmic Ray Conference (ICRC 2011)*, vol. 2, p. 161, 2011.

[102] M. J. Tueros *et al.*, "Estimate of the non-calorimetric energy of showers observed with the fluorescence and surface detectors of the Pierre Auger Observatory," in *Proceedings, 33rd International Cosmic Ray Conference (ICRC 2013)*, 2013.

[103] V. Verzi *et al.*, "The Energy Scale of the Pierre Auger Observatory," in *Proceedings, 33rd International Cosmic Ray Conference (ICRC 2013)*, 2013.

[104] F. Sanchez *et al.*, "The AMIGA detector of the Pierre Auger Observatory: an overview," in *Proceedings, 32nd International Cosmic Ray Conference (ICRC 2011)*, 2011.

[105] A. Aab *et al.*, "Prototype muon detectors for the AMIGA component of the Pierre Auger Observatory," *Journal of Instrumentation*, vol. 11, no. 02, p. P02012, 2016.

[106] J. L. Kelley *et al.*, "AERA: the Auger Engineering Radio Array," in *Proceedings, 32nd International Cosmic Ray Conference (ICRC 2011)*, 2011.

[107] A. Aab *et al.*, "Probing the radio emission from air showers with polarization measurements," *Phys. Rev. D*, vol. 89, p. 052002, Mar 2014.

[108] R. Engel *et al.*, "Upgrade of the Pierre Auger Observatory (AugerPrime)," in *The Pierre Auger Observatory: Contributions to the 34th International Cosmic Ray Conference (ICRC 2015)*, 2015.

[109] S. Argirò *et al.*, "The offline software framework of the Pierre Auger Observatory," *Nuclear Instruments and Methods in Physics Research Section A: Accelerators, Spectrometers, Detectors and Associated Equipment*, vol. 580, no. 3, pp. 1485–1496, 2007.

[110] A. Porcelli, *Measurement of the Depth of Shower Maximum in the Transition Region between Galactic and Extragalactic Cosmic Rays with the Pierre Auger Observatory.* PhD thesis, Karlsruhe Institute of Technology, June 2014.

[111] A. Porcelli *et al.*, "Measurements of X_{max} above 10^{17} eV with the fluorescence detector of the Pierre Auger Observatory," in *The Pierre Auger Observatory: Contributions to the 34th International Cosmic Ray Conference (ICRC 2015)*, 2015.

[112] J. Brack *et al.*, "Auger Fluorescence Detector Absolute Calibration January and June 2010," *Internal GAP-Note 2010-118*, 2010.

[113] B. Gookin *et al.*, "November Absolute Calibration, Addendum to GAP 2010-118," *Internal GAP-Note 2011-037*, 2011.

[114] F. Meyer and F. Vernotte, "Time tagging tests in Besancon Observatory," *Internal GAP-Note 2001-050*, 2001.

[115] M. Settimo, L. Perrone, G. Cataldi, I. De Mitri, and D. Martello, "Parameterisation of the "Lateral Trigger Probability" functions at low energies," *Internal GAP-Note 2007-069*, 2007.

[116] S. Falk, D. Kruppke-Hansen, H.-J. Mathes, S. Müller, R. Ulrich, and M. Unger, "A First Look at HEAT Data ," *Internal GAP-Note 2010-123*, 2010.

[117] E. J. Ahn, J. Bellido, S. BenZvi, R. Engel, F. Schüssler, R. Ulrich, and M. Unger, "Measurement of the Depth of Shower Maximum of Cosmic Rays above 1 EeV," *Internal GAP-Note 2009-078*, 2009.

[118] J. Abraham *et al.*, "Measurement of the depth of maximum of extensive air showers above 10^{18} eV," *Phys. Rev. Lett.*, vol. 104, p. 091101, Mar 2010.

[119] The Pierre Auger collaboration, "Interpretation of the depths of maximum of extensive air showers measured by the Pierre Auger Observatory," *JCAP*, vol. 2013, no. 02, p. 026, 2013.

[120] T. Bergmann *et al.*, "One-dimensional hybrid approach to extensive air shower simulation," *Astroparticle Physics*, vol. 26, pp. 420–432, 2007.

[121] T. Pierog *et al.*, "First Results of Fast One-dimensional Hybrid Simulation of EAS Using CONEX," *Nucl. Phys. Proc. Suppl.*, vol. 151, pp. 159–162, 2006.

[122] J. Bellido. private communication, 2015.

[123] M. Unger. private communication, 2015.

[124] V. Verzi. private communication, 2015.

[125] B. Dawson *et al.*, "Proposal for an update of the Auger Energy Scale," *Internal GAP-Note 2012-124*, 2012.

[126] S. Andringa, R. Conceicao, and M. Pimenta, "Mass composition and cross-section from the shape of cosmic ray shower longitudinal profiles," *Astroparticle Physics*, vol. 34, no. 6, pp. 360–367, 2011.

[127] K. Cranmer, "Kernel estimation in high-energy physics," *Computer Physics Communications*, vol. 136, no. 3, pp. 198 – 207, 2001.

[128] W. Verkerke and D. Kirkby, "The RooFit toolkit for data modeling," *ArXiv Physics e-prints*, June 2003.

[129] K. A. Olive *et al.*, "Review of Particle Physics," *Chin. Phys. C*, vol. 38, p. 090001, 2014.

[130] M. Unger and J. Bellido, "Supplementary Material for the 'long X_{max} Paper'," *Internal Note*, August 2014.

[131] J. Pekala, P. Homola, B. Wilczynska, and H. Wilczynski, "Atmospheric multiple scattering of fluorescence and Cherenkov light emitted by extensive air showers," *Nuclear Instruments and Methods in Physics Research Section A: Accelerators, Spectrometers, Detectors and Associated Equipment*, vol. 605, no. 3, pp. 388–398, 2009.

[132] M. Unger, R. Engel, F. Schüssler, and R. Ulrich, "Lateral shower light distributions in the Cherenkov-Fluorescence-Matrix Profile Reconstruction," *Internal GAP-Note 2008-052*, 2008.

[133] K. Louedec and J. Colombi, "Effect of the aerosol size on multiple scattering Proposal for an updated systematic uncertainty on energy and depth of maximum," *Internal GAP-Note 2013-116*, 2013.

[134] S. Falk, R. Engel, R. Ulrich, and M. Unger, "Telescope Alignment Studies," *Internal GAP-Note 2011-123*, 2011.

[135] C. De Donato *et al.*, "Using star tracks to determine the absolute pointing of the Fluorescence Detector telescopes," *Internal GAP-Note 2005-008*, 2005.

[136] M. Prouza *et al.*, "Star tracking using background data of FD telescopes," *Internal GAP-Note 2005-041*, 2005.

[137] M. Scuderi *et al.*, "Alignment method of the P. Auger Observatory fluorescence telescopes based on the Central Laser Facility events," *Internal GAP-Note 2006-061*, 2006.

[138] P. Younk and B. Fick, "FD Telescope Alignment Using CLF Laser Shots," *Internal GAP-Note 2006-087*, 2006.

[139] E. Varela, H. Salazar, and J. Bellido, "HEAT-Co Systematics due to the SD/FD time offset," *Talk - Pierre Auger Analysis Meeting 2013*, 2013.

[140] J. Bäuml *et al.*, "Measurement of the Optical Properties of the Auger Fluorescence Telescopes," in *Proceedings, 33rd International Cosmic Ray Conference (ICRC 2013)*, 2013.

[141] M. Unger, J. Bäuml, R. Engel, and R. Ulrich, "Simulation of the Point Spread Function of the FD Telescopes and its Effect on the Reconstructed Energy and X_{max}," *Internal GAP-Note 2013-069*, 2013.

[142] S. P. Knurenko and A. Sabourov, "The depth of maximum shower development and its fluctuations: cosmic ray mass composition at $E_0 \geq 10^{17}$ eV," *Astrophysics and Space Sciences Transactions*, vol. 7, no. 3, pp. 251–255, 2011.

[143] S. P. Knurenko and A. Sabourov, "Study of cosmic rays at the Yakutsk EAS array: Energy spectrum and mass composition," *Nuclear Physics B - Proceedings Supplements*, vol. 212–213, pp. 241–251, 2011.

[144] T. Abu-Zayyad *et al.*, "Measurement of the Cosmic-Ray Energy Spectrum and Composition from 10^{17} to $10^{18.3}$ eV Using a Hybrid Technique," *Astrophys. J.*, vol. 557, no. 2, pp. 686–699, 2001.

[145] R. U. Abbasi *et al.*, "Indications of Proton-Dominated Cosmic-Ray Composition above 1.6 EeV," *Phys. Rev. Lett.*, vol. 104, p. 161101, Apr 2010.

[146] P. Tinyakov *et al.*, "Latest results from the telescope array," *Nuclear Instruments and Methods in Physics Research Section A: Accelerators, Spectrometers, Detectors and Associated Equipment*, vol. 742, pp. 29–34, 2014.

[147] R. Abbasi *et al.*, "Study of Ultra-High Energy Cosmic Ray composition using Telescope Arrays Middle Drum detector and surface array in hybrid mode," *Astroparticle Physics*, vol. 64, pp. 49–62, 2015.

[148] S. Buitink *et al.*, "A large light-mass component of cosmic rays at 10^{17} - $10^{17.5}$ eV from radio observations," *Nature*, vol. 531, p. 70, 2016.

[149] E. Bertin, "Global fluctuations and gumbel statistics," *Phys. Rev. Lett.*, vol. 95, p. 170601, Oct 2005.

[150] M. De Domenico, M. Settimo, S. Riggi, and E. Bertin, "Reinterpreting the development of extensive air showers initiated by nuclei and photons," *JCAP*, vol. 1307, p. 050, 2013.

[151] G. Cowan, *Statistical Data Analysis*. Oxford science publications, Clarendon Press, 1998.

[152] W. A. Rolke, A. M. Lopez, and J. Conrad, "Limits and confidence intervals in the presence of nuisance parameters," *Nucl. Instrum. Meth.*, vol. A551, pp. 493–503, 2005.

[153] R. Brun and F. Rademakers, "{ROOT} - An object oriented data analysis framework," *Nuclear Instruments and Methods in Physics Research Section A: Accelerators, Spectrometers, Detectors and Associated Equipment*, vol. 389, no. 12, pp. 81 – 86, 1997.

[154] T. K. Gaisser, T. Stanev, and S. Tilav, "Cosmic Ray Energy Spectrum from Measurements of Air Showers," *Front.Phys.China.*, vol. 8, pp. 748–758, 2013.

[155] M. Urban, "Investigation of the Mass Composition of Ultra High Energy Cosmic Rays with the Pierre Auger Observatory," Master's thesis, RWTH Aachen University, September 2013.

[156] M. Urban, M. Erdmann, and D. Kümpel, "Investigation of the Mass Composition using the Gumbel Parameterization for X_{max}," *Internal GAP-Note 2014-009*, 2014.

Acknowledgements

Firstly, I would like to thank my supervisor Prof. Dr. Thomas Hebbeker for the opportunity to take part in his research group and at the Pierre Auger Observatory. His support, experience and criticism helped me very much to develop and perform this analysis. I'm also very thankful for the various opportunity to present current research results at conferences and to travel to many collaboration meetings. In addition, I would like to thank Prof. Dr. Christopher Wiebusch, who agreed to be the co-corrector of this thesis.

Furthermore, I need to thank the mass composition group and especially its task leaders Jose Bellido and Alexey Yushkov. I learned a lot during the sessions and corresponding discussions. In this context, my special thanks also go to Michael Unger, for all the help with my analysis and software issues and as well for the help in the data reconstruction and simulation processes. I also want to thank my X_{max} working group colleagues Tom Harrison and Alessio Porcelli for all the fruitful discussions and the joined effort to publish our current mass composition results.

Additionally, I want to thank the whole Aachen Auger group and all colleagues of the Physics Institute IIIA and IIIb of the RWTH Aachen University for the wonderful time. I enjoyed both to work with you all professional and to spend time with you besides work. Thank you all for the pleasant working atmosphere.
For the critical proofreading of this thesis, I give my special thanks to Christine Peters, Markus Lauscher, Tim Niggemann and Larissa Paul, for all their patience and the helpful comments.

Last but not least, I'm very grateful to my wife Larissa, who helped me keeping up the whole time. Also many thanks go to my parents and my brother for their encouragement and support to study physics.